ASSESSMENT OF GEOTHERMAL POTENTIALS OVER PART OF NORTHERN NIGERIA USING AEROMAGNETIC AND RADIOMETRIC DATA

BY

ORAJIUKA, RITA CHIUGO
(NSU/PHD/GEP/0010/18/19)

Ph.D. PHYSICS (APPLIED GEOPHYSICS)

MAY, 2024

ASSESSMENT OF GEOTHERMAL POTENTIALS OVER PART OF NORTHERN NIGERIA USING AEROMAGNETIC AND RADIOMETRIC DATA

BY

ORAJIUKA, Rita Chiugo

(NSU/PHD/GEP/0010/18/19)

A THESIS SUBMITTED TO THE SCHOOL OF POSTGRADUATE STUDIES, NASARAWA STATE UNIVERSITY KEFFI, IN PARTIAL FULFILMENT OF THE REQUIREMENTS FOR THE AWARD OF DEGREE OF DOCTOR OF PHILOSOPHY (PHD) IN PHYSICS (APPLIED GEOPHYSICS)

DEPARTMENT OF PHYSICS

FACULTY OF NATURAL AND APPLIED SCIENCES

NASARAWA STATE UNIVERSITY, KEFFI

NIGERIA

DECLARATION

I hereby declare that this thesis has been written by me and it is a report of my research work. It has not been presented in any previous applications for Doctor of Philosophy in Physics (Applied Geophysics). All quotations are indicated and sources of information specifically acknowledged by means of references.

Orajiuka Rita Chiugo
NSU/PHD/GEP/0010/18/19

29/05/24
Date

CERTIFICATION

The Thesis "Assessment of Geothermal Potentials over part of Northern Nigeria using Aeromagnetic and Radiometric Data" meets the regulations governing the award of Doctor of Philosophy in Physics (Applied Geophysics), of the School of Postgraduate Studies, Nasarawa State University, Keffi, and is approved for its contribution to knowledge.

Prof. Charles O. Ofoegbu Chairman, Supervisory Committee	13/5/2024 Date
Prof. Abu Mallam Member, Supervisory Committee	13/5/2024 Date
Dr. Ibrahim Umar Head of Department	13/05/2024 Date
Prof. Lucas W. Lumbi Internal Examiner	13/05/2024 Date
Prof. Makwin D. Makut Dean of Faculty	13/05/2024 Date
Prof. Nasir K. Abdullahi External Examiner	13/05/2024 Date
Prof. Maikano M. Ari Dean, School of Postgraduate Studies	13/05/24 Date

DEDICATION

This work is dedicated in honour of Mr and Mrs Horatus Orajiuka of Blessed Memory for their love and efforts towards my education.

ACKNOWLEDGEMENTS

My sincere gratitude goes to the Almighty God for His sustenance and strength to embark on this academic journey.

My profound gratitude to the members of the supervisory committee, Prof. Charles Ofoegbu and Prof. Abu Mallam for their constructive reviews and directives.

I want to specially thank the Head and the entire staff of Physics Department for their support and encouragement.

To Dr. Samsom Yusuf, I appreciate all your guidance and corrections.

To my family and friends especially Nora Gideon, Henry Gideon, Amarachi Orajiuka. Dr. Taiwo Adewunmi, Mr. Tunde Adeyemo, Mr. Tomiwa Akanbi, Mr. Micheal Ebiem, Chinyere Chikwendu, Chidiebere Okeke, Gloria Aigbe, Onyinye Adindu, Kenechukwu Osonwa, Chukwuka Ossai, Helen Akeh, Cyprain Oligbi, thank you for your prayers and support.

ABSTRACT

Uninterrupted energy supply has been an issue in Nigeria and decentralizing our grids with an alternate and renewable energy source such as geothermal energy is a solution. This study aimed to assess the geothermal potentials in parts of Northern Nigeria using aeromagnetic and radiometric data. In the research, high-resolution aeromagnetic and radiometric data covering between latitudes 7.5°N and 10.0°N and longitudes 7.5°E and 10.0°E and a total of 25 aeromagnetic sheets from Northern Nigeria were used to conduct the research. The data is first processed to obtain detailed information on the geological structure of the region using various digital processing techniques. The region is fundamentally underlain by structures associated with the Pan-African Orogeny and an intra-cratonic rift structure that has been compressionally folded. The Curie Point Depth (CPD) of the area was determined using spectral analysis technique and the result ranges from 7.47 km to 29.34km with a mean value of 18.59km. The geothermal gradient ranges from 19.768°C/km to 77.64°C/km with a mean value of 34.29°C/km while the heat flow (Q) ranges from 49.62 mW/m^2 to 194.88 mW/m^2 with a mean value of 86.07 mW/m^2. The result of the radiometric interpretation shows a radiogenic heat production of about 5.2$\mu W/m^3$. These results show anomalous heat flow in parts of the study area which can be suitable geothermal sites thus enabling the development of geothermal energy sources in Nigeria. This will contribute towards energy security and economic development in the country.

TABLE OF CONTENTS

Title Page		i
Declaration		ii
Certification		iii
Dedication		iv
Acknowledgement		v
Abstract		vi
Table of Contents		vii
List of Tables		xi
List of Figures		xiii

CHAPTER ONE

INTRODUCTION

1.1.	Background to the Study	1
1.2.	Statement of the Problem	3
1.3.	Aim of the Study	4
1.4.	Objectives of the Study	4
1.5.	Significance of the Study	5
1.6.	Scope of the Study	5
1.7.	Definition of Operational Terms	6

CHAPTER TWO

LITERATURE REVIEW

2.1 Conceptual Framework 9

2.1.1. Rock Magnetism 9

2.1.2. Demagnetization 9

2.1.3. Magnetic Method 10

2.1.4. Magnetic Susceptibility 10

2.1.5. Aeromagnetic Survey 13

2.1.6. Magnetic Anomaly 14

2.1.7. Curie Point Temperature 15

2.1.8. Radiometric Method 15

2.2. Empirical Review 16

2.2.1. Previous Studies in the Area 31

2.2.2. General Geology 36

2.2.2.1. Geology of the Study Area 39

2.2.2.2. The Benue Trough 42

2.2.3. The Basement Complex 44

2.2.4. The Sedimentary Formations 45

2.2.4.1. The Lafia Formation 48

2.2.4.2. The Agwu Formation 48

2.2.4.3. The Ezeaku Group 48

2.2.4.4. The Awe Formation 48

2.2.4.5. The Keana Formation 49

2.2.4.6. The Nkporo Formation 49

2.2.4.7. The Asu River Group 49

2.2.4.8. The Bima Sandstone 50

2.2.5. The Geothermal System 50

2.2.6. The Hydrothermal Resources 53

2.2.6.1. The Geysers 53

2.2.6.2. Hot Springs 54

2.2.6.3. Fumaroles 54

2.3. Theoretical Framework 55

2.3.1 The Spectral Method 55

2.3.2. The Derivatives 56

2.3.3. Analytic Signal 58

2.3.4. The Curie Point Depth 60

2.3.5. The Centroid Method 60

2.3.6. The Geothermal Gradient and Heat Flow Determination 62

2.3.7. Radiometric Theory 63

2.3.8. The Shuttle Radar Topographic Mission 64

CHAPTER THREE

MATERIALS AND METHODS

3.1. Materials 65

3.2. Methods 65

3.2.1. Location of the Study 65

3.2.2. Method of Data Acquisition 67

3.2.3. Method of Data Analysis 67

CHAPTER FOUR

DATA PRESENTATION AND ANALYSIS

4.1. Data Presentation 69

4.2. Data Analysis 71

4.2.1. Reduction of TMI to the Equator 71

4.2.2. The Derivatives 73

4.2.3. The Analytic Signal 80

4.2.4. The CET Grid Analysis 82

4.2.5. Shuttle Radar Topographic Mission 84

4.2.6. Analysis of the CPD, Gradient and Heat Flow 86

4.2.7. Analysis of Radiometric Data 98

4.2.8. Discussion of Findings 111

CHAPTER FIVE

SUMMARY, CONCLUSION AND RECOMMENDATION

5.1. Summary 117

5.2. Conclusion 119

5.3. Recommendations 121

5.4. Limitations of the Study 121

5.5. Suggestions for Further Studies 122

References 123

Appendix

LIST OF TABLES

Table 2.1:	Common Rock Types	12
Table 4.1:	Result of the Estimated Values of Z_0, Z_t and Z_b for 81 Spectral Blocks	87
Table 4.2:	Statistical Analysis of the Radioelements across the Rock Profiles	107
Table 4.3:	Radiogenic Heat Production Values across 70 Rock Profiles	109

LIST OF FIGURES

Fig. 2.1:	Geological Map of Nigeria Showing the Study Area	37
Fig. 2.2:	Geological Map of the Study area	41
Fig. 2.3:	Stratigraphy across Benue Trough	43
Fig. 2.4:	Stratigraphy Succession of Middle Benue Trough	47
Fig. 2.5:	A Typical Geothermal System	52
Fig. 3.1:	The Location Map of the Study Area	66
Fig. 4.1:	The Total Magnetic Intensity Map of the Study Area	70
Fig. 4.2:	The TMI Reduced to the Equator	72
Fig. 4.3:	The First Vertical Derivative Map	74
Fig. 4.4a:	The Horizontal Derivative Map in X-Direction	75
Fig. 4.4b:	The Horizontal Derivative Map in Y-Direction	76
Fig. 4.4c:	The Tilt Derivative	78
Fig. 4.4d:	The Total Horizontal Derivative	79
Fig. 4.5:	The Analytic Signal Map of the Study Area	81
Fig. 4.6a:	Lineament Map of the Study Area	83
Fig. 4.6b:	Rose Diagram showing Lineament Trends	83
Fig. 4.7:	Shuttle Radar Topographic Mission Map	85
Fig. 4.8:	Graph of Block b1 and b2	89
Fig. 4.9:	Graph of b3 and b4 Showing the Determined Values of Z_o & Z_t	90
Fig. 4.10:	Curie Point Depth Map	91
Fig. 4.11:	Geothermal Gradient Map of the Study Area	93
Fig. 4.12:	Heat Flow Map of the Study Area	94

Fig. 4.13:	3D Surface Anomaly Map of the Study Area	95
Fig. 4.14:	Water Shed showing the Direction of Flow	96
Fig. 4.15:	Plot of CPD against Heat Flow	97
Fig. 4.16:	Equivalent Potassium Concentration Map	99
Fig. 4.17:	Equivalent Thorium Concentration Map	100
Fig. 4.18:	Equivalent Uranium Concentration Map	101
Fig. 4.19:	Potassium –Thorium Ratio Map	104
Fig. 4.20:	Ternary Map of the Study Area	105
Fig. 4.21:	Radiogenic Heat Production Map	106

LIST OF APPENDIX

Appendix A: (Spectral Plots of 81 Overlapping Blocks (55km by 55km) 139

CHAPTER ONE

INTRODUCTION

1.1 Background to the Study

Energy is needed for human activity on a regular basis. For a country, it is vital for infrastructural development, economic growth, security, poverty eradication and job creation. Most countries suffer from uninterrupted energy supply and that has affects their future economic growth which depends on a sustainable, accessible and environmentally friendly (Abraham & Nkitnam, 2017). If energy cannot be accessed, then poverty and deprivation sets in causing a decline in the economy. Just as in poverty eradication, energy can be linked Energy with the socioeconomic development including education and health (Oyedepo, 2012).

PricewaterhouseCoopers (PwC) confirmed in 2016 that Nigeria had one of the lowest usages of electricity per capital in Africa. The majority of the energy we use comes from traditional fossil fuels like coal, oil, diesel, natural gas, kerosene, etc. Fossil fuels are depleting, but they also exacerbate environmental issues by releasing toxic by-products that worsen pollution and cause global warming. It is necessary to investigate more dependable energy producing sources.

Geothermal energy can be utilized directly as a renewable energy source to generate electricity. It is produced by the heat that is contained under the surface. As stipulated by Downing and Gray (1986), geothermal energy is a combination of energy from the formation of the earth and from the radioactive decay of the isotopes (uranium, thorium and potassium) found within the Precambrian basement rocks.

Different geodynamic processes, like lineaments from tectonic activities manifesting in the surface and some geothermal resources, occur during rifting. The magma is rising to the surface, which explains why when examining the rift zones' evolution and dynamics, discontinuities like faults and fractures are crucial (Komolafe *et al.*, 2012).

Onwuemesi (1997) stipulates that when it comes to geothermal investigation, the subsurface is our interest because the subsurface holds information about the heat sources and geothermal

reservoirs that are needed to produce heat energy. The temperature at the surface is relatively low but as you go deeper into the earth it increases due to the combination of residual heat from the earth's formation and the radioactive decay of Uranium, Potassium and Thorium.

The Curie point depth refers to that point where the temperature of the rocks in the crust is higher than the Curie temperature of magnetic minerals, which causes them to lose their magnetic properties. Curie point depth (CPD) using a magnetic anomaly map can also be seen as the deepest level where we get discernible signatures in the crust, according to Spector and Grant (1970).

In areas where the temperature gradient is high, there is greater potential for geothermal energy production. To access the heat and convert it to usable energy, we need to drill into the subsurface and harness the hot rock or fluid. Although not all subsurface reservoirs are suitable for geothermal energy production, the reservoir must be fractured, with a sufficient depth, temperature and permeability to allow the fluids to flow.

Therefore, understanding the subsurface geology and thermal structures of the region which might serve as conduits, are crucial for identifying areas with geothermal potential and for assessing the viability of geothermal energy production.

The hottest geothermal regions are typically found along major plate boundaries where earthquakes and volcanoes are concentrated. According to Ikumbar *et al.* (2013), mantle plumes, subduction zones, and rift zones contain geothermal regions with sufficient heat flow to support power plants. Therefore, we selected the Nigerian Benue Trough, a large geological feature in West Africa that makes up almost half of the research region and is a Rift Basin.

Considering the growing disparity between Nigeria's energy supply and demand as well as the need to preserve a greener environment, it is necessary to shift to a more sustainable and cleaner energy source (such as geothermal energy). Thus, this study makes use of radiometric and

magnetic information from aircraft to evaluate the geothermal potentials in several regions of Northern Nigeria.

1.2 Statement of the Problem

Nigeria is faced with several confrontations in the electricity sector which impacts the availability, reliability and distribution of electricity to its population. Nigeria struggles with inadequate electricity generation to meet the growing demand. Because the current power plants are not operating at full capacity, there are regular power disruptions and load shedding. Many people in Nigeria still do not have access to consistent energy. According to the World Bank. as of 2020, Nigeria's electricity consumption is one of the lowest (115.33 kWh) approximately 57%, leaving a large portion of the population without reliable power supply (USAID, 2020). While Nigeria has significant renewable energy potentials, integrating them into our grid has been limited. Despite its physical manifestations, geothermal energy is yet to be fully utilized in Nigeria. Using data from drilling wells, numerous analyses are being conducted on the subsurface temperature distribution of rock mass in sedimentary basins and the basement (Abraham *et al.*, 2014).

Nevertheless, no additional efforts have been made in the design and development, and this is still having an impact on the power industry. For this reason, Nigeria should begin exploring its geothermal potential in order to supply the nation's growing energy needs.

In an effort to prevent global warming and safeguard the environment, countries are now looking to alternative energy sources to meet their energy needs. A lot of Gases are being flared daily which releases some volatile organic compounds and other greenhouse gases to the atmosphere. As pointed out by Seiyaboh and Izah (2017a), these harmful gases not only pollute the environment but also cause respiratory problems, cardiovascular issues and other health impacts on nearby communities. The heavy metals and toxic chemicals found in them destroy our

vegetation, contaminate the water bodies and make our soil unproductive for farming. This in turn creates a negative impact on our ecosystems and biodiversity.

As the population of the country increases and the existing energy source can no longer satisfy the needs of the people, it is necessary to look into another source of energy that the country is endowed with which can sustain and meet the need of the country. Renewable energy resources like geothermal energy which is clean and sustainable must be explored to support the existing hydropower.

Nigeria's energy shortage, which has been a dynamic dilemma and a threat to the nation's economy, must thus be addressed with renewable energy alternatives. This can also solve the issue of impending industrialization as well as an enabling environment that forces many businesses to operate at a loss and maintains blackouts in many individual residences (Obande *et al.*, 2013).

1.3 Aim of the Study

The research study targets assessing geothermal attributes in parts of Northern Nigeria using aeromagnetic and aero-radiometric geophysical methods.

1.4 Objectives of the Study

The outlined objectives of the research are as follows:

I. Determine the centroid depth and the depth to the top of the magnetic basement;
II. Calculate Curie Point Depth;
III. Ascertain the trends and patterns of the lineaments;
IV. Calculate the area's geothermal gradient;
V. Estimate the heat flowing in the region;
VI. Estimate the region's production of radiogenic heat

1.5 Significance of the Study

The study is noteworthy because it intends assessing the geothermal potential zones in some Northern part of Nigeria by interpreting the airborne magnetic and radiometric datasets. This can serve as a backbone to our existing grids.

Geothermal energy has attracted increasing attention as an effective addition to the national grids of countries, even in Africa. The outcome of this research would be valuable to generation and distribution companies in Nigeria in solving its energy crisis and for private investors who might want to explore its direct use.

The Earth's heat is thought to be restricted; technology and related expenses are the only things limiting its utilization, but there is still plenty of potential for it to produce energy that humans can use. Geothermal energy is constantly available and thus the generation of electricity is achieved at a low cost and with high efficiency (Gupta *et al.*, 2016). For more than a billion years to come, the earth's continuous heat flux guarantees an endless supply of energy. Numerous nations are demanding an energy transformation as they recognize the benefits of geothermal power as a flexible and base-load renewable energy source.

We need to understand that in a magnetic layer of the lithosphere, the variations seen at the bottom can be used for structural interpretation in that region. Understanding the spatial differences in depth, heat flow, gradient, and radiogenic heat produced in the research area can help comprehend the region's thermal structures.

As more states and regions of the world discover the potential and opportunity, production will become viable in more of them. This will create business opportunities that will strengthen the nation's economy, and help to alleviate poverty in the region.

1.6 Scope of the Study

Using 25 aeromagnetic and aero-radiometric data sheets, the investigation was conducted in a few chosen locations in Northern Nigeria. Eight states will be included in the study: FCT,

Nasarawa, Kaduna, Bauchi, Plateau, Taraba, Benue, and Kogi. In these regions, the depths, gradients, and heat values were ascertained through the application of the spectrum analysis method. The amount of radiogenic heat generated in the region was computed using the radiometric approach.

1.7 Definition of Operational Terms

Magnetic Field: A magnetic field is an electric charge that is in motion and is subject to magnetic force. It explains the distribution of a magnetic force inside and outside of a magnetic material.

Magnetic Susceptibility: The ease with which a material becomes magnetized or reacts to an external field is known as its magnetic susceptibility.

Magnetic Anomaly: A change brought on by differences in the magnetism of rocks found in the crust.

Total Magnetic Intensity (TMI): a measure of the intensity of the magnetic field caused by different rock minerals.

Spectral Analysis: it is a vital tool used in interpreting the frequency constituents of the magnetic field beneath the subsurface.

High-Resolution Aeromagnetic Data (HRAD): They are data acquired using an aircraft through a magnetometer that measure and also record the intensities of the magnetic field.

International Geomagnetic Reference Field (IGRF): it is a mathematical coefficient or standard used in describing Earth's main field.

Renewable Energy: An energy type that comes from natural resources, which can be regenerated more quickly than they are used up.

Geothermal Energy: this is the energy derived from the crust's interior heat. It combines the energy from the planet's creation with the radioactive decay of radioelement isotopes.

Geothermal Reservoir: is a fractured or porous rock formation through which the heat from the surface can be harnessed and made economically profitable.

Geothermal Gradient: This can be understood as how the Earth's internal temperature rises with depth.

Hydrothermal Alteration: is defined as a geological process that occurs when rocks or minerals interact with hydrothermal fluids changing their physical and chemical compositions.

Gamma Ray Spectroscopy: Gamma ray spectrometry also known as the radiometric method is a scientific technique used in determining the age of rocks, minerals, heat production, and other geological applications. It determines the natural radio element distribution on the surface.

Curie Point Depth: The depth where temperature of the rocks in the crust is higher than the magnetic minerals' curie temperature, which results in the loss of the minerals' magnetic characteristics.

Sedimentary Basin: a low point in the crust of the planet where sediments have accumulated and subsidence has happened.

Lineaments: can be described as a linear feature on the earth's surface such as faults or fractures.

Stratigraphy: is a field of geology that examines the various strata (rock layers) and how they are layered; it is used to describe and categorize the age and composition of rocks.

Wavelength: is the separation of two identical wave crests or troughs, whether they are electromagnetic, sound, or any other type of wave.

Amplitude: is the amount or magnitude of energy transferred by a wave. It is the highest distance between the peak or trough of the wave and the equilibrium position.

Frequency: the quantity of waves oscillating in a given time, expressed in Hertz.

Geysers: a vent that periodically ejects turbulent water out of it while also producing steam.

Hot springs: produced when underground water that has been heated emerges onto the surface of the Earth. Either shallow pools of molten rock or faults that go to hot rock deep within the crust heat the groundwater.

Fumaroles: Fumaroles are hydrothermal features that occur when steam and volcanic gases escape from openings in the Earth's crust. They are often associated with volcanic activity and are commonly found in areas with active or dormant volcanoes, geothermal fields, and geologically active regions.

Centre for Exploration Targeting (CET): This grid is a crucial tool for identifying linear discontinuities and structural edges in data related to gravity and magnetic fields.

Fractures: are discontinuities in mechanical characteristics and displacement where cohesiveness of rocks or minerals is weakened.

Faults: a discontinuity or fracture caused by a substantial shift in a volume of rock resulting from the movement of the rock mass.

Shuttle Radar Topographic Mission (SRTM): is a high-resolution elevation data that is crucial for mapping and visualizing the topography of a geothermal area. This data shows regions with elevated surface temperatures that can help us identify the faulted pathways which can serve as conduits for fluids and heat.

Radiogenic Heat Production (RHP): is a physical metric that is derived indirectly from the amount of the major radiogenic elements (K, Th, and U) found in rocks by trace element analysis.

CHAPTER TWO

LITERATURE REVIEW

2.1 Conceptual Framework

2.1.1 Rock Magnetism

Rocks exhibit strong magnetic mineral properties depending on the size, structure, and mineral. There are non-destructive ways to analyze these minerals owing to rock magnetism. The impact of humans on mineralogy can be measured using techniques like temperature-dependent remanence, ferromagnetic resonance, and magnetic hysteresis (Rochette *et al.*, 1992).

Kearey and Brooks (1991) emphasized that the magnetic mineral contained in rocks determines the magnetic character they exhibit. Since magnetic measurements are more sensitive to changes in both space and time, they are used to estimate minor, localized alterations in the crustal field.

Basic igneous rocks have high magnetite content, and as such exhibits high magnetism. The magnetic properties of metamorphic rocks and other sedimentary rocks could possibly vary. Generally, the magnetism in solid minerals can be classified as diamagnetic, paramagnetic, ferromagnetic, ferromagnetic, and sometimes anti-ferromagnetic. While ferromagnets, ferrimagnets, and some anti-ferromagnets exhibit a substantially greater response to the field and have remanence, diamagnets, and paramagnets convey a weak magnetism since they have no remanence (Reeves, 2005).

2.1.2 Demagnetization

Over the course of the rock history, processes include burial, weathering, tectonic deformation, heating, fluid circulation, metamorphism, etc., acquire the various magnetization compounds. These Rocks can also lose their power of magnetization through a process called demagnetization. This can be due to natural processes over time, heating, hammering or externally achieved by using an alternating magnetic field to cause an evenly aligned magnet to dis-align thereby generating a fine domain structure. This demagnetization is associated with the

high susceptibility of the magnetic sources and prevents interference with electronic instruments (Tarling, 1983).

2.1.3 Magnetic Method

A geophysical method called the magnetic method shows the strength of the magnetic field and its fluctuations below the surface. Our understanding of the underlying geology is aided by the anomalies found in the magnetic attributes of rocks. Geoscientists can quickly and affordably obtain geophysical data using the magnetic approach. In technical and environmental applications, it can be applied to the identification of pipes, cables, tanks, drums, piles, toxic waste, archeological artifacts, tectonic process studies, and geological features. The magnetic approach has the benefit of high accuracy in detecting low-depth target geological features connected to heat sources, volcanic intrusions, aquifers, and metal objects, in addition to being quick and inexpensive in data collecting (Pantelis & Eleni, 2016).

2.1.4 Magnetic Susceptibility

The degree to which a material reacts to magnetism on application of an external field is known as the magnetic susceptibility, or k. Susceptibility can vary based on the field values, the temperature values and the measurement direction. The knowledge of rock-magnetic parameters has been useful in studying environmental systems, ground magnetism, magnetic anomaly interpretation, fluvial processes, palaeo-magnetism etc. (Thompson & Oldfield, 1986).

It is the most used magnetic parameter used in environmental surveys as it measures the ease at which a material magnetizes. Magnetic susceptibility is determined by the values of mass-specific susceptibility (χ) and volume susceptibility (k, dimensionless). The mass-specific susceptibility of 10-6 m3kg-1 is frequently given in units in environmental geophysics.

Magnetic susceptibility can be practically applied in archaeology, environmental science, and mineral detection. Hence, the susceptibility of rocks is extremely valuable in determining

different lithologies (Kearey & Brookes, 1991). Table 2.1 shows examples of the common rock types and their susceptibilities.

Table 2.1: Common rock types and susceptibility

Rocks	Susceptibility range (x10^{6}emu)	Average
Sedimentary Rocks		
Limestone Gypsum Shale Sandstone Coal Oil	All very low (<1)	
Igneous Rocks		
Granite	0 – 400	200
Basalt	20 – 14,500	6,000
Gabbro	80 – 7,200	6,000
Peridotite	7,600 – 15,600	13,000
Metamorphic Rocks		
Quartize	-	350
Schist	25 – 240	120
Slate	0 – 300	50
Gneiss	10 – 2000	-

(Telford *et al.*, 1990)

2.1.5 Aeromagnetic Survey

This survey measures the strength and direction of the magnetic field during an aerial geophysical survey. It measures also, the magnetic anomaly variations in the Earth's subsurface. It allows us to view the distribution and trends of subsurface structures. It is ideal for both a reconnaissance survey and a direct survey. In a lesser time, larger area in the subsurface can be filled with a minimum field support (Burger *et al.*, 2006).

Aeromagnetic surveys can be employed for the detection, localization, and characterization of magnetic sources. The observed variation in the magnetic field shows the variable distribution of minerals (mostly magnetite) at the subsurface. The majority of the flown surveys are done to support surface mapping, which aids detection of magnetic effects of structures in unassailable environments, such as those with water bodies, sand, vegetation, and locations where the bedrock has been covered by overburden. Additionally, magnetic surveys are capable of locating magnetic sources deep under the Earth's crust (tens of kilometers) (Pilkington, 2007).

Besides aeromagnetic surveying vast land coverage, it is cost-effective (Kearey & Brookes. 1991). This makes it an attractive technique for investors in geophysical exploration since there is no need sending personnel into the survey area for data collection.

However, an airborne survey has its own issue when it comes to position fixing. When such problems are encountered, we deploy the use of aerial photography to capture the terrain simultaneously with the magnetic readings.

The speed of surveying and the ability to survey inaccessible areas made aeromagnetic survey a preferred survey method to ground survey. Along with lessening the impact of sensor drift and time fluctuation in the magnetic field, the speed also lowers the cost per line mile. This improves data accuracy and reliability and also eliminates operational problem associated with irregular terrains.

According to Adetona and Abu (2013), a magnetic survey serves the following purposes:

i. Marking the boundaries of volcano-sedimentary belts beneath more recent layers of sand, or in severely altered terrain where recent lithologies cannot be distinguished.
ii. The identification and exposition of fractures and faults as possible mineral host sites as well as a proxy for factors beyond the genetics and mineralization in the neighbouring rocks.
iii. Identification and delineation of post-tectonic intrusive rocks.
iv. The direct identification of certain ore deposits.

2.1.6 Magnetic Anomaly

In aeromagnetic surveys, the measured magnetic anomaly variations are used in the mapping and delineation of an area. These anomalies can be as a result of the chemical composition of the rocks or caused by geologic structures like dykes, faults, folds, and basement intrusions (Kearey & Brookes, 1991).

Furthermore, a number of useful techniques are employed in the analysis of aeromagnetic anomaly data, including the centroid method (Spector & Grant, 1970; Bhattacharya & Leu, 1977); the spectral peak method (Connard *et al.*, 1983; Blakely, 1995); the use of spectral analysis (Ofoegbu & Onuoha, 1991); three-dimensional Hilbert transformation (Ofoegbu & Mohan, 1990); and advancing the spectral peak using forward modeling (Ravat 2004; Finn & Ravat, 2004; Ross *et al.*, 2004). These techniques have demonstrated impressive results when implemented in various research fields. I adopted the centroid method in analysing the aeromagnetic data in this research work.

Magnetic survey can be used in both terrestrial and marine archaeology (Clark & Emerson, 1991). Decades ago, most of the surveys were done as ground surveys. In recent times, most magnetic surveys are airborne surveys. This study will be making use of airborne data set of magnetic and radiometric because of their high resolutions.

2.1.7 Curie Point Temperature

That temperature point where all magnetic minerals are lost is known as the Curie temperature. At this temperature, certain materials undergo a phase transition and exhibit a change in their magnetic properties.

According to OpenAI (2023), at the temperature below the Curie point, ferromagnetic materials exhibit spontaneous magnetization, where the magnetic moment of the atom aligns in a parallel manner resulting in a net magnetic field. The Curie point temperature varies depending on the specific material and can be affected by the rock composition, crystal structure, and external conditions.

The Curie temperature is significant in manipulating and understanding magnetic minerals as it defines the temperature range within which the ferromagnetic behavior is exhibited. It is now known that several minerals exhibit temperature-dependent variations in their magnetic activity. Therefore, magnetic minerals and domains can be identified based on the temperature-susceptibility curves' form.

2.1.8 Radiometric Method

The Gamma-ray spectrometry is known for measuring the natural radiation of the subsurface. Radioactive decay is the basic concept of this method that uses a scientific technique to determine age of rocks, minerals, heat production, and other geological applications. Some unstable parent rock isotopes over time spontaneously decay to transform into different daughter isotopes or elements during this process (OpenAI, 2023).

We use gamma-ray to measure the concentration fluctuations of naturally occurring radio elements (U, K, Th). The various lithological units and the surface distribution of these rocks can be mapped and described using these measures (Anderson & Nash, 1997; Graham, 1993; Jaques *et al.*, 1997).

When compared to other geophysical techniques, the gamma-ray spectrometric method has demonstrated greater performance in surface mapping (Darnley & Ford, 1989). It is also applied for mineral ore detection and environmental radioactive pollution detection using the principle of radiation emission. Most researchers (Elawadi *et al.*, 2004; Youssef & Elkhodary, 2013; Nigm & Khameis, 2009; El-Sadek *et al.* 2002) have used the radiometric technique to remap lithological rock units. This method can be used to delineate some geological structures that are not captured using the potential field methods.

Additionally, the detection and identification of zones that have been altered by water are more accurate and valuable with this technology. The Th/K ratio is the strongest diagnostic for identifying potassic alteration zones, according to Shives *et al.*, (1997). As a result, several writers have identified alteration zones successfully using the suggested technique (Irvine & Smith, 1990; Feebrey *et al.*, 1998; Wemegah *et al.,* 2015).

The isotopes of radioactive elements spontaneously release high-energy electromagnetic waves known as spectrometric gamma-rays, which have a shorter wavelength, are less invasive, and have potential geological applications. Additionally, since a decrease in equivalent thorium concentration and an increase in potassium concentration are indications that the ore deposit has been altered. Creating a K/eTh ratio map aids in identifying those areas that have been hydrothermally modified.

2.2. Empirical Review

It has been demonstrated that the magnetic approach is an effective instrument for processing and understanding possible aeromagnetic data. Many authors have made extensive use of it (Mayhew 1982, 1985; Blakeley 1988; Okubo *et al.*, 1991; Tsokas *et al.*, 1998), and it has undergone constant improvement (Salem *et al.*, 2014; Dimgba *et al.*, 2020).

Spector and Grant (1970) illustrated the use of gradient of the power spectrum from spectral analysis method to evaluate depth to the top of a magnetic source (Z_t). This idea was now improved by Bhattacharyya and Leu (1975, 1977) who now devised a means to find the centroid

depth of the magnetized rock (Z_0). These two ideas were combined and improved by Okubo *et al.* (1985) then further expanded to develop a new method that can help us get the basal depth of magnetized bodies (Z_b).

Okubo *et al.* (1985) used spectrum analysis and local aeromagnetic data to examine the depths of the Japanese islands of Kyushu and their environs. From the Aso caldera north to the town of Yabakei, as well as the vicinity of Mount Unzen, had the shallowest depths, which were 7km below sea level. There was a strong correlation between the depth map, the heat regime, and regional geology data. The shallow depths coincide with the locations of the geothermal power facilities that are currently in operation. They concluded that the method provides geologically reasonable results and can be used for geothermal assessment. Their work is similar to this study in terms of the method of data analysis and aim.

Ofoegbu and Hein (1991) in their work "Analysis of Magnetic Data over Part of the Younger Granites Province of Nigeria" employed spectrum analysis over the region to propose a source depth average of 286 meters. Their two-dimensional modeling revealed some bodies that were more detailed than those that were modeled with local gravity data. Peripheral demagnetization may have resulted from hydrothermal alteration to some extent in these substances. This work is similar to theirs in terms of location and the spectral method of analysis.

Negi *et al.* (1987) studied the vast variations in lithospheric thickness and depth of the Indian subcontinent and predicted the depth might vary from 18 km to 68 km and the thickness from 38 km to 186 km. Their estimations are in good agreement with seismological and MAGSAT data. Areas with shallow Curie depth and thick lithospheric layers are as a result of the thinness of the crust, high gradient and anomalous heat. Additionally, their study made a strong case for the broader application of magneto-thermometry in the study of geodynamics. Conversely to my work, they used a different method to investigate the Curie depth in the area.

Anakwuba and Chinwuko (2015) worked on the one-dimensional spectral analysis and Curie depth isotherm of the Eastern Chad Basin and ascertained spectral analysis effective for analyzing magnetic anomalies. Their conclusion shows a depth variation of 21.45km at the Mafa-Bama area and 31.52km at the Maiduguri-Gwoza area. Numerous studies conducted in various parts of the world have confirmed relationships between average crustal temperature and Curie-temperature depths. Their research is similar to my work since we both used the same method of analysis to investigate the Curie depth.

Onwuemesi (1997) opined that the dip in Nigeria's Benue Trough caused fluctuations in the sedimentary thickness. Using one-dimensional spectral analysis, they analyzed the basement's depth ranging from 0.9 to 5.6 kilometers. The depth of the Curie isotherm varies between 16 and 30km and geothermal gradients ranging from 20°C/km to 35°C/km. The findings showed that the temperature isotherm inside the basin is a gradually rising and dropping shape rather than a flat-level surface. This work is similar as we both used the spectral analysis method for data interpretation but at different locations.

Ikumbur *et al* 2013 conducted research on the analysis of aeromagnetic data over part of the southern Bida Basin, Nigeria. Two depth sources were identified using the spectral analysis method's results. The sources with deeper depths span 2.81 km to 3.24 km, whereas the ones with shallower depths span 0.45 km to 1.49 km. Their findings showed a linear depression as well as sedimentary build-up trending in an east-west orientation. Their work was similar as we both used the aeromagnetic data and spectral analysis method of interpretation to investigate the depths in the area but in different location.

Musa *et al.* (2021) with spectral analysis technique outlined and identified the origin of linear structures in the region in their study "First Horizontal and First Vertical Derivatives from High-Resolution Aeromagnetic Data over the Gongola Basin Upper Benue Trough North-eastern Nigeria." Additionally, they employed the horizontal derivative filter, which produced thin and

continuous contact spots. On the other hand, the borders of near-surface geological structures and magnetic bodies were distinguished by the vertical derivative filter. Their findings will be used to demarcate possible danger zones for natural hazards, locate nuclear power facilities, and suggest locations to be avoided when building bridges and dams. Their work used the same enhancement filters used in this research to detect the edges of magnetic bodies.

Ofoegbu (1985a) analyzed the power spectral of the aerial data in Benue Trough excluding anomalous components attributable to shallow sources. From their data, the resultant long wavelength anomalies were inverted. The Curie isotherm of the area was from 18km to 27km. He used a similar method of analysis as used in this study over the same area to investigate the Curie isotherm in the area.

Sheu *et al.* (2021) estimated the basement depth using power spectra on the magnetic residual anomaly data of the Upper Sokoto Basin. The outcome showed that the area's basement is 1.386km deep on average. Their work used the same type of data set and method of analysis as used in this research work but over a different location.

Shehu *et al.* (2016) evaluated the geothermal prospects of the Sokoto Basin using the spectral centroid approach to analyze the acquired aerial data. According to their findings, the centroid depth is from 6.27km to 14.30km with an average of 9.90km, the basal depth is from 11.13km to 27.83km with an average of 18.57km, and the depth to the top of the sources varies from 0.59km to 2.11km and averages 1.22km. Although conducted over a different location, their study made used a similar data set, spectrum method of data analysis, and sorts of analysis.

Akin and Çýftçý (2011) evaluated the heat flow of the kirþehýr massif and the sources of the heat produced due to radioactivity. With the values of the heat transfer rock samples taken from the field, the amount of heat moving in that area was computed, and it was found to have varied between 53 and 108mW/m^2. Additionally, the heat map previously created with aero-radiometric

data was used to determine the radiogenic heat produced from that region. Considering the study of thermal flow in the area, it was determined that 8–38% of the region's average heat flow values is radiogenic, while 60–92% are mantle-sourced. This work is similar because we both used the same data to estimate the radiogenic heat production but in a different location.

According to Onyewuchi *et al.* (2012), since some deformation concepts and theories of ore formation can be associated with their depositions, specific geological folds, faults, joints, veins, and contacts can be identified. Additionally, they provide a regional pattern by showing us the geometry of subsurface structures in a given area that controls the major regional lineaments. Their study is similar to this research work in terms of structural and geological dispositions.

The Nigerian Geological Survey Agency conducted an aerial survey of a significant portion of Nigeria, which was interpreted by Ajakaiye *et al.*, (1991). Their analysis's findings show magnetic lineation, areas with unique magnetic interpretations, and field levels that are thought to be representations of tectonic structures associated with igneous intrusive rocks of different ages. The total field variations are from the Benue Trough, which is believed to be a Rift Basin, and the crystalline shield area, which has features of Jurassic granitic ring complexes and volcanoes. They applied the upward and downward continuation filters, frequency domain filtering, and interpretation of the area's surface and subsurface structures. Although their work was on structural interpretation, it was done in a similar location.

Olowofela *et al.* (2012) using a power spectrum and aeromagnetic data, calculated the basement depths of the Abeokuta Area in southwest Nigeria. According to the findings, the deeper source depth is 2.797km, while the depth is 0.467km is the shallow source. They concluded that the larger depth of 2.797km is attributable to the basement, while the shallower depth of 0.467km is likely caused by intrusive within the sediment. This work uses the same data set but analysed over different locations.

Megwara and Udensi (2014) used aeromagnetic data to conduct structural analysis over the surrounding basement rocks and portions of the southern Bida basin to identify linear structures and determine how these characteristics affected the tectonic activities in the area. The result of the Euler de-convolution method shows the average depth to magnetic sources is 0.128km, with a range of 0.01km to 0.51km. Although they worked on structural analysis, they used the same data collection and analysis technique as this study project.

Orajiuka *et al.* (2020) did depth estimation using aeromagnetic data in some areas within the Anambra Basin to delineate linear structures. From the source parameter depth result, a maximum depth of 4.8km and that of the Euler de-convolution showed a maximum thickness of 4.5km making the sediment thick enough for hydrocarbon accumulation. This research used the same aeromagnetic data set but different data analysis.

Kuforijimi and Christopher (2017) evaluated the Southern Anambra Basin's aero-radiometric data to determine the possibility of radiogenic heat production. The research region, which spans an area of roughly 33,708 sq. km, is bordered by 7° and 9°N latitude and 6° and 7°E longitude. The goal of the project was to map out all of the area's geothermal locations and learn as much as possible about the possible impacts of heat energy and radioactive heat produced in Nigeria. The authors calculated ratios of the three radio-elements to assess the radiogenic heat produced. The heat generated by radioactivity ranged from 0.01$\mu W/m^3$ to 5.43$\mu W/m^3$, with the maximum heat output of 5.43$\mu W/m^3$ found around Aimeke and Ogobia. Similar to my research work, they used the same dataset to prospect the radiogenic heat produced over the same location.

Megwara *et al.* (2013) quantified the heat in both basement and southern Bida using both magnetic and aerial radiometric data. The study's findings show the heat generated ranges from 0.91 to 4.53$\mu W/m^3$ and average 2.28$\mu W/m^3$. From magnetics, heat flow value ranging from 69.16mW/m^2 to 124.82mW/m^2 and 90.95mW/m^2 on the average. They concluded that Katakwa

is a prospective area to exploit for geothermal purposes. Our work is similar as they used the same data set as mine to investigate the same geothermal potential but in different locations.

Ofor *et al.* (2014) worked on the thermal flow in the Sokoto Basin, Nigeria using the spectral technique. According to spectral study results, the centroid depth in the Sokoto basin varies from 6.35km to 13.05km, while the basement is deepest in the northeastern section near the Niger Republic, ranging between 0.61km and 1.54km. Additionally, it proposed that a Curie-point isotherm ranging from 11.36km to 22.30km, along with associated gradient and heat flow values between 26.18 and 44.62°C/km and 52.36 and 98.57mW/m^2, respectively, underlie the basin. The center region around Tambuwal has the greatest heat flow. The heat from a typical continental region at an average is 60mW/m^2, with good values being between 80.60mW/m^2 and 100mW/m^2 which are good geothermal sources. This study used the same data type and spectral method of analysis but in a different location.

Shehu and Nwankwo (2015) used high-resolution aero-radiometric data in the Sokoto Basin, Nigeria to study the heat produced in the crust by radio activities. Finding clean, renewable energy sources preferable to fossil fuels was the goal of the research. By computing Radiogenic Heat Production (RHP) by the radioelements in geothermal resources, the job was accomplished. Thus, for 5,153 data, the average Radiogenic Heat Production was 1.07μW/m^3, and the range of values was 0.07 to 5.48μW/m^3. Using the Rybach's standard of 2.25μW/m^3 for rocks and sedimentary formation, Sokwoi, Binji, Kaoje, and Konkwosso areas have RHP values of 1.56μW/m^3, 1.52μW/m^3, 2.03μW/m^3 and 1.79μW/m^3 respectively and does not have geothermal potentials. The Kalmalo, Sokoto, Argungu, Dange, BirninKebbi and Giru areas with 3.62μW/m^3, 3.10μW/m^3, 2.82μW/m^3, 5.48μW/m^3, 2.70μW/m^3 and 2.67μW/m^3 respectively, have high RHP values. These points to unusual geothermal conditions, suggesting that geothermal exploration there may be beneficial in order to use it as a substitute for Nigeria's reliance on fossil fuels for energy. Additionally, the regions with anomalous values are lithologically consistent with the

greatest known amounts of shale, granite, and limestone with high concentrations of ^{40}K, ^{238}U, and ^{232}Th. In line with my work, they used the same data set to assess geothermal potentials in a different area.

Abraham *et al.* (2014) investigated the Ikogosi warm spring in Ekiti State, southwest Nigeria. quantifying it for geothermal energy using spectral analysis. Their study's findings showed an average heat of 91.2 ± 2.1mW/m^2 flowing in the region and a Curie depth of 15.1 ± 0.6km. Magmatic intrusions were identified as the cause of the low basal depth seen at the warm spring source. They concluded that there is potential for more geothermal research in the area. This work is similar because they used the same aeromagnetic data set and spectral method analysis in investigating the Curie depth but in a different location.

Müjgan *et al.* (2005) used the moving windows power spectrum to analyze the Curie point depth of Western Anatolia in their study of CPD and thermal flow. The findings indicate that the Curie depth ranges are, respectively, 4 to 14km and 6-22km. Their result agrees with the results of (Aydin *et al.*, 2005). They concluded from their results that the spectral analysis method yields better results in estimating basal depths and heat flow when compared to mid-point depth determination. This study similar to mine used the same spectral method of analysis to ascertain the depth and heat flowing in the region.

Nuri *et al.* (2005) investigated the heat-conducting structures across complex zones that are deformed in South-west Turkey. The Curie depth result varies from 9km to 20km. To get insight into the spatial boundaries of brittle failure in the area, these depths were compared with the seismic activity. According to the research, there was a low seismic signature within the active seismic zones which is due to shallow CPD and strong heat flow. Significant earthquakes are likely to happen along the edges of the thermal domes. This study similar to mine used the same spectral method of analysis to investigate the thermal structures in Turkey.

Hsien-Hsiang *et al.* (2014) investigated the CPD in Taiwan. The values obtained are from 6 to 17km, with the highest geothermal gradient varying from 36°C/km to 88°C/km. The boundary of the continent-arc region showed high heat flow values, indicating shallower Curie point depths, while two geometric basement highs, with low gradients and heat flow, revealed deep Curie depths. Similar to my research work, this study used the same method of investigation to get the Curie point depth and heat values in Taiwan.

Ross *et al.* (2006) in California examined how feasible the Curie-isotherm depths can be compared with structures that generate heat in the lithosphere. In their results, they found that the high heat flow between 80 to 85mW/m^2 and a shallow Curie depth of 20km to 30km were from coast ranges of California whereas a lesser heat flow of 50mW/m^2 deeper Curie depths of 30km to 45km came from the Great Valley. This study as well as mine investigated the thermal depth and heat regime linking them to the thermal structures but in a different location.

Esmaeil *et al.* (2015) studied the crustal structure within Southeast Australia and Tasmania with passive seismic and magnet data sets using spectral analysis. The Curie depth was investigated and set side by side with the depth of the seismic Moho discontinuity. The result showed a slight variation between the Moho depth (20km to 38km) and the CPD (25km to 45km). This study used the same spectral method of analysis to investigate the Curie depth but with different data sets.

Anakwuba *et al.* (2016) used spectrum analysis of the local aeromagnetic data to calculate the isotherm and heat flux in eastern Chad Basin of Nigeria. The result showed Curie depth between 21.45km and 31.52km which occurred at Mafa-Bama and Maiduguri-Gwoza area respectively. We both used the same method of analysis to calculate the heat dimension but in different environments.

Mohammed *et al.* (2010) in their study of the geological structures within the crust that cut across complex deformation zones in Birjand used the spectral technique to investigate the depth in the region. The result shows variation between 10.3km and 16km. This study is similar to mine because both used the same data type and method to investigate the Curie depth but in a different zone.

Saibi *et al.* (2015) with the aeromagnetic data studied the Curie depth of Western Afghanistan using spectral analysis linking it to geothermal activities in the area. Results showed shallower depths (16km to 21km) located at Helmand Basin, intermediate depths (21km to 27km) located at the south Helmand Basin, the deep curie depths (25km to 35km) located at the Farad block, and the very deep curie depths (35km to 40km) located at the western part of the North Afghanistan. The geothermal gradient is 14.50°C/km to 36.25°C/km, and the heat flowing across the study area ranges from 35.25mW/m^2 to 90mW/m^2. In comparison to my work, they used the same data set and method of analysis for their investigation in Afghanistan.

Lawal (2020) combined aeromagnetic and aero-radiometric Data to delineate structures, and hydrothermal Alteration Zones in Part of South-western Nigeria. He estimated both the shallow and deep-seated sources using analytic signal technique. The spectrum shows an average value of 2960m, but the depth varied from 270 to 2800m. From the aero-radiometric analysis, the concentrations of the radioelements with the ternary map reveal the lithological units and areas that have been hydrothermally modified. Through this study, lineament structures, and volcanic intrusions were identified. Observed cracks, radiation zones, and other features have been roughly understood using the combination of magnetic and radiometric maps. This study used the same data and method of analysis to delineate structure in a different location.

Spectral analysis was used by Bilim *et al.* (2016) to study the thermal structures of the Menderes Massif and the Aegean Region, Western Turkey. The estimated depth range shown by the result

is 6.21km to 12.41km. This effort, which is consistent with my research, examined the Curie point depth in another country using the spectral method.

Xi *et al.* (2015) using aeromagnetic data studied the geothermal morphology in the Guangdong province of China. The findings indicate that the average Curie point depth is 22km, the thermal gradient varies from 19 to 35.8°C/km, and the average surface heat flow is 73.60mW/m^2. This study and mine are comparable in that they both examined the Curie point depth at a different location using the same data set and analytic technique.

Xu *et al.* (2017) use EMAG2 magnetic anomaly data to calculate the basal depth and the top of the magnetic layer in North China. The range of depth is 18 to 32 kilometers. The Bohi Sea was found to be the location with the shallowest depths in the CPD, which is deeper in the western than in the eastern parts of North China. The CPD values when compared with the heat flow data showed a heat production value of 0.41μW/m^3 to 1.31μW/m^3 with thermal conductivity of 1.8Wm$^{-1}k^{-1}$ to 3.2Wm$^{-1}k^{-1}$. This work is similar because they used the same data type and method to analyse the Curie depth in a different location relating it to heat production values.

Kai *et al.* (2017) determined Southeast Tibet's Curie point depth using satellite magnetic anomalies and the spectrum analysis method. The projected CPD results range from 1.5 to 36km, with a mean heat flow that is 70.48 mW/m^2 higher than China's mean continental flow of 63mW/m^2. The magnetic anomalies were used to determine the Curie depth, which is equivalent to the magnetic crust's basal surface. Their work is alike in terms of the spectral method of analysis and estimations of heat flow but was done in a different location.

Nyabeze and Gwavava (2016) investigated the potential of the geothermal resources of Soutpansberg Basin in South Africa. They delineated an anticline at depths 2.0km to 3.5km in the central part of the Basin and stated that the potential heat sources can be seen around depths of 4.8km and 11.1km. Similarly, my study also assessed the geothermal potentials but in a different country.

Patra *et al.* (2013) in their work "Integrated Interpretation of Satellite Imagery, Aeromagnetic, Aero-radiometric and Ground Exploration Data-sets to Delineate Favorable Target Zones for Unconformity Related Uranium Mineralization, Khariar Basin, Central India. Post-sedimentary faults and fractures were identified in the region. This was done by integrating satellite imagery data with magnetic derivative maps. Litho-contacts were identified using radiometric and satellite imaging. Lineament/fault intersections were linked to hydro-geochemical abnormalities. According to a thorough analysis, Banwapara to the north of Kulharighat is a recommended location for in-depth uranium investigation. This study used aeromagnetic and radiometric data for structural analysis and Uranium exploration while my work used the same data set but for heat flow analysis in a different region.

Tselenti (1991) combined the aeromagnetic and heat flow data of Greece to determine Curie Point Depth. The correlation between heat flow and Curie depths shows an inverse relationship which was used to generate the Curie isotherms. According to the findings, the Curie depths in the region vary from 1km below the Greek volcanic arc to 20km in western Greece. This study same as mine attempts to define the CPD using aeromagnetic data in another country.

An acquired magnetic data was used by Mono *et al.* (2018) to investigate the Curie point depths, geothermal gradients, and near-surface heat flow in the Loum-Minta (Centre-East Cameroon). Using the spectral technique, the depth ranges from 5.22km to 14.35km. The heat values are from 101.05 to 277.7mW/m^2 and the gradient from 40.42°C/km to 111.11°C/km. This study is the same as mine in terms of the data set used, the data analysis, and the method of analysis but in a different country.

Zhou *et al.* (2016) researched on structural index estimation and anomaly depth using different height analytic signals data. They proposed a new inversion technique for anomaly interpretation. This method combines the analytic signals at different heights to identify the

structural index and suppress the anomaly noise. The depths to the sources were also determined. The method was utilized on a real magnetic anomaly that was observed and is known to be caused by a dike in Southern Illinois. The results are consistent with the information from the drilling and the inversion results of the region. This work used the same analytic signal enhancement technique used in my work for the interpretation of magnetic anomaly but not on the thermal flow.

Elbarbary *et al.* (2018) used spectral analysis to study the geothermal resources in Egypt investigating the Curie depths. Results showed that the Curie depths range from 8.6km to 35.7km, the thermal gradient 16.3°C/km to 67.4°C/km and the heat flow values 47.1mW/m^2 to 195.5mW/m^2. This work except for location is similar to mine in data type, data analysis, and method of data analysis.

Abraham *et al.* (2012) used data from fifteen profiles obtained around the region to understudy the reservoir permeability of the Ikogosi Warm Spring. A thorough examination of demagnetized rocks was conducted which assumedly indicates the size of the geothermal reservoir. They delineated the boundaries of the geothermal reservoir using the data from their investigation, which demonstrated a substantial correlation between demagnetized rocks and reservoir permeability. Their work is similar to mine in that it attempts to designate hydrothermal zones for geothermal potentials.

Igwesi and Umego (2013) analysed the aerial data of Lower Benue Trough using power spectrum technique. Average reported depth to the magnetic source was 3.03 km, and intrusive bodies were observed within the sediment. They came to the conclusion that the tectonic phases that occurred from the separation of the African Continent from South America governed the depositions in the Benue Trough. Their study used the same data set and method as mine in some of my locations but for a different purpose.

Ofor and Udensi (2014) in their study to determine the heat flowing in Sokoto Basin Nigeria investigated the Curie depth. The result ranges from 11.36 to 22.30km, the geothermal gradient 26.18°C/km to 44.62°C/km and the heat between 52.36mW/m^2 to 98.57mW/m^2. This study is similar to mine in terms of the data type, data analysis and method of analysis except for the area of study.

Chukwu *et al.* (2017) investigated the geothermal energy potential of a portion of the Niger Delta Basin in Southern Nigeria. The values of the heat vary from 25.3419mW/m^2 to 84.4010mW/m^2. the thermal gradient from 12.0676°C/km to 40.1919°C/km, and the CPD from 7.4644km to 24.8600km. This study also is the same as mine since we both used the same data type and method to analyze the Curie depth and heat flow but at different locations.

Akinlalu *et al.* (2017) used spectral technique to delineate the geologic structures that favour mineralization in Southern Ilesa Schist Belt Nigeria. The result shows depth difference from 73m to 345m. This study used the same data set and method of analysis as mine but for mineral exploration in a different region.

Nwankwo and Sunday (2017) using the centroid approach, computed the depth, gradient, and surface heat of the entire Bida Basin in their regional study. According to their findings, there is variation in the CPD between 15.57 and 29.62km, the geothermal gradient span from 19.58 to 37.25°C/km, and the heat flow between 48.41 and 93.12mW/m^2. This study is similar to my work in terms of data type, data analysis and method of data analysis and also near the study area.

Usman *et al.* (2018) used spectrum analysis to investigate the magnetic mineral delineation in Southern Bida Basin, Nigeria. According to their report, the region's average gradient and thermal flow are 23.07°C/km and 57.66mW/m^2, respectively. The Curie isotherm is 24.76km on

the average. Asides proximity to my location, this work is similar to mine in terms of the data analysis done.

Bello *et al.* (2017) in lower Benue Trough of Anambra Basin estimated the Curie depth, heat regime, and thermal gradient using aeromagnetic dataset. On the average, over the research region, the CPD was 5km, geothermal gradient 32.1°C/km, and heat flow 80.1mW/m^2. This study was done in an area similar to mine using the same data set and method of analysis.

Using local aerial data, Mohammed *et al.* (2019) examined the potential across a portion of the upper Benue Trough for geothermal exploitation, which corresponds to the Kaltungo, Guyok, Lau, and Dong areas. The Curie depth results show that it varies from 12.43 to 33.91km, and the area's heat flow varies from 17.10mW/m^2 to 46.66mW/m^2. This is a similar work to mine in terms of location, data analysis and the method of interpretation.

Kamba *et al.* (2018) in order to ascertain the sedimentary thickness in a section of the lower Sokoto Basin looked into the depths using aerial magnetic data from the region. Two notable magnetization layers were identified, with depths ranging from 2.506km to 3.2km and from 0.589km to 1.249km. The Curie depth in the Sokoto Basin was examined using the same data format as mine; however, the heat flow was not examined.

Bernard *et al.* (2020) in their paper "Airborne Electromagnetic, Magnetic, and Radiometric Surveys at the German North Sea Coast Applied to Groundwater and Soil Investigations" compiled data from 13 different helicopter-borne surveys that were collected over a 15-year period. Numerous structures that are crucial to comprehending subsurface hydrogeological processes were discovered by the helicopter-borne surveys. The interaction between fresh groundwater and seawater is the most notable. Understanding the movement of freshwater lenses on islands, saltwater incursions, and undersea groundwater releases is improved by structural research on fresh-saline interfaces, both onshore and offshore. It is essential to understand the

distribution of clayey and sandy sediments in order to accurately describe and model groundwater aquitards and aquifers. This work is similar to mine since we used the same data type but for different targets.

2.2.1 Previous Work in the Area

A lot of geophysical works have been done in the study area using magnetic method and electrical resistivity method most especially for mineral exploration and groundwater investigation respectively. Little has been done in search of geothermal resources using an integrated geophysical approach around the region.

Anudu *et al.* (2011) interpreted the lineament of Wamba and its surrounding using satellite imagery to check the groundwater potential of the area. They reported the lineament trends to be NE-SW, NNE-SSW, E-W, NNW-SSE, and N-S directions. The major contours are in the NE-SW and NNE-SSW directions. The lengths of the lineaments vary between 1.4km and 15km with most less than 4km. This work was done in my location but with a different data type, method of interpretation, and target.

Abdullahi *et al.* (2019) investigated the basement depth in parts of the lower and middle Benue Trough of Nigeria, with spectral analysis of the aeromagnetic data. They stated that the depths vary between 1km and 9km. Their work is very similar in terms of the data type and method of analysis and was also done in the same location but only for basement depth estimation.

Anudu et al. (2012) analyzed the aeromagnetic data over Wamba and North Central Nigeria. According to their statement, residual magnetic intensity levels ranged from 160nT to 220nT, while total magnetic intensity values varied from 7960nT to 8020nT in the basement portion of the area. They also outlined the region's structural lineament tendencies. The NE-SW, NNE-SSW, and NW-SE structural lineament trends were the main ones, whereas the ENE-WSW and E-W trends were the minor ones. As per earlier research conducted in the Benue Trough by

(Ajakaiye *et al.*, 1986; Olasehinde *et al.*, 1990), the majority of these tendencies align. This work uses the same aeromagnetic data set and in the same location but for structural analysis only while mine was for heat flow analysis.

The data of Mutum-Biyu and its surroundings in north-eastern Nigeria's Taraba state was examined by Kasidi and Nur (2012). The shallow source linked to near-surface intrusion, ranges from 37 meters at Gurumpawa to 590 meters at Gidan Shanu, while the deep source extends from 661 meters near Jalingo to 2722 meters at Bantaji town. Their work used the same data type as mine and the same location but not for geothermal assessment.

Udochukwu *et al.* (2019) utilized spectrum analysis of the aerial data to investigate the geothermal sources in the Maoguno region in northeastern Nigeria. The average Curie depth is 13.387km, with a range of 10.318km to 24.476km. Heat flow varies from 59.242mW/m^2 to 136.176mW/m^2 and 112.364mW/m^2 averagely. The heat gradient varies from 23.697°C/km to 56.212°C/km with an average of 46.195°C/km. This work is similar to mine in data type used, data analysis, method of data analysis, and some locations.

Kasidi and Nur (2013) in their estimation of depths, flow regime, and thermal Gradient used aerial data over Jalingo and Environs, North-eastern Nigeria. The result of the Curie depth shows 24 to 28km, the geothermal gradient from 21°C/km to 23°C/km, and the heat flow varies from 53mW/m^2 to 61mW/m^2. This study did the same analysis as mine and in a proximity region as mine.

Irumhe *et al.* (2019) did a depth assessment to characterize the sedimentary thickness, heat flow, geothermal gradient, and structural features in areas of North Central Nigeria. Between 4.41 and 10.96km are the depths, 207.19mW/m^2 of heat flow and 82.87°C/km geothermal gradient are present. Their work is very similar to mine; as we investigated the Curie depth with same data sets and method of analysis.

Eletta and Udensi (2012) in central Nigeria using the power spectrum investigated the Curie isotherm. From their result, we could see depth variations between 2km and 8.4km. They did similar work in my location using the same aeromagnetic data type and method of data analysis but did not estimate the heat flowing in the location.

Anudu *et al.* (2020) using three grid-based semi-automated depth-estimation approach, conducted a thorough interpretation of HRAD to study the tectonics and basement pattern of the middle Benue Trough. From their findings, there are multiple elongated shallow basement ridges less than 1800m and seven deep sedimentary sub-basins greater than 2500m whose predominant tectonic trends in NE-SW direction. This work was done in my exact location but the data analysis is different.

Kwaya *et al.* (2016) studied the thermal gradient in the Chad Basin, Nigeria alongside the heat regime. They utilized the surface temperature of 19 oil wells, and 24 boreholes drilled at depths away from 100 meters. The results showed a geothermal gradient of 2.8°C/km to 5.88°C/km and heat flow of 45mW/m^2 to 90mW/m^2. This work is similar to my work because they studied the heat flow for geothermal potential. However, it was done in a different location and did not attempt to study the Curie depths in the region.

Adewunmi *et al.* (2021) integrated two aerial datasets to ascertain the heat flowing within the Bornu Basin and its surroundings in northeastern Nigeria: implications for the prospecting of geothermal energy. The study's findings demonstrated that there was likely geothermal energy present in the studied area because the high heat flow region, which ranged from 80 to 100mW/m^2, and the maximum radiogenic heat flow region, which ranged from 2.2 to roughly 2.5μW/m^3, agreed with each other. The concordance between the two heat flows indicates that geothermal research is feasible in the southeast portion of the area. This study is the same with

my research work in terms of the data set used, method of data analysis, and the data analysis but was done in a different location.

Eze *et al.* (2019) worked on integrating the in-situ radiometric signatures and aero-radiometric data to map parts of the Southern Benue Trough and Anambra Basin. They found that igneous rocks in the area are biotite-rich granitic rock that are more radioactive than other rocks. The largest concentration of radioelements can be found in the shale and the granitic rocks. The potassium feldspars and felsic rocks (biotite granite and coarse porphyritic granite) have greater potassium percentages (1.5% and 3.7%), respectively. The area's pyroclastic rocks have no evidence of potassium mineral content. The average values of Abakaliki consolidated shale are 2.40% Potassium, 4.80ppm Uranium, and 20.1ppm Thorium. This work was completed in the same place using one of my data types, but it did not try to explore the area's depth.

Nwosu (2013) with spectral analysis reassessed the magnetic basement depth in the middle Benue Trough utilizing the HRAM to gauge the region's potential for hydrocarbon deposit. The deeper sources are found to range from 2.33km to 5.66km. For shallower sources, the depth values range from 0.07km to 0.42km, with an average depth of 0.21km. This study used the same data type and method of analysis as mine but for hydrocarbon exploration, not geothermal exploration target.

Adewumi and Salako (2018) to identify mineral potential zones qualitatively analyzed aeromagnetic data collected from a portion of Nasarawa State. The vertical derivatives depict structures resembling lineaments that may serve as the host for minerals found in the research area. The downward trend that continues at depths of 50 and 100 meters reveals the veins where igneous and metamorphic rocks are known to accumulate magnetic materials, particularly gold. The analytic signal map reveals that the northern end of the signal has magnetic amplitude highs, and the majority of the demarcated line segments also match the other filters that were applied. Targets for mineral exploration and the mapping of shallow basement formations can be

achieved by enhancing short wavelength anomalies with the tilt derivative map. The structures control the minerals, thus the observed lineaments in the northern half could host these minerals given the general agreement of the filter results. This study was done in my location using the same data type and method of analysis but for mineral exploration, not geothermal potentials.

Obi *et al.* (2008) interpreted the basinal structure of the Yola arm which is a part of the upper Benue Trough Nigeria with aeromagnetic data. They revealed an anticlinal feature within the area. This feature is prominent on residual and basement depth maps. Major lineaments were revealed along NE-SW and NW-SE. The modeled architecture revealed sedimentary thickness of 2.0km to 3.5km towards the Southwest and Southeast. A decreasing depth of about 1.0 to 1.5km was estimated towards the Northeast and Southwest of the arm. This work was done in the same area using the same data type but different in terms of data analysis.

Kurowska and Schoeneich (2010) used the information gathered from pumping tests done from deep water wells 700 to 500 meters in the Bida, Borno, and Sokoto Basins, as well as other basins, to investigate Nigeria's geothermal exploration. According to the database, the temperature gradient was 0.9 to 7.6°C/100m in Sokoto Basin and 1.1 to 5.9°C/100m in Borno Basin. The geothermal anomaly map result for both Basins revealed a major source of geothermal heat associated with certain deep tectonic structures in the Precambrian basement beneath the sedimentary complex. In terms of heat analysis, this study is similar to mine but the data types used for the analysis are different.

Opara *et al.* (2015) did a detailed study on the structures of the Jos-Bukuru Younger Granite Ring Complexes deduced from Landsat-TM Data. Numerous lineaments were seen in the northwest, central, and southwestern regions according to the results of the structural studies. Structural tendencies in NW-SE, NE-SW, N-S, and E-W directions were identified by trend analysis of the lineaments, with NW-SE and NE-SW dominating the region. These patterns line up with the local Paleo-tectonic fracture zones' locations and orientations. It was discovered that

the Basement complex's underlying Precambrian rock included features that governed the structural patterns. This work was done in my location using a different data type and did not attempt to obtain the Curie depth and heat flow in the area.

Sabinus *et al.* (2018) with magnetic data interpreted the surface and subsurface structures across a section of the Northern Nigerian province known as Younger Granite. The aeromagnetic study's findings showed some clear magnetic anomalies in the region where outcropping ring complexes are spatially congruent. In addition to outcropping ring complexes, some unexposed ring complexes were also identified. It discovered lineaments as structural elements with a predominant NE-SW tendency. The ring complexes of Northern Nigeria were also found to have a variety of surface designs and shapes as well as structural orientations that dip both inward and outward with depth. Their study was done in the same location as mine and with the same data type but not for geothermal exploration.

2.2.2 General Geology

Nigeria lies within the Pan African belt with coordinates between latitudes 4°N and 15°N and longitudes 3°E and 14°E. Nigeria has a diverse geology that spans millions of years and is characterized by a variety of rock formations, mineral resources, and geological features. According to Kogbe (1989), crystalline rocks and sediments, which are found in about equal amounts, dominate Nigeria's geology. Nigeria's geology is primarily composed of the Basement Complex, Younger Granites, and Sedimentary Basins (Fig. 2.1) (Obaje, 2009). The Basement Complex is of Precambrian (older granites, schist belts, and migmatite-gneiss complex) in age. The Jos region and adjacent north-central Nigerian regions are the focal points of many Jurassic (200–145 million years old) ring complexes comprising the younger granites structurally distinct from the older granites. For the sedimentary basins, we have the sediment fill that is between Cretaceous and Tertiary in age; the Niger Delta, the Anambra Basin, the Lower, Middle, and Upper Benue Trough, the Chad Basin, the Sokoto Basin, and the Mid-Niger (Obaje, 2009).

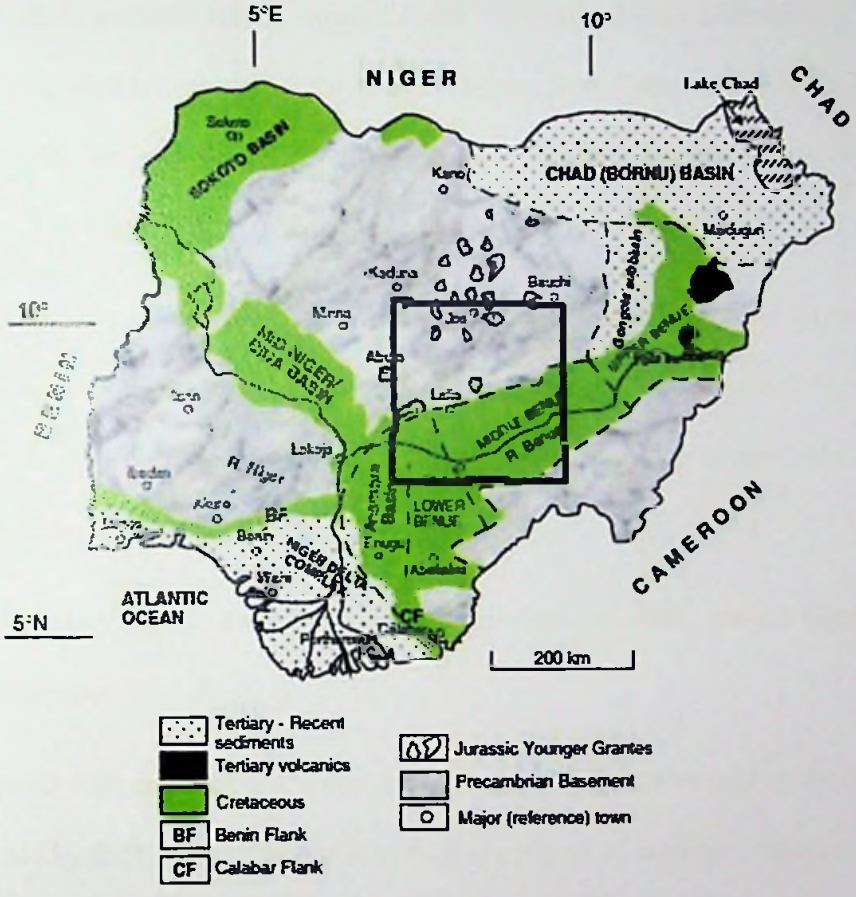


Fig. 2.1: Geological Map of Nigeria showing the study location (Obaje, 2009)

The Migmatite-Gneiss which are undifferentiated with the older granite are found northwest in the districts of Karu, Gurku, Panda, Gitata, and Nasarawa Eggon; north-central in Keffi, Garaku, Akwanga, and Nasarawa Eggon; and northeast in Wamba and its (Obaje *et al.*, 2004). As a result, part of the research area is situated inside Nasarawa State's sedimentary zone, which is mainly made up of sedimentary rocks with ages ranging from Cretaceous to Tertiary. These strata extend from Obi, Jangwa, Awe, through Keana, then towards Lafia and Doma. Some of the key geology of Nigeria according to OpenAI (2023) are highlighted as follows:

The Basement Complex: The southwestern and central parts of Nigeria are underlain by a Precambrian Basement Complex. This complex consists of crystalline rocks such as gneisses, migmatites, schists, and granites. It is an important source of minerals including tin, tantalite, columbite, and gemstones.

Sedimentary Basins: these have several sedimentary basins, and are significant for their oil and gas reserves.

Niger Deltaic environment: a vast, low-lying coastal plain formed by the deposition of sediments carried by the Niger and Benue Rivers. It is a region of extensive mangrove swamps, creeks, and distributaries. The deltaic environment has abundant oil and gas reserves.

Plateaus and Highlands: central Nigeria has several plateaus and highlands. The Jos Plateau is the most prominent among them. It is an elevated region characterized by a cooler climate and fertile soils. The plateau is underlain by granite and is known for its tin mining activities.

Volcanic Activity: In the northeastern part of Nigeria, there are volcanic features associated with the Cameroon Line, a chain of volcanic mountains and plateaus. The most notable volcanic mountain in Nigeria is Mount Cameroon, located just across the border with Cameroon.

Rift Valleys: Nigeria has a series of rift valleys that are characterized by faulting and are potential sources of hydrocarbon deposits.

Coastal Features: Nigeria's coastline stretches over 800 kilometers along the Gulf of Guinea. It features sandy beaches, barrier islands, lagoons, and estuaries. The coastline is influenced by coastal erosion, sedimentation, and the interaction between marine and freshwater systems.

These are some of the key geological aspects of Nigeria. The country's geology contributes to its natural resource wealth, including oil, gas, minerals, and agricultural productivity.

The study region is divided roughly in half by the Precambrian basement and some Jurassic Younger Granites, and the other half by the sediments of the Benue Trough.

2.2.2.1 Geology of the Study Area

The research region (Fig. 2.2) is mainly situated in the middle of the Benue Trough and a tiny portion of the lower Benue Trough, from latitudes 7.5°N and 10.0°N and longitudes 7.5°E and 10.0°E. The Nigerian Benue Trough is the core portion of an elongated, massive intracratonic rift formation that originated in the Late Jurassic to Early Cretaceous Period inside the Pan-African mobile belts' Precambrian to Early Palaeozoic crustal bedrock (Burke & Whiteman, 1973; Fairhead & Binks, 1991; Nwajide, 2013; Anudu, 2017).

The Trough is a mega-shear zone and is completely situated between the Charcot oceanic fracture zones and the offshore Chain (Ajakaiye *et al.*, 1986, 1991; Fairhead *et al.*, (2013).

The Benue Trough has generally been subjected to trans-tensional (strike-slip and extensional) tectonics, which has produced strike-slip faults with portside displacement and extensional faults/fracture systems (Benkhelil *et al.*, 1989; Guiraud & Maurin, 1992). Additionally, several pull-apart sub-basins characterized by a parallel formation were formed in a NE-SW pattern, with the majority of them exhibiting the shape of a rhombus. The sedimentary basin that stretches to the southeast of the study region contains the Cretaceous strata of the faulted rift system of the Trough.

The region comprises of sedimentary basin, and Precambrian basement complex hosting also the younger granites. This Precambrian basement is made up of igneous-volcanic rocks, granites and

Quaternary alluvial deposits. The rocks in the North Central areas according to Ekwueme (1987) are composed of gneiss, quartzites, granites, migmatites, schists, and phyllites. The Trough consists of shale, sandstones, silt, silty shale, and limestone intruded by dolerite dykes (Kogbe, 1989). Alluvial deposits of Quaternary to recent age, including silt, clays, gravel, and fine and coarse sands, are deposited along the major river valley. There are thick alluvial deposits along the Niger and Benue Rivers up to 15km broad and 30m thick to thin discontinuous sands (Adelana *et al.*, 2008).

The middle Benue Trough region's basement morphology, geometry, and precise sediment thickness are still poorly unknown despite the geological and economic interest (Ofoegbu, 1985; 1989; Anuda *et al.*, 2012).

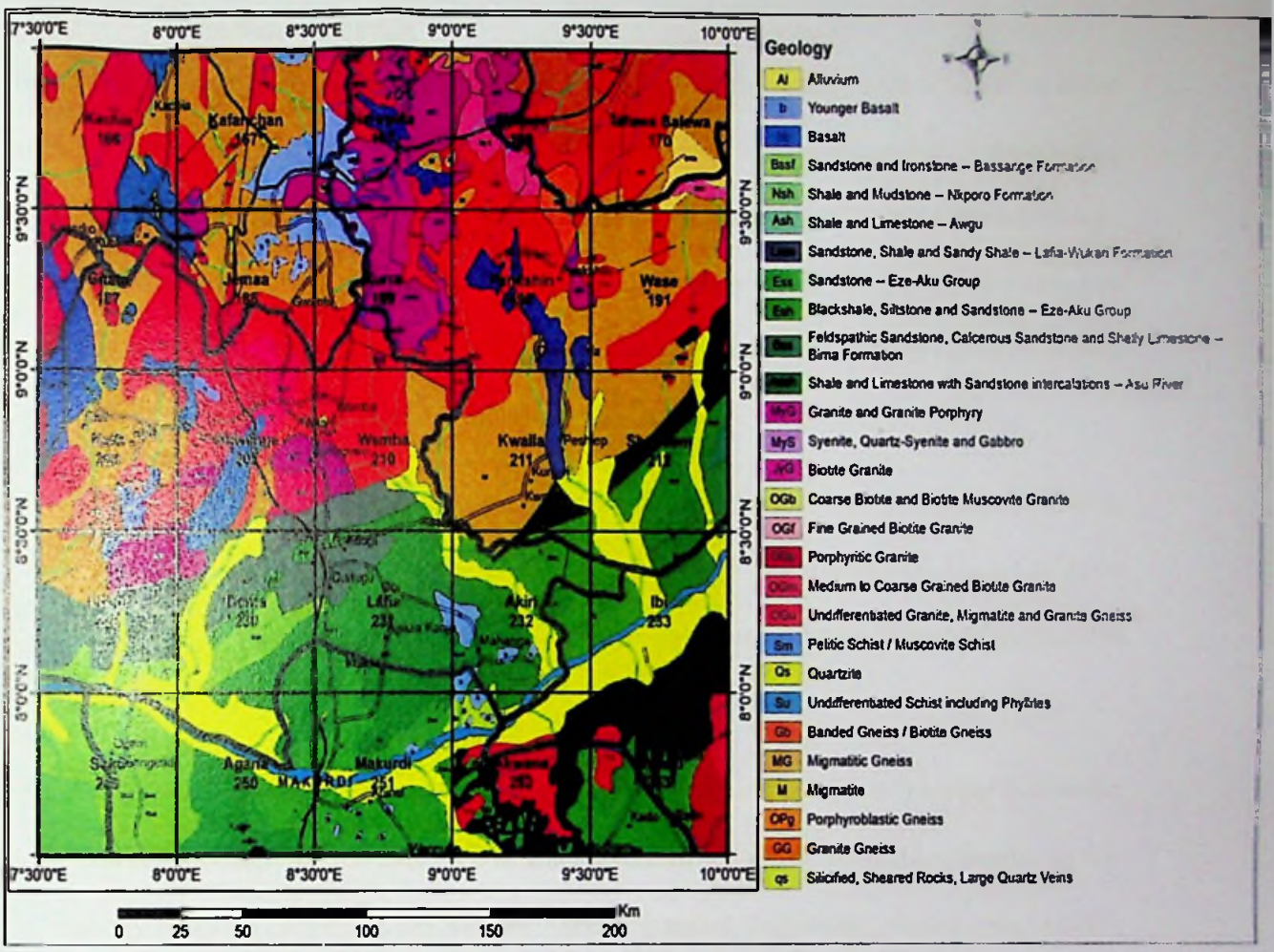


Fig. 2.2: Geological Map of the Study Area (NGSA, 2023)

2.2.2.2 The Benue Trough

Benue Trough is an elongated Cretaceous Rift Trending North-easterly with a length of about 800km, 150km wide from the Gulf of Guinea, and believed to have originated from the opening of the South Atlantic (Ofoegbu, 1988). Before separation and opening of South Atlantic, African and South American continents were joined and Benue Trough is said to represent the rifting of these two continents. Benue Trough, the Gulf of Guinea and most North-eastern Brazilian Basins are genetically related with similar compressional features,

Numerous mafic/felsic intrusive and basalt lavas, along with a small zone filled with lead-zinc mineralization, are characteristics of the Trough (Olade, 1979). The trough's geological analysis has shown that it is full of cretaceous rocks that range in age from middle Albian to Maestrichtian (Offodile & Reyment, 1977).

Benue Trough has a coherent stratigraphy (Fig. 2.3) and structural condition from the Southwest to the Northeast notable by the existence of folds in the ENE- WSW orientation. Bordering the sedimentary rocks on either side are the Pan African granites, migmatites, muscovites, schists, and gneisses making up the crystalline basement (Benkhelil, 1989).

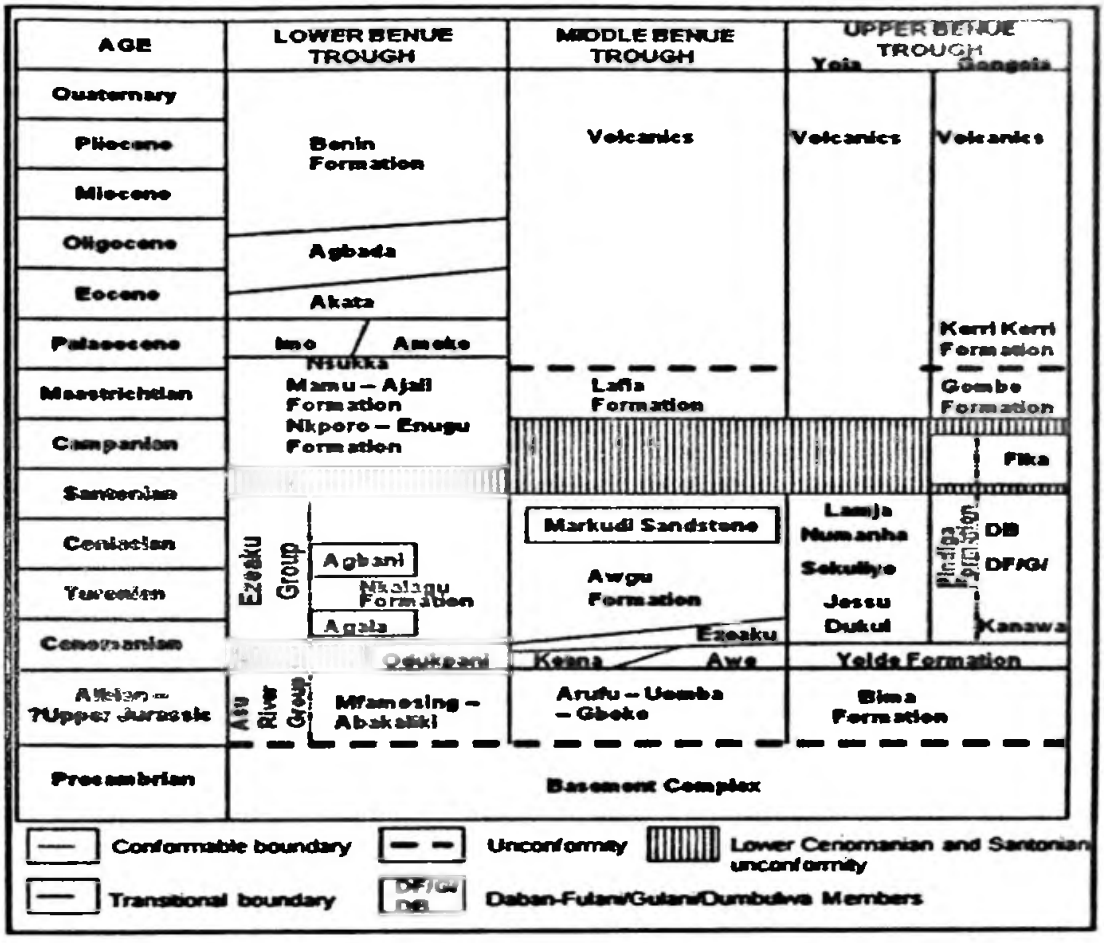


Fig. 2.3: Stratigraphy across Benue Trough (Guiraud, 1990).

2.2.3. The Basement Complex

The Precambrian Basement underlies half of the study region, with sedimentary rocks and more recent granite intrusions covering the remaining half. The Precambrian Basement rocks and the magmatic rocks make up the crystalline rocks in the research area. Throughout the geological period, these crystalline basement rocks have undergone varying degrees of deformation. In the Triassic-Jurassic, newer granites that contained tin intruded upon them (Bowden & Kinnaird, 1984; Anudu *et al.*, 2020).

The sediments are underlain by crystalline basement from the remains of the sedimentary rocks and diverse plutonic rocks. The basement has an irregular topography and is extensively invaded by intrusive bodies of different sizes that form a massive body over time (Ofoegbu, 1985a).

The basement complex rocks, which date from the Precambrian to the Early Palaeozoic, are primarily made up of gneisses, migmatites, granite-gneisses, granodiorites, pegmatites, schists, marbles, amphibolites, and phyllites. Syenites, gabbros, quartzites, and large quartz veins are also present in trace amounts (Dada, 1999).

The Younger Granites province of Nigeria is majorly found within the north-central of Nigeria. They are a set of Jurassic ring complexes that intruded the basement complex of the Precambrian age. These granites are part of the broader Pan-African orogeny that happened 600 to 500 million years ago.

From the study of Ofoegbu and Hein (1991), the younger granites are outlined in an elliptical manner with 5 diameters that range from 10km to 25km. These younger granites are characterized by their coarse-grained texture and composition, primarily consisting of quartz, feldspar (potassium feldspar and plagioclase), and mica (biotite and muscovite).

The division of Africa and South America has lineaments from the distant past that have been linked to the positioning of the younger granites. The ones found in Nigeria are tectonically significant since its genetic relationship is same as the complexes in South America, Cameroon,

Niger, and Algeria. These ancient lineaments according to Wright (1976) since they served as conduits for the volcanic materials might have had an impact on the emplacement sites. These granites' ages are decreases from north to south, and this age trend suggests that mantle plume activity played a part in the younger granites' emplacement.

2.2.4. The Sedimentary Formations

The lower, middle, and higher divisions of the Benue Trough are separated by compression and constitute an intra-cratonic rift structure. The middle and lower portions of the trough comprise the majority of the southern half of the study region. The unstable Rift-Rift Fault (RRF) triple junction scenario, which caused plate dilatation and the opening of the Gulf of Guinea, was the mechanism of the trough's creation, but it is still up for debate (Benkhelil, 1989; Obaje *et al.*, 2004; Patrick *et al.*, 2013).

According to research done by Offodile (1976), the six sedimentary formations that make up the middle Benue Trough (Fig. 2.4) are the Asu River Group, Keana Formation, Awe Formation, Ezeaku Formation, Awgu Formation, and Lafia Formation. The Asu River Formation is the oldest, dating from the middle to Albian, while the Lafia Formation represents the youngest, dating from Maestrichtian.

The Markudi Formation, Nkporo Formation, and Bima Formation are also located within the research region. The Awgu Formation's deposition ends the marine sedimentation in the region. The Ezeaku Formation was deposited at the beginning of maritime transgression in the Late Cenomanian. During the late Albian to early Cenomanian recession, the Awe Formation was deposited. Fluvial-deltaic sediments were deposited during the Cenomanian retreat, resulting in the Keana Formation (Obaje, 1994). The youngest formation in this area is Lafia Formation, not having the same strata but deposited on top of Awgu Formation in the Maastrichtian under continental conditions (fluviatile). Further information on the subject is in the works of Cratchley & Jones (1965), Osazuwa *et al.* (1981), Ofoegbu (1985), and Patrick *et al.* (2013).

The geology (Maurin *et al.*, 1986; Guiraud *et al.*, 1989; Guiraud, 1990; Aina *et al.*, 1996) and magnetism of certain structures in this area have been the subject of several published investigations (Benkhelil *et al.*, 1988; 1989). With a few running in the N-S direction, the major faults and shear zones are oriented in NE-SW, NNE-SSW, NW-SE, ENE-WSW, and ESE-WNW directions.

Furthermore, several studies (Offodile, 1980; Whiteman, 1982; Wright *et al.*, 1985; Nwajide, 2013; Anudu, 2017) have reported on the region's mineral deposits (barites, lead-zinc sulfides, salts, coals, and warm to hot springs/brines).

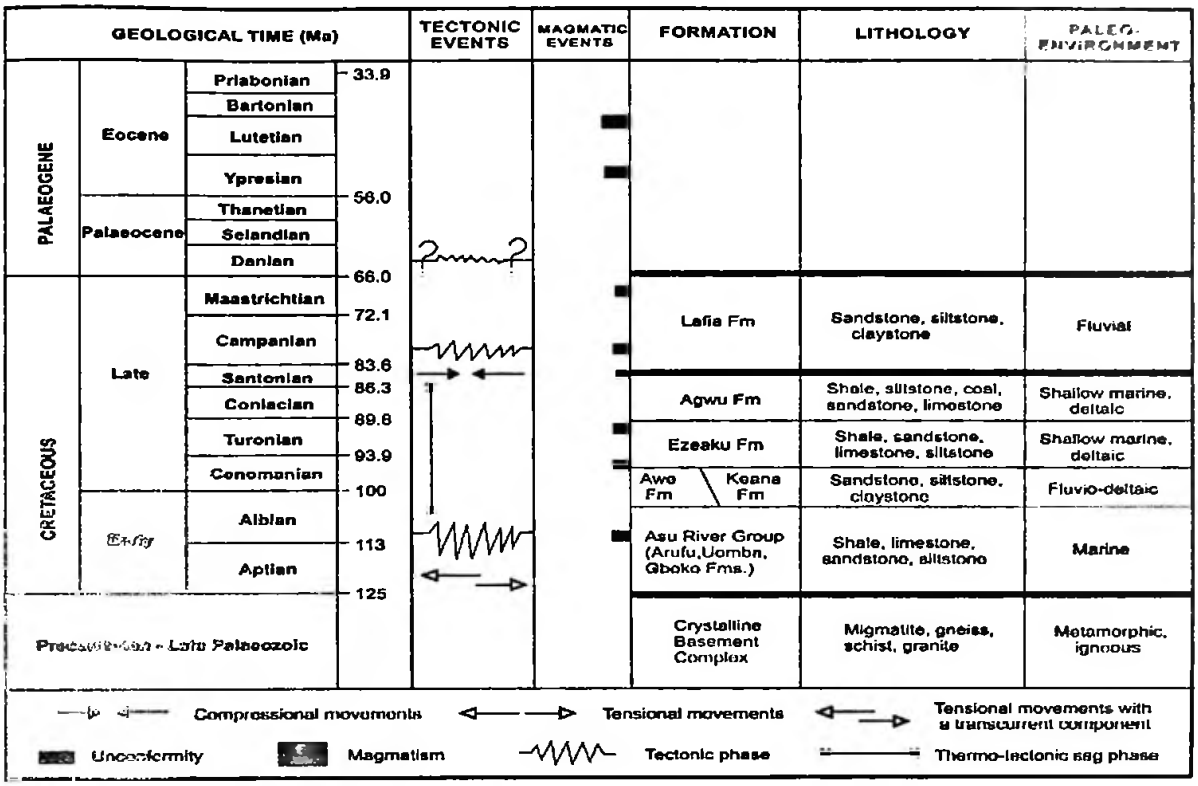


Fig. 2.4: Stratigraphy Succession of the Middle Benue Trough (Anudu *et al.*, 2020).

2.2.4.1 The Lafia Formation

Lafia Formation is a geological unit found in Nasarawa State Nigeria. The Formation belongs to the Cretaceous period, from the late Santonian to the Maastrichtian stages, which are approximately 100 to 89 million years ago. It is the youngest formation found in the sedimentary basin of the Benue Trough, in Nigeria (Zaborski, 1998).

Its deposition is of continental fluvial composition, which lies on the Awgu Formation. It is composed of limestone, sandstones, siltstones, calcareous shale, and coal. The Lafia formation's rocks are distinguished by clays, clay stones, red loose sands, ferruginized sandstones, and foggy mudstones. The formation is feldspathic, friable, and fine to coarse-grained. According to Nuhu *et al.* (2019), the thickness of the layer varies between 10 and 150 meters in the Lafia area, however, it becomes thinner towards the north and dwindles towards the southwest of the town.

2.2.4.2 The Agwu Formation

Agwu formation marks the end of marine sedimentation in the region's **stratigraphy**. The Formation was formed in a shallow marine-deltaic environment. The composition consists of limestones, sandstones, siltstones, coals, and shaly formation (Offodile, 1976).

2.2.4.3 The Ezeaku Formation

The Wadata Limestone and the Konshisha River Group in the Makurdi region are lateral equivalents of the Ezeaku Formation. The Ezeaku Formation coincides with the start of maritime transgression in the Late Cenomanian. The primary constituents of the sediments are beds of limestone that are fine to medium sandstones, and calcareous shales (Oguadinma, 2019).

2.2.4.4 The Awe Formation

The deposition of the Awe Formation happened within late Albian to early Cenomanian as transitional beds. According to Salako *et al.* (2020), the formation is made up of clays, carbonaceous shale, and pale, flaky calcareous sandstones with medium to coarse grains. The

formation comprises of coarse-grained, cross-bedded feldspars, sandstones, with different and distinct groups of limestone and shale at the upper level.

2.2.4.5 The Keana Formation

The Keana Formation is a geological unit found in Nigeria, specifically in the central part of the country particularly in Nasarawa State, where the town of Keana is located. The Formation belongs to the Cretaceous period, more specifically the Albian stage, which was approximately 100 to 113 million years ago. The deposits of the Keana Formation are of fluvial-deltaic sediments as a result of the Cenomanian regression. They consist of feldspathic sandstones intercalated with shales and limestones (Okwudiri *et al.*, 2017).

2.2.4.6 Nkporo Formation

The Nkporo Shale Formation is a geological unit found in south-eastern Nigeria, particularly in the Nkporo area of Abia State. Age and Stratigraphy of the Nkporo Shale Formation is of Cretaceous age, specifically belonging to the Lower Cretaceous period and a part of the Albian stage. The lithology and depositional Environment of the Formation primarily consists of shale, a fine-grained clay mineral. Shales typically form in quiet, low-energy environments such as lakes, lagoons, coal swamps, and marine basins. The Nkporo Shale Formation suggests deposition in a marine environment and contains fossilized remains of various marine organisms. Fossils commonly found in shales include microfossils such as foraminifera, radiolarians, and ostracods (OpenAI, 2023).

2.2.4.7 The Asu River Group

Asu River Formation was deposited in a marine environment. The Asu River Group, sometimes called the maritime Albian Arufu, Uomba, and Gboko Formations, were the first to sediment in southern to middle Benue Trough (Offodile, 1976). The Asu River Group represents the oldest formation in the middle Benue Trough, dating from the middle to the Albian era. The lithological

composition consists of clays, micaceous siltstones, mudstones, shales, and limestones (Offodile. 1976; Obaje, 1994).

2.2.4.8 The Bima Sandstone

Bima sandstone is one of the deposits in the upper Benue plain that rests inconsistently on the basement complex rocks and is the oldest sedimentary rock in the area. It is widely exposed throughout the Gongola Basin's eastern and northern borders. Saleh *et al.* (2019) opined that the medium to highly coarse cross-bedded conglomeratic sandstone that makes up the Bima Formation is arkosic and kaolinitic. It grades southward into the contemporaneous muri, Keana, and Makurdi sandstone in the middle Benue Trough. It has three memberships: the lower, middle, and upper members.

Bima 1 is primarily from the Zambuk Ridge with variable lithology. Its thickness is about 1500m thick, with a basin-wide angular unconformity at its upper boundary, according to Guiraud's (1990). Bima 2 has a thickness of 50-200m with coarse-grained sandstones dominated by large-scale trough cross-bedding. Bima 3 is homogeneous and has medium to fine-grained sandstone with tabular cross-bedding.

2.2.5 The Geothermal System

A geothermal system (fig. 2.5) refers to the natural heat energy stored within the crust and its utilization for different purposes, such as power generation, direct heating, and cooling. The components of a geothermal system as outlined by (OpenAI, 2023) include:

Heat Source: the heat source of a geothermal system is mainly derived from the radioactive decay of elements, primarily uranium, thorium, and potassium found in the mantle and crust and residual heat from the origin of the earth.

Reservoir: the reservoir is the underground area where the geothermal heat is stored. It is typically a permeable rock formation, such as fractured rocks or porous sediments, capable of holding and transmitting heat.

Fluids: Geothermal fluids play a crucial role in the system. They can be in the form of water or steam, and they circulate through the reservoir and then transfer as heat to the surface. Geothermal fluids can be naturally occurring, derived from groundwater, or they can be artificially injected into the reservoir to enhance the geothermal system's performance.

Production Well: A production well is drilled into the geothermal reservoir to take out the hot fluids from the underground. The fluids, steam or hot water, flow up the well to the surface.

Surface Facilities: Once the geothermal fluids reach the surface, they are directed to surface facilities, which typically include separation equipment to separate the steam or hot water from any impurities or gases present in the fluid.

Power Generation System: In a geothermal power plant, the extracted steam or hot water is used to drive turbines, which in turn generate electricity. The power generation system includes turbines, generators, and other auxiliary equipment necessary for electricity production.

Utilization System: Geothermal heat can also be utilized for direct applications such as district heating, industrial processes, and agricultural purposes. In these systems, the hot water or steam is used directly without the need for electricity generation.

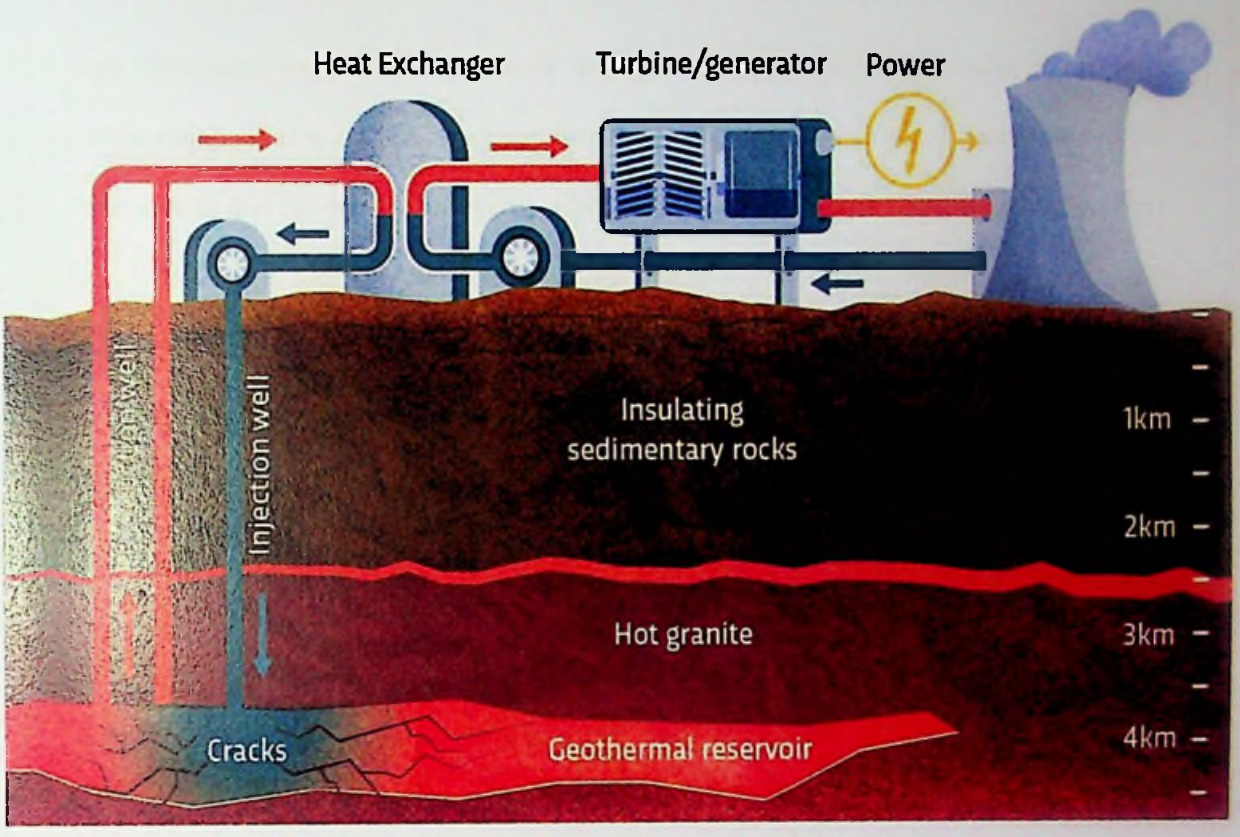


Fig. 2.5: A Typical Geothermal System (OpenAI, 2023)

2.2.6 Hydrothermal Resource

The term "hydrothermal" describes heated water resources, which are found in naturally occurring hydrothermal resources. They are the result of favorable geological features such open fissures or cracks that permit fluid movement between them and the groundwater. The meteoric water is heated by the rocks' higher temperatures, and at a very high temperature, they can be extracted either as steam or hot water to the surface for direct use or electricity generation. Hot, wet rocks, sedimentary environments, and volcanic settings all contain these hydrothermal resources (ThinkGeoenergy, 2022).

2.2.6.1 Geysers

These are circular holes or vents that periodically eject water and steam. Geysers are very uncommon occurrences that arise from specific hydrogeological circumstances found in a limited number of locations on Earth. The geyser is always as a result of nearby magma, and most geyser field sites are situated close to active volcanic zones ("Geyser", 2023).

The process starts with groundwater passing through primarily SiO2-rich rhyolitic rocks, which are heated by a deep magma body. Parts of the rhyolitic rocks disintegrate as hot groundwater passes through them. Temperature is the primary factor that determines how much silica the groundwater can dissolve, while there are other factors as well. Groundwater can dissolve more silica from the rock at high temperatures than it can at lower ones. The silica-rich waters cool to the ambient temperature and evaporate as this water rises to the surface and bursts into a geyser. Left behind, silica creates a sinter deposit that is also referred to as geyserite (USGS, 2020).

Most of the geysers are in Yellowstone National Park (USA). We also have a few others in Russia, Iceland, New Zealand, and Iceland. These locations have geologically recent volcanic activity and hot rocks.

2.2.6.2 Hot springs

A hot spring is created when heated subterranean water rises to the Earth's surface. The molten rock bodies or hot rock circulates through faults to the deep crust and heat the groundwater. Hot springs are typically found in areas with volcanic activity, geothermal areas, or regions with significant tectonic activity so they are major indicators of geothermal manifestation in an area ("Hotspring", 2023).

2.2.6.3 Fumaroles

Fumaroles are hydrothermal features that occur when steam and volcanic gases escape from openings in the Earth's crust. They are often associated with volcanic activity and are commonly found in areas with active or dormant volcanoes, geothermal fields, and geologically active regions. Fumaroles form when hot gases and steam, often derived from magma or heated rocks beneath the surface, flow through openings and fractures in the crust. As they get to the surface, they are released into the atmosphere through openings called fumarolic vents. Fumaroles emit a mixture of gases, which can include water vapour (steam), carbon dioxide, sulfur dioxide, hydrogen sulfide, hydrogen, and other gases. The specific composition of the gases can vary depending on the geological conditions and the type of volcanic activity (OpenAI, 2023).

Fumaroles, due to the interaction between the hot gases and the rock material can alter the surrounding rocks which results in the formation of various minerals like sulfur, sulfates, and other hydrothermal minerals, which may deposit around the fumarolic vents. The gases emitted by fumaroles can be harmful if inhaled in high concentrations. Volatile conditions around fumaroles can lead to ground instability and the formation of acid-sulfate soils. Fumaroles provide valuable insights into the geothermal activity and volcanic processes occurring beneath the Earth's surface. They are often studied by geologists and volcanologists to better understand volcanic systems, monitor volcanic activity, and assess the potential risks associated with volcanic eruptions.

2.3 Theoretical Framework

2.3.1 The Spectral Method

One of the most effective techniques used for data analysis in different fields of science, geophysics, environment, oceanography, atmospheric science, astronomy, and engineering is the spectral depth analysis approach. It can either be applied in the time and frequency domain. Spector and Grant (1970) introduced the use of power spectrum approach that gives depth to the top of the magnetic layer. The following authors like Bhattacharyya & Leu (1975), Treitel *et al.* (1971), Okubo *et al.* (1985), Tanaka *et al.* (1999), Ravat (2004), and Ross *et al.*, (2006) enhanced the method.

According to Hinze *et al.* (2013), we can use the power spectrum (P_s) from magnetic sources at a particular average depth (z) to know the top of the magnetic sources by:

$$P_S(k) = Ce^{-4\pi zf} = Ce^{-2zk} \quad (2.1)$$

f is the frequency of the signal. K is the wave number that corresponds to $2\pi f$ while C is a constant. Taking the logarithm on both sides of equation 2.1, we have

$$In\, P_S(K) = InC - 4\pi zf = InC - 2z(k) \quad (2.2)$$

A linear segment resulting from the anomaly at a specific depth Z would be derived by plotting the logarithm of the power spectrum against frequency. The radial spectrum's logarithm plot gives us a straight line whose slope is 2Z. To get the ensemble's depth of burial, we next say

$$Z = \frac{-M}{2} \quad (2.3)$$

And m, is the slope of the graph.

2.3.2 The Derivatives

The vertical derivatives, which can be measured in the frequency or space domain, are frequently used to highlight the shallowest geological source in total magnetic field data. With the vertical derivative filter, we can narrow the width of the anomaly to detect the source bodies more accurately (Cooper, 2006). This enhancement gives you a clearer and sharper image of the underlying structure thereby reducing the complexity of the anomaly. The transformation becomes noisy too since the short wavelength noise is amplified.

Vertical derivatives highlight the anomalous field's short wavelength component while downplaying its long wavelength component. The first differential order of the vertical derivative significantly reduces the regional effect of the data and is an excellent method for identifying abnormalities over discrete structures found in the field data. Vertical derivatives in the space domain are not considered in the same way as horizontal derivatives, according to Fairhead (2007), because they require knowledge of the divergent and decrease in height. What derivatives do is quantify the spatial rate of change of the earth's field in vertical and horizontal directions. The expression for the magnetic force $F_{(r)}$ is obtained from Coulomb's law for magnetic poles m_1 and m_2 separated by a distance r as

$$\vec{F}(r) = \frac{m_1 m_2}{\mu r^3}\vec{r} \qquad (2.4)$$

In practice, the scenario is satisfied if we assume two very long bar magnets with two poles near together and the other two far away. The poles are somewhat of a fiction as they can only exist in pairs. The value μ is the permeability of the medium surrounding the magnetic field strength $\vec{H}(r)$ and is expressed as

$$\vec{F}(r) = (\frac{m}{\mu r^3})\vec{r} \qquad (2.5)$$

And the magnetic induction $\vec{B}(r) = \mu\vec{H}(r), the\ magnetic\ field\ \vec{B}(r)$ can be derived from a scalar potential function $A(r)$ as

$$\vec{B}(r) = -\vec{\nabla}A(r) \tag{2.6}$$

This potential may be defined as the work done in moving a unit pole against the magnetic field as:

$$A(r) = -\int_{\infty}^{r} \vec{B}(r).\overrightarrow{dr} = m/\mu r \tag{2.7}$$

The first and the second vertical component of the field $\vec{B}$ are the derivatives of the potential in the direction of the vertical axis. They are respectively

$$\frac{\partial B}{\partial z} = -\frac{\partial^2 A}{\partial z^2} \quad and \quad \frac{\partial^2 B}{\partial z^2} = -\frac{\partial^3 A}{\partial z^3} \tag{2.8}$$

As the gravity potential A satisfies the Laplace's equation: $\nabla^2 A = 0$, the magnetic potential everywhere within a region containing magnetic material satisfies the Poisson equation.

$$\nabla^2 A = 4\pi\nabla.\vec{M}(r) \tag{2.9}$$

Where the magnetic body is a continuous distribution of dipoles resulting in a vector dipole moment per unit volume, $\vec{M}(r)$

There are modern methods used for edge detection and depth-to-source estimation that rely on horizontal and vertical derivatives for accuracy (Nabighian *et al.*, 2005).

The horizontal derivative technique according to Fairhead (2007) has been considered the simplest method used by researchers to detect the contact location of faults, due to the gradient is largest at the edge of horizontal bodies.

According to Christensen and Dransfield (2002), the magnetic vector filter's initial horizontal derivatives continue to reveal extra details regarding the directional fluctuations of the entire magnetic field. The derivative result known as a horizontal derivative map highlights the discontinuities in the anomalous pattern and reveals the anomalous texture. Hogg (2004) asserts that first horizontal derivatives can provide greater accuracy and advanced resolution at broader line spacing when attempting to map linear features, like faults or dykes, from magnetic data.

Summing of the gradient in an orthogonal direction gives the horizontal derivative of an anomaly field. So, if we consider M(x,y) as the magnetic field, then the horizontal derivatives are:

$$HGM\ (x, y) = \sqrt{(\frac{dm}{dx})^2 + (\frac{dm}{dy})^2} \quad (2.10)$$

The Tilt Derivative remains one of the most powerful grid enhancement tools, together with sun-shading. Since it acts as a type of automatic gain control, it is better at revealing low-amplitude features than fractional vertical derivatives such as the FVD and remains the simplest and most effective way to enhance features in aeromagnetic grids (Verduzco *et al.*, 2004).

Stewart and Miller (2018) stated that the tilt derivative is a geometrical function of the vertical $\frac{dF}{dz}$ and horizontal $\frac{dF}{dx}$ and $\frac{dF}{dy}$ derivatives of the field F, with values between ± π/2. The tilt derivative (TD) as normally calculated is given by:

$$TD = Tan^{-1}\left[\frac{dF/dz}{\sqrt{(\frac{dF}{dx})^2+(\frac{dF}{dy})^2}}\right] \quad (2.11)$$

2.3.3 The Analytic Signal

For anomalies to be detected above their sources, the analytical signal is used to give us information about magnetic anomalies that is independent of the inclination of the earth's inducing field, that is, independent of the direction of magnetization and the direction of the field (Milligan & Gunn, 1997).

The analytical signal is the square root of the sum of squares of the derivatives in x, y and z directions:

$$A = sqrt(dx * dx + dy * dy + dz * dz) \quad (2.12)$$

Where A, is the analytical signal, dx, dy, dz are the derivatives in the x, y, z directions.

Since the analytic signal involves calculating derivatives of magnetic anomalies, it can be determined most readily in the wavenumber domain. According to Roest *et al.* (1992), the three orthogonal gradients of the total magnetic field can be used to calculate the amplitude of the 3-D analytical signal (AS) at point (x, y):

$$AS\ (x, y) = \sqrt{(\frac{\partial T}{\partial x})^2 + (\frac{\partial T}{\partial y})^2 + (\frac{\partial T}{\partial z})^2} \quad (2.13)$$

Where AS (x, y) is the amplitude of the analytical signal at point (x, y) and T is the observed magnetic field.

The 2D analytic signal of the magnetic anomaly T can be expressed as

$$AS\ (x, z) = \sqrt{(\frac{\partial T}{\partial x})^2 + (\frac{\partial T}{\partial z})^2} \quad (2.14)$$

Where $\partial T/\partial x$, and $\partial T/\partial z$, are the horizontal and vertical derivatives of the magnetic anomaly respectively.

According to Ma and Li (2013), the 2D analytic signal of the magnetic anomaly generated by the source that is located at a horizontal location of x_0 and depth of z_0 can be given by

$$A(x, z) = \frac{k}{[(x-x_0)^2 + (z-z_0)^2]^{(N+1)/2}} \quad (2.15)$$

Where k is a constant value, and N is the structural index of the source, which represents the nature index of the source, N = 0 for a contact, N = 1

For Dikes

$$A(x, z) = \frac{k}{[(x-x_0)^2 + (z-z_0)^2]} \quad (2.16)$$

For horizontal cylinder

$$A(x, z) = \frac{k}{[(x-x_0)^2 + (z-z_0)^2]^{(3)/2}} \quad (2.17)$$

Ofoegbu and Mohan's (1990) definition of the analytic signal's amplitude differs from this one. Rather than using a vector addition, they performed a scalar addition of the two horizontal derivatives. Nabighian (1984) provided an implied suggestion for the scalar addition in his expression of the generalized analytic signal. Nevertheless, a function that is sensitive to a

coordinate system rotation is obtained by the scalar addition of two horizontal derivatives. In reality, as demonstrated by the example provided by Ofoegbu and Mohan (1990), this leads to a focus on structures that are parallel to the orientation of the selected x and y axes.

2.3.4 The Curie Point Depth

The depth at which the temperature of rocks in the Earth's crust surpasses the Curie temperature of magnetic minerals, rendering them non-magnetic, is known as the Curie depth. Geophysicists can determine the temperature of rocks at various depths under the Earth's crust by measuring the Curie depth (OpenAI, 2003).

The majority of geothermal reservoirs in a geothermal environment are thought to get their heat from a level known as the Curie point depth for the geothermal source, which is the magnetic chamber. Curie-point temperature depths offer broad insights into geothermal gradients and the distribution of temperatures locally and regionally.

In the context of geothermal potential, the Curie depth is important because it provides information about the geothermal gradient in the Earth's crust that helps us identify areas with high geothermal potential, as regions with high thermal gradients are likely to have a greater amount of heat available for geothermal energy production.

The radially averaged power spectrum procedure which provides depth to the top of the magnetic layer was introduced by Spector and Grant (1970]). Additionally, this method was improved by Treitel *et al.* (1971), Bhattacharyya and Leu (1975), Connard *et al.* (1983), Okubo *et al.* (1985), Blakely (1995), Tanaka *et al.* (1999), Ravat (2004) and Ross *et al.* (2006). These methods allow the thermal structure of a region to be obtained by using magnetic anomaly values.

2.3.5 The Centroid Method

Bhattacharyya and Leu proposed a method in 1977 for finding the centroid of rectangular parallelepiped sources. Okubo *et al.* (1985) also employed this technique. The method uses an azimuthally averaged frequency-scaled Fourier spectrum in the low wavenumber region to

estimate the depth to the centroid (Z_o), and the slope of the same spectrum in the high wavenumber region to estimate the depth to the top of the source.

From Pamuk and Özsöz (2022), simplified definition of the radially averaged spectrum can be given as:

$$P(|k|) = Ae^{-2|k|z_t}\ (1 - e^{-|k|(z_b - z_t)})^2 \qquad (2.18)$$

A is constant, k is wavenumber, z_b & z_t are depth to the top and bottom of the source

Applying the natural logarithm to both sides of equation 2.18

$$\ln [P(|k|) = \ln [A] - 2z_t(k) + 2 \ln [1-e^{-|k|(z_b - z_t)}] \qquad (2.19)$$

For high and medium value of wavenumber, the exponential component in equation 2.19 can be ignored.

$$\ln P[(|k|) = \ln [A] - 2z_t(k) \qquad (2.20)$$

Dividing equation 2.20 by 2 we have:

$$\ln [P(|k|)^{1/2}] = C - z_t(k) \qquad (2.21)$$

Where C is constant. The slope of equation 2.21 gives the depth to the top of magnetic layer z_t

To get the centroid depth, we multiply equation 2.18 by $e^{-|k|(z_0 - z_0)}$ and divide by 2

$$\ln [P(|k|)^{1/2}] = Ae^{-|k|z_0}(e^{-|k|(z_t - z_0)} - e^{-|k|(z_b - z_0)}) \qquad (2.22)$$

Z_0 is the centroid depth of the magnetic source. Replacing the exponential term in equation 2.22 by first term of their Taylor Series expansion, we have

$$\ln [P(|k|)^{1/2}] \approx Ae^{-|k|z_0}(z_b - z_t) \qquad (2.23)$$

where $z_b - z_t$ is the thickness of the magnetic crust. Substituting and rearranging

$$\ln[\frac{P(|k|)^{1/2}}{k}] = \ln D - Z_0|k| \qquad (2.24)$$

The slope of equation 2.24 gives the centroid depth of the magnetic source

Equations (2.21) and (2.24) are straight line equations and to compute Z_t and Z_0 it is necessary to calculate the slope of the straight line at high- and low-wavenumbers. Finally, the depth to the bottom of the magnetic source Z_b (DBMS) according to Okubo *et al.* (1985) can be calculated as:

$$Z_b = 2Z_0 - Z_t \qquad (2.25)$$

For this research, we adopted the centroid method of calculating the Curie point depth which has been proven effective and yields satisfactory results.

2.3.6 The Geothermal Gradient and Heat Flow Calculation

The geothermal gradient is a measure of how temperature increases with depth within the Earth's crust. It is typically measured in degrees Celsius per kilometer (°C/km). A lower geothermal gradient means that there is less temperature increase with depth, indicating that the rock layers in the crust are not conducting heat as efficiently. In contrast, a higher geothermal gradient indicates that there is a greater temperature increase with depth, suggesting that the rock layers are more thermally conductive.

Both the lithosphere and asthenosphere have an impact on surface heat flow. Values of regional heat flow derived from the surface make a substantial contribution to the evaluation of the region's geological structure. Curie point depth values will be used in this investigation to get geothermal gradient data. Fourier's law is the fundamental relationship for conductive heat transfer in the computation of heat flow and thermal gradient (Nwankwo *et al.*, 2011).

According to Tanaka *et al.* (1999), Curie temperature (θ) can be determined using the equation:

$$\theta = \left[\frac{dT}{dz}\right] z_b \qquad (2.26)$$

Where Z_b, is the CPD. The geothermal gradient will then be

$$\frac{dT}{dZ} = \frac{\theta}{Z_b} \quad (2.27)$$

In this research we assumed that heat flow direction is vertical and dT/dZ constant. The heat flow values were obtained using the heat equation

$$q = k\frac{dT}{dZ} \quad (2.28)$$

Where q is heat flow, and k is the coefficient of thermal conductivity. I adopted the thermal conductivity of 2.5 $Wm^{-1}K^{-1}$ and assumed the study area to be isothermal (580°C) (Bektaş *et al.*, 2007; Nwankwo *et al.*, 2011; Pamuk, 2019).

2.3.7 Radiometric Theory

Radiometry is a technique for measuring electromagnetic radiation and its distribution in terms of its power, polarization, and spectral content relevant to a particular source. This theory is used to estimate concentrations of the radioelements: Potassium (40K), Uranium (238U), and Thorium (232Th) which are long-lived radioactive elements of interest for geothermal resources. The Precambrian basement is mostly covered by newer sedimentary and granitic rocks that release radiogenic geothermal heat. Radiation such as protons, neutrons, gamma rays, alpha particles, and beta particles are emitted in tandem with it. High-energy electromagnetic radiation, known as gamma particles, has a distinct energy for every decay reaction. Using aerial gamma-ray spectroscopy (AGRS) measurement, the amount of heat-producing elements (HPE) in the sedimentary and igneous rocks of the Earth's crust would be measured in counts per second. The concentration of certain decaying isotopes can be ascertained using their spectra (Gilmore, 2008).

The spectrometer records gamma-ray spectra while in flight, and in order to account for the effects of gamma ray interaction and attenuation during the flight from the source to the detector in the helicopter, a number of processing steps must be taken. We mostly followed the standard operating procedures outlined in the IAEA's recommendations (IAEA, 2003).

We applied the window approach to the spectra after stabilization. This technique is based on energy windows in the gamma spectrum linked to uranium (U), thorium (Th), and potassium (K), the three naturally occurring radioelements. The system-specific calibration parameters were utilized to apply multiple processing and correction stages to the window count rates. Using Rybach's equation, the radiogenic heat production (RHP) can be calculated as;

$$RHP\ [\mu wm^{-3}] = \rho\ (0.035C_k\ [\%] + 0.0.97\ C_u\ [ppm] + 0.026\ C_{th}\ [ppm]) \qquad (2.29)$$

Where *RHP* is radiogenic heat production in μWm^{-3}, ρ is average rock density (kg m^{-3}), C_k is the average concentration of *K* by % weight. C_u and C_{th} are the average concentrations of U and Th (ppm), respectively.

2.3.8. The Shuttle Radar Topographic Mission

Using the ArcGIS software, the Shuttle Radar Topographic Mission (SRTM) gridded data covering the study area converted to a map. The Shuttle Radar Topography Mission data was used in the geothermal interpretation because it provides high-resolution elevation data, which is important for mapping and visualizing the topography of a geothermal area. Accurate topographic maps enable us to identify potential areas for geothermal resource exploration and development. By analyzing the elevation data from SRTM, we can calculate the temperature increase with depth in a given area. Higher elevations often correlate with higher geothermal gradients, which can indicate areas of greater geothermal potential.

With SRTM data, we can identify and characterize fault zones within a geothermal area. Faults can play a significant role in geothermal systems, as they provide pathways for the circulation of fluids and heat. With the elevation data, fault patterns and basin morphology can be understood which is crucial for assessing the potential for geothermal reservoirs.

CHAPTER THREE

MATERIALS AND METHODS

3.1. Materials

The following materials were used for this research work;

I. High-speed computer system.

II. Software; Oasis Montaj v. 8.4, Matlab 2016, ArcGIS 10.8, Rockworks, Surfer version 13, and Microsoft Excel.

III. Data sets; aeromagnetic, aero radiometric data and SRTM

3.2 Methods

3.2.1 Location of the Study

The study was done in some parts of Northern Nigeria. The region cuts across eight states of Nigeria, namely, Nasarawa, Kaduna, Bauchi, Plateau, Taraba, Benue, Kogi, and FCT (Fig. 3.1). It is located approximately between longitudes 7°30E – 10°E and latitude 7.30°N – 10°N with an estimated total area of 75,625km^2. The study area consists of parts of Benue Trough (majorly the middle Benue Trough and some lower part of the Trough), and the Precambrian Basement Complex intruded by the Jurassic Younger Granites. Most of the hot/warm springs in Nigeria are housed within the study area. The study area is covered with 60% Basement complex rocks while the remaining 40% is made up of sedimentary rocks of the Benue Trough

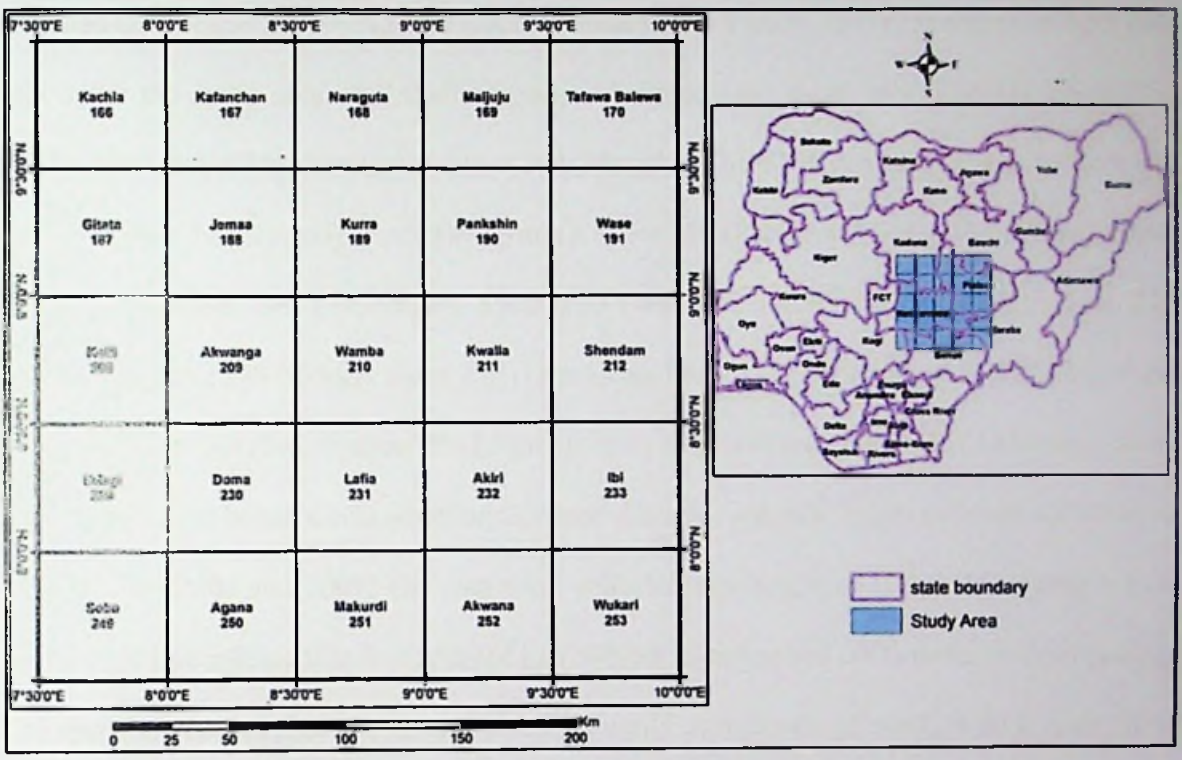


Fig. 3.1: The location Map of the study area

3.2.2. Method of Data Acquisition

The aeromagnetic and aero radiometric dataset used in this research work was acquired from the Nigerian Geological Survey Agency (NGSA) Abuja. The Twenty-five (25) sheets of both data that cover the study area with their respective locations are sheet 166 (Kachia), Sheet 167 (Kafanchan), Sheet 168 (Naraguta), Sheet 169 (Maijuju), Sheet 170 (Tafawa Balewa), Sheet 187 (Gitata), Sheet 188 (Jemaa), sheet 189 (Kurra), Sheet 190 (Pankshin), Sheet 191 (Wase). Sheet 208 (Keffi), sheet 209 (Akwanga), Sheet 210 (Wamba), Sheet 211 (Kwalla), sheet 212 (Shendam), sheet 229 (Udegi), sheet 230 (Doma) and sheet 231 (Lafia), sheet 232 (Akiri), sheet 233 (Ibi), sheet 249 (Soko), sheet 250 (Agana), sheet 251 (Makurdi), sheet 252 (Akwana), sheet 253 (Wukari). On behalf of the Nigerian Geological Survey Agency, Fugro gathered the airborne data between 2005 and 2009. The data were collected at a height of 100 meters along a 500-meter flight line spacing that was oriented in a NW-SE direction and 2000-meter tie line spacing. The maps are half-degree sheets contoured primarily at intervals of 10nT, with a scale of 1: 100,000. The geomagnetic gradient was eliminated from the aeromagnetic data using the International Geomagnetic Reference Field (IGRF) of 2005 and other filtering. The sum of 33,000nT was eliminated from the total magnetic field as the regional field leaving the residual for the data processing.

The Shuttle Radar Topography Mission (SRTM) data was obtained using ArcGIS software. The SRTM is mounted on a space shuttle and obtains Earth's surface data by remote sensing technology utilizing synthetic aperture radar. The data collected was converted into height data which is referred to as a Digital Elevation Model (DEM) and then utilized for analysis.

3.2.3 Methods of Data Analysis

The Spectral Analysis Method as pioneered by Bhattacharya (1966) and later by Spector and Grant (1970) which has been adopted and improved by many authors (Bhattacharya & Leu, 1975; Mishra & Naidu, 1974; Shuey *et al.*, 1977; Cornad *et al.*, 1983; Onuoha *et al.*, 1994; Nwogbo, 1997; Eleta & Udensi, 2012; Salako & Udensi, 2013; Kasidi & Nur, 2013; Tanaka *et*

al., 1999) was adopted in this research work in the determination of average depth to the top of magnetic basement, centroid depth, Curie point depth, the geothermal gradient and the heat flow in the region.

The Radiometric Method as pioneered by Rybach's (1976) empirical formula was used in calculating the radiogenic heat produced in the area and the result will be set side by side with that of the magnetic heat flow.

Shuttle Radar Topography Mission data was utilized in visualizing the topography of the geothermal area because it provides high-resolution elevation data. By analyzing the elevation data from SRTM, we can assess topographic features, identify the fault patterns and analyze basin characteristics.

CHAPTER FOUR

DATA PRESENTATION AND ANALYSIS

4.1. Data Presentation

The data was obtained using a computer-based modern magnetometer that captures data on aircraft attitude, altitude, magnetic, navigational, and temporal aspects. A set of leveled flight-line data interpolated onto a regular grid of magnetic field intensity values encompassing the survey zone serves as the final representation of these collected data. These values are shown as a colour map, where each magnetic field value is given a particular colour corresponding to its magnitude as shown in Fig. 4.1. The long wavelength and short wavelength features were effectively displayed in the combined colored map.

The TMI map of the study area shows that there are both high and low magnetic anomaly signatures ranging from 33,088.67 to 33132.23nT in the region. It was subjected to IGRF to remove the regional components from the earth's magnetic field and the residual ranges from -88.6735 to 132.2331nT.

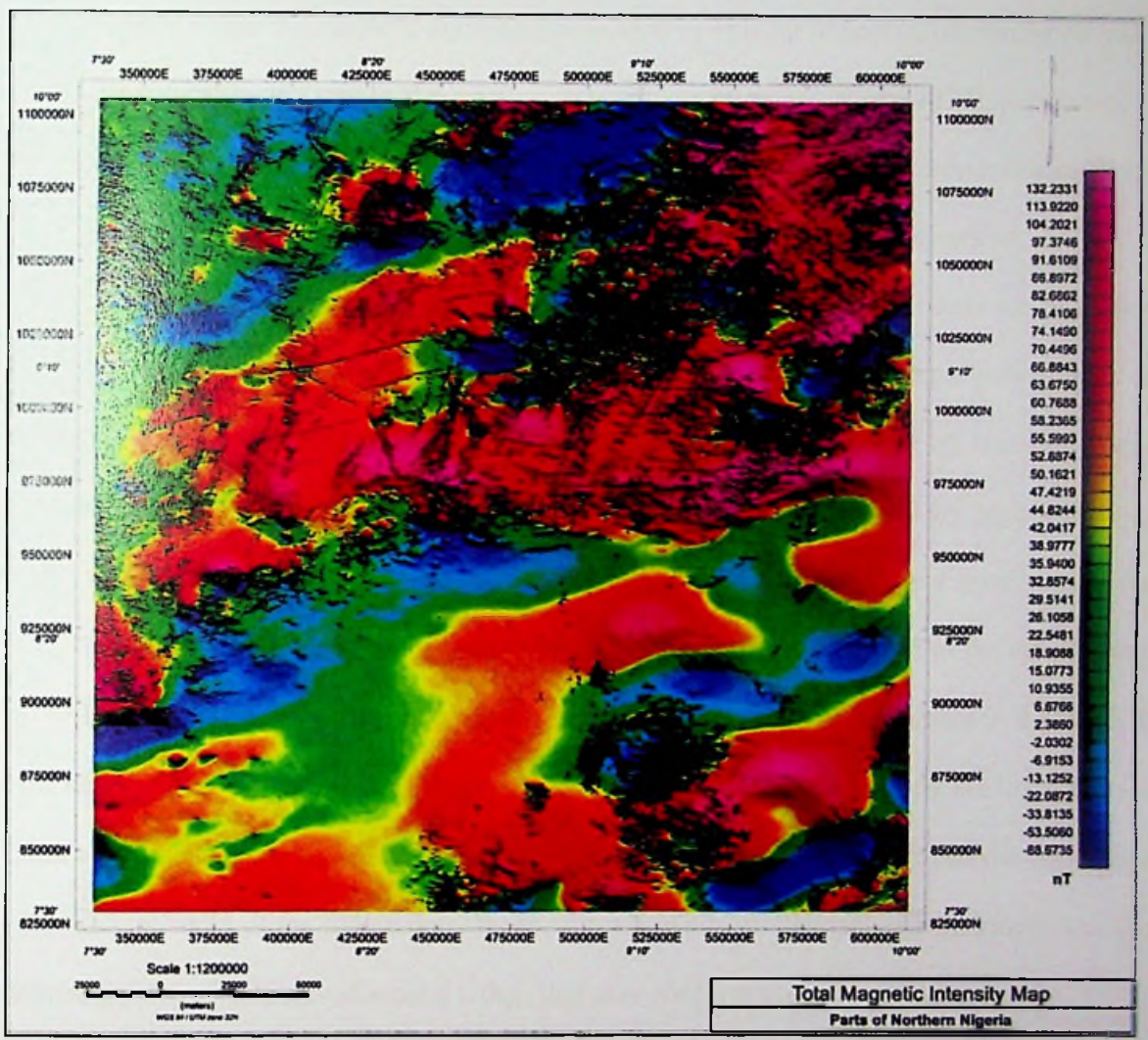


Fig. 4.1: The Total Magnetic Intensity Map of the Study Area

4.2 Data Analysis

4.2.1 Reduction to the Equator

The TMI map after removing the regional effect was further reduced to the equator (Fig. 4.2) to symmetrically center the magnetic anomalies over their origins for improved interpretation since the research location is close to the equator. According to Redford *et al.* (2010), decreasing to the equator is the optimum option if the study area has a low inclination because reducing to the pole becomes unstable and produces linear artifacts along the declination's direction.

The sedimentary basins (part of middle Benue Trough and lower Benue Trough) are correlated with the magnetic variations within the study area, which are long wavelength bodies found in the center and southern regions of the study area. The Northern side of the study area corresponding to the Nigerian Northern Basement Complex is dominated by high-frequency magnetic bodies, indicating magnetic bodies at shallow depths. The different signatures in the earth's magnetic fields are due to different lithological units, variations due to the morphology of the basement, and the sedimentary rocks. The major lineaments are dominant in the NE-SW direction and others in the NEE-SWW, ESE-SSW, and NW-SE trending. There is a linear feature (fault or fracture) thought to be a major divide that creates a boundary between the crystalline rocks and the rocks of the sedimentary basin with a fold around Shedam and Gerkawa. A major depression was also observed around Udegi that may conform to the River Benue.

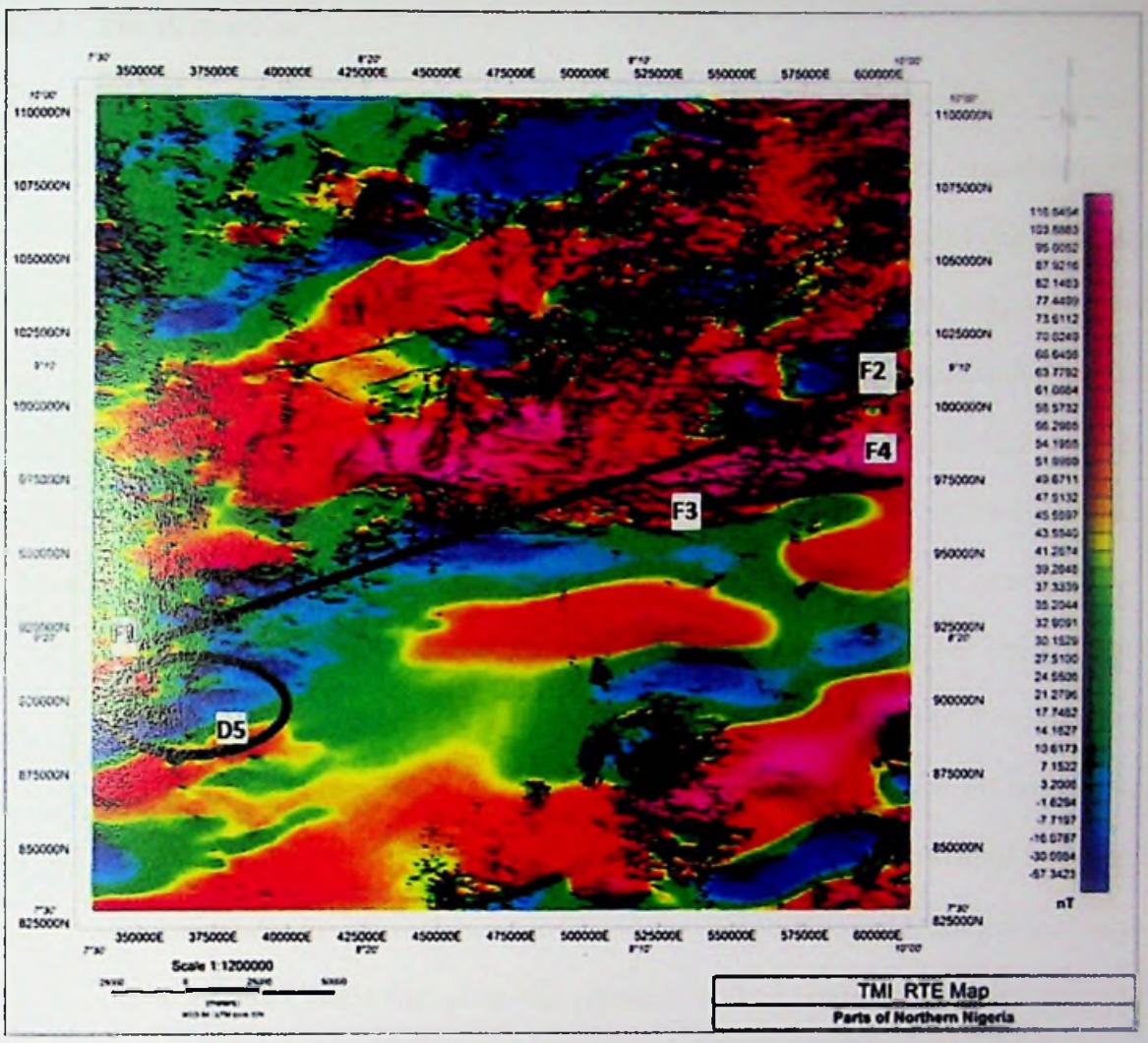


Fig. 4.2: The TMI Reduced to equator Map

4.2.2 The Derivatives

The vertical derivatives are filters in magnetic interpretation used to enhance shallow anomalies by sharpening the edges of these anomalies, making them apparent. The first vertical derivative map (Fig. 4.3) gives a better visualization of closely spaced anomalies by quantifying the change in the signal as a function of the survey heights, thereby eliminating the long wavelength components of the magnetic field. Notably, the linear features after the filter application are well-defined compared to the total field profile. The result shows areas with high magnetic frequencies in the northern side of the study area that implies areas with shallower depths to causative sources, and lower frequencies in the southern area indicating deeper sources.

The vertical gradients show variable magnetic contrast whose amplitude varies from -0.0305nT/m to 0.0312nT/m. The high gradient values are attributed to areas of felsic and mafic rocks found in the crystalline basement and some granitic intrusions around the sedimentary basin. A few low gradient values seen in the crystalline basement can be attributed to the fault pattern and contacts due to intense shearing in those areas. We observed also, low gradient values around the sedimentary basin that show the presence of fluid, alluvium deposits, and other sedimentary formations in the basin.

The horizontal derivative when viewed in the x and y directions (Fig. 4.4a and b) enabled us to enhance the data, remove regional trends, and focus on sharp magnetic contrast which emphasizes rapid changes in the magnetic field. We observed the structures became more apparent in the horizontal directions. The map emphasizes more on the lateral variations which show the geological boundaries and linear structures like faults trending NE-SW, ENE-WSW direction, and the lesser faults trending in the E-W direction. The amplitudes of these variations (dx and dy) ranges from (-0.0305nT/m to 0.0312nT/m) and from (-0.0802nT/m to 0.0780nT/m).

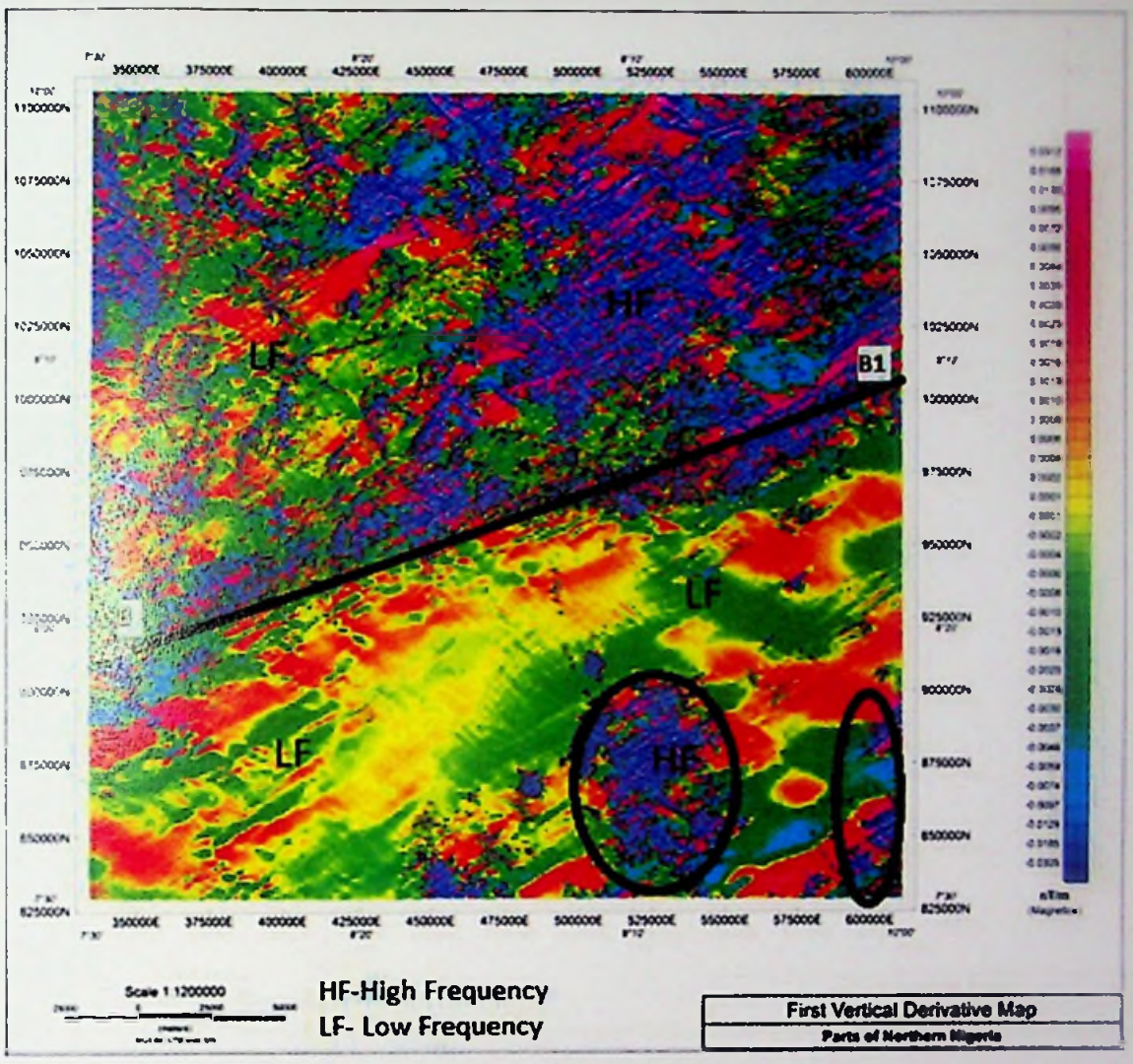


Fig. 4.3: The First Vertical Derivative Map

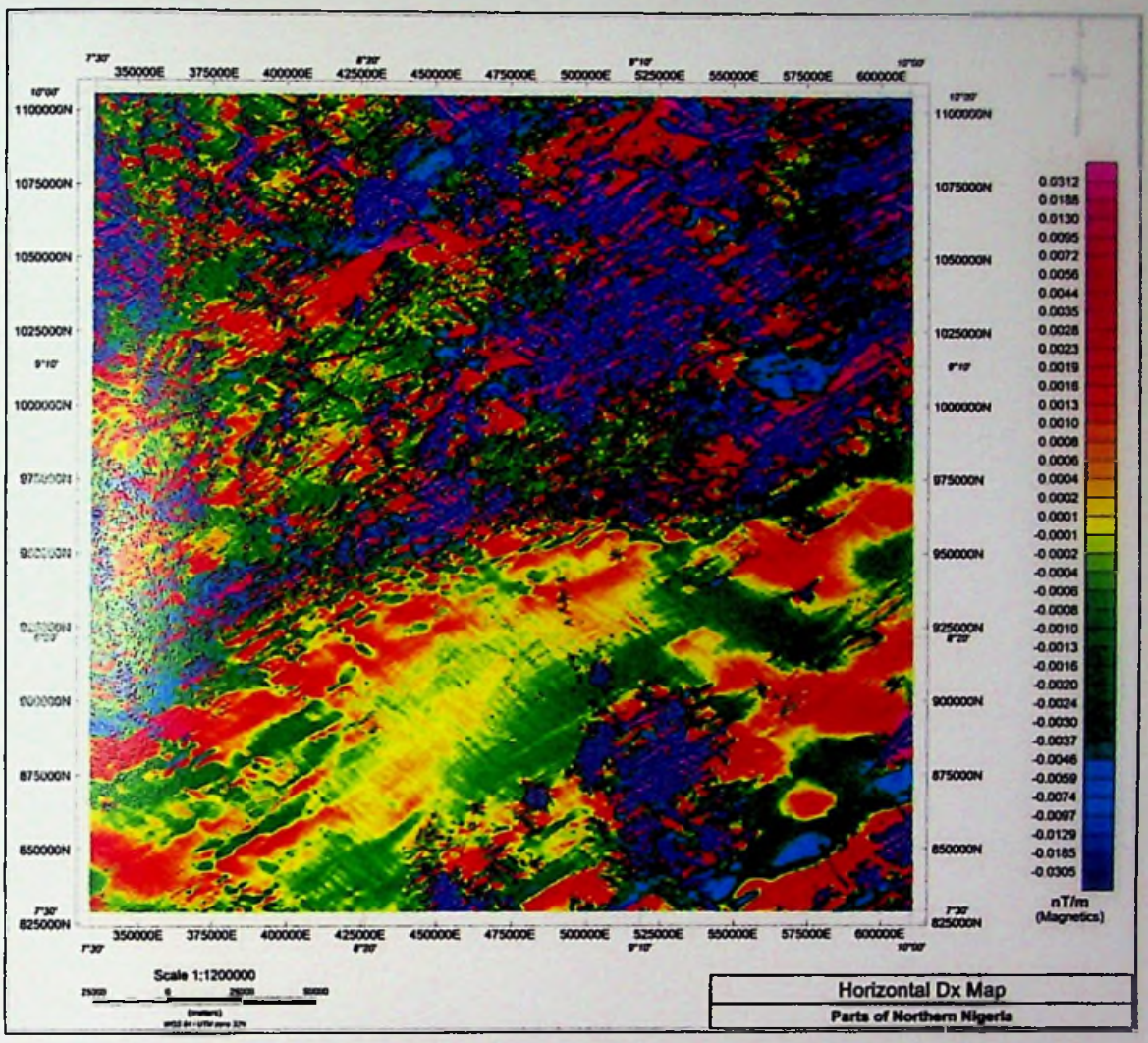


Fig. 4.4a: The Horizontal Derivative Map in x-direction

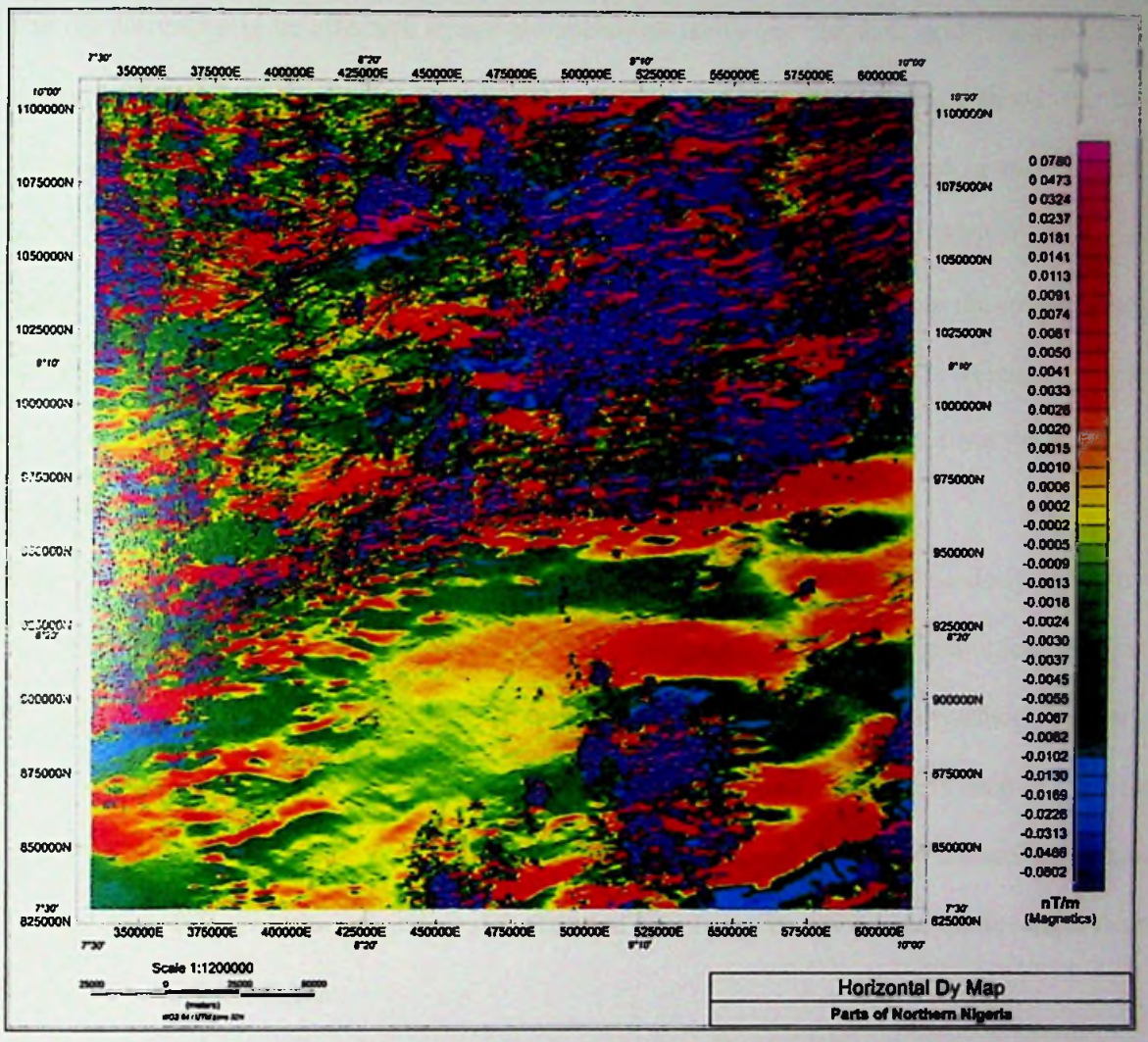


Fig. 4.4b: The Horizontal Derivative Map in y- direction

The tilt derivative is an effective image enhancement technique for data grids because of its ability to detect low-amplitude signals. The tilt derivative map (Fig. 4.4c) shows the low amplitude details are enhanced which we could barely see in the RTE grid or the 1st-order derivative. Its amplitude ranges from -1.5975rad to 1.7940rad. The tilt derivative is very dependent on the inclination of the magnetic field and has no information about the susceptibility of the causative bodies or the strength of the geomagnetic field because it is a function of the ratio of the vertical and horizontal derivatives of field intensity. The zeros of the tilt angle are over the edges of the source body, and the amplitude is over the center.

The total horizontal derivative map (Fig. 4.4d) which is the summation of the derivatives in x and y directions clearly shows the contacts of different rock units and their geological features. We could see the linear features, major faults in thick dark lines, and the subsurface boundary. The short linear and curvilinear features trending W-E, N-W direction majorly seen in the west of the study area are concentrated within the magnetic source bodies of muscovite schist, porphyritic granites, biotite granites, and the banded granite gneiss whose amplitude ranges from 0.0006nT/m to 0.1261nT/m.

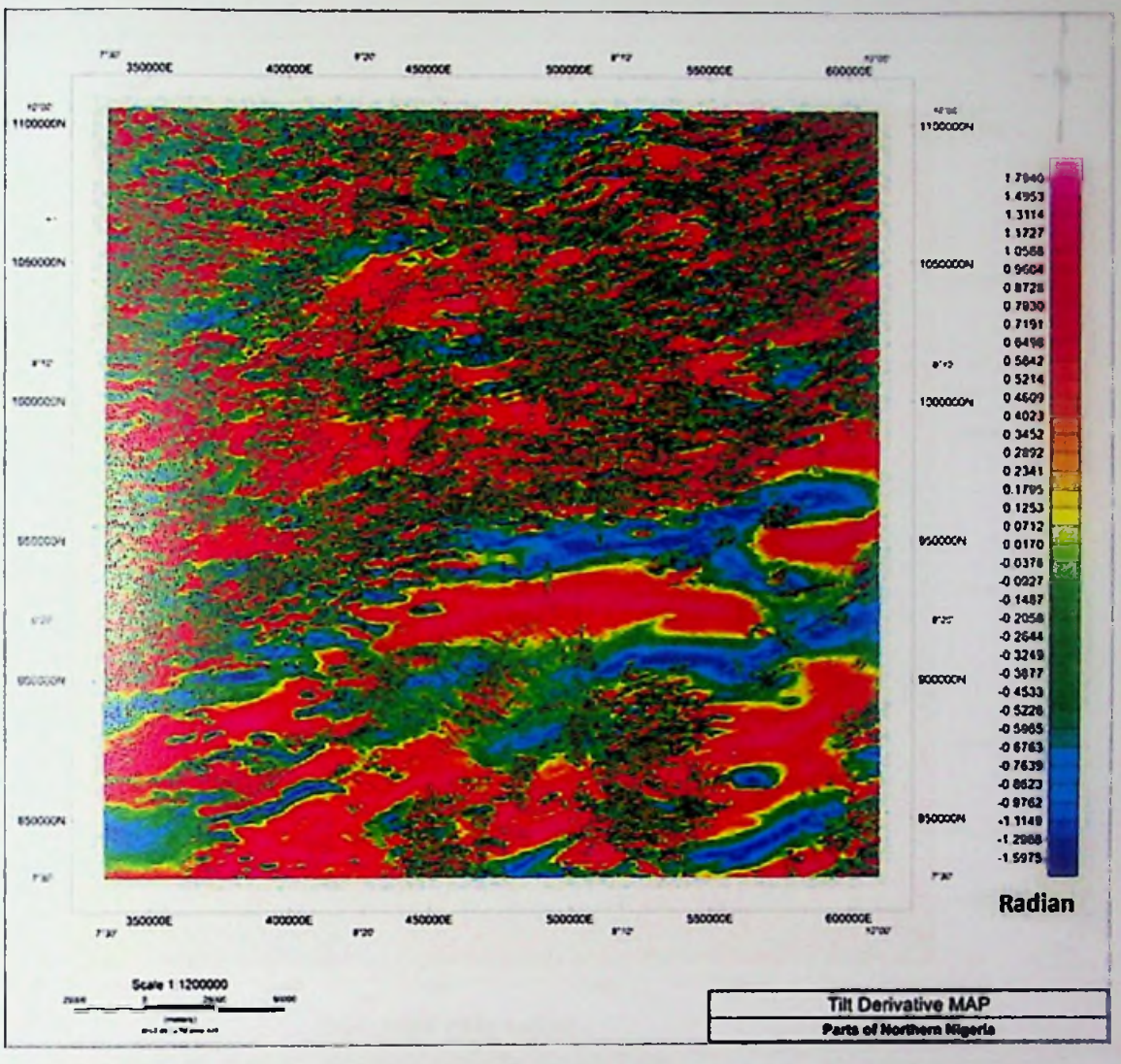


Fig. 4.4c: The Tilt Derivative Map

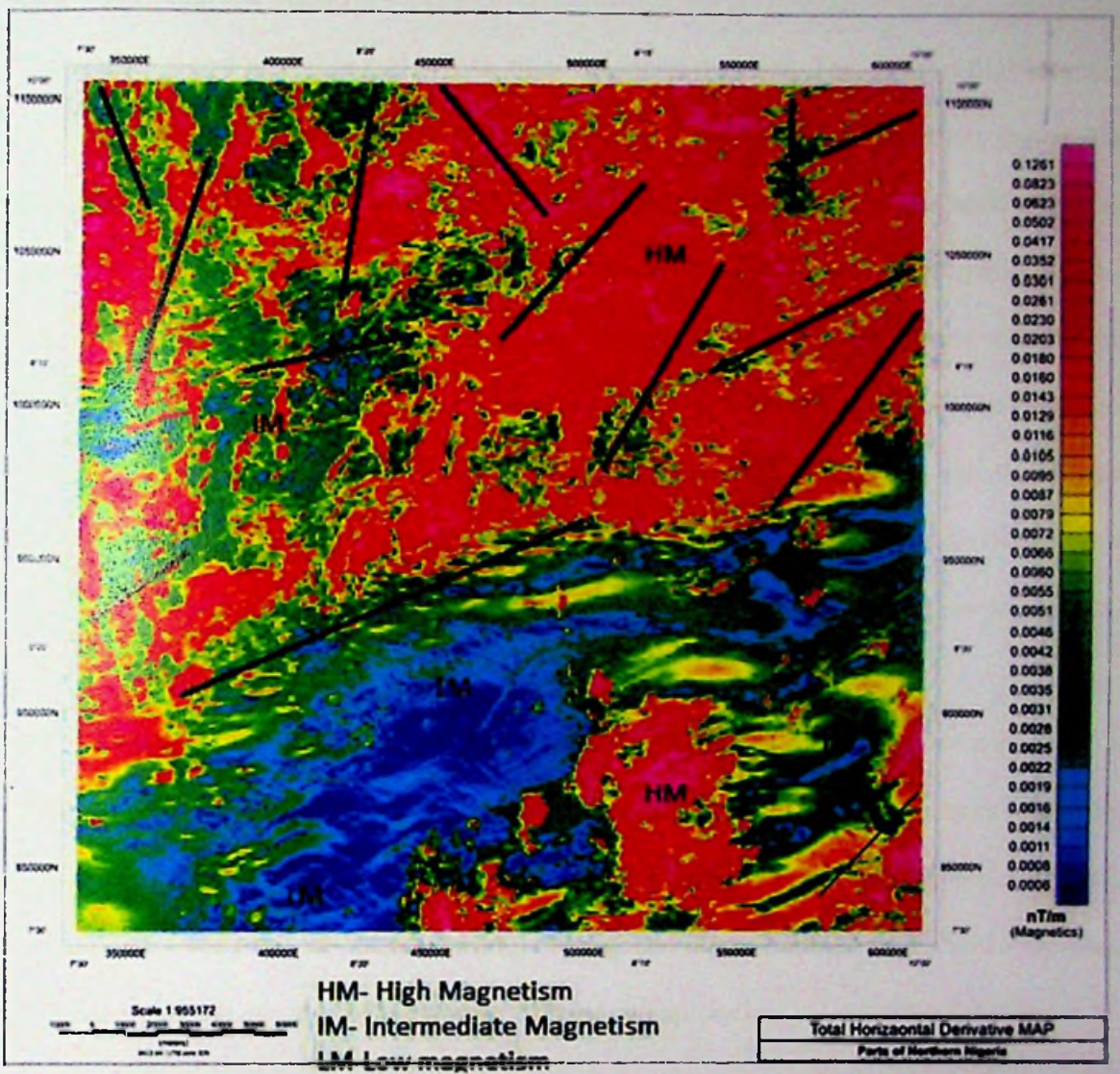


Fig. 4.4d: Total Horizontal Derivative Map showing fault lines and edges of the anomalies

4.2.3 The Analytic Signal

The analytic signal map (Fig.4.5) reveals three magnetic domains. The areas of high magnetic gradient are majorly in the north-eastern area and a few in the western and southern region. This high magnetic signal ranges from 0.0656nT/m and 0.1879nT/m and can be attributed to outlines of magnetic sources which is associated with intruded granitic bodies (Porphyritic granites, Young Jurassic Granites, Banded Granitic Gneiss, biotite granites, Quartz Syenite and Gabbro). The area of intermediate magnetic intensities ranges from 0.0096nT/m to 0.0371nT/m which might be zones with rocks of meta-volcanic and meta-sediments. The low magnetic intensity 0.0011nT/m to 0.0371nT/m are seen mostly in the sedimentary basin shows a relatively low magnetic contrast of the sediment and its surrounding rocks and also deeper seated magnetic sources in the zone.

The low-intermediate amplitude signature seen around the basement complex can either be attributed to rocks that have undergone significant alteration processes or zones where the magnetic sources within the basement are deep-rooted thereby causing weak magnetic responses. We could also see from the map, networks of magnetic discontinuities which could represent fractured zones and can also be of interest for mineral exploration.

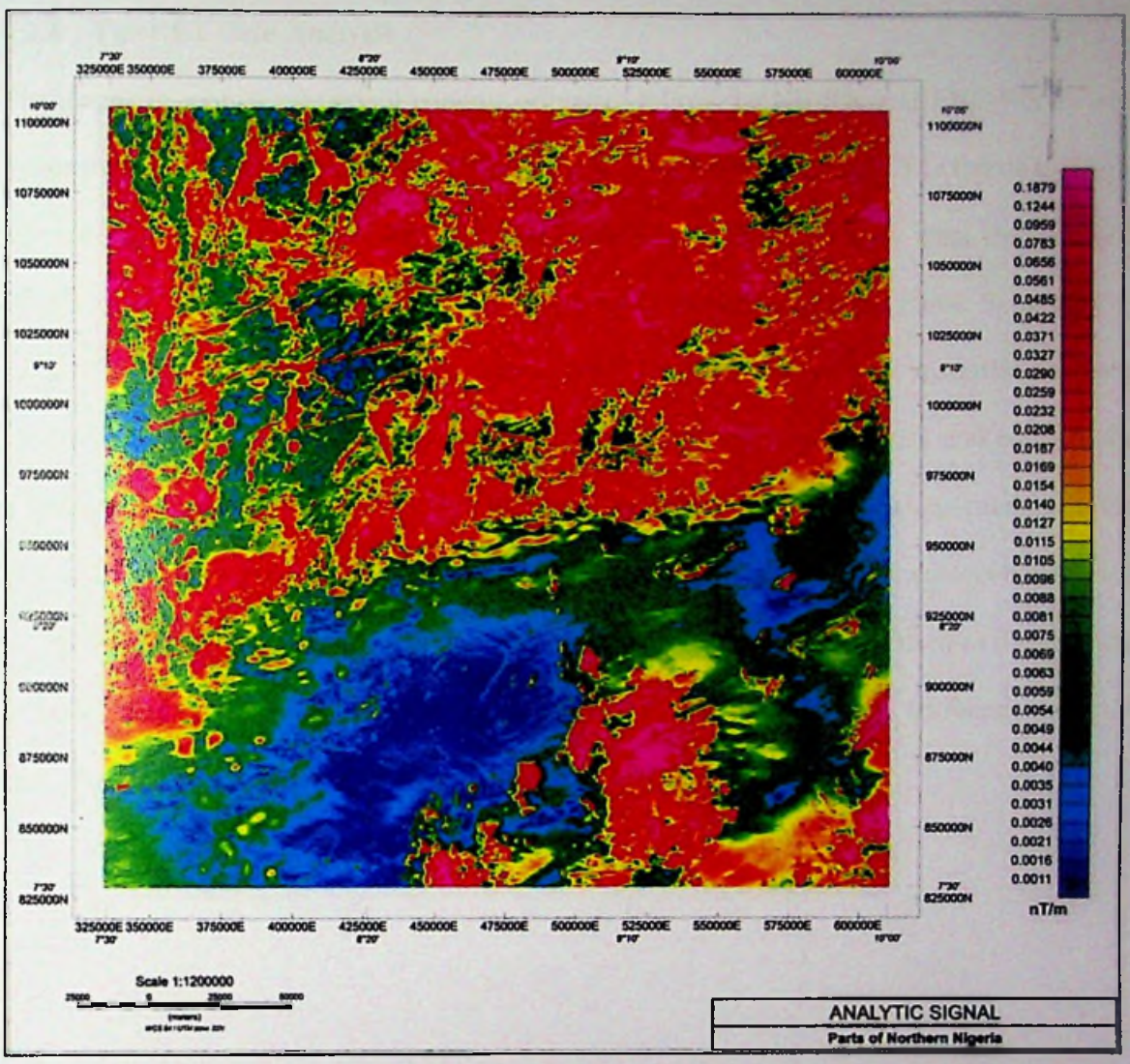


Fig. 4.5: The Analytic Signal Map of the Study Area

4.2.4 The CET Grid Analysis

The magnetic anomaly structural patterns primarily follow the NE-SW and ENE-WSW, with minor trends seen in E-W, ESE-WNW, SE-NW, and SE-NNW directions. The trends highlight the variety of the earth's crust. To find linear features in the RTE anomaly map, the CET grid analysis was gradually performed. These procedures include using the Phase Symmetry to identify and highlight structural discontinuities; Textural Analysis to quantify magnetic variations; and Amplitude Threshold to filter out the low amplitude signals and enhance the prominent geological features. A vectorization lineament map (Fig. 4.6a) was produced. The lineament characteristics on this map correspond to geological borders, rock contact boundaries, structural trends, and structures like faults and fractures. A rose diagram is used to illustrate the orientation of these inferred lineaments (Fig. 4.6b). The rose diagram correlates with the orientation of the lineaments deduced in Figs. 4.3, 4.4a, b and 4.6a.

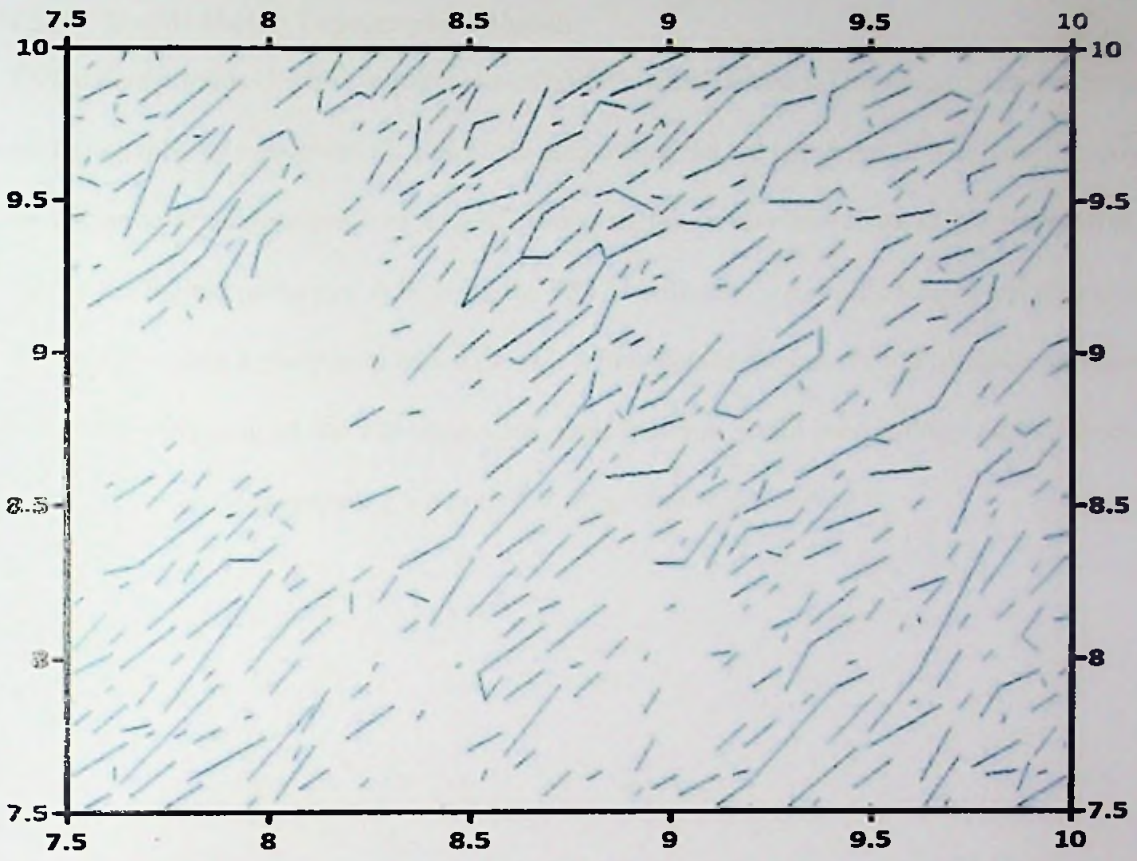


Fig. 4.6a: lineament Map of the Study Area

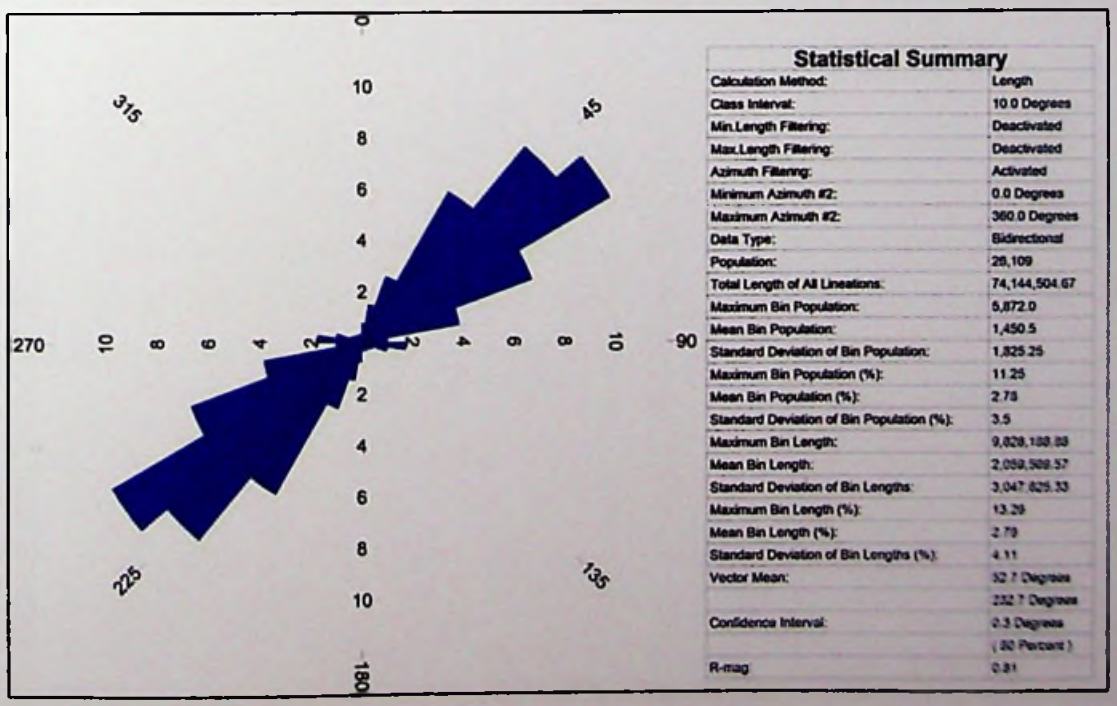


Figure 4.6b: Rose Diagram showing Lineament Trends

4.2.5 Shuttle Radar Topographic Mission

SRTM data provides high-resolution elevation data, which is crucial for mapping and visualizing the topography of a geothermal area. This map was extracted using ArcGIS software to display the elevation of the research area. Fig. 4.7 shows regions with elevated surface temperatures and clearly the faulted pathways. Analyzing the SRTM critically, we could identify and characterize fault zones within a study area which provide pathways for the circulation of fluids and heat. A better understanding of the elevation data, fault patterns, basin morphology and sedimentary deposits is crucial for assessing the potential for geothermal reservoirs.

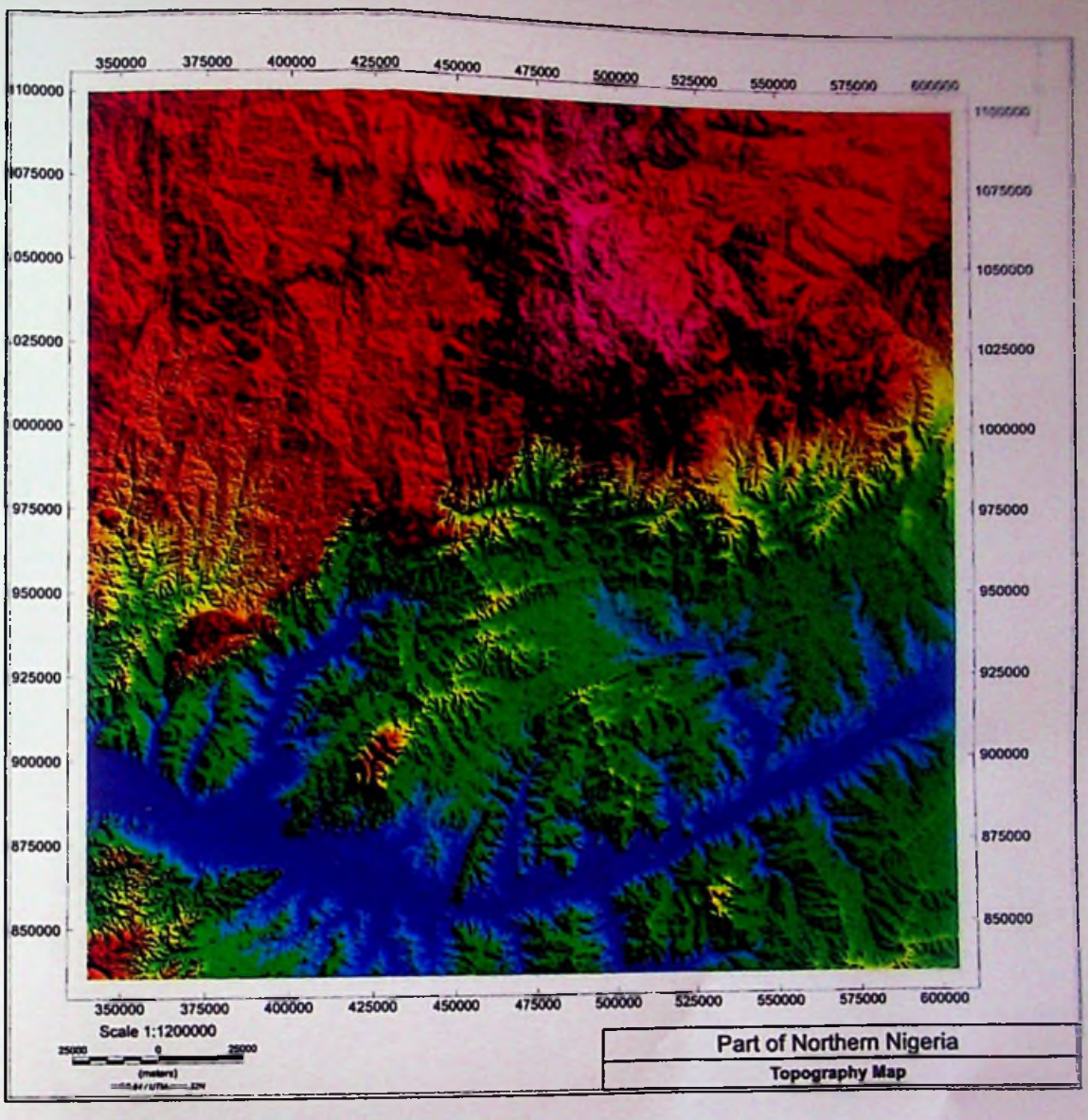


Fig. 4.7: SRTM Map of the Study Area

4.2.6 Analysis of the CPD, Geothermal Gradient and Heat Flow

To calculate the Curie Point Depth to the magnetic sources in the study location, the anomaly data that was acquired in the time domain was divided into 81 overlapping square blocks and converted to the frequency domain. The resultant frequency data was displayed as a power spectrum showing the amplitude of the magnetic signals at different frequencies (wavenumber). Using a written programming language which allows you display the depth to the top of the magnetic source and the centroid depth on the same graph using Matlab software, a graph of the logarithm of the spectral power (lnP) against the wave number (Fig. 4.8 & 4.9) was plotted. The depth to the top of the magnetic basement (Z_t) was obtained using equation 2.21 from the slope of the high wavenumber while the centroid depth was obtained using equation 2.24 from the slope of low wavenumber. The basal depth (Curie point depth) was determined using Eq. 2.25. From the spectral blocks of 55×55 km^2, the Curie point depth (CPD) estimated is from 7.47km to 29.4km. The maximum depth as seen in the contour map of the CPD (Fig. 4.10) is at the center of the study area and the minimum depths seen around the North-eastern, upper north, and South-western parts of the study area.

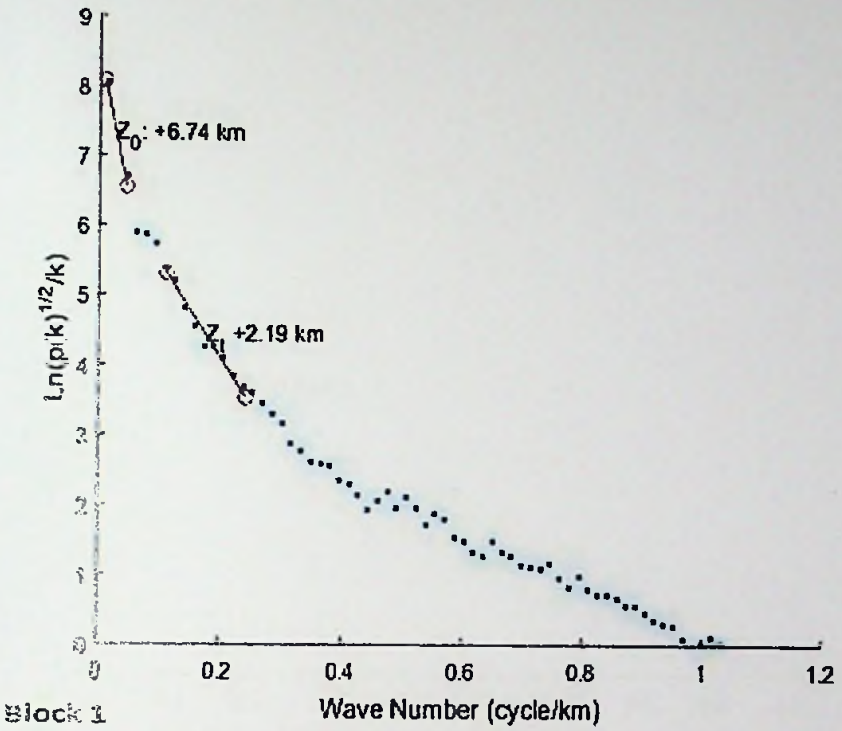
Table 4.1 shows the result of the depth to the top of the magnetic source Z_t, the centroid depth Z_0, the CPD (Z_b), the geothermal gradient, and the heat flow from 81 spectral square blocks of 55km by 55km window using the spectral analysis technique.

With a Curie temperature of 580°C, equation (2.25) was used to compute the geothermal gradients in the research region as shown in Fig. 4.11. The geothermal gradient varies from 19.768°C/km to 77.64°C/km with a mean value of 34.29°C/km. The research area's southwest and northern regions are where the high gradient zones are visible. According to Bain (2000), these high gradient zones are suggestive of fracture/shear zones.

Table 4.1: Results of Z_o, Z_t, Z_b, Gradient and Heat Flow calculated from 81 spectral blocks using 55km x 55km window

Block no	Longitude (°)	Latitude (°)	Z_0 (km)	Z_t (km)	Z_b (km)	Gradient (°C/km)	Heat flow (mW/m^2) 2.5 W/mK	Heatflow (mW/m^2) 2.7W/mK
1	7.75	9.75	6.74	2.19	11.29	51.37	128.95	138.71
2	8.00	9.75	12.6	3.38	21.82	26.58	66.72	71.77
3	8.25	9.75	7.70	2.55	12.85	45.14	113.29	121.87
4	8.50	9.75	7.68	2.11	13.25	43.77	109.87	118.19
5	8.75	9.75	8.95	1.73	16.17	35.87	90.03	96.85
6	9.00	9.75	12.7	3.03	22.37	25.93	65.08	70.00
7	9.25	9.75	9.40	2.52	16.28	35.63	89.42	96.19
8	9.50	9.75	6.04	1.78	10.30	56.31	141.34	152.04
9	9.75	9.75	9.69	1.86	17.52	33.11	83.09	89.38
10	7.75	9.50	13.4	2.09	24.71	23.47	58.92	63.38
11	8.00	9.50	10.2	2.32	18.08	32.08	80.52	86.62
12	8.25	9.50	7.64	2.40	12.88	45.03	113.03	121.58
13	8.50	9.50	8.76	2.33	15.19	38.18	95.84	103.09
14	8.75	9.50	11.4	2.33	20.47	28.33	71.12	76.50
15	9.00	9.50	11.1	2.46	19.74	29.38	73.75	79.33
16	9.25	9.50	5.12	1.78	8.46	68.56	172.08	185.11
17	9.50	9.50	5.98	1.72	10.24	56.64	142.17	152.93
18	9.75	9.50	10.3	2.27	18.33	31.64	79.42	85.43
19	7.75	9.25	11.2	2.92	19.48	29.77	74.73	80.39
20	8.00	9.25	11.3	2.73	19.87	29.19	73.27	78.81
21	8.25	9.25	11.7	4.85	18.55	31.27	78.48	84.42
22	8.50	9.25	13.4	4.39	22.41	25.88	64.96	69.88
23	8.75	9.25	12.2	3.86	20.54	28.24	70.88	76.24
24	9.00	9.25	8.49	3.96	13.02	44.55	111.81	120.28
25	9.25	9.25	10.1	1.84	18.36	31.59	79.29	85.29
26	9.50	9.25	8.32	2.08	14.56	39.84	99.99	107.55
27	9.75	9.25	10.2	3.89	16.51	35.13	88.18	94.85
28	7.75	9.00	13.3	2.84	23.76	24.41	61.27	65.91
29	8.00	9.00	13.3	2.59	24.01	24.16	60.63	65.22
30	8.25	9.00	15.3	3.08	27.52	21.08	52.90	56.90
31	8.50	9.00	11.8	5.16	18.44	31.45	78.95	84.92
32	8.75	9.00	16.8	4.78	28.82	20.12	50.51	54.34
33	9.00	9.00	4.71	1.95	7.47	77.64	194.89	209.64
34	9.25	9.00	9.06	3.01	15.02	38.62	96.92	104.26
35	9.50	9.00	12.2	3.14	21.26	27.28	68.48	73.66
36	9.75	9.00	8.11	2.10	14.12	41.08	103.10	110.91
37	7.75	8.75	8.70	2.79	14.61	39.70	99.64	107.19
38	8.00	8.75	8.23	2.05	14.41	40.25	101.03	108.67
39	8.25	8.75	10.9	1.94	19.86	29.20	73.30	78.85
40	8.50	8.75	13.1	1.65	24.55	23.63	59.30	63.79
41	8.75	8.75	14.5	2.75	26.25	22.10	55.46	59.66

42	9.00	8.75	11.3	2.62	19.98	29.03	72.86	78.38
43	9.25	8.75	12.4	2.29	22.51	25.77	64.67	69.57
44	9.50	8.75	13.4	3.01	23.79	24.38	61.19	65.83
45	9.75	8.75	12.9	2.94	22.86	25.37	63.68	68.50
46	7.75	8.50	11.3	4.65	17.95	32.31	81.10	87.24
47	8.00	8.50	6.12	2.33	9.91	58.53	146.90	158.02
48	8.25	8.50	10.2	1.60	18.8	30.85	77.44	83.30
49	8.50	8.50	12.3	3.95	20.65	28.09	70.50	75.84
50	8.75	8.50	16.2	3.06	29.34	19.77	49.62	53.37
51	9.00	8.50	15.2	5.75	24.65	23.53	59.06	63.53
52	9.25	8.50	15.0	4.85	25.15	23.06	57.88	62.27
53	9.50	8.50	14.1	6.03	22.17	26.16	65.67	70.64
54	9.75	8.50	12.5	5.18	19.82	29.26	73.45	79.01
55	7.75	8.25	9.01	4.75	13.27	43.71	109.71	118.01
56	8.00	8.25	8.24	3.37	13.11	44.24	111.05	119.45
57	8.25	8.25	8.59	3.48	13.7	42.34	106.26	114.31
58	8.50	8.25	16.1	3.85	28.35	20.46	51.35	55.24
59	8.75	8.25	15.6	5.28	25.92	22.38	56.17	60.42
60	9.00	8.25	10.1	4.67	15.53	37.35	93.74	100.84
61	9.25	8.25	12.5	1.45	23.55	24.63	61.82	66.50
62	9.50	8.25	16.2	5.25	27.15	21.36	53.62	57.68
63	9.75	8.25	9.06	2.82	15.3	37.91	95.15	102.35
64	7.75	8.00	8.36	4.58	12.14	47.78	119.92	129.00
65	8.00	8.00	11.3	4.44	18.16	31.94	80.17	86.23
66	8.25	8.00	10.7	2.86	18.54	31.28	78.52	84.47
67	8.50	8.00	6.05	4.21	7.89	73.51	184.51	198.48
68	8.75	8.00	14.1	2.16	26.04	22.27	55.91	60.14
69	9.00	8.00	14.1	2.83	25.37	22.86	57.38	61.73
70	9.25	8.00	10.6	2.39	18.81	30.83	77.40	83.25
71	9.50	8.00	12.70	2.60	22.8	25.44	63.85	68.68
72	9.75	8.00	10.9	3.15	18.65	31.10	78.06	83.97
73	7.75	7.75	7.79	4.69	10.89	53.26	133.68	143.80
74	8.00	7.75	9.93	3.65	16.21	35.78	89.81	96.61
75	8.25	7.75	11.8	4.83	18.77	30.90	77.56	83.43
76	8.50	7.75	11.1	4.85	17.35	33.43	83.91	90.26
77	8.75	7.75	7.97	3.40	12.54	46.25	116.09	124.88
78	9.00	7.75	13.4	3.54	23.26	24.94	62.59	67.33
79	9.25	7.75	11.2	2.34	20.06	28.91	72.57	78.07
80	9.50	7.75	10.6	5.76	15.44	37.56	94.29	101.42
81	9.75	7.75	9.88	3.50	16.26	35.67	89.53	96.31



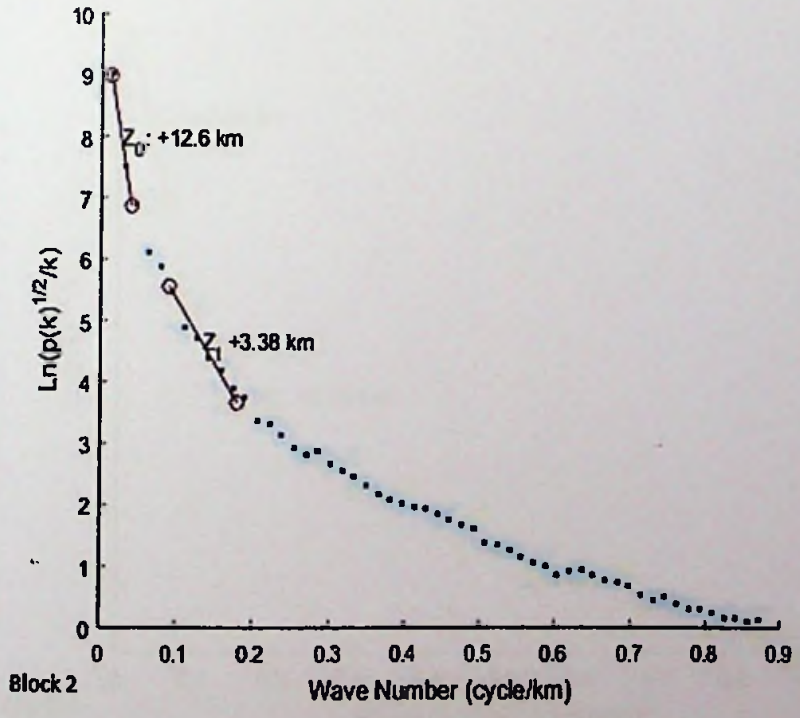
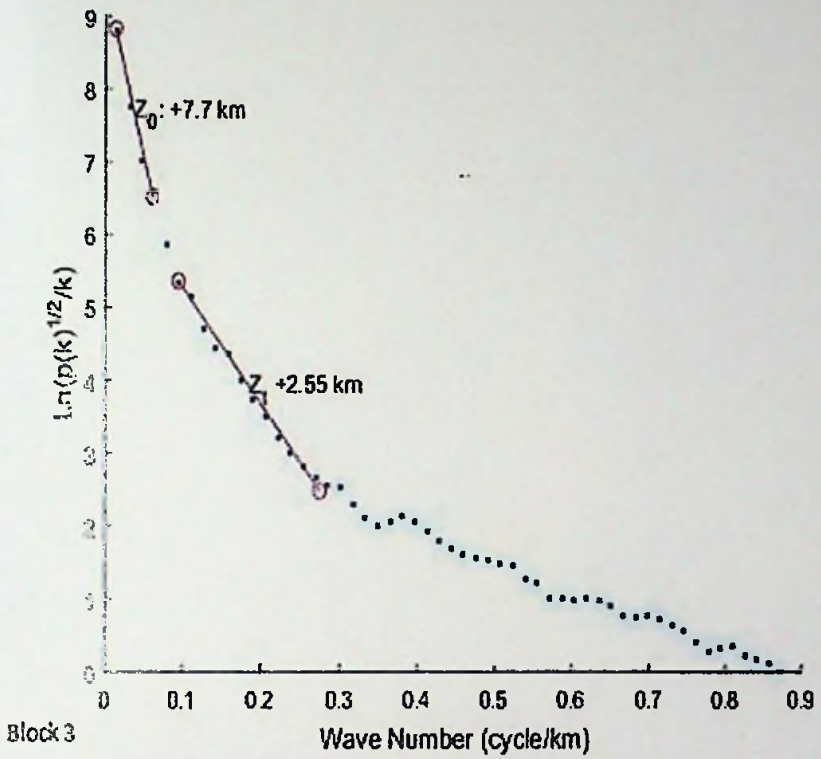


Fig. 4.8: Graph of Blocks b1 and b2 showing the determined values of Z_o and Z_t



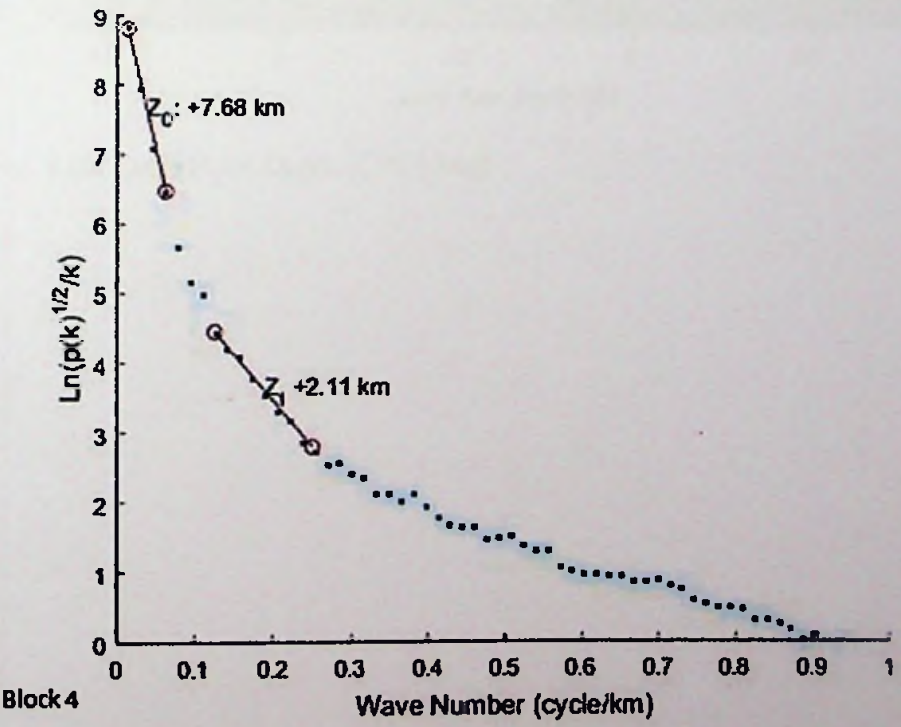


Fig. 4.9: Graph of Blocks b3 and b4, showing the determined values of Z_o and Z_t

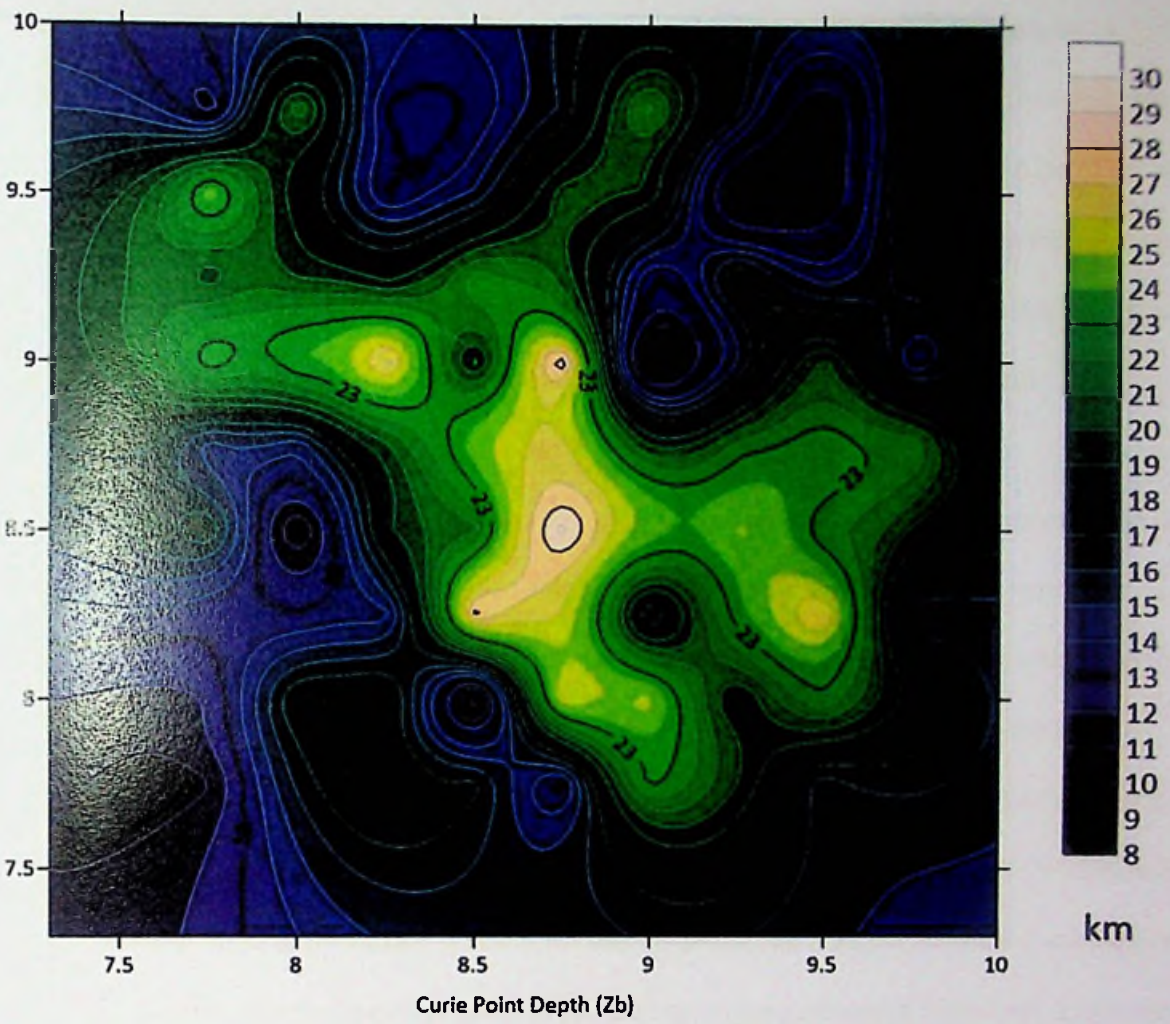


Fig. 4.10: Curie Point Depth (CPD) Map

The amount of heat flowing in the region was estimated for each of the spectral blocks of 55 × 55km^2 using equations (2.24) and a thermal conductivity of 2.51W/m°K adopted from the study of Nwankwo *et al.*, (2011). The heat flow map (Fig. 4.12) ranges from 49.62mW/m^2 to 194.88mW/m^2 with a mean value of 86.07mW/m^2. The higher heat flow was seen in the Northern areas around Maijuju, Panyam, Pankshin, Kafanchan, and Kachia in the Southwestern part of the area corresponding to Udegi, Soko, Ogam, Obangedde, Doma down to Makurdi.

Fig 4.13 is the 3D surface magnetic anomaly map which provides a visual representation of magnetic variations observed in the subsurface in three-dimensional space. These variations can be caused by underlying geological structures, faults, or other subsurface features with different magnetic properties. The map shows major depressions, intrusions, and uplifts in the area.

Fig. 4.14 is the 3D watershed map of the study area clearly showing the directions of flow within the region. Watershed maps can help identify the pathways of groundwater flow. Watersheds often converge in specific areas. These confluence areas can indicate potential subsurface geological features like faults or fractures, which are crucial for geothermal reservoirs. Hot water can flow along these pathways, making them potential sites for geothermal exploration.

From the spectral analysis, when you compare the results of the heat flow with that of the CPDs (Fig. 4.15), it showed an almost inversely proportional relationship. This means that regions with high heat flow correspond to regions of shallower CPD and vice versa which agrees with most published works.

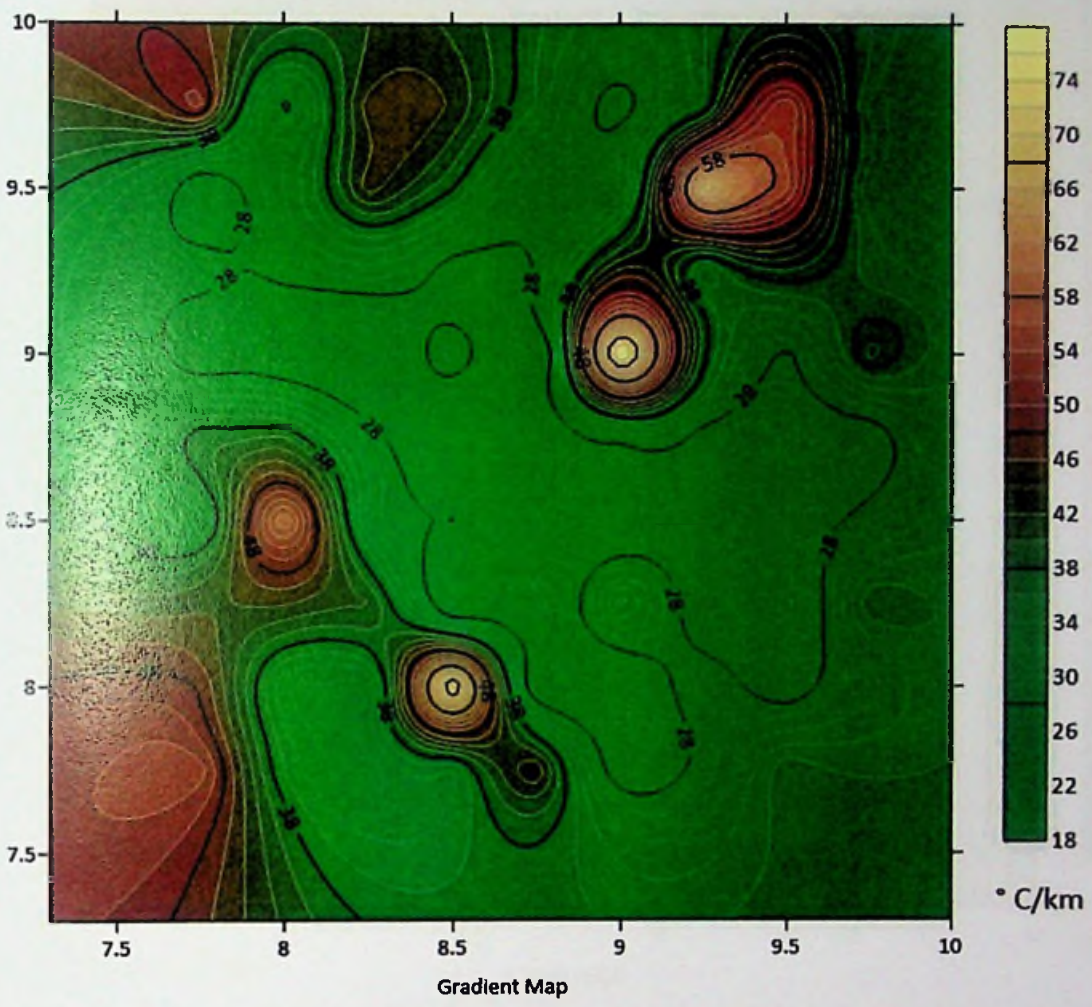


Fig. 4.11: Geothermal Gradient Map of the Study Area

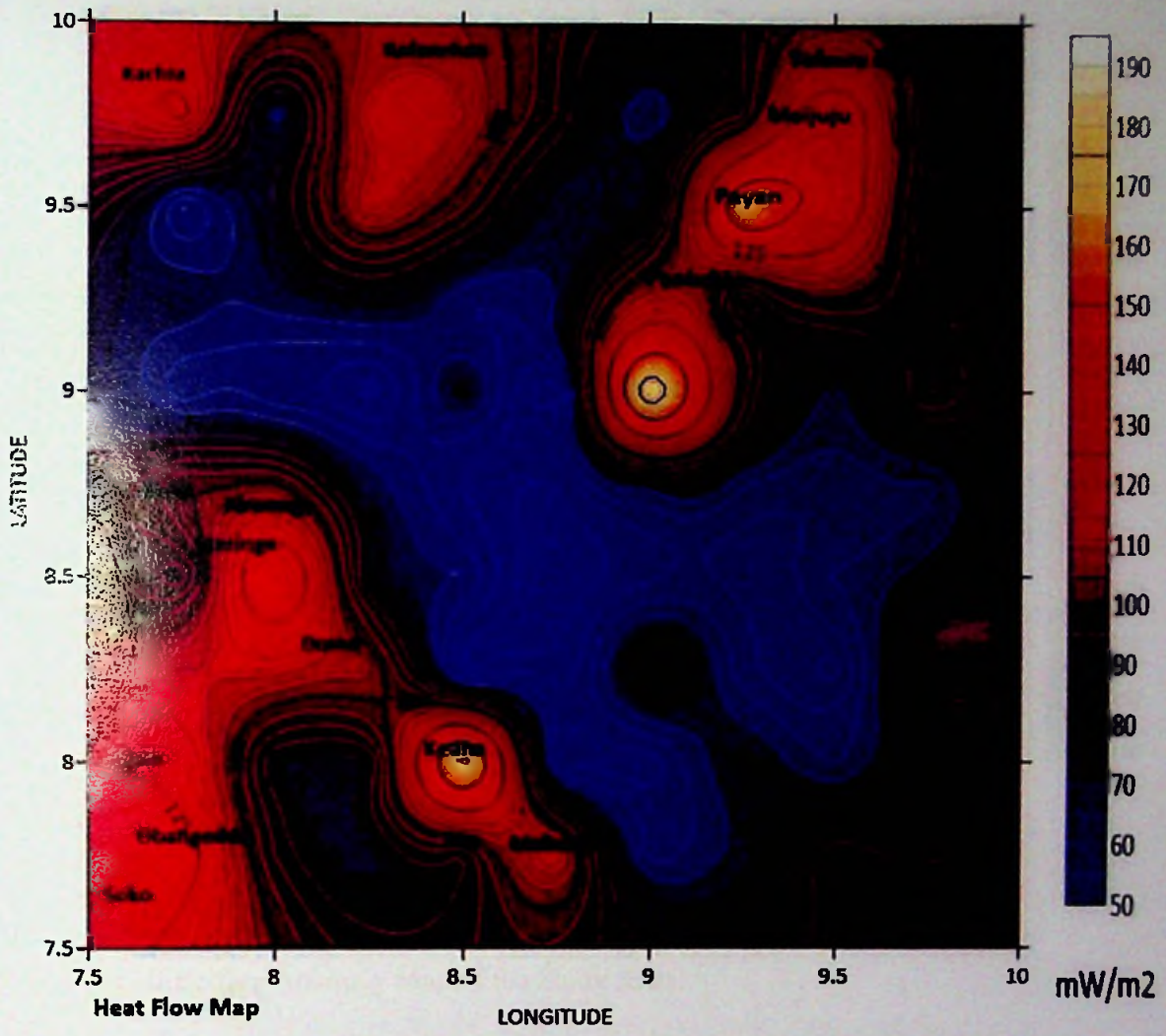


Fig. 4.12: Heat Flow Map of the Study Area

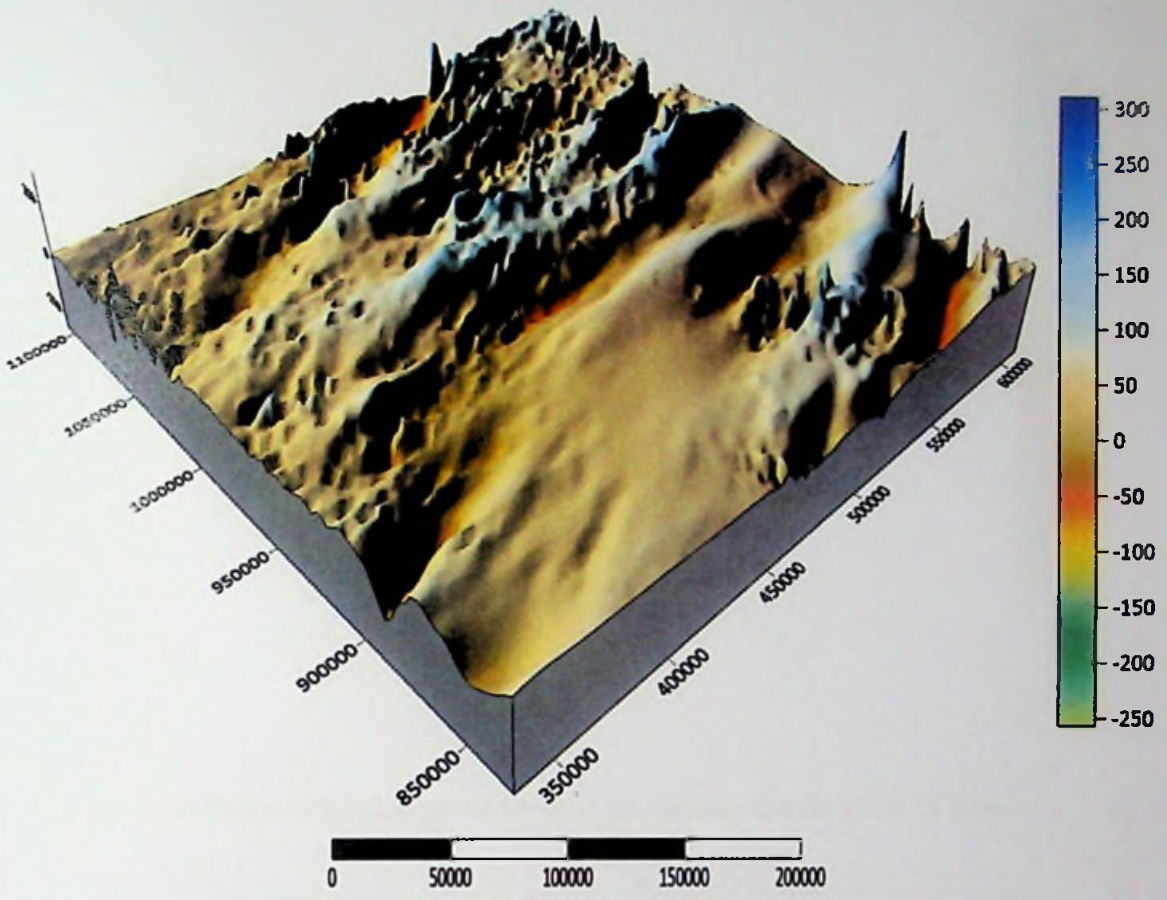


Fig. 4.13: 3D Surface Anomaly Map of the Study Area

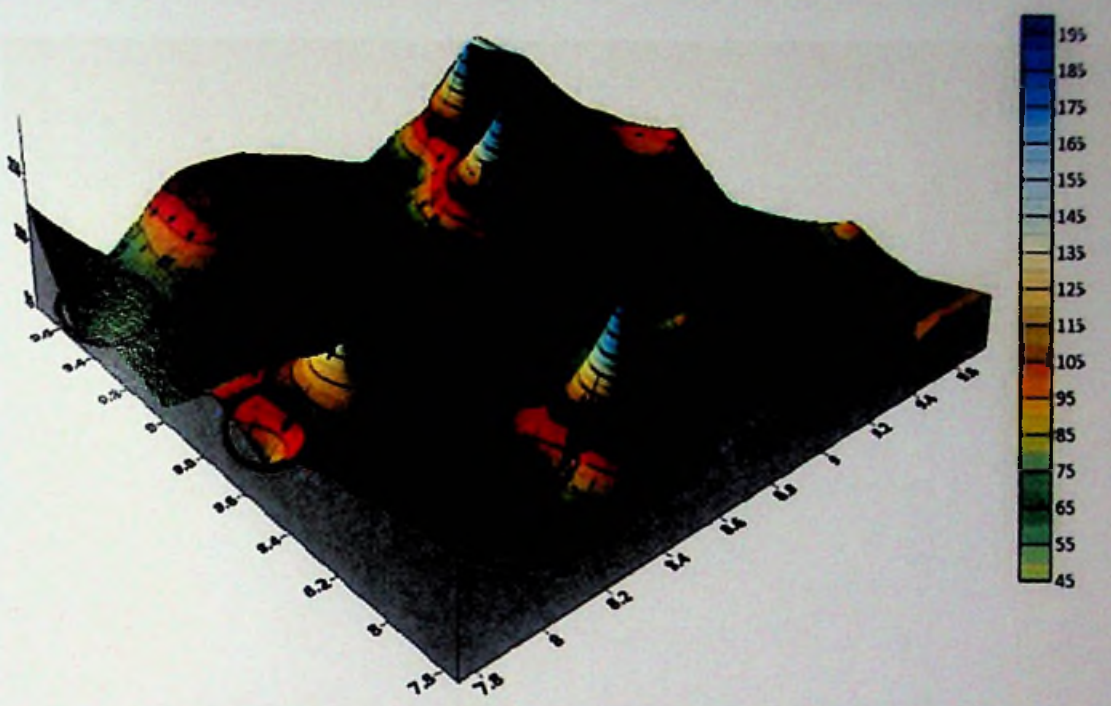


Fig. 4.14: Water Shed Map of the Study Area showing the direction of flow

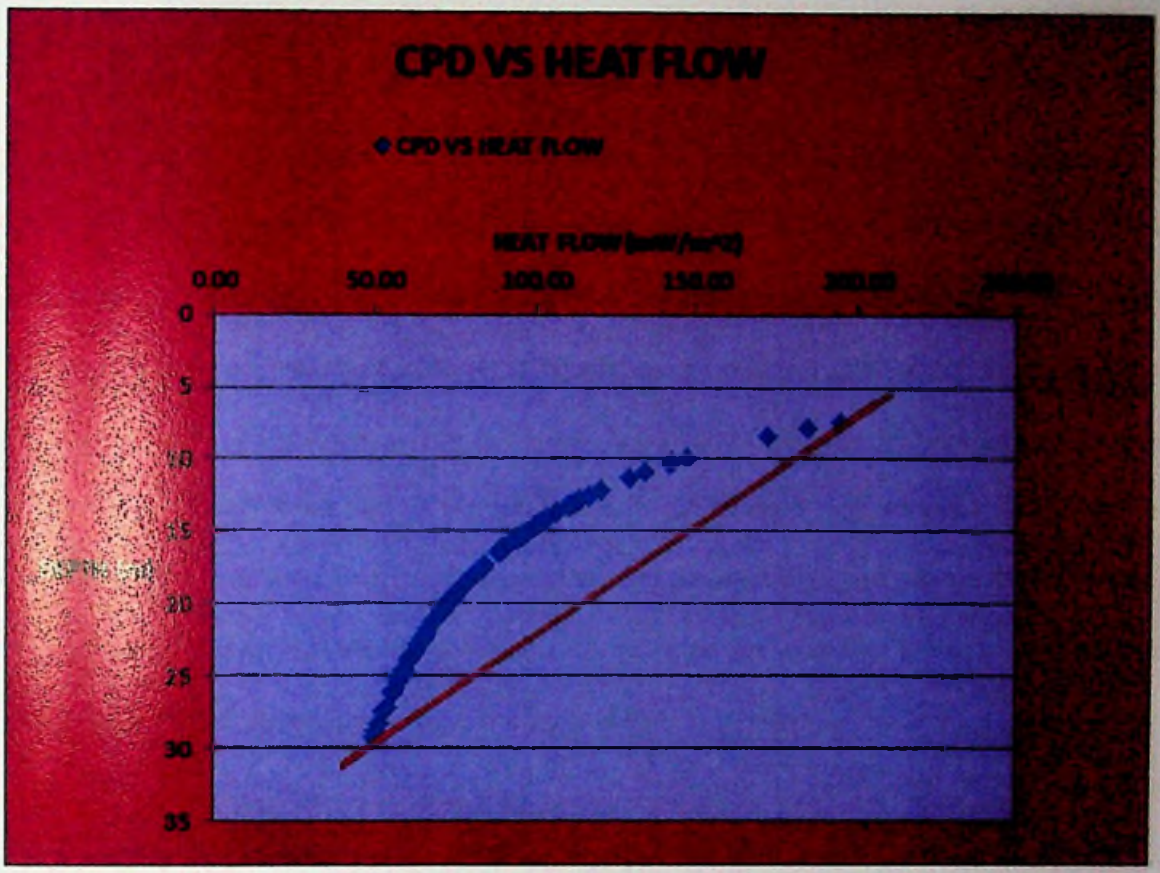


Fig. 4.15: Plot of CPD and Heat Flow of the Study Area

4.2.7 Analysis of Radiometric Data

The Potassium (K), Thorium (eTh), and Uranium (eU) concentration maps (Fig.4.16, 4.17, and 4.18) respectively show how the radioactive elements in the study area are distributed. These maps (K, eTh, eU) are used to correlate the geological features and rock units within the area. They are characterized by different colouration showing the high, intermediate, and low concentration zones. Fig. 4.16 shows a very high concentration of potassium in the northeast of the area hosting the granitic rocks, some northern areas, and in the Southeastern part where granites intruded the sediments. The intermediate concentration was seen within the basement around the northern areas and in the south within the sedimentary formation while the low concentrations were seen both in some areas around the basement and sedimentary formation. The potassium map is very helpful when it comes to the mapping of litho-contacts. The potassium concentration values range from 0 to 4.8%.

Fig 4.17 (eTh map), shows a very high concentration within the basement rocks and a very low concentration at the geological boundary of the basement complex and the sedimentary formation corresponding to the Lafia Formation. We have low concentrations also in the Agwu shale formation, the Asu River Group, and along the River Benue. The value ranges from 5.3 to 41.5 ppm.

Fig. 4.18 (eU map) shows high concentration in the northern area and the southern area corresponding to the Bassange formation and the Nkporo Group. We have a very low concentration in the Lafia Formation, Agwu Shale, along the River Benue housing the Alluvium deposits and some areas in the basement complex. The Uranium concentration value ranges from 1.2 to 8.5ppm.

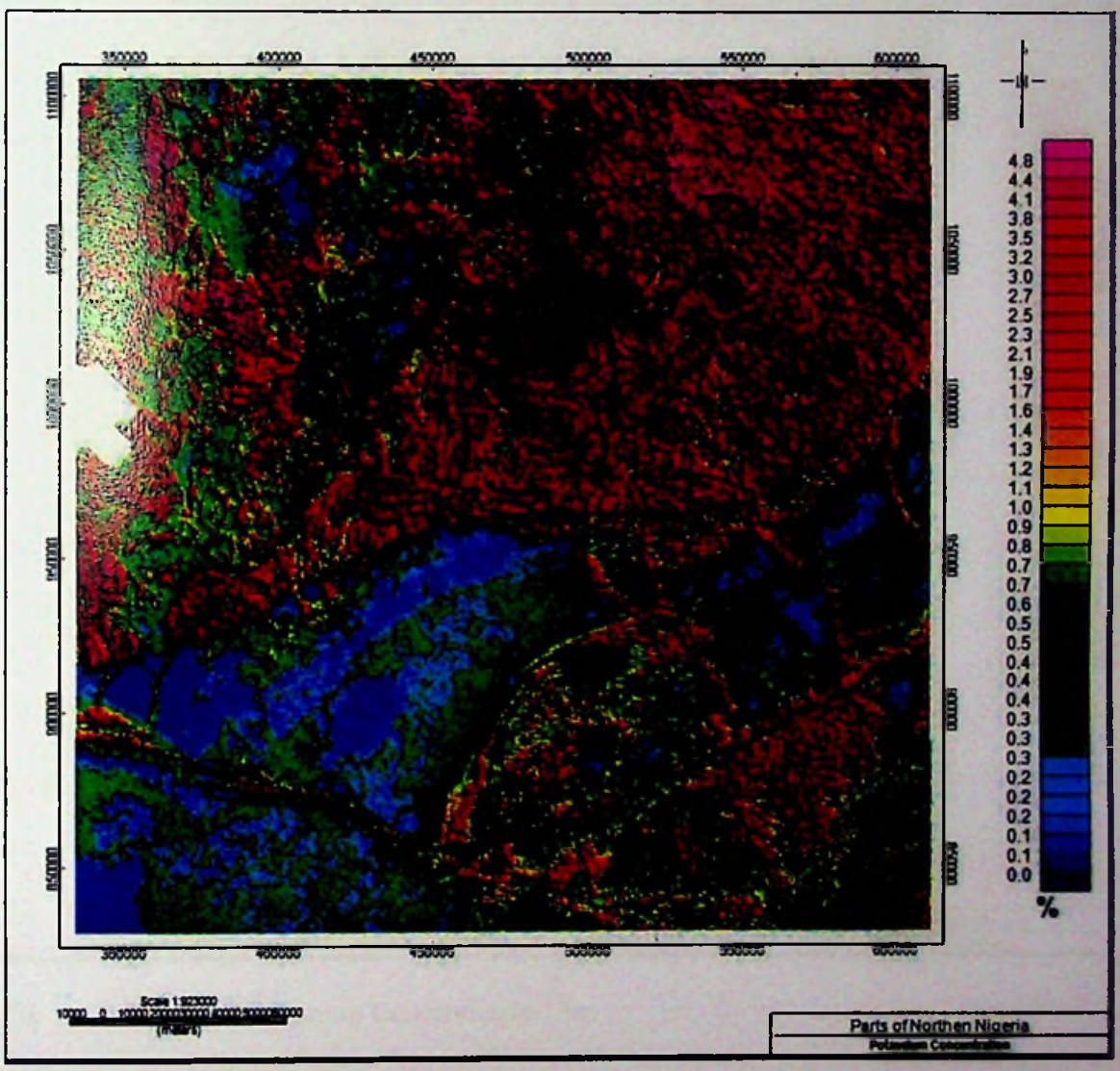


Fig. 4.16: Equivalent Potassium Concentration Map

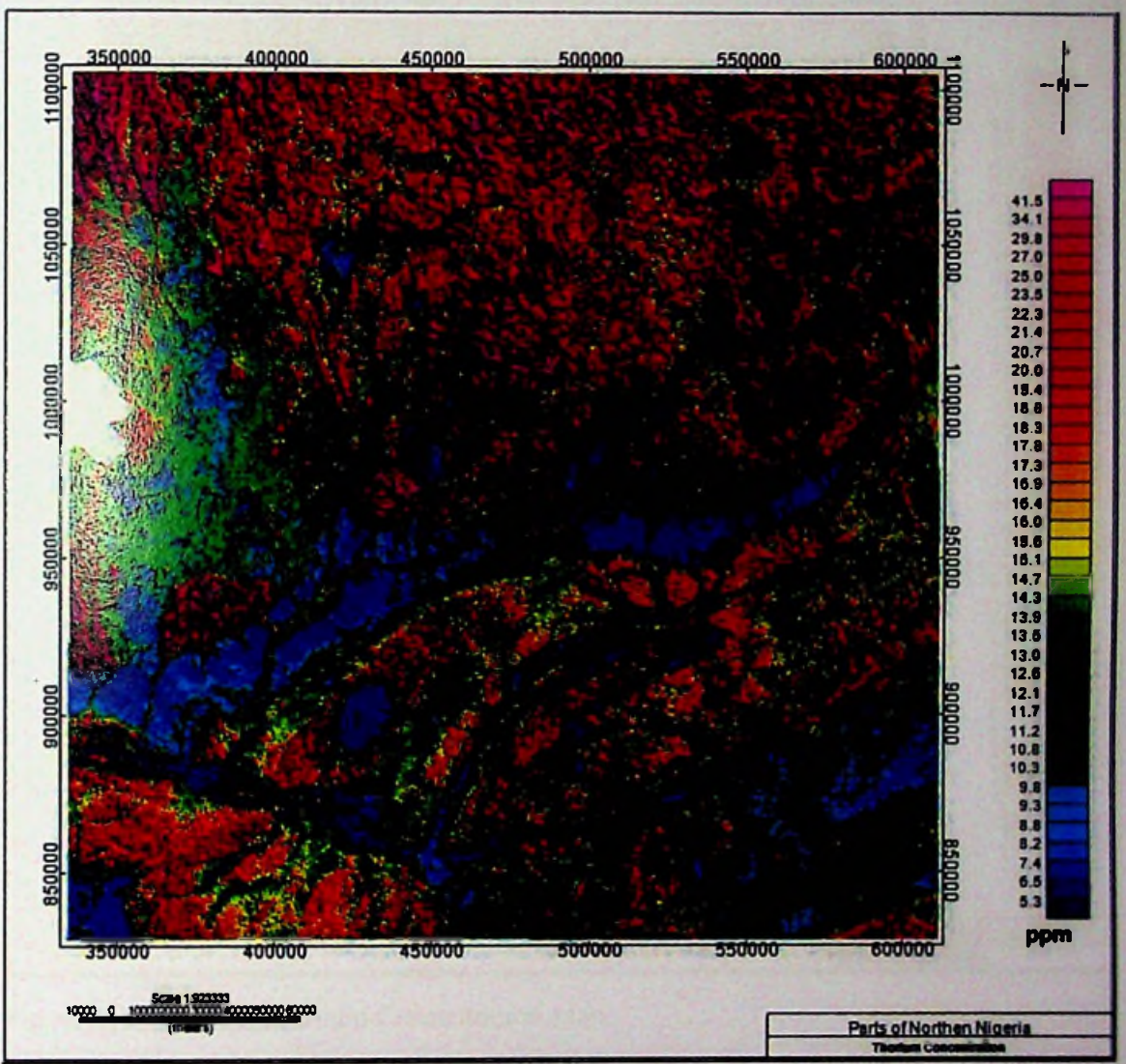


Fig. 4.17: Equivalent Thorium Concentration Map

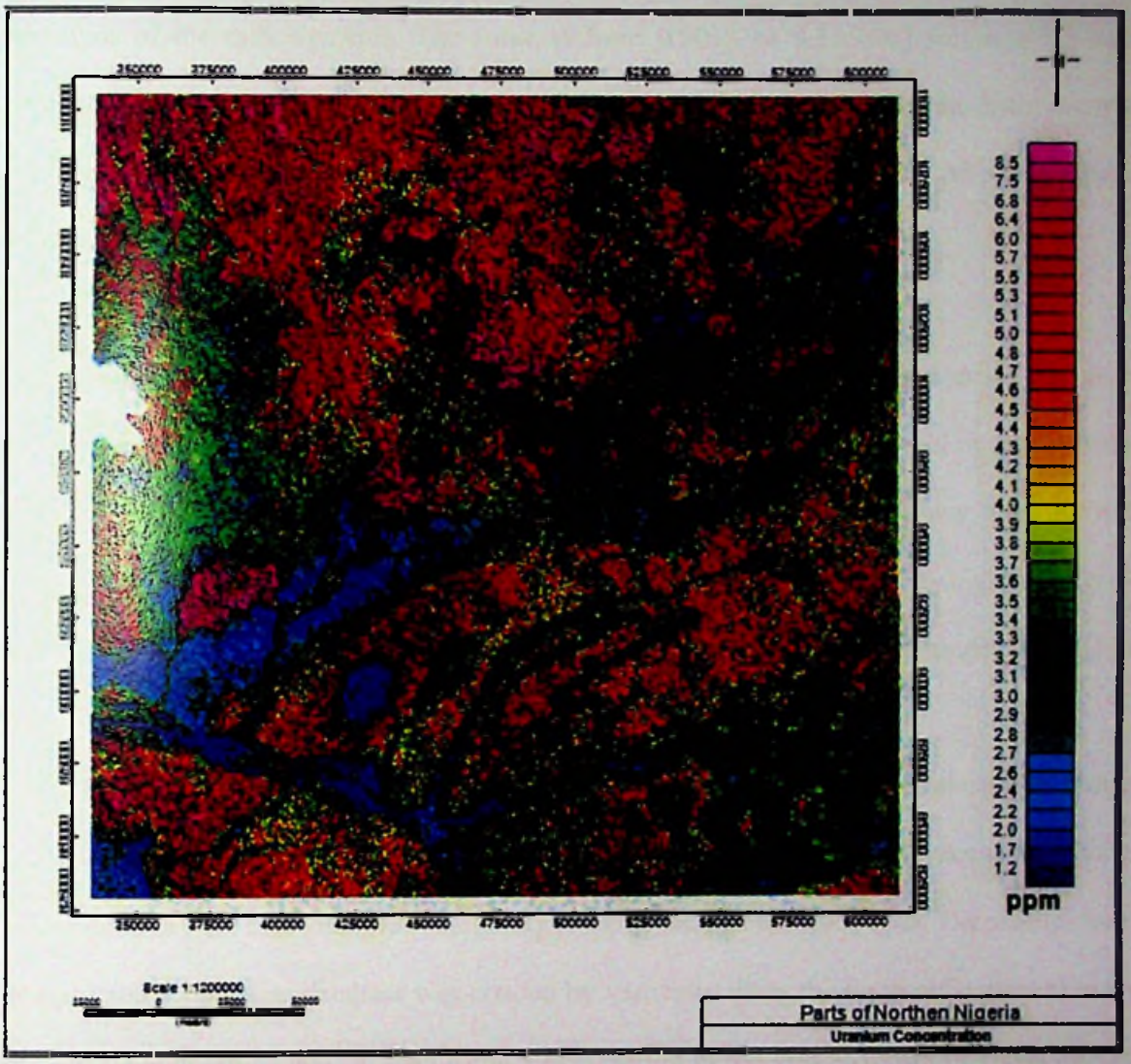


Fig. 4.18: Equivalent Uranium Concentration Map

The ratio map of Potassium-Thorium element (Fig. 4.19) was produced to help in identifying variations of the radioelements. The value is from 0.0018 to 0.3766%/ppm showing high concentration around the granitic rocks and Asu River Group. This shows the hydrothermal alteration zones which are of interest in geothermal exploration because they serve as channels for fluids.

The Ternary Map (Fig. 4.20) produced shows the composite concentration of the three radiogenic elements (K, Th, and U) with a red-green-blue colour representation respectively. The red-magenta zones show high potassium contents, the yellow-green show high thorium content, and the blue show the uranium contents in the area. The area with very high contents of the three radioelements shows white colouration while areas with dark shades show low concentration of the three radioelements.

Table 4.2 shows the statistical calculation of the minimum value, maximum value, mean value, and standard deviation of the 70 profiles taken across each rock unit. The types of rock units across the area were first identified using the geological map of the study area. The profiles were mapped and a statistical database was created by vertically tiling the three radioelement maps (K, Th, U) with the geological map using a grid profile in the grid & image of Oasis Montaj software.

Table 4.3 shows the different lithology and the individual heat dissipated across each rock profile with the total radiogenic heat production (RHP) across the entire profiles. The RHP across the study area was calculated using equation 2.29.

Many authors (Abraham *et al.*, 2014; Kuforijimi &Christopher, 2017; Megwara *et al.*, 2013; Taufiq *et al.*, 2021) have accepted the radiogenic heat production computed from equation 2.27, which was first determined by Rybach (1976). To determine the radioelement's heat contribution to the radiogenic heat produced in the area, the concentration values of each radioelement was

multiplied by a numerical constant (0.035 for K, 0.026 for Th, and 0.097 for U). The total radiogenic heat generation within the research area is then calculated by multiplying these values by the average rock density (2.67 kg/m^3) in the area. The Oasis Montaj program was used to create a map of the research area's radiogenic heat generation (Fig. 4.21).

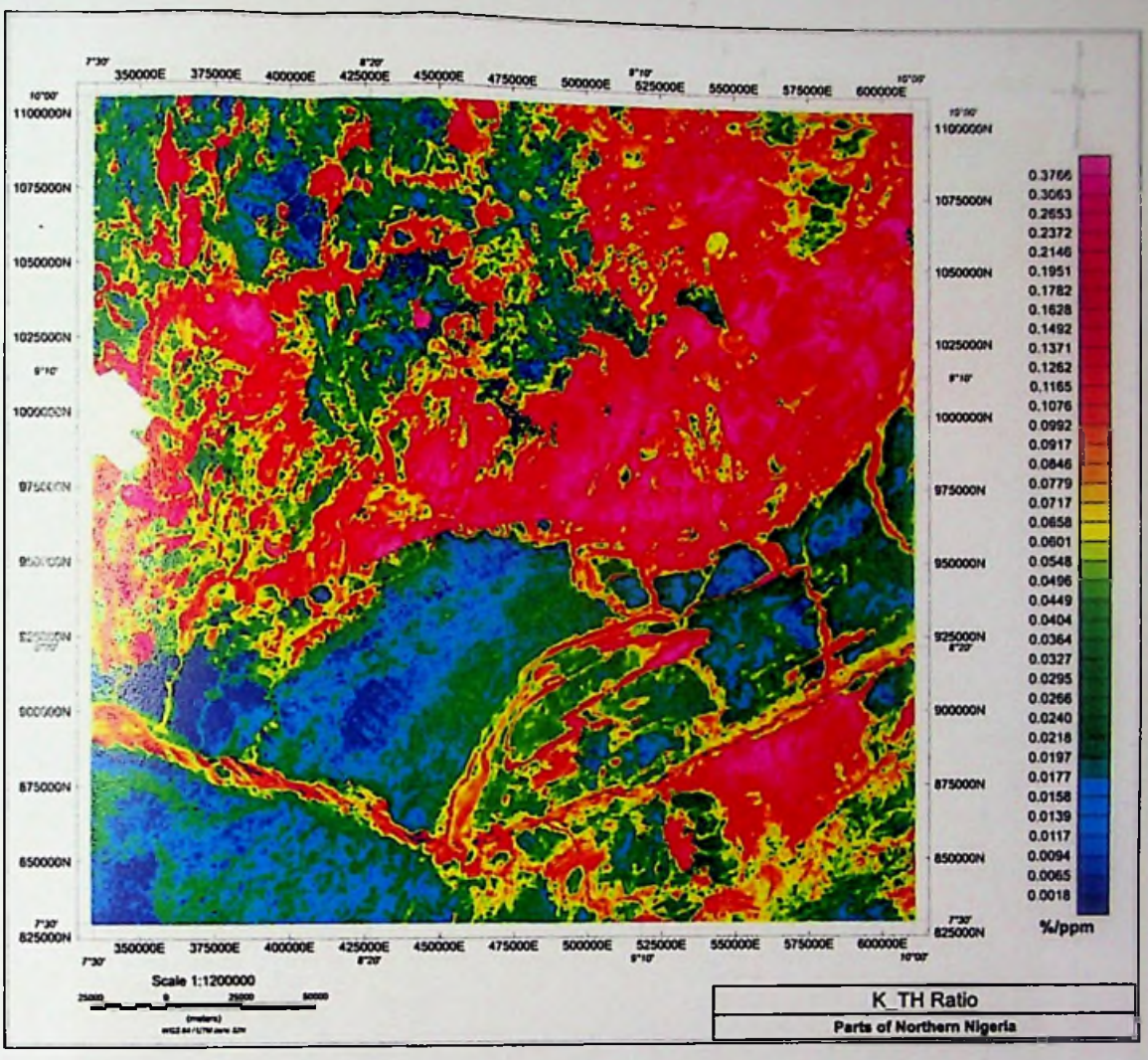


Fig. 4.19: Potassium – Thorium ratio map



Fig. 4.20: The Ternary Image Map of the Study Area

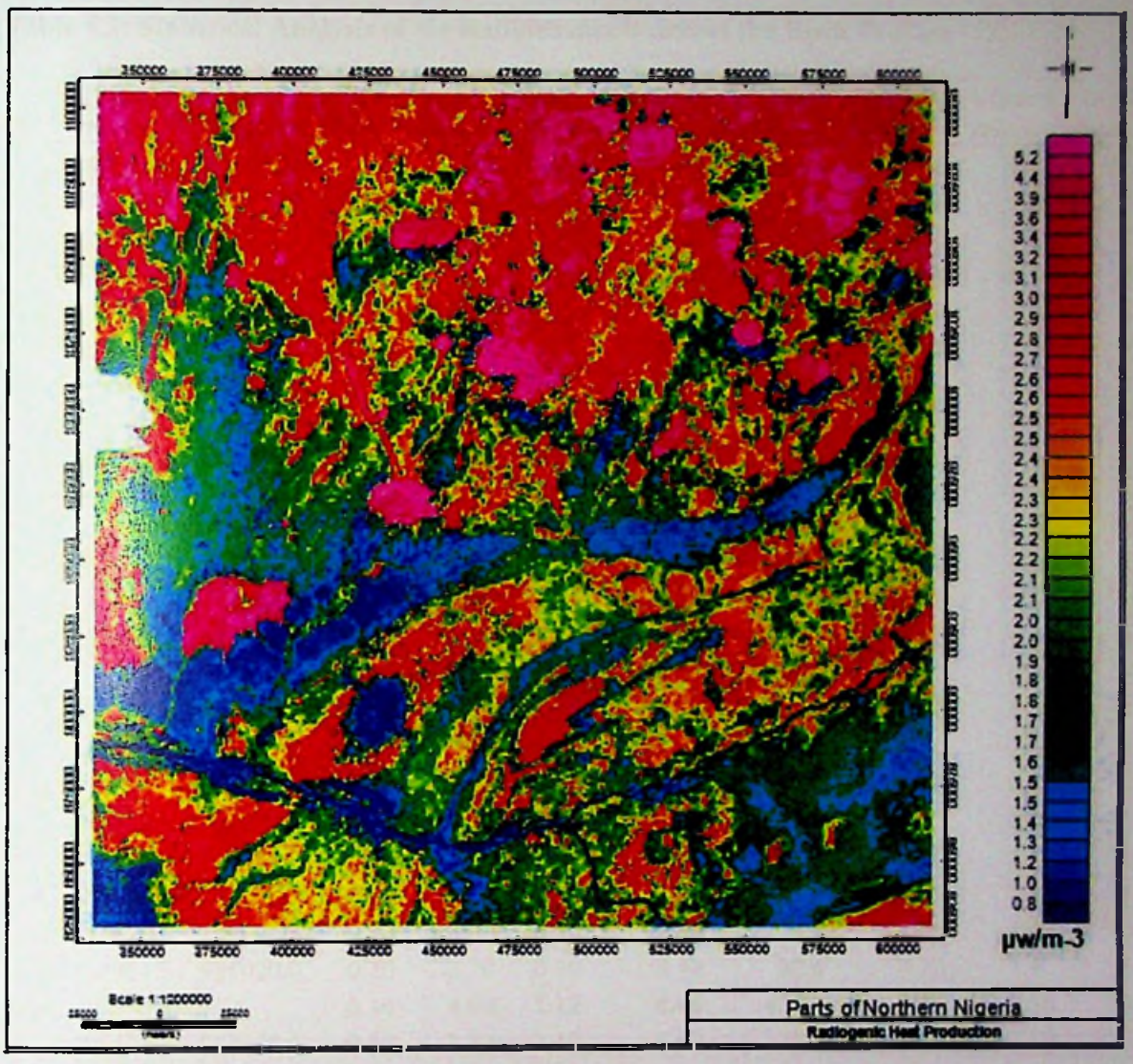


Fig. 4.21: Radiogenic Heat Production Map

Table 4.2: Statistical Analysis of the Radioelements across the Rock Profiles

Profile	Easting	Northing	K(%) min	K(%) max	K(%) SD	Th(ppm) min	Th(ppm) max	Th(ppm) SD	U(ppm) min	U(ppm) max	U(ppm) SD
B1	440332.4	1064403	-0.40	7.60	1.80	4.40	43.6	8.40	0.50	10.8	2.00
B2	438481.0	1034508	-0.20	3.60	0.60	4.40	32.4	4.00	2.60	8.40	0.80
B3	501927.2	907027.5	0.00	2.10	0.50	4.80	32.8	6.80	2.60	7.10	1.10
B4	527274.0	1014990	-0.10	7.20	1.50	8.30	40.3	6.40	-0.60	7.30	1.40
B5	541920.6	982954.9	0.50	4.90	1.10	4.50	25.3	4.50	2.00	5.80	0.80
Average			**-0.04**	**5.08**	**1.10**	**5.28**	**34.88**	**6.02**	**1.42**	**7.88**	**1.22**
Sc1	379608.6	1099219	-0.10	4.60	1.30	4.50	36.7	5.50	3.40	12.2	1.40
Sc2	380516.7	1045824	0.20	7.90	1.70	8.40	45.2	8.20	-0.60	9.50	1.80
Sc3	339048.5	993364.9	0.60	3.50	0.60	6.30	26.6	4.50	0.50	6.30	1.10
Sc4	367706.9	939920.2	0.10	3.50	0.60	5.30	22.8	3.70	-0.70	4.90	0.90
Sc5	405856.1	949088.7	0.50	2.50	0.40	6.70	39.4	6.90	-0.30	9.30	1.80
Average			**0.26**	**4.40**	**0.92**	**6.24**	**34.14**	**5.76**	**0.46**	**8.44**	**1.40**
GG1	440535.8	1004005	0.10	4.60	1.00	4.00	41.5	5.70	1.60	7.40	1.10
GG2	448547.1	994859.9	0.00	4.30	1.00	5.20	43.3	6.70	1.00	8.80	1.20
GG3	458628.0	971062.0	0.10	5.40	1.10	3.10	35.1	5.00	0.00	7.70	1.20
GG4	509855.7	1036612	-0.10	4.40	1.40	10.2	32.1	4.60	1.40	7.30	1.00
GG5	524842.7	1007678	0.00	5.20	1.20	3.80	34.5	5.80	-1.60	7.20	1.30
Average			**0.02**	**4.78**	**1.14**	**5.26**	**37.3**	**5.56**	**0.48**	**7.68**	**1.16**
M1	583388.5	1024426	0.30	6.50	1.20	3.00	38.6	9.10	0.50	7.60	1.40
M2	515692.9	966189.3	0.30	4.40	1.30	3.90	39.9	6.70	1.40	7.00	1.10
M3	408602.6	1071132	-0.30	5.00	1.40	11.2	31.9	3.50	2.90	9.10	1.20
M4	343620.4	1063526	0.00	3.60	0.80	9.80	72.4	12.3	1.70	10.1	1.90
M5	357961.6	986020.0	0.20	3.70	0.90	4.40	28.4	4.70	1.40	7.10	1.10
Average			**0.10**	**4.64**	**1.12**	**6.46**	**42.24**	**7.26**	**1.58**	**8.18**	**1.34**
OG1	395167.7	987568.4	0.20	5.40	1.10	5.80	29.4	4.00	-1.50	7.80	1.30
OG2	362236.7	1072965	-0.20	5.40	1.50	6.70	87.7	10.8	2.10	16.8	2.40
OG3	582800.8	1082104	1.10	4.90	0.80	8.50	78.8	13.3	1.70	10.0	1.60
OG4	587036.3	1006421	1.90	6.10	0.90	9.50	38.2	4.90	1.40	6.60	1.00
OG5	530611.0	852708.9	0.00	5.20	1.20	3.80	34.5	5.80	-1.60	7.20	1.30
Average			**0.60**	**5.40**	**1.10**	**6.86**	**53.72**	**7.76**	**0.42**	**9.68**	**1.52**
YG1	456772.9	1049332	-1.60	9.20	1.80	9.20	108.3	12.9	-4.10	13.8	3.00
YG2	457062.7	1049473	-1.70	7.70	1.70	4.60	98.2	13.3	-1.20	15.3	2.70
YG3	478158.0	1022942	-0.50	4.70	1.20	3.20	59.4	13.3	-1.70	13.7	2.80
YG4	378997.1	924688.7	-0.30	3.90	1.10	2.90	111.9	15.2	0.10	27.7	4.10
YG5	445803.2	956421.7	0.10	3.90	1.20	4.80	18.0	3.00	-1.70	7.00	1.40
Average			**-0.80**	**5.88**	**1.40**	**4.94**	**79.16**	**11.54**	**-1.72**	**15.5**	**2.80**
AL1	405878.8	919523.2	-0.10	1.40	0.30	3.40	17.6	2.50	0.40	5.00	0.70
AL2	397308.9	876487.7	-0.10	2.50	0.40	-3.60	21.3	5.20	-0.80	5.80	1.40
AL3	568764.9	933841.7	-0.10	3.30	0.70	2.90	25.4	4.10	2.20	7.20	0.90
AL4	529401.4	911279.1	0.20	3.50	0.80	5.20	24.1	4.40	2.50	6.30	0.80
AL5	566308.6	890507.4	0.20	4.00	1.00	3.90	19.4	2.80	1.50	6.30	0.90
Average			**0.02**	**2.94**	**0.64**	**2.36**	**21.56**	**3.80**	**1.16**	**6.12**	**0.94**

LF1	346669.3	902115.0	-0.10	1.80	5.00	4.90	29.6	5.40	-0.60	6.40	1.30
LF2	379289.2	903608.4	-0.10	0.70	0.20	5.30	21.3	2.30	0.80	4.80	0.60
LF3	454660.1	943294.3	0.00	0.50	0.10	3.60	18.1	3.30	0.50	6.10	1.20
LF4	414994.8	917348.7	0.00	0.60	0.10	6.00	21.7	3.50	0.90	8.30	1.60
LF5	452504.0	921925.8	0.00	0.70	0.10	9.30	29.5	3.90	1.60	11.0	1.60
Average			**-0.04**	**0.86**	**1.10**	**5.82**	**24.04**	**3.68**	**0.64**	**7.42**	**1.26**
ASH1	472653.8	920401.6	0.00	0.70	0.10	9.00	20.4	2.60	2.50	6.70	0.60
ASH2	432986.8	890509.5	-0.10	0.70	0.10	5.00	23.4	3.60	1.00	7.00	1.20
ASH3	464130.0	935669.3	0.10	0.50	0.10	7.80	23.2	2.50	2.80	7.60	1.00
ASH4	587043.3	952714.0	0.10	2.10	0.30	7.80	19.0	2.30	2.50	5.30	0.50
ASH5	5141448	898445.2	0.10	2.50	0.60	2.40	30.0	5.30	1.20	6.40	1.20
Average			**0.04**	**1.30**	**0.24**	**6.40**	**23.2**	**3.26**	**2.00**	**6.60**	**0.90**
EG1	591960.0	929918.1	0.00	3.00	0.60	6.90	30.8	5.00	2.70	7.60	0.80
EG2	490633.6	906673.7	0.10	1.80	0.40	7.50	28.7	4.90	2.10	7.50	1.20
EG3	483319.8	875551.9	0.10	2.60	0.60	4.30	26.8	4.90	1.40	6.50	1.00
EG4	483313.0	865787.8	-0.40	2.00	0.50	-3.10	24.1	6.60	-0.10	5.90	1.50
EG5	547061.6	925002.8	0.00	2.10	0.40	5.50	25.5	4.50	2.60	7.60	0.90
Average			**-0.04**	**2.30**	**0.50**	**4.22**	**27.18**	**5.18**	**1.74**	**7.02**	**1.10**
NSH1	351226.4	883204.8	-0.10	0.60	0.20	4.70	28.9	5.00	0.20	7.50	1.70
NSH2	377784.7	887466.4	-0.10	1.40	0.30	1.90	13.2	5.60	-0.20	7.40	1.60
NSH3	416227.7	902718.5	-0.10	0.50	0.20	4.80	15.5	4.20	0.60	9.20	1.80
NSH4	409178.0	887142.9	0.00	1.10	0.30	3.30	16.4	6.10	0.60	9.90	2.40
NSH5	430235.2	907299.1	-0.10	0.60	0.10	3.70	10.1	4.70	0.50	7.80	1.70
Average			**-0.08**	**0.84**	**0.22**	**3.68**	**16.82**	**5.12**	**0.34**	**8.36**	**1.84**
BSSF1	338746.3	866447.6	0.10	0.80	0.10	12.1	23.2	2.60	2.40	7.90	1.40
BSSF2	350615.3	873436	0.00	0.80	0.20	13.8	23.6	1.90	2.50	7.70	0.90
BSSF3	360054.3	861519.8	-0.10	0.60	0.10	14.8	24.6	2.10	2.70	8.50	1.20
BSSF4	364361.4	851500.6	0.00	0.60	0.10	9.90	26.1	2.40	2.20	10.4	1.70
BSSF5	372309.3	849050.4	0.10	0.80	0.10	11.5	25.8	2.60	1.00	8.40	1.30
Average			**0.02**	**0.72**	**0.12**	**12.42**	**24.66**	**2.32**	**2.16**	**8.58**	**1.30**
ARISH1	520534.4	845399.4	0.10	1.80	0.40	9.00	26.5	3.80	1.90	7.30	1.00
ARISH2	546801.0	851481.2	0.30	2.10	0.50	7.60	18.6	2.40	2.30	5.20	0.60
ARISH3	559579.4	874013.1	0.40	4.00	1.00	7.30	15.0	1.80	1.70	4.60	0.60
ARISH4	598971.5	886252.5	0.00	1.30	0.20	5.20	13.9	1.70	1.80	5.40	0.60
ARISH5	594993.6	875279.7	0.20	2.50	0.60	5.90	18.9	2.30	2.30	4.90	0.60
Average			**0.20**	**2.34**	**0.54**	**7.00**	**18.58**	**2.40**	**2.00**	**5.48**	**0.68**
BSS1	607511.1	988758.2	0.10	1.90	0.30	9.40	20.1	1.90	2.30	4.80	0.60
BSS2	582824.9	965590.3	0.00	2.70	0.70	7.30	29.4	3.90	2.10	6.10	0.70
BSS3	536425.7	940547.4	0.10	1.90	0.50	10.8	22.2	2.40	3.50	5.80	0.50
BSS4	390603.6	847204.9	0.00	0.40	0.10	10.6	24.5	2.80	2.90	8.70	1.00
BSS5	597106.8	1002768	1.00	3.50	0.70	8.10	21.4	3.30	1.90	5.00	0.70
Average			**0.24**	**2.08**	**0.46**	**9.24**	**23.52**	**2.86**	**2.54**	**6.08**	**0.70**

Table 4.3: Radiogenic Heat Production Values

ithology	Easting	Northing	Density	K% mean	Th(ppm) mean	U(ppm) mean	(Mean) TC	Ok	Oth	Ou	TO	RHP
asalt	440332.4	1064403	2.98	1.80	20.80	4.80	27.40	0.06	0.54	0.47	1.07	3.19
	438481.0	1034508	2.98	0.70	19.70	4.80	25.20	0.02	0.51	0.47	1.00	2.99
	501927.2	907027.5	2.98	0.80	16.10	4.60	21.50	0.03	0.42	0.45	0.89	2.64
	527274.0	1014990	2.98	2.80	19.20	3.50	25.50	0.10	0.50	0.34	0.94	2.79
	541920.6	982954.9	2.98	2.20	14.70	3.70	20.60	0.08	0.38	0.36	0.82	2.44
verage			2.98	**1.66**	**18.10**	**4.28**	**24.04**	**0.06**	**0.47**	**0.42**	**0.94**	**2.81**
hist	379608.6	1099219	2.64	1.00	20.70	6.60	28.30	0.04	0.54	0.64	1.21	3.60
	380516.7	1045824	2.64	2.50	18.40	4.40	25.30	0.09	0.48	0.43	0.99	2.62
	339048.5	993364.9	2.64	1.80	12.50	3.00	17.30	0.06	0.33	0.29	0.68	1.79
	367706.9	939920.2	2.64	0.80	10.90	2.40	14.10	0.03	0.28	0.23	0.54	1.44
	405856.1	949088.7	2.64	1.40	14.20	3.60	19.20	0.05	0.37	0.35	0.77	2.03
verage			2.64	**1.50**	**15.34**	**4.00**	**20.84**	**0.05**	**0.40**	**0.39**	**0.84**	**2.22**
eiss	440635.8	1004005	2.80	1.50	15.90	4.30	21.70	0.05	0.41	0.42	0.88	2.47
	448547.1	994859.9	2.80	1.70	16.30	4.20	22.20	0.06	0.42	0.41	0.89	2.49
	458628.0	971062.0	2.80	2.90	12.30	3.80	19.70	0.10	0.32	0.37	0.79	2.21
	509855.7	1036612	2.80	1.70	20.10	4.50	26.30	0.06	0.52	0.44	1.02	2.85
	524842.7	1007678	2.80	2.70	14.60	2.80	20.10	0.09	0.38	0.27	0.75	2.09
erage			2.80	**2.10**	**15.84**	**3.92**	**22.00**	**0.07**	**0.41**	**0.38**	**0.87**	**2.42**
gmatite	583388.5	1024426	2.74	3.90	18.00	3.60	25.50	0.14	0.47	0.35	0.95	2.61
	515692.9	966189.3	2.74	2.00	12.00	3.50	17.50	0.07	0.31	0.34	0.72	1.98
	408602.6	1071132	2.74	1.50	19.00	5.30	25.80	0.05	0.49	0.51	1.06	2.91
	343620.4	1063526	2.74	1.30	24.50	5.00	30.80	0.05	0.64	0.49	1.17	3.20
	357961.6	986020.0	2.74	1.40	14.40	3.90	19.70	0.05	0.37	0.38	0.80	2.20
erage			2.74	**2.02**	**17.58**	**4.26**	**23.86**	**0.07**	**0.46**	**0.41**	**0.94**	**2.58**
l Granites	395167.7	987568.4	2.72	1.70	13.30	3.70	18.70	0.06	0.35	0.36	0.76	2.08
	362236.7	1072965	2.72	1.50	22.60	5.60	29.70	0.05	0.59	0.54	1.18	3.22
	582800.8	1082104	2.72	2.80	31.50	5.20	39.50	0.10	0.82	0.50	1.42	3.87
	587036.3	1006421	2.72	3.80	16.90	3.30	24.00	0.13	0.44	0.32	0.89	2.43
	530611.0	852708.9	2.72	2.70	14.60	2.80	20.10	0.09	0.38	0.27	0.75	2.03
rage			2.72	**2.50**	**19.78**	**4.12**	**26.40**	**0.09**	**0.51**	**0.40**	**1.00**	**2.72**
nger												
nites	456772.9	1049332	2.67	1.80	24.90	5.20	31.90	0.06	0.65	0.50	1.21	3.24
	457062.7	1049473	2.67	1.60	25.00	5.30	31.90	0.06	0.65	0.51	1.22	3.26
	478158.0	1022942	2.67	1.50	30.10	6.80	38.40	0.05	0.78	0.66	1.49	3.99
	378997.1	924688.7	2.67	1.10	18.20	4.80	24.10	0.04	0.47	0.47	0.98	2.61
	445803.2	956421.7	2.67	1.30	10.10	2.70	14.10	0.05	0.26	0.26	0.57	1.52
rage			2.67	**1.46**	**21.66**	**4.96**	**28.08**	**0.05**	**0.56**	**0.48**	**1.10**	**2.92**
vium	405878.8	919523.2	2.60	0.40	7.10	2.10	9.60	0.01	0.18	0.20	0.40	1.05
	397308.9	876487.7	2.60	0.50	5.80	1.30	7.60	0.02	0.15	0.13	0.29	0.77
	568764.9	933841.7	2.60	0.50	15.20	4.40	20.10	0.02	0.40	0.43	0.84	2.18
	529401.4	911279.1	2.60	1.30	16.00	4.30	21.60	0.05	0.42	0.42	0.88	2.28
	566308.6	890507.4	2.60	2.50	11.40	3.50	17.40	0.09	0.30	0.34	0.72	1.88
rage			2.60	**1.04**	**11.10**	**3.12**	**15.26**	**0.04**	**0.29**	**0.30**	**0.63**	**1.63**

	346669.3	902115.0	2.50	0.40	10.10	2.00	12.50	0.01	0.26	0.19	0.47	1.18
	379289.2	903608.4	2.50	0.10	8.50	2.20	10.80	0.00	0.22	0.21	0.44	1.09
	454660.1	943294.3	2.50	0.10	9.70	2.80	12.60	0.00	0.25	0.27	0.53	1.32
	414994.8	917348.7	2.50	0.20	11.80	3.80	15.80	0.01	0.31	0.37	0.68	1.71
	452504.0	921925.8	2.50	0.30	17.80	5.30	23.40	0.01	0.46	0.51	0.99	2.47
rage			2.50	**0.22**	**11.58**	**3.22**	**15.02**	**0.01**	**0.30**	**0.31**	**0.62**	**1.55**
u	472652.8	920401.6	2.50	0.40	14.80	4.00	19.20	0.01	0.38	0.39	0.79	1.97
	432986.8	890509.5	2.50	0.20	13.00	3.70	169.00	0.01	0.34	0.36	0.70	1.76
	464138.0	935669.3	2.50	0.30	15.80	4.90	21.00	0.01	0.41	0.48	0.90	2.24
	587043.3	952714.0	2.50	0.40	12.70	3.80	16.90	0.01	0.33	0.37	0.71	1.78
	514648	898445.2	2.50	0.80	13.90	3.90	18.60	0.03	0.36	0.38	0.77	1.92
rage			2.50	**0.42**	**14.04**	**4.06**	**48.94**	**0.01**	**0.37**	**0.39**	**0.77**	**1.93**
aku	591960.0	929918.1	2.50	0.60	17.40	4.50	22.50	0.02	0.45	0.44	0.91	2.27
	490633.6	906673.7	2.50	0.70	16.30	4.70	21.70	0.02	0.42	0.46	0.90	2.26
	483319.8	875551.9	2.50	1.10	14.20	3.40	18.60	0.04	0.37	0.33	0.74	1.84
	483313.0	865787.8	2.50	0.80	13.00	2.90	16.70	0.03	0.34	0.28	0.65	1.62
	547061.6	925002.8	2.50	0.60	16.30	4.90	21.80	0.02	0.42	0.48	0.92	2.30
erage			2.50	**0.76**	**15.44**	**4.08**	**20.26**	**0.03**	**0.40**	**0.40**	**0.82**	**2.06**
poro	351226.4	883204.8	2.50	0.20	16.20	4.00	20.40	0.01	0.42	0.39	0.82	2.04
	377784.7	887466.4	2.50	0.30	13.20	3.60	17.10	0.01	0.34	0.35	0.70	1.76
	416227.7	902718.5	2.50	0.20	15.50	4.80	20.50	0.01	0.40	0.47	0.88	2.19
	409178.0	887142.9	2.50	0.30	16.40	5.30	22.00	0.01	0.43	0.51	0.95	2.38
	430235.2	907299.1	2.50	0.10	10.10	3.00	13.20	0.00	0.26	0.29	0.56	1.39
erage			2.50	**0.22**	**14.28**	**4.14**	**18.64**	**0.01**	**0.37**	**0.40**	**0.78**	**1.95**
ssange	338746.3	866447.6	2.50	0.40	17.60	5.10	23.10	0.01	0.46	0.49	0.97	2.42
	350615.3	873436.0	2.50	0.40	17.60	4.70	22.70	0.01	0.46	0.46	0.93	2.32
	360054.3	861519.8	2.50	0.30	18.80	5.40	24.50	0.01	0.49	0.52	1.02	2.56
	364361.4	851500.6	2.50	0.30	19.70	6.20	26.20	0.01	0.51	0.60	1.12	2.81
	372309.3	849050.4	2.50	0.30	18.90	5.50	24.70	0.01	0.49	0.53	1.04	2.59
erage			2.50	**0.34**	**18.52**	**5.38**	**24.24**	**0.01**	**0.48**	**0.52**	**1.02**	**2.54**
u River	520534.4	845399.4	2.50	0.60	16.70	4.60	21.90	0.02	0.43	0.45	0.90	2.25
	546801.0	851481.2	2.50	1.00	12.40	3.50	16.00	0.04	0.32	0.34	0.70	1.74
	559579.4	874013.1	2.50	2.10	10.00	3.10	15.20	0.07	0.26	0.30	0.63	1.59
	598971.5	886252.5	2.50	0.40	8.80	3.20	12.40	0.01	0.23	0.31	0.55	1.38
	594993.6	875279.7	2.50	0.90	10.40	3.20	14.50	0.03	0.27	0.31	0.61	1.53
erage			2.50	**1.00**	**11.66**	**3.52**	**16.00**	**0.04**	**0.30**	**0.34**	**0.68**	**1.70**
na	607511.1	988758.2	2.50	0.40	14.00	3.50	17.90	0.01	0.36	0.34	0.72	1.79
	582824.9	965590.3	2.50	0.70	16.50	4.20	21.40	0.02	0.43	0.41	0.86	2.15
	536425.7	940547.4	2.50	0.60	17.70	4.60	22.90	0.02	0.46	0.45	0.93	2.32
	390603.6	847204.9	2.50	0.20	16.90	4.80	21.90	0.01	0.44	0.47	0.91	2.28
	597106.8	1002768	2.50	2.30	12.50	2.80	17.60	0.08	0.33	0.27	0.68	1.69
erage			2.50	**0.84**	**15.52**	**3.98**	**20.34**	**0.03**	**0.40**	**0.39**	**0.82**	**2.05**

4.2.8 Discussion of Findings

In analyzing the Total Magnetic Field Intensity of the area, variations in the intensity map (Fig. 4.1) were observed. The regional trend conforms to the suspected rifted structures of the orogeny trending with the major lineaments dominant in NE-SW direction and others in NEE-SWW. ESE-SSW, and NW-SE trending. The regions of magnetic lows corresponded to the low amplitude values and regions of magnetic highs corresponding to the high amplitude values. The low-anomaly values are from -88.67nT to 47.42nT whiles the high-anomaly values range from 50.16nT to 132.23nT. The high magnetic amplitude intensities notably around the Northeast of the area corresponding to regions with high magnetic mineral contents are of Pre-Cambrian to Pan-African Crystalline Basement. The lower amplitude magnetic intensities are seen from the East towards the South of the area coinciding with the sediments of the Benue Trough.

The Map of the First Vertical Derivative (Fig. 4.3) enhances the anomaly trends and structures showing clearly the boundary of the basement and the sediments (B-B1). It assists us in eliminating magnetic field features with long wavelength and enhances the closely spaced anomalies by quantifying the signal change as a function of survey height. The findings reveal regions with low magnetic frequencies (LF) in the southern region, indicating deeper sources, and high magnetic frequencies (HF) in the northern portion of the study area, indicating locations with shallower depths to causal sources. The vertical gradients show variable magnetic contrast whose amplitude varies from $-0.0305 nTm^{-1}$ to $0.0312 nTm^{-1}$. The high gradient values can be attributed to areas of felsic and mafic rocks found in the crystalline basement and some granitic intrusions around the sedimentary basin shown in thick circles. A few lower gradient values seen also in the crystalline basement can be attributed to the fault pattern and contacts due to intense shearing in those areas. We have observed also low gradient values around the sedimentary basin which shows the presence of fluid, alluvium deposits, and other sedimentary formations in the basin.

The tilt derivative is an impressive image enhancement technique that can detect low amplitude signals in magnetic interpretation. The tilt derivative map (Fig. 4.4c) shows the enhancement of low amplitude signals not evident in the RTE grid or the FVD ranging from -1.5975nT to 1.7940nT with the trends and lineaments devoid of angular influence.

The total horizontal derivative map (THDR) sums both derivatives in the x and y directions and clearly shows the contacts of different rock units and their geological features. We could see the linear features, major faults in thick dark lines, and the subsurface boundary. The short linear and curvilinear features trending E-W direction majorly seen in the west of the area are concentrated within the bodies of muscovite schist, porphyritic granites, biotite granites, and the banded granite gneiss. The amplitude ranges from 0.0006nT/m to 0.1261nT/m.

In the analytic signal method, the sources are assumed to be isolated dipping contacts of different geological units. Observing the peaks in the amplitude signal can help locate the contacts and estimate the strike directions. The analytic signal map (Fig. 4.5) shows the edges of the magnetic sources in both vertical and horizontal dimensions independent of magnetization direction.

Figures 4.6a & b are the lineament map and rose diagram of the research area, which also highlight the heterogeneity of the earth's crust, illustrate the structural tendencies of the magnetic anomalies, which are primarily NE - SW, and ENE - WSW with minor trends in the E-W, ESE - WNW, and SE - NW directions. To find linear structures, the CET grid analysis tool was gradually applied to the RTE anomaly map. These procedures included amplitude thresholding to emphasize the significant geological features and filter out the low amplitude signals, phase symmetry to highlight and detect any structural discontinuity, and textural analysis to quantify magnetic changes. A vectorization lineament map was produced.

Fig 4.8 and 4.9 are the logarithm plots of the power spectrum against wavenumber. The gradient is determined and the depths of these sources are estimated. The lower wavenumber is attributed

to the centroid depth while the higher wavenumber is attributed to the depth to the top of the magnetic sources.

Table 4.2 displays the spectral results across the blocks. The area was divided into 81 overlapping square blocks of window size 55 by 55 km. The different values for the centroid depths Z_0, depth to the top of the magnetic source Z_t, and the Curie point depth Z_b as displayed.

The value of the Curie point depth ranges from 7.47km to 29.4km with a mean value of 18.59km. These variations seen in the Curie point depths as reported by (Ross *et al.*, 2006) can be due to variations in the geological and lithological rock attributes. Conversely as seen in (Tanaka, 1999; Adewunmi *et al.*, 2021); the variations can be attributed to volcanic and geothermal regions if ranges below 10km; to island arches and ridges if between 10 – 20km, while 20km and above is ascribable to plateaus, 30 km and above is attributed to trenches.

The result of the CPD compares favourably with Shehu *et al.* (2016) whose Curie point depth ranges from 11.13km to 27.83km within the Sokoto Basin; Ofor *et al.* (2014) whose Curie point depth ranges from 11.31km to 22.5km around Sokoto basin; Mohammed *et al.* (2019) with Curie depths between 12-33km in the upper Benue Trough and Udochukwu *et al.* (2019) with Curie point depth ranging from 10.32km to 24.48km in Northeastern Nigeria. Conversely, Irumhe *et al.* (2019) got their lowest depth to be 4.41km in north-central Nigeria.

The geothermal gradient map (Fig.4.11) shows some variations in depth due to different lithology and rock types. The value ranges from 19.77°C/km to 77.64°C/km with a mean value of 34.29°C/km which is in agreement with Okubo *et al.* (1985) who opined that the geothermal gradient in the continental crust is between 30°C/km to 50°C/km. Also, the result agrees with Nwankwo & Sunday (2017), got their geothermal gradient in the Bida basin to be 19.58°C/km to 37.25°C/km; Bello *et al.* (2017) with an average geothermal gradient of 32.1°C/km around

the lower Benue Trough; Udochukwu *et al.* (2019) with a gradient of 23.7°C/km to 56.2°C/km in North-eastern Nigeria.

The heat flow estimation shows that the heat in the area ranges from 49.62mW/m^2 to 194.88mW/m^2 with a mean value of 86.07mW/m^2 which conforms with the work of Irumhe *et al.*, (2019); the work of Bello *et al.* (2017) who calculated an average heat flow of 80.1mW/m^2 around the lower Benue Trough; Ofor *et al.* (2014) estimated averagely a heat flow of 80.60mW/m^2 within the Sokoto Basin and Udochukwu *et al.* (2019) estimated a heat flow range of 59.24mW/m^2 to 136.18mW/m^2 in Northeastern Nigeria (Tafawa Balewa, Maijuju, Wase, Pankshin, and Payan), in the Northwest of the study area (Kachia and Kafachan), in the Southwest areas around Udegi, Doma, Akwanga, Soko, Ogam, and Obagandde towards Markudi and parts of Akiri, Ibi, Wukari and Rafin. The heat flow estimated average is 86.07mW/m^2 and above the normal heat flow in continental areas implying the existence of anomalous heat flow (Jessop et al 1976; Obande *et al.*, 2014).

The watershed map helped us understand groundwater interaction for both recharge and discharge areas. We could identify recharge areas where surface water infiltrates the ground and recharges aquifers. Understanding these areas is vital because geothermal reservoirs are often recharged by infiltrating meteoric water that is heated by the Earth's geothermal gradient, and discharge areas where groundwater emerges as springs or seeps which can also indicate potential geothermal reservoirs.

The radiometric analysis includes the K (%) map, eTh map (ppm), eU (ppm) map, K Th ratio map, ternary image map, and the RHP map (Figs. 4.16, 4.17, 4.18, 4.19, 4.20, and 4.21).

The Potassium (K) map, Fig. 4.16 shows a very high concentration of potassium ranging from 1.6 to 4.8% in Northeastern part of the area hosting granitic rocks, some northern areas, and in

the south-eastern part where granites intruded the sediments. From the works of Lawal (2020), these can be attributed to meta-sediments, younger granites, and metamorphic rocks. The intermediate concentration was seen within the basement around the north of the study area and in the south of the study area within the sedimentary formation whiles the low concentrations ranging from 0.1 to 1.4% were seen both in some areas around the basement and sedimentary formation can be associated with meta-volcanic and carbonate rocks.

Fig 4.17 (eTh map), shows a very high concentration ranging from 18.3 to 41.5 ppm within the basement which can be tied with metagabbros, quartz syenides, and talc carbonate rocks. A low concentration from 5.3 to 10ppm at the boundary of the basement rocks and the sedimentary formation was observed corresponding to the Lafia Formation, Bima sandstone, and also at the Asu River Group.

Fig. 4.18 (eU map) shows high concentrations ranging from 4.6 to 8.5 ppm associated with older granites, younger granites, and some metamorphic rocks. These high concentrations were seen in the northern part of the area and also the southern side corresponding to the Bassange formation and the Nkporo Group. We have a very low concentration in the Lafia Formation, Agwu Shale, along the River Benue housing the Alluvium deposits, and some areas in the basement housing the meta-sediments and meta-volcanic and Schist rocks.

For the Potassium-Thorium ratio map (Fig. 4.19) which is significantly used in locating signatures associated with hydrothermal alterations. The strong indicators which range from 0.107%/ppm to 0.376%/ppm are of pink-red colouration showing areas that have been hydrothermally altered which serves as pathways for the movement of fluids. These areas are linked to the schist, migmatites, syenites, gabbros, and the Asu River Group of the sedimentary formation. Low concentrations are seen around Lafia, Nkporo, Agwu, Ezeaku, and Bassange Formations.

By modulating the three colours, red for potassium, green for thorium, and blue for uranium, to reveal the intensities of the three radioelements, the ternary map (Fig. 4.20) was created. The white colour found in some areas shows high concentrations of the three elements, and the dark colouration shows low concentration of the three elements. The red-magenta zones show high potassium contents, the yellow-green show high thorium content, and the blue show the uranium contents within the region.

Table 4.2 shows the statistical calculation of the minimum value, maximum value, mean value, and standard deviation of the 70 profiles taken across each rock unit. The types of rock units across the area was first identified using the geological map of the study area. The profiles were mapped and a statistical database was created by vertically tiling the three radioelement maps (K, Th, U) with the geological map using a grid profile in the grid & image of Oasis Montaj software.

Table 4.3 shows the different lithology and the individual heat dissipated across each rock profile with the total radiogenic heat production (RHP) across the entire profiles. The RHP across the study area was calculated using equation 2.29.

Fig. 4.21 is a radiogenic heat production map showing the total amount of heat from the entire study area with most of the heat coming from the basement and a few from the sedimentary formations. The radiogenic heat production ranges from 0.6μw/m^3 to 5.2μw/m^3 in conformity to the work of Megwara *et al.* (2013) who calculated a radiogenic heat production range of 0.91μW/m^3 to 4.53μW/m^3 within the Southern Bida Basin; Adewunmi *et al.* (2021) who estimated the RHP of about 2.2μW/m^3 to 2.5μW/m^3 within Northeastern Nigeria. This result agrees with Rybach's average of 2.25μW/m^3 used as a standard estimation for granitic and sedimentary rocks.

CHAPTER FIVE

SUMMARY, CONCLUSION AND RECOMMENDATION

5.1. Summary

This research involves both qualitative and quantitative analysis of the High-Resolution Aeromagnetic and aero radiometric Data. The anomaly data was deployed to investigate the depth of the anomalies and estimate the heat flow in the region for geothermal exploration.

The magnetic anomaly map after reducing to the equator shows high magnetic signatures mainly at the basement complex and parts of the sedimentary formation intruded by some granitic rocks. There are low magnetic signatures across the sedimentary basin and a few in the basement. The high magnetic signatures are due to the basement rocks (granites, quartz, migmatites, syenites. gabbros, etc.) and intrusive bodies while the low signatures can be due to fluids in the sediments, deep-seated magnetic rocks or shearing activities. To enhance the magnetic signatures of the data, some magnetic filters were applied. The first vertical derivative map shows the vertical changes with depth and enhances the shallower sources while suppressing the deeper ones. Lineaments are trending NE-SW and ENE-WSW direction. The analytic signal technique clearly shows the edges and contacts of the anomalies and the geological boundary.

The lineament map and the rose diagram show the structural trends of the lineaments that agree with the 1VD majorly NE-SW, ENE-WSW, and E-W directions.

With the SRTM map, we were able to visualize the elevation of the area and understand the basin morphology. The SRTM shows regions with elevated surface temperatures and faulted pathways which can serve as conduits for the circulation of fluids and heat.

The spectral analysis technique was deployed in analyzing the frequency components of the magnetic data beneath the earth's surface. The time domain data was transformed to the frequency domain using Fourier Transform. The resultant frequency domain data was represented as a power spectrum which shows the amplitude of the magnetic signals at different frequencies. The graph of the logarithm of the power spectrum against wave number plotted was used to calculate the depths. The Curie depth results 7.47km to 29.34km were used to estimate the geothermal gradients and heat flowing in the region. The result gave 19.77°C/km to 77.64°C/km and 49.62mW/m^2 to 194.89mW/m^2 respectively.

The watershed map of the heat flow shows the direction of flow which reveals areas where water converges that can be attributed to geological features like faults serving as pathways for groundwater. It also helped us to understand the recharge areas where subsurface water infiltrates the ground and recharges the aquifer and the discharge areas where the underground water emerges as seeps or springs. These are very vital in geothermal exploration.

The radiometric interpretation of the radiogenic elements (potassium, thorium, and uranium) shows concentration of the three elements in the region. The K (%) map shows high concentration in the basement granitic rocks and the Asu River Group within the sediment. The Th (ppm) map shows high concentrations with the granites, gneiss, meta gabbros, schists, quartz-syenites, and carbonate rocks while low concentrations around the migmatites, Lafia formation, Bima sandstone, and Asu River Group. The U (ppm) map shows high concentrations within the older and younger granites and some metamorphic rocks. The k/eTh ratio map shows hydrothermal alteration zones that have been weathered by water pressure. The ternary map shows distribution of the three radioelements within the region.

The heat produced by radioactivity in the area was calculated using the Rybach (1976) equation and the contour map produced. The contour map of the radiogenic heat production shows areas with high amount of heat flow majorly from basalts, migmatites, older, and younger granites. Integrating aeromagnetic and radiometric data, there was significant correlation in the heat generated within the area. The anomalous heat flows were coming mainly from the basement rocks than in the sedimentary formation.

5.2. Conclusion

Presently, most of our energy in use is gotten from conventional fossil fuels like coal, diesel, natural gas, etc. thereby centralizing our grids. Uninterrupted energy supply has always been an issue in Nigeria as almost 40% of the population has little or no access to electricity because we do not have a backbone to the existing national grids.

As the population of the country increases and the existing energy source can no longer satisfy the energy needs of the people, we need to explore other alternate and reliable energy sources to decentralize our grids.

Renewable energy source like geothermal energy is a solution to our energy crisis. The energy is generated from the heat that comes from the subsurface and can either be used directly or for electricity generation. The heat from the earth is only limited to technology and its associated cost but the potential is enough to serve mankind. It is clean and reliable.

To access the heat and convert it to usable energy, we need to drill into the subsurface and harness the geothermal reservoirs which are fractured hot granitic and volcanic rocks and also over-pressured sediments. The depths of these reservoirs and how they vary with temperature is vital. Hence the Curie point depth and geothermal gradient are key to estimating the heat that flow in a region.

The trends of the anomalies are majorly in the NE-SE, ENE-WSW direction which is a product of the Pan African Orogeny. These lineaments serve as conduits for groundwater movement.

The Curie point depths calculated in the study area range from 7.47km to 29.4km with a mean of 14.5km. The estimated geothermal gradient in the study area ranges from 19.77°C/km to 77°C/km with a mean of 34.29°C/km agreeing with some researchers in the region.

The Heat flow analysis from this work was estimated to be from 49.62mW/m^2 to 194.88mW/m^2 with an average of 86.07mW/m^2. The map of the heat flow shows high heat flow around the Northeast of the study area (Tafawa Balewa, Maijuju, Wase, Pankshin, and Payan), in the Northwest of the study area (Kachia and Kafachan), in the Southwest areas around Udegi, Doma, Akwanga, Soko, Ogam, and Obagandde towards Markudi and parts of Akiri, Ibi, Wukari and Rafin. The heat flow estimated average is 86.07mW/m^2 and above the normal heat flow in continental areas implying the existence of anomalous heat flow.

Using the radiometric data, the result of the radiogenic heat production in the study area ranges between 0.6μW/m^3 to 5.2μW/m^3 while the heat from the profiled rocks vary from 0.765μW/m^3 to 3.99μW/m^3.

Integrating results of the heat flow from aeromagnetic interpretation and radiometric interpretation, a positive correlation was observed. For the aeromagnetic data, the high heat flows were coming from granitic and volcanic rocks of the basement and some fractured areas in the sedimentary basin ranging from 80mW/m^2 -194mW/m^2 in correlation with the region of maximum radiogenic heat flow ranging from 2.25μW/m^3 to 5.2μW/m^3.

In conclusion, the Curie point depth (7.47km to 29.4km), geothermal gradient (19.77°C/km to 77.64°C/km), the high heat flow (49.62mW/m^2 to 194.88mW/m^2), and radiogenic heat

production of ($0.76\mu W/m^3$ to $3.99\mu W/m^3$) coming from the profiled rocks and ($0.6\mu W/m^3$ – $5.22\mu W/m^3$) from the entire region is anomalous and shows those areas have potential for further geothermal exploitation.

5.3. Recommendations

This research work has succeeded in estimating the geothermal gradients in the area, identifying the heat sources, and quantifying them. Using the SRTM data, possible fluid flow paths and fault patterns were observed. With the derivatives, fault trends and geological contacts were identified. Using the spectral analysis technique, the depth of these heat sources was estimated. A good understanding of the resistivity of the study area is valuable for understanding geothermal systems since it relates to the parameters (porosity, water-rock interaction, salinity, temperature, etc.) that correlate to geothermal activities.

Therefore, the following are recommended:

i. Borehole temperature logging should be done in these areas with high heat flow to ascertain its potential.

ii. Integration of geological, geochemical, and other geophysical methods like the micro-tremor survey method, seismic survey, and magneto-telluric technique, etc. to minimize uncertainties associated with estimating temperatures and depths.

iii. Introduce the Ambient Noise Differential Adjoint Tomography method which allows researchers to have a better visualization of rocks with fluids

iv. Well drilling being the most accurate technique should be considered by the government to ascertain these areas for geothermal exploration.

5.4 Limitations of the Study

i. Assumption that magnetization is isothermal

ii. Non uniqueness in interpretation due to the heterogeneity of the subsurface

iii. Inability to account for magnetic anomalies outside the study area

iv. Influence of non-thermal factors

v. Financial constraints due to inability to get sponsorship

5.5 Suggestions for Further Studies

Based on the results of this research work, I would suggest further studies be done in the study area as follows:

I. Studies to characterize thermal fluids in the areas identified with high heat flow

II. Developing a conceptual model for the geothermal reservoir in the study area

III. Estimating the geothermal heat flow using Thermal Infrared Remote sensing (TIR)

References

Abdullahi, M., Kumar, R. & Singh, U. K. (2019). Magnetic Basement Depth from High Resolution Aeromagnetic Data of Part s of Lower and Middle Benue Trough (Nigeria) Using Spectral Method. *Journal of African Earth Sciences*, 150(1), 337-345.

Abraham, E. M., Lawal, K. M., Ekwe, A. C., Alile, O., Murana, K. A. & Lawal, A. A. (2014). Spectral Analysis of Aeromagnetic Data for Geothermal Energy Investigation of Ikogosi Warm Spring-Ekiti State, South-western Nigeria. *Geothermal Energy,* 2(1),1. *doi:10.1186/s40517-014- 0018-9.*

Abraham, E. M., Lawal, K. M. & Akaolisa, C.C. (2012). Magnetic Analysis to Determine the Permeability of a Geothermal Reservoir: Case Study of the Ikogosi Warm Spring Area Ekiti, Southwestern Nigeria. *Nigerian J. Physics,* 23(1), 121-131.

Abraham, E. M. & Nkitnam, E. E. (2017). Review of Geothermal Energy Research In Nigeria: The Geoscience Front. *International Journal of Earth Science and Geophysics,* 3(15).

Abraham, E. M., Oweris, A. & Murana, K. A. (2014). Structural Mapping of Ikogosi Warm Spring Area Using Aeromagnetic Derivation and Euler Depth Estimates. *International Journal of Natural and Applied Science,* 3(1), 15-20.

Adelana, A. M. S., Olasehinde, I. P., Bale, B. R., Vrbka, P., Edet, E. A. & Goni, B. I. (2008). *An Overview of the Geology and Hydrogeology of Nigeria.* Doi:10.1201/9780203889497.ch11. Retrieved 31st May, 2018.

Adetona A. A. & Abu, M. (2013). *Estimating the thickness of sedimentation within the Lower Benue and upper Anambra Basins, Nigeria, using both Spectral depth determination and Source Parameter Imaging*. ISRN Geophysics, Hindawi Publishing Corporation.

Adewumi, T. & Salako, K. A. (2018). Delineation of Mineral Potential Zone Using High Resolution Aeromagnetic Data over Part of Nasarawa State, North Central, Nigeria. *Egyptian Journal of Petroleum*, 27(1), 759–767. https://doi.org/10.1016/j.ejpe.2017.11.002.

Adewumi, T., Salako K. A., Usman A. D. & Udensi E. E. (2021). Heat Flow Analysis over Bornu Basin and Its Environs, Northeast Nigeria, Using Airborne Magnetic and Radiometric Data: Implication for Geothermal Energy Prospecting. *Arabian Journal of Geosciences,* 14(1), 1355.

Aina, A., Olorunfemi, M. O. & Ojo, J. S. (1996). An Integration of Aeromagnetic and Electrical Resistivity Methods in Dam Site Investigation. *Geophysics,* 61 (2), 349–356.

Ajakiaye, D. E., Hall, D. H., Millar, T. W., Verheijen, P. J. T., Awad, M. B. & Ojo, S. B. (1986). Aeromagnetic Anomalies and Tectonic Trends in and Around the Benue Trough, Nigeria. *Nature*, 319(1), 582–584.

Ajakiaye, D. E., Hall, D. H., Ashiekaa, J. A. & Udensi, E. E. (1991). Magnetic Anomalies in The Nigerian Continental Mass Based on Aeromagnetic Surveys. *Tectonophysics*, 192(1), 211-230.

Akin, Uður & Çýftçý, Yahya. (2011). Heat Flow of the Kirþehýr Massif and Geological Sources of the Radiogenic Heat Production. *Mineral Res. Expl. Bull.*, 143(1), 53-73.

Akinlalu, A. A., Adelusi, O. A., Olayanju, M. G., Adiat, N. A. K., Omoshoyi, O. G., Anifowose, B. Y. A & Akeredolu E. B. (2017). Aeromagnetic Mapping of Basement Structures and Mineralization Characterization of Ilesa Shist Belt, South Western Nigeria. *Journal of African Earth Sciences*, 138(1), 383-391.

Anakwuba, E. K. & Chinwuko A. I. (2015). One Dimensional Spectral Analysis and Curie Depth Isotherm of Eastern Chad Basin. *Nigeria Journal of Natural Science Research.* ISSN 2224-3186 (Paper) ISSN2225 – 0921(Online), 5(19), 14-22.

Anakwuba, E. K., Chinwuko I. & Onyekwelu, C. (2016). Estimation of Curie Isotherm and Heat Flow of Eastern Chad Basin, Nigeria from Spectral Analysis of Aeromagnetic Data. *SEG, International Conference and Exhibition,* Barcelona, Spain. 3-6 2016.

Anderson, H. & Nash, C. (1997). Integrated Litho-Structural Mapping of the Rössing Area. Namibia Using High Resolution Aeromagnetic, Radiometric, Landsat Data and Aerial Photographs. *Explor. Geophys.,* 28(2), 185–191.

Anudu, G. K., Essien, B. I., Onuba, L. N. & Ikpokonte, A. E. (2011). Lineament Analysis and Interpretation for Assessment of Groundwater Potential of Wamba and Adjoining Areas, Nasarawa State, Northcentral Nigeria. *Journal of Applied Technology in Environmental Sanitation*, 1(2), 185-198.

Anudu, G. K., Onuba, L. N., Onwuemesi, A. G. & Ikpokonte, A. E. (2012). Analysis of Aeromagnetic Data over Wamba and Its Adjoining Areas in North-Central Nigeria. *Earth Sciences Research Journal*, 16(1), 25-33.

Anudu, G. K. (2017). *Evaluation of the Crustal Structure of the Middle Benue Trough Nigeria Based on the Analysis of Potential Field Data*. PhD Thesis, University of Aberdeen, Aberdeen, Scotland United Kingdom (Unpublished), pp. 391.

Anudu, G. K., Stephenson, R. A., Ofoegbu, C. O. & Obrike S. E. (2020). Basement Morphology of the Middle Benue Trough, Nigeria, revealed from Analysis of High-Resolution Aeromagnetic Data Using Grid-Based Operator Methods. *Journal of African Earth Sciences,* 162 (2020), 103724.

Bain, J. E. (2000). Eastern Gulf data reveal play concepts. *The American oil and Gas Reporter,* 38 – 41

Bektaş, Ö. D., Ravat, A., Büyüksaraç, Bilim, F. & Ateş, A. (2007). Regional Geothermal Characterisation of East Anatolia from Aeromagnetic, Heat Flow and Gravity Data. *Journal of Pure Appl. Geophys.*, 164(5), 975-998.

Bello, R., Ofoha, C. C., & Wehiuzo, N. (2017). Geothermal Gradient, Curie Point Depth and Heat Flow Determination of Some Part of Lower Benue Trough and Anambra Basin, Nigeria Using HRAD. *Physical Science International Journal*, 15(2), 1-11.

Bernard, S., Malte, I. S., Steuer, A., Deus, N. & Wiederhold, H. (2020). Airborne Electromagnetic, Magnetic and Radiometric Surveys at German North Sea Coast Applied to Groundwater and Soil Investigations. *Journal of Remote Sensing*, 12(10), 16-29.

Blakely, R. J. (1995). *Potential Theory in Gravity and Magnetic Applications*. Cambridge University Press, Cambridge

Benkhelil, J. (1982). Benue Trough and Benue Chain. *Geological Magazine*, 119(1), 155168.

Benkhelil, J. (1986). Structure and Geodynamic Evolution of the Intracratonic Benue Trough (Nigeria). Elf Nig. Ltd., Nigeria. *Bull Centres Rech. Explor. Prod. Elf-Aquitaine* (BCREDP) 12(1), 29-128.

Benkhelil, J. (1989). The Origin and Evolution of the Cretaceous Benue Trough (Nigeria). *Journal of African Earth Sciences*, 8(1), 251-282.

Benkhelil, J., Dainelli, P., Ponsard, J. F., Popoff, M. & Saugy, L. (1988). The Benue Trough: Wrench-fault Related Basin on the Border of the Equatorial Atlantic. In: Manspeizer, W. (Ed.), *Triassic-Jurassic Rifting: Continental Breakup and the Origin of the Atlantic Ocean and Passive Margin*. Part A, Developments in Geotectonics 22. Elsevier Science Publishers B. V., Amsterdam, the Netherlands. pp. 998p.

Benkhelil, J., Guiraud, M., Ponsard, J. F. & Saugy, L. (1989). The Bornu-Benue Trough, the Niger Delta and its Offshore: Tectono-sedimentary Reconstruction during the Cretaceous and Tertiary from Geophysical Data and Geology. In: Kogbe, C.A. (Ed.), *Geology of Nigeria* (2nd Rev. Ed.). Rock View (Nigeria) Ltd., Jos. pp. 277–309.

Bhattacharyya, B. K. & Leu, L. K. (1975). Analysis of Magnetic Anomalies over Yellowstone National Park: Mapping of Curie Point Isothermal Surface for Geothermal Reconnaissance. *Journal of Geophysical Research*, 80(1), 4461-4465.

Bhattacharyya, B. K. & Leu, L. K. (1977). Spectral Analysis of Gravity and Magnetic Anomalies due to Rectangular Prismatic Bodies. *Geophysics*, 42(1), 41–50.

Bilim F., Akay, T., Aydemir, A. & Kosaroglu, S. (2016). Curie Point Depth, Heat Flow and Radiogenic Heat Production Deduced from the Spectral Analysis of the Aeromagnetic Data for the Geothermal Investigation on the Menderes Massif and the Aegean Region, Western Turkey. *Geothermics*, 60(1), 44-57.

Bowden, P. & Kinnaird, J. A. (1984). Geology and Mineralisation of the Nigerian Anorogenic Ring Complexes. *Beith Geol. Jahrb.* B, 56(1), 197–299.

Burger, R. H., Sheehan, A. F. & Jones, C. H. (2006). *Introduction to Applied Geophysics*. WW.Norton, 600p ISBN 0-393-92637-0.

Burke, K. C., Dessauvagie, T. F. J. & Whiteman, A. J. (1970). Geologic History of the Benue Valley and Adjacent Areas. In: Dessauvagie T.F.J. and Whiteman, A.J. (Eds.). *African Geology*. University of Ibadan Press, Nigeria, 187-206.

Burke, K. C. & Whiteman, A. J. (1973). Uplift, rifting and the Break-up of Africa. In: Tarling, D.H., Runcorn, S.K. (Eds.). *Implications on Continental Drift to Earth Sciences*. pp. 735–755.

Christensen, A. & Dransfield, M. (2002). Airborne Vector Magnetometry over Banded Iron Formations. *72nd Annual International Meeting, Society of Exploration Geophysics*, 13-16.

Chukwu, G. C., Udensi, E. E., Abraham, M. E., Ekwe C. A. & Selemo O. A. (2017). Geothermal Energy Potential from Analysis of Aeromagnetic Data of Part of Niger Delta Basin, Southern Nigeria. *https://doi.org/10.1016/j.energy.2017.11.040.*

Clark, D. & Emerson, D. (1991). Notes on the Rock Magnetization Characteristics in Applied Geophysical Studies. *Explor. Geophys.*, 22(3), 547-555.

Connard, G., Couch, R. & Gemperle, M. (1983). Analysis of Aeromagnetic measurements from the Cascade Range in Central Oregon. *Geophysics*, 48(1), 376-390.

Cooper, G. R. J. (2006). Interpreting Potential Field Data Using Continuous Wavelet Transforms of their Horizontal Derivatives. *Comput. Geosci.* 32984–992.

Cratchley, C. R. & Jones, G. P. (1965). An Interpretation of the Geology and Gravity Anomalies of the Benue Valley Nigeria. *Journal of Geology and Geophysics*, 1, 126. Development Journal (ISSN 1595-9104).

Dada, S. S. (1999). Geochemistry and Petrogenesis of the Reworked Archaean Gneiss Complex of North-Central Nigeria: Major and Trace Element Studies on Kaduna Amphibolite and Migmatitic Gneisses. *Glob. J. Pure Appl. Sci.* 5, 535–543.

Darnley, A. G. & Ford, K. L. (1989). Regional airborne gamma-ray surveys: A review. In *Proceedings of Exploration' 87: Third Decennial International Conference on Geophysical and Geochemical Exploration for Minerals and Groundwater, Special Volume No. 3, 960 pp, ed. Garland, G.D., Geological Survey of Canada.*

Dimgba, B. C, Obiora, D. N., Abangwu, J. U. & Ugbor, D. O. (2020). Study of Curie Point Depth and Heat Flow from Spectral Analysis of Aeromagnetic Data for Geothermal Potential of Gubio, Chad Basin, Nigeria. SN *Appl. Sci.*, 2(8),1–9.

Downing, R. A. & Gray, D. A. (1986). Geothermal energy - the potential in the United Kingdom. *British Geological Survey Report*, 3 – 7.

Ekwueme, G. N. (1987). Structural Orientations and Pre-Cambarian Deformation Episodes of Uwet Area Oba Massif. *Prec-Cambarian Research*, 34(1), 269-289.

Elawadi, E., Ammar, A. & Elsirafy, A. (2004). Mapping Surface Geology Using Airborne Gamma-Ray Spectrometric Survey Data. A case study. In *Proceedings of the 7th SEGJ International Symposium, Japan.*

Eletta, B. E. & Udensi, E. E. (2012). Investigation of Curie Point Isotherm from the Magnetic Field of Easter Sector of Central Nigeria. *Global Journal of Geosciences*, 2(4), 101-106.

Elbarbary, S., Abdel Zaher, M., Mesbah, H., El-Shahat, A. & Embaby, A. (2018). Curie Point Depth, Heat Flow and Geothermal Gradient Maps of Egypt Deduced from Aeromagnetic Data. *Renewable and Sustainable Energy Reviews*, 91(1), 620-629.

El-Sadek, M. A. (2002). Application of Thorium-Normalized Airborne Radio-Spectrometric Survey Data of Wadiaraba Area, North-Eastern Desert, Egypt, as a Guide to the Recognition of Probable Subsurface Petroleum Accumulations. *Applied radiation and isotopes*, *57*(1), 121-130.

Esmaeil, E., Anya, M. R., Michael, R., Mathew, J. C., Daniel, B. & Mark, D. (2015). Insight into the Continental Structure of South East Australia and Tasmania Form Passive Seismic and Magnetic Datasets. Geophysics and Geology Together for Discovery. *24th International Geophysical Conference and Exhibition 15th - 18th Perth, Western Australia* ASEG-PESA 2015 – Perth Australia.

Eze, M. O., Mamah, L. I. & Oha, A. I. (2019). Integration of in situ measurement of Radiometric Signatures and Aeroradiometric Data in Geologic Mapping of parts of Southern Benue Trough and Anambra Basin. *Arabian Journal of Geosciences*, 12(125), 1-12.

Feebrey, C. A., Hishida, H., Yoshioka, K. & Nakayama, K. (1998). Geophysical Expression of Low Sulphidation Epithermal Au-Ag Deposits and Exploration Implications–Examples from the Hokusatsu Region of SW Kyushu, Japan. *Resource Geology*, *48*(2), 75-86.

Fairhead, J. D. (2007). *Gravity and Magnetics in Today's Oil and Mineral Industry*. GETECH Group Plc. Kitson House. Elmete Hall Roundhay, Leeds. LS821J UK.

Fairhead, J. D. & Binks, R. M. (1991). Differential Opening of the Central and South Atlantic Oceans and the opening of the West African Rift System. *Tectonophysics,* 187(1), 191-203.

Fairhead, J. D., Green, C. M. & Guiraud, R. (2013). The Role those Plate Tectonics Inferred Stress Changes and Stratigraphic Unconformities Have on the Evolution of the West and Central African Rift System and the Atlantic Continental Margins. *Tectonophysics*. 594(1), 118–127.

Finn, C. A. & Ravat, D. (2004). Magnetic Depth Estimates and their Potential for Constraining Crustal Composition and Heat Flow in Antarctica, EOS. *Trans. Am. Geophys. Un.*, 85(47), Fall Meet. Suppl., Abstract T11A-1236.

Geyser (2023 *"Definition of geyser noun from Cambridge Dictionary. Online".Retrieved 2011 07-09*). www.en.wikipedia.org/wiki/geyser.

Gilmore, G. (2008). *Practical Gamma-ray Spectroscopy* (2nd Ed.) Wiley, UK.

Graham, D. F. & Bonham-Carter, G. F. (1993). Airborne Radiometric Data-A Tool for Reconnaissance Geological Mapping using a GIS. *Photogrammetric Engineering and Remote Sensing*, *59*(8), 1243-1249.

Guiraud, M. (1990). Tectono-Sedimentary Framework of the Early Cretaceous Continental Bima Formation (upper Benue Trough, NE Nigeria). *J. Afr. Earth Sci.*, 10(1), 341–353.

Guiraud, R. & Maurin, J. C. (1992). Early Cretaceous Rifts of Western and Central African. In: Ziegler, P.A. (Ed.), Geodynamics of Rifting, Vol. II. Case History Studies on Rifts. North and South America and Africa. *Tectonophysics*, 213(1), 153–168.

Gupta, R., Pathak, A. K. & Singh, H. M. (2016). Geothermal Energy: An Overview. *International Journal of Scientific and Technical Advancements*, 2(4), 107-110.

Hsien-Hsiang, H., Chieh-Hung, C., Pie-Ying, L. & Horng-Yuan, Y. (2014). Curie Point Depth from Spectral Analysis of Magnetic Data in Taiwan. *Journal of Asian Earth Science,* 90(1), 26-33. Journal homepage:www.elsevier.com/locate/js htpps://www.doi.org/10.1016.j.jseaes.2014.04.007.

Hinze, W. J., Von Frese, R. R. B. & Saad, A. H. (2013). *Gravity and Magnetic Exploration Principles, Practices, and Applications*. Cambridge University Press, New York, pp.515.

Hogg, S. (2004). GT Gradient Tensor Gridding Geologic Structures and Examples. www.shapegeophysics.com/, 2004.

Hotspring (2023). "Definition *of hotspring noun from Cambridge. dictionary online. www.en.wikipedia.org.wiki/hotsprings.*

IAEA (2003). *Guidelines for Radioelement Mapping using Gamma Ray Spectrometry Data.* (International Atomic Energy Agency), Vienna.

Igwesi, D. & Umego, M. (2013). Interpretation of Aeromagnetic Anomaly over Some Part of Lower Benue Trough Using Spectral Analysis Technique. *International Journal of Scientific & Technology Research,* 2(8),153-165.

Ikumbur, E. B., Onwuemesi, A. G., Anakwuba, E. K., Chinwoko, A. I. & Usman, A. O. (2013). Spectral Analysis of Aeromagnetic Data over Part of the Southern Bida Basin, West-Central Nigeria. *International Journal of Fundamental Physical Sciences,* 3(1), 27-31. Insights from New Source Rock Facies Evaluation Petroleum Technology.

Irumhe, P. E., Obiadi, I. I., Obiadi, C. M., Ezenwaka, C. K. & Mgbolu, C. C. (2019). Estimating Sedimentary Pile Thickness, Structural Lineaments and Heat Flow in Parts of North Central Nigeria from Aeromagnetic Data. *Solid Earth Sci.,* 4(3),92–101.

Irvine, R. J. & Smith, M. J. (1990). Geophysical Exploration for Epithermal Gold Deposits. *Journal of Geochemical Exploration*, 36 (3), 375-412.

Jaques, A. L., Wellman, P., Whitaker, A., & Wyborn, D. (1997). High-Resolution Geophysics in Modern Geological Mapping. *AGSO Journal of Australian Geology and Geophysics*, 17 (2), 159-173.

Jessop, A. M., Hobart, M. A. & Sclater. (1976). The World Heat Flow Data Collection in 1975. *Geothermal Services of Canada*, 50(1), 55-77.

Kai, Y., Junhui, X., Wei, G., Chaoyang, L. & Xiaoyang, W. (2017). Curie Point Depth from Spectral Analysis of Magnetic Data in the South East Tilbet. *Earth Sciences*, 6(5), 88-96.

Kamba, A. H., Muhammad, S. & Illo, A. G. (2018). Basement Depth Estimation of Some Parts of Lower Sokoto Sedimentary Basin, Northwestern Nigeria Using Spectral Depth Analysis. *International Journal of Marine, Atmosphere and Earth Science*, 6(1), 1-9.

Kasidi, S. & Nur, A. (2012). Analysis of Aeromagnetic Data Over Mutum-Biyu and Its Environs, North-eastern, Nigeria. *Research Journal in Engineering and Applied Sciences*, 1(1), 142-148.

Kasidi, S. & Nur, A. (2013). Estimation of Curie Point Depth, Heat Flow, and Geothermal Gradient Inferred from Aeromagnetic Data over Jalingo and Environs. *International Journal of Science and Emerging Technology*, 6(6), 294-301.

Kearey, P. & Brooks, M. (1991). *An Introduction to Geophysical Exploration*. Black Well Scientific Publications.

Kogbe, C. E. (1989). Paleogeographic history of Nigeria from Albian times. In: Kogbe, C.A. (Ed.). *Geology of Nigeria*. Rock View Nigeria Limited, Jos, pp. 257–275.

Komolofe, A. A., Kuria, N. Z., Woldai, T., Noomen, M. & Anifowose, B.Y.A. (2012). Integrated Remote Sensing and Geophysical Investigations of the Geodynamic Activities at Lake Magadi, Southern Kenyan Rift. *International Journal of Geophysics*, 20(12),1-15. Doi:10.1155/2012/318301.

Kuforijimi, O. & Christopher, A. (2017). Assessment of Aero-radiometric Data of Southern Anambra Basin for the Prospect of Radiogenic Heat Production. *J. Appl. Sci. Environ. Manage.*, 21(1), 743-748.

Kurowska, E. & Schoeneich, K. (2010). Geothermal Exploration in Nigeria. *Proceedings of World Geothermal Congress*, 2010. Bali, Indonesia, 25-29 April 2010.

Kwaya, M. Y., Kurowska, E. & Arabi, A. S. (2016). Geothermal Gradient and Heat Flow in the Nigeria Sector of the Chad Basin, Nigeria. *Computational Water Energy Environ. Eng.*, 5(2),70

Lawal, T. O. (2020). Integrated Aeromagnetic and Aeroradiometric Data for Delineating Lithologies, Structures, and Hydrothermal Alteration Zones in Part of Southwestern Nigeria. *Arab. J. Geosci.*, 13(16), 1–19.

Li, C-F., Shi, X., Zhou, Z., Li, L., Geng, J. & Chen, B. (2010). Depths to the Magnetic Layer Bottom in the South China Sea Area and their Tectonic Implications. *Geophys. J. Int.*, 182(3), 1229–1247. https://doi.org/10.1111/j.1365-246X.2010.04702.x

Ma, Guoqing & Li, Lili. (2013). Direct Analytic Signal (DAS) Method in the Interpretation of Magnetic Data. *Journal of Applied Geophysics*, 88, 101-104.

Maurin, J. C., Benkhelil, J. & Robineau, B. (1986). Fault Rocks of the Kaltungo Lineament, N.E. Nigeria and their Relationship with Benue Trough Tectonics. *J. Geol. Soc. Lond.* 143, 587–599.

Mayhew, M. A. (1982). Application of Satellite Magnetic Anomaly Data to Curie Isotherm Mapping. *J. Geophys Res.*, 87(1), 4846–4854.

Mayhew, M. A. (1985). Curie Isotherm Surfaces Inferred from High-Altitude Magnetic Anomaly Data. *J. Geophys Res.*, 90(1), 2647–2654.

Megwara, U. J., Udensi, E. E., Olasehinde, P. I., Daniyan, M. A. & Lawal, K. M. (2013). Geothermal and Radioactive Heat Studies of Parts of Southern Bida Basin, Nigeria and the Surrounding Basement Rocks. *Int. J. Basic Applied Science,* 2(1), 125–139.

Megwara, U. J. & Udensi E. E. (2014). Structural Analysis Using Aeromagnetic Data: Case Study of Part of Southern Bida Basin Nigeria and Surrounding Basement Rocks. *Earth Science Research*, 3(2), 27-42.

Milligan, P. R. & Gunn, P. J. (1997). Enhancement and Presentation of Airborne Geophysical Data. *AGSO Journal of Geological and Geophysics*, 17 (2), 63-75.

Mohammed, M. K., Hesam, Y. & Mohammed H. Z. (2010). Recent Researches in Environmental and Geological Sciences. Analysis of Deep Geological Structures by Variety of Curie Point Depth in Birjand Area, East of Iran. Retrieved 11th January 2020 from mkhatib@birjand.ac.ir, mkhatibm@yahoo.com. ISBN 978-161804-110-4.

Mohammed, A., Adewumi, T., Kazeem, S. A., Abdulwaheed, R., Adetona, A. A. & Usman, A. (2019). Assessment of Geothermal Potentials in Some Parts of Upper Benue Trough Northeast Nigeria Using Aeromagnetic Data, *J. Geosci. Engin., Env., Technol.*, 4(1). 7-15.

Mono, A. J., Ndougsa-Mbarga, T., Tarek, Y. & Ngoh, D. J. (2018). Estimation of Curie Point Depth, Geothermal Gradients and Near Surface Heat Flow from Spectral Analysis of Aeromagnetic Data in the Loum-Minta Area (Centre-East Cameroon). *Egyptian Journal of Petroleum*, 27(4), 1291-1299.

Mishra, D. C. & Naidu, P. S. (1974). Two Dimensional Power Spectrum and Analysis of Aeromagnetic Fields. *Geophysical Prospecting*, 22(2), 345-353.

Müjgan S., Oya P., & Ilknur K. (2005). Determination of the Curie Point Depth and Heat Flow from Magsat Data of Western Anatolia. *Journal of Balkan Geophysical Society*. 8(1), 149-160.

Musa, H., Bello, R., Raheem, O. & Abe, A.O. (2021). First Horizontal and First Vertical Derivatives from High Resolution Aeromagnetic Data over the Gongola Basin Upper Benue Trough Northeastern Nigeria. *Global Journal of Pure and Applied Sciences*. 27(1), 181-192.

Nabighian, M. N. (1972). The Analytic Signal of Two-Dimensional Magnetic Bodies With Polygonal Cross-Section: Its Properties and Use for Automated Anomaly Interpretation. *Geophysics*, 37 (3), 507–517.

Nabighian, M. N. (1984). Toward a Three-dimensional Automatic Interpretation of Potential Field Data via Generalized Hilbert Transforms: Fundamental Relations. *Geophysics*. 49(1), 780-786.

Nabighian, M. N., Grauch, V. J. S., Hansen, R. O., Lafehr, T. R., Li, Y., Peirce, J. W., Phillips, J. D. & Ruder, M. E. (2005). The Historical Development of the Magnetic Method in Exploration. *Geophysics*, 70(1), 33-61.

Negi, J. G., Agrawal, P. K. & Pandey, O. P. (1987). Large Variation of Curie Depth and Lithospheric Thickness beneath the Indian Subcontinent and a case for Magnetothermometry. *Geophysical Journal International*, 88(3), 763-775.

NGSA (2023). Geological Map of the Study Area Extracted from the Geological Map of Nigeria. Nigeria Geological Survey Agency.

Nigm, A. A. & Khameis, A. A. (2009). Utilizing the Airborne Gamma-Ray Spectrometric Data in Mapping the Contact Zone between the Precambrian and Phanerozoic Rocks at North Gabalelshallul Area, Central Eastern Desert, Egypt. *NRIAG Journal of Astronomy and Geophysics Special Issue*, 143-167.

Nuhu, D. U., Igwe, O. & Idris I. G. (2019). Evaluation and Characterization of Groundwater of the Maastrichtian Lafia Formation, Central Benue Trough Nigeria. *J. Earth Syst. Sci.* 128(1), 168.

Nuri D, M. Timur U, Z. Mumtaz H, & Naci O. (2005). Curie Point Depth Variations to Infer Thermal Structure of the Crust at the African Eurasian Convergence Zone, SW Turkey. *Journ. Earth Planets Space*, 57(1), 373-383.

Nwajide, C. S. (2013). *Geology of Nigeria's Sedimentary Basins*. CSS Press (A division of CSS Bookshops Limited) Lagos Nigeria, pp. 565.

Nwankwo, L. I., Olasehinde, P. I. & Akoshile, C.O. (2011). Heat Flow Anomalies from the Spectral Analysis of Airborne Magnetic Data of Nupe Basin, Nigeria. *Asian Journal of Earth Sciences*, 4(1), 20-28.

Nwankwo, L. & Sunday J. A. (2017). Regional Estimation of Curie Point Depth and Succeeding Geothermal Parameters from Recently Acquired HRAD of the Entire Bida Basin, North Central Nigeria. *Geoth. Energy Sci.*, 5(1), 1-9.

Nyabeze, P. K. & Gwavava, O. (2016). Investigating Heat and Magnetic Source Depths in the Soutpansberg Basin, South Africa: Exploring the Soutpansberg Basin Geothermal Field. *Geotherm Energy*, 4(8). DOI 10.1186/s40517-016-0050-z.

Nwogbo, P. O. (1997). Mapping the Shallow Magnetic Sources in the Upper Benue Basin in Nigeria from Aeromagnetic. *Spectra*, 4(4), 325-333.

Nwosu, O. B. (2013). Spectral Re-Evaluation of the Magnetic Basement Depth over Parts of Middle Benue Trough Nigeria, Using HRAM. *International Journal of Scientific and Technology research*, 2(1), 35-41.

Obaje, N. G. (2009). *Geology and Mineral Resources of Nigeria*. Lecture Notes in Earth Sciences. Bhattacharji S, Neugebauer HJ, Reitner J, Stuwe K, Springer, New York.

Obaje, N. G. (1994). Coal Petrology, Microfossils and Palaeoenvironments of Cretaceous Coal Measures in the Middle Benue Trough of Nigeria. *Tubinger Mikropalaontologische Mitteilugen*, 11(1), 1150.

Obaje, N. G., Wehner, H., Scheeder, G., Abubakar, M.B. & Jauro, A. (2004). Hydrocarbon prospectivity of Nigeria's inland basins: from the viewpoint of organic geochemistry and organic petrology. *AAPG (Am. Assoc. Pet. Geol.) Bull.*, 88 (3), 325-353.

Obande, E. G., Lawal, K. M. & Ahmed, A. L. (2013). Geothermal Characterization Using Spectral Analysis and Apparent Magnetization of Wikki Warm Spring, Northern Nigeria. *Journal of Mining and Geology,* 49 (1), 53 – 63.

Obande, E. G, Lawal, K.M. & Ahmed, A. L. (2014). Spectral Analysis of Aeromagnetic Data for Geothermal Investigation of Wikki Spring, North-East Nigeria. *Geothermics*, 50(1), 85-90.

Obi, D. A., Okereke C. S., Egeh, U. E. & Olagundoye, O. O. ((2008). Basinal Structure of Yola Arm of the Upper Benue Trough Nigeria: Evidence from Aeromagnetic Data. *Journal of Geological Sciences*, 6(2), 175-183.

Offodile, M. E. (1976). The Geology of the Middle Benue Nigeria. Cretaceous Research, Paleontological Institute: University of Uppsala. *Special Publication*, 4(1), 1-166.

Offodile, M. E. (1976b). A review of the geology of the cretaceous of the Benue Valley. In: Kogbe C.A. (ed.). *Geology of Nigeria*. Elisabethan Publishing Co., Lagos, pp. 319–330.

Offodile, M. E. (1977). A review of the geology of the cretaceous Benue Trough in Geology of Nigeria (Ed. Kogbe, C.A), *Elizebeth press Lagos* pp. 319-330.

Offodile, M. E. & Reyment, R. A. (1977). Stratigraphy of the Keana-Awe area of the middle Benue region of Nigeria. *Bull. Geol.*, 7(1), 37-66 Institutions University of Uppsala (N.S).

Offodile, M. E. (1980). A Mineral Survey of the Cretaceous of the Benue Valley, Nigeria. *Cretac. Res.*, 1(1), 101–124.

Offodile, M. E. (1984). The Geology and Tectonics of Awe Brine Field. *Journal of Earth Sciences*, 2(1), 191-202.

Ofoegbu, C. O. (1985). A Review of the Geology of the Benue Trough, Nigeria. *Journal African Earth Sciences*, 283-291.

Ofoegbu, C. O. (1985a). Interpretation of Aeromagnetic Anomalies Profile across the Benue Trough of Nigeria. *J. Afr. Earth Sci.*, 3(3),283–291. doi:10.1016/0899-5362(85)90001-6

Ofoegbu, C. O. (1988). An Aeromagnetic Study of Part of the Upper Benue Trough, Nigeria. *Jour. Afr. Earth Sci.*, 7(1), 77 - 90.

Ofoegbu, C. O. & Onuoha, K. M. (1991). Analysis of Magnetic Data over the Abakaliki Anticlinorium of the Lower Benue Trough, Nigeria: Petroleum geological implications. *Mar. Petrol. Geol.*, 8(2), 174 – 183.

Ofoegbu, C. O. & Mohan, N. I. (1990). Interpretation of Aeromagnetic Anomalies over Parts of South Eastern Nigeria using Three Dimensional Hilbert Transformations. *Pageoph*, 134(1), 13-29.

Ofoegbu, C. O. & Hein, K. (1991). Analysis of Magnetic Data over part of the Younger Granite Province of Nigeria. *Pure and Applied Geophysics*,136(2-3), 173-189.

Ofor, N. P. & Udensi, E. E. (2014). Determination of the heat flow in the Sokoto Basin, Nigeria using Spectral Analysis of Aeromagnetic Data. *Journal of Natural Sciences Research*, 4(6), 83-93.

Oguadinma, T. C. & Aku, M. O. (2019). Delineation of Sedimentary Thickness of Lafia and Environs using Aeromagnetic Data. *World Journal of Innovative Research (WJIR)*, 7(2), I64-70.

Okubo, Y., Graf, R. J., Hansen, R. O., Ogawa, K. & Tsu, H. (1985). Curie-point depths of the Island of Kyushu and surrounding areas, Japan. *Geophysics*, 50(3), 481-494. https://doi.org/10.1190/1.1441926

Okubo. Y., Makino, M & Kasuga, S. (1991) Magnetic Model of the Subduction Zone in the North-east Japan Arc. *Tectonophysics*, 192(2),103– 115.

Okwudiri, A. A., Lilian, C. O. & Okwara, I. C. (2017). Depositional Framework and Stratigraphy of the konshisha Area, Southern Benue Trough. *Global Journal of Geological Science,* 15(1), 41-55.

Olade, M. A. & Elueze, A. A. (1979). Petrochemistry of Ilesha Amphibolites and Precambrian Crustal Evolution in the Pan-African Domain of SW Nigeria. *Precambrian Research*, 8 (3-4), 303 – 318.

Olasehinde, P. I., Pal, P. C. & Annor, A. E. (1990). Aeromagnetic Anomalies and Structural Lineament in the Nigerian Basement Complex. *Journal of African Earth Sciences*, 11(1), 3-4.

Olowofela, J. A., Akinyemi, O. D., Idowu, O. A., Olurin, O. T. & Ganiyu, S. A. (2012). Estimation of Magnetic Basement Depths beneath the Abeokuta Area, South west Nigeria from Aeromagnetic Data using Power Spectrum. *Asian Journal of Earth Sciences*, 5 (3), 70.

Onuoha, K. M., Ofoegbu, C. O. & Ahmed, M. N. (1994). Spectral Analysis of Aeromagnetic Data over the Middle Benue Trough, Nigeria. *Journal of Mining and Geology*, 30, (2), 211-217.

Onwuemesi, A. G. (1997). One Dimensional Spectral Analysis of Aeromagnetic Anomalies and Curie Depth Isotherm in the Anambra Basin of Nigeria. *Journal of Geodynamics*, 23(2), 95-107.

Onyewuchi, R. A., Opara, A. I., Ahiarakwem, C. A. & Oko, F. U. (2012). Geological Interpretations Inferred from Airborne Magnetic and Landsat Data: Case Study of Nkalagu Area, Southeastern Nigeria. *International J. Sci. and Tech.* 2(4), 178 - 191.

Opara, A. I., Chinaka, J. C., Udoete, R. L., Emberga, T. T., Echetana, H. N., Ugwueghu, I. E., Nwokocha, K. C., Ijeoma, K. C. & Onyema, J. C. (2015). Structural Interpretation of the Jos-Buruku Younger Granite Ring Complexes Inferred from Landsat-TM Data. *Journal of Geosciences & Geomatics*, 3(3), 56-67.

OpenAI (2023). Geothermal Energy. Accessed on 23rd April 2023. ChatGPT. https://openai.com/geothermalenergy/chatgpt.

Orajiuka, R. C., Mallam, A. & Ofoegbu, C. O. (2020). Depth Estimation in Part of Anambra Basin, Nigeria Using Source Parameter Imaging and Euler De-Convolution Method. *Nigerian Journal of Mining and Geology*, 56(2), 309-318.

Osazuwa, I. B., Ajakaiye, D. E. & Verheiien, P. J. T. (1981). Analysis of the Structure of Part of the Upper Benue Rift Valley on the Basis of New Geophysical Data. *Earth Evolution Sciences*, 2, 126135.

Oyedepo, S. O. (2012). Energy and Sustainable Development in Nigeria: The Way Forward. *Energy, Sustainability and Society*, 2(1), 15.

Pamuk, E. & Özsöz, I. (2022). Estimation of Curie Depths & Heat Flow from Spectral Analysis of EMAG2 Magnetic Data in Cyprus Island. *Annals of Geophysics*, 64(4) GT427; doi:10.4401/ag-8741

Pantelis, S. & Eleni, K. (2016). *Geophysics: Principles, Applications & Emerging Technology*. Nova Publisher USA. Pp.13-47.

Patra, I., A. K., Chaturvedi, A. K., Srivastava, P. K. & Ramayya, M. S. (2013). Integrated Interpretation of Satellite Imagery, Aeromagnetic, Aeroradiometric, and Ground Exploration data sets to Delineate Favorable Target Zones for Unconformity Related Uranium Mineralization, Khariar Basin, Central India. *Journal Geological Society of India*, 81(1), 299-308.

Patrick, N. O., Fadele, S. I. & Adegoke, I. (2013). Stratigraphic Report of the Middle Benue Trough, Nigeria: Insights from Petrographic and Structural Evaluation of Abuni and Environs Part of Late Albian- Cenomanian Awe and Keana Formations. *The Pacific Journal of Science and Technology*, 14(1), 557-570.

Pamuk, E. (2019). Investigating Edge Detection, Curie Point Depth and Heat Flow Using EMAG2 Magnetic and EGM08 Gravity Data in the Northern Part of Eastern Anatolia, Turkey. *Turkish J. Earth Sci.*, 28(6), 805-821.

Pilkington M. (2007). Aeromagnetic Surveying. https://www.researchgate.net/publication/304176944 DOI:10.1007/978-1-4020-4423-6-1

Ravat, D., Pignatelli, A., Nicolosi, I. & Chiappini, M. (2007). A Study of Spectral Methods of Estimating the Depth to the Bottom of Magnetic Sources from Near-Surface Magnetic Anomaly Data. *Geophys. J. Int.*, 169(2), 421-434.

Ravat, D. (2004). Constructing Full Spectrum Potential Field Anomalies for Enhanced Geodynamical Analysis Through Integration of Surveys from Different Platforms (INVITED). *Eos, Transactions, American Geophysical Union* 85 (47), Fall Meeting, Abstract G44A-03.

Reeves, C. (2005). *Aeromagnetic Surveys: Principles, Practice and Interpretation.* Geosoft. pp. 68.

Redford, S. (2010). Processing and Interpretation of Airborne Geophysical Data: Phase II. http://www.mmsd.gov.ng/Downloads/Reford_Process_Interp.pdf Accessed June, 13, 2014.

Rochette, P., Jackson, M. & Aubourg, C. (1992). Rock Magnetism and the Interpretation of Anisotropy of the Magnetic Susceptibility. *Reviews of Geophysics*, 30(3), 206-226.

Roest, W.R., Verhoef, J. & Pilkington, M. (1992). Magnetic Interpretation using the 3-D Analytic Signal. *Geophysics,* 57(1), 116–125.

Ross, H. E., Blakely, R. J. & Zoback, M. D. (2004). Testing the Utilization of Aeromagnetic Data for the Determination of Curie-Isotherm Depth. *EOS, Trans. Am. Geophys. Un.*, 85(47), Fall Meet. Suppl., Abstract T31A-1287.

Ross, H. E., Blakely, R. J. & Zoback, M. (2006). Testing the Use of Aeromagnetic Data for the Determination of Curie Depth in California. *Geophysics*, 71(5), 51- 59.

Rybach, L., (1976). Radioactive Heat Production in Rocks and its Relation to other Petrophysical Parameters. *Pure and Applied Geophysics*, 114, 309-318.

Sabinus, I., Oga I. A., Abdulsalam N. N., & Onuoha M. K. (2018). Improved Mapping of the Structural Disposition of some Younger Granite Ring Complexes of Nigeria Using HRAD. *Journal of Geology and Geophysics,* 7(1), 443.

Saibi, H., Aboud, E. & Gottsmann, J. (2015). Curie Point Depth from Spectral Analysis of Aeromagnetic Data for Geothermal Reconnaissance in Afghanistan. *Journal of African Earth Sciences*, 11, 92-99.

Salako, K. A. & Udensi, E. E. (2013). Spectral Depth Analysis of Parts of Upper Benue Trough and Borno Basin, NorthEast Nigeria, Using Aeromagnetic Data. *International Journal of Science and Research* (IJSR), 2(8), 2319-7064.

Salako, K. A., Adetona, A. A., Rafiu, A. A., Alahassan, U. D., Aliyu, A. and Adewumi, T. (2020). Assessment of Geothermal Potential of Parts of Middle Benue Trough, North-East Nigeria. *Journal of the Earth and Space Physics*, 45(4), 27-42.

Saleh, M. B., Babale, S. I. & Terrang, S. U. (2019). Petrographic and Sediment Logical Studies of Bima Sandstone and Out Cropped at Lokoro Area, Yola Arm of the Benue Trough, North-eastern Nigeria. *International Journal of Science and Technoledge*, 7 (6), 38-41.

Salem, A., Green, C., Ravat, D., Singh, K. H., East, P., Fairhead, J. D., Mogre, S., Biegert, E. (2014). Depth to Curie Temperature across the Central Red Sea from Magnetic Data using the De-Fractal Method. *Tectonophysics*, 624(625), 75–86.

Seiyaboh, E. I. & Izah S. C. (2017a). A Review of the Impacts of Gas Flaring in Vegetation and Water Resources in the Niger Delta Region of Nigeria. *International Journal of Economy Energy and Environment,* 2(24), 48-55.

Shehu, A. T. & Nwankwo, L. I. (2015). Radiogenic heat production in the crust using high resolution aero radiometric (HRAR) data in parts of Sokoto Basin, *Nigeria. Journal of Science, Technology, Mathematics, and Education,* 11, 120-130.

Shehu, A. T., Olatunji, S. & Lawal, T. O. (2016). Assessment of Geothermal Potential of the Sokoto Basin, Northwestern Nigeria Using Spetral Centroid Analysis of High Resolution Aeromagnetic (HRAM) Data. *Journal of Science, Technology, Mathematics and Education*, 12, 27-36.

Sheu, A. T., Udensi, E. E., Adeniyi, J. O. & Jonah, S. A. (2021). Spectral Analysis of the Magnetic Residual Anomalies over the Upper Sokoto Basin, Nigeria. *Zuma Journal of Pure and Applied Science*, 6(2), 37-49.

Shives, R.B., Charbonneau, B. & Ford, K.L. (1997). The Detection of Potassic Alteration by Gamma-ray Spectrometry-recognition of Alteration Related to Mineralization. In: Gunins AG (ed.). *Proceedings of exploration 97: Fourth Decennial International conference on mineral exploration*, 741–752.

Shuey, R. T., Schellinger, D. K., Tripp, A. C. & Alley, L. B. (1977). Curie Depth Determination from Aeromagnetic Spectra. *Geophysical Journal Royal Astronomical Society*, 50, 75-101.

Spector, A. & Grant, F. S. (1970). Statistical Models for Interpreting Aeromagnetic Data. *Geophysics*, 35(1), 293-302.

Taufiq, S., Okeke F. N., Obiora, D. N. & Ibuot, J. (2020). Assessment of geothermal potential of parts of Sokoto Basin, Northwest Nigeria using aero-radiometric data. *Springer Nature Switzerland AG 2020.* https://doi.org/10.1007/s40808-020-01013-3.

Tanaka, A., Okubo, Y. & Matsubayash, O. (1999). Curie Point Depth Based on Spectral Analysis of the Magnetic Anomaly Data in East and South-East Asia. *Tectonophysics*, 306(3-4), 461-470.

Tarling, D. H. (1983). *Paleomagnetism: Principles and Applications in Geology, Geophysics & Archeology*. London, New York: Chapman & Hall.

Telford, W. M., Geldart, L. P. & Sherif, R. D. (1990). *Applied Geophysics*. Cambridge: Cambridge University Press.

ThinkGeoEnery, (2022). An Overview of Geothermal Resources. Accessed 22nd June, 2023. https://www.thinkgeoenergy.com/geothermal/an-overview-of-geothermal-resources/.

Thompson, T. & Oldfield, F. (1986). *Environmental Magnetism*. Allen and Unwin: London, 1986.

Treitel, S., Clement, W. G. & Kaul, R. K. (1971). The Spectral Determination of Depths to Buried Magnetic Basement Rocks, *Geophys. J. Int.*, 24(4), 415-428.

Tselentis, G. A (1991). An Attempt to Define Curie Depth in Greece from Aeromagnetic and Heat Flow Data, *PAGEOPH,* 136(1), 87-101.

Tsokas, G. N., Hansen, R. O. & Fytikas, M. (1998). Curie Point Depth of the Island of Crete (Greece). *Pure Appl. Geophys.,* 152(4),747–757

Udochukwu, C. B., Akiishi, M. & Tyovenda, A. A. (2019). Estimation of Geothermal Gradient and Heat Flow for Determination of Geothermal Energy Sources In Monguno Area of North Eastern Nigeria. *Journal of Geography, Environment and Earth Science International*, 20(1), 1-8.

USGS (2020). Geysers. United States Geological Survey. Usgs.gov/news/geysers *retrieved March 23, 2020*

USAID (2020). Nigeria Power Generation Capacity. Accessed 3rd March, 2021. https://www.usaid.gov/powerafrica/nigeria.

Usman, O. A., Ezeh, C. C., Omali, O. A., & Chinwuko I. A. (2018). Integration of Aeromagnetic Interpretation and Induced Polarization Methods in Delineating Mineral Deposits and Basement Configuration within Southern Bida Basin, North West Nigeria. *Conference of the Arabian Journal of Geosciences.* CAJG 2018: On significant applications of geophysical methods, pp. 69-71.

Verduzco, B., Fairhead, J. D., Green, C. M. & MacKenzie, C. (2004). New Insight into Magnetic Derivatives for Structural Imaging. *The Leading Edge*, 23(2), 116-119.

Wemegah, D. D., Preko, K., Noye, R. M., Boadi, B., Menyeh, A., Danuor, S. K. & Amenyoh, T. (2015). Geophysical Interpretation of Possible Gold Mineralization Zones in Kyerano, South-western Ghana using Aeromagnetic and Radiometric datasets. *Journal of Geoscience and Environmental Protection*, 3(4), 67-82.

Whiteman, A. J. (1982). *Nigeria: its Petroleum Geology Resources and Potential* (Vol.1). Graham and Trotman, London UK, pp.176-238; Vol. 2.

Wright, J. B. (1976). Origins of the Benue Trough – a critical review. In: Kogbe, C.A. (Ed.). *Geology of Nigeria*. Elizabethan Publication Co., Lagos, pp. 313–318.

Wright, J. B., Hastings, D. A., Jones, W. B. & Williams, H. R. (1985). *Geology and Mineral Resources of West Africa*. George Allen & Unwin (Publishers) Ltd, London UK, pp. 190.

Xi, Y., Wang, Y., Hu, X., Liu, S., Zhao, Y. & Liu, T. (2015). Geothermal Structure Revealed by Curie Isotherm Surface in Guangdong Province. *The Society of Exploration Geophysicists and the Chinese Geophysical Society GEM Chengdu: International Workshop on Gravity, Electrical and Magnetic Methods and Their Applications Chengdu China.*

Xu, Y., Hao, T., Zeyen, H. & Nan, F. (2017). Curie Point Depths in North China Craton Based on Spectral Analysis of Magnetic Anomalies. *Pure Appl. Geophys.*, 174(1), 339-347.

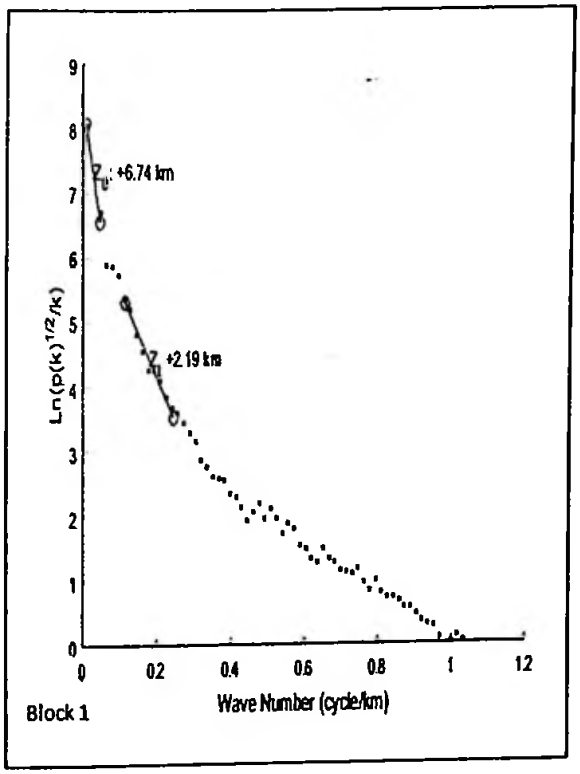
Youssef, M. A. & Elkhodary, S. T. (2013). Utilization of Airborne Gamma-ray Spectrometric Data for Geological Mapping, Radioactive Mineral Exploration and Environmental Monitoring of South-eastern Aswan city, South Eastern Desert, Egypt. *Geophysical Journal International*, 195 (3), 1689-1700.

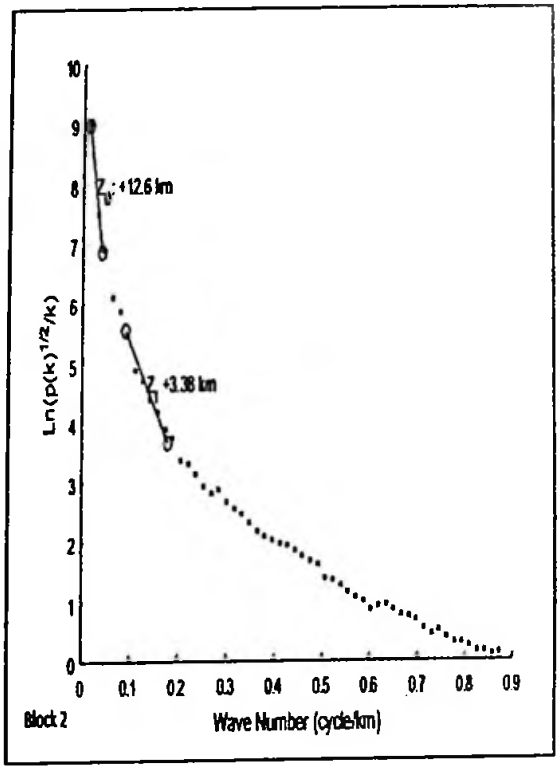
Zaborski, P. M. (1998). A Review of the Cretaceous System in Nigeria. *Afr. Geosci. Rev.*, 5(4) 387.

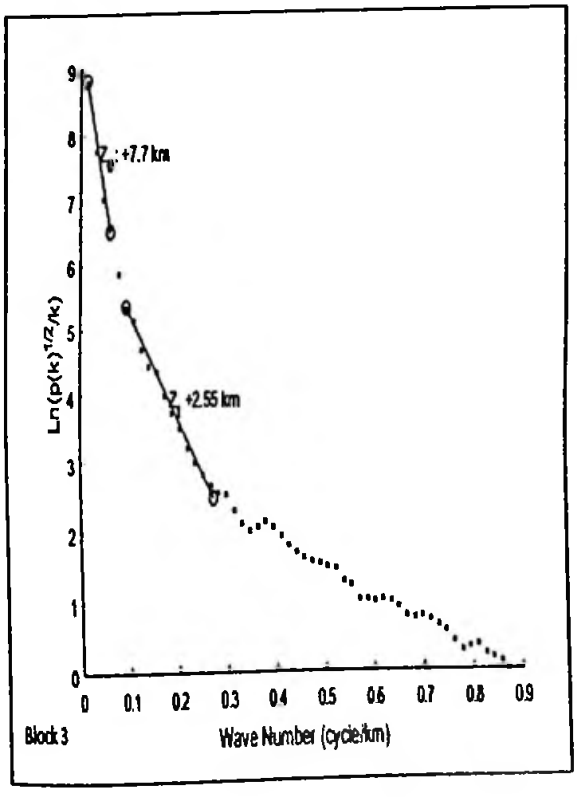
Zhou, S., Huang, D. & Su, C. (2016). Magnetic Anomaly Depth and Structural Index Estimation Using Different Height Analytic Signal Data. *Journal of Applied Geophysics*, 132(1), 146-151.

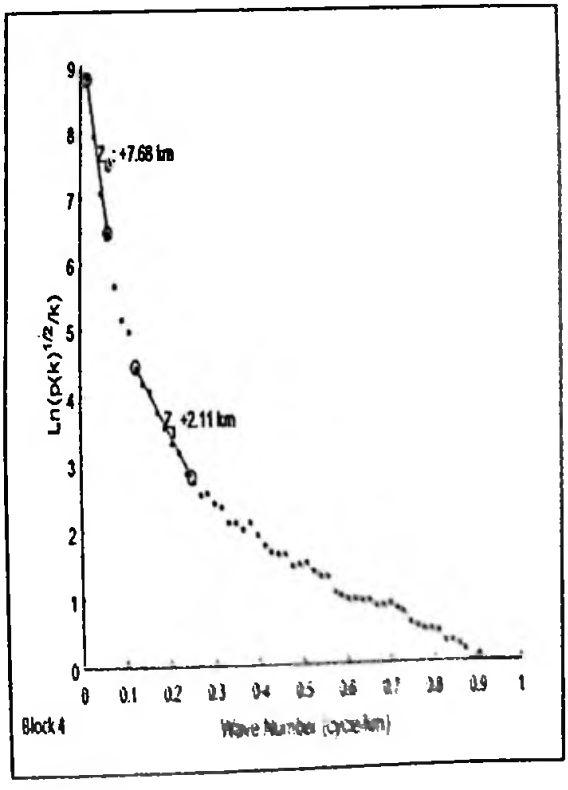
APPENDIX A

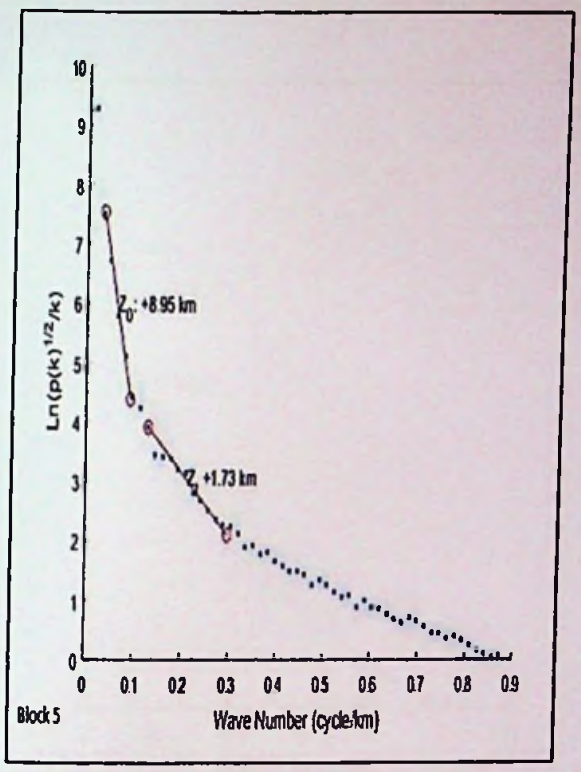
SPECTRAL PLOTS FOR 81 OVERLAPPING BLOCKS (55KM BY 55KM)

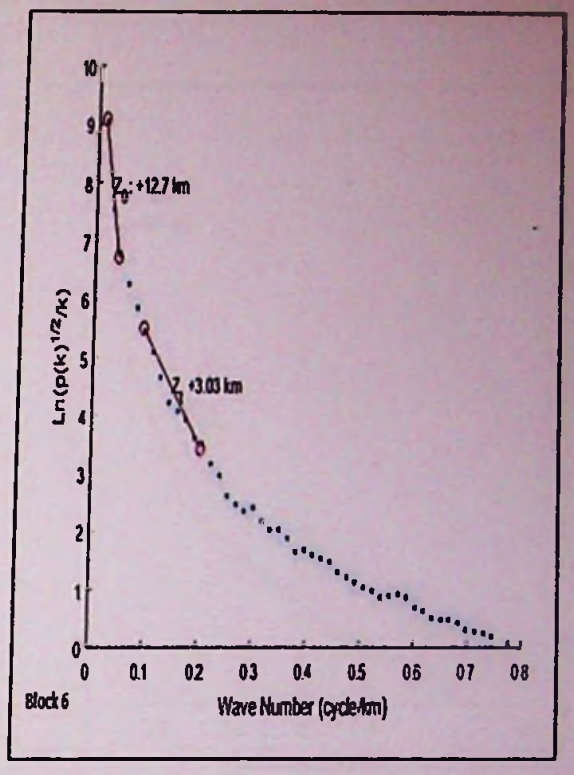


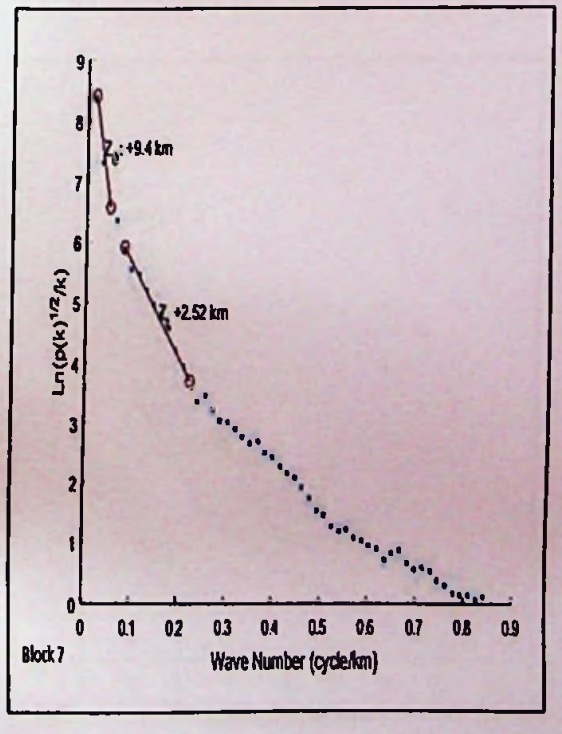


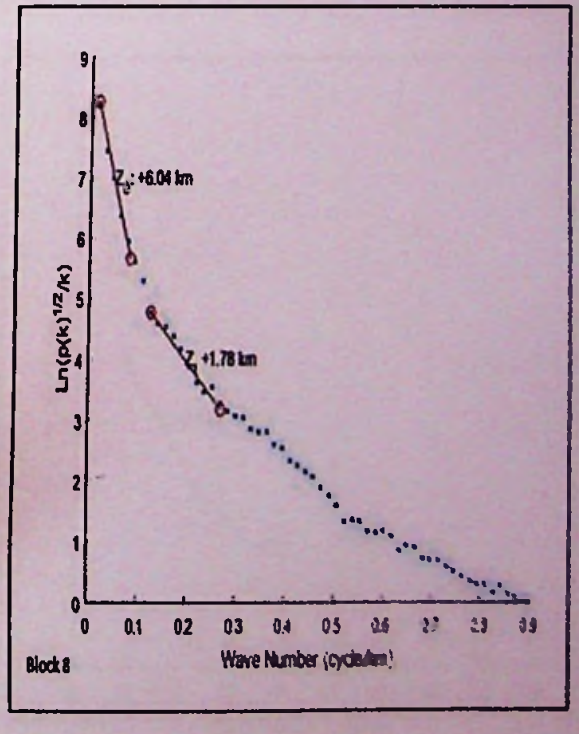


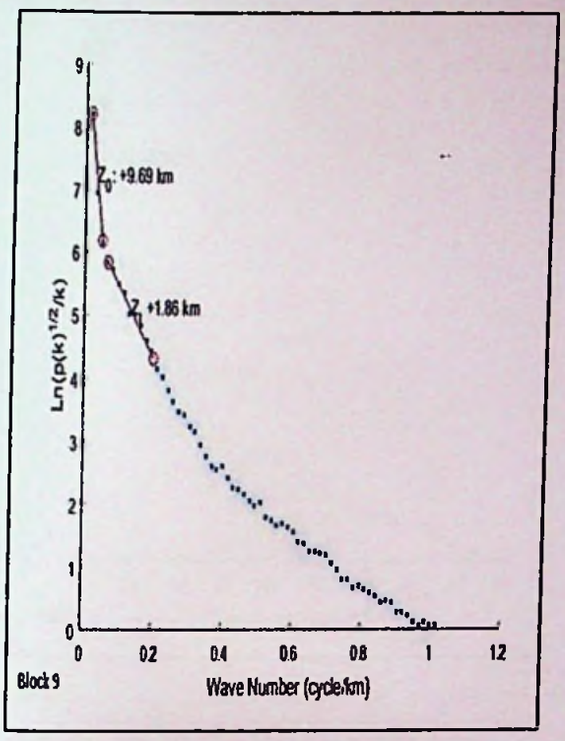


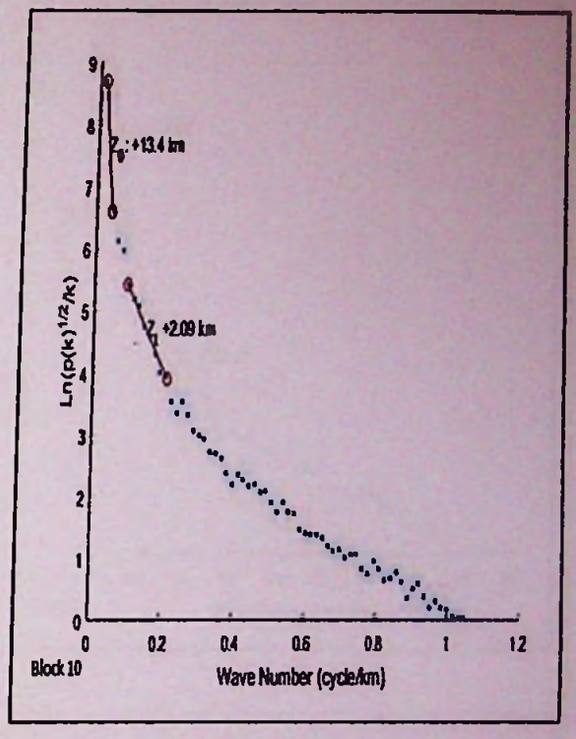

Ln(p(k)^1/2/k)
Z0 : +8.95 km
Z1 +1.73 km
Block 5
Wave Number (cycle/km)

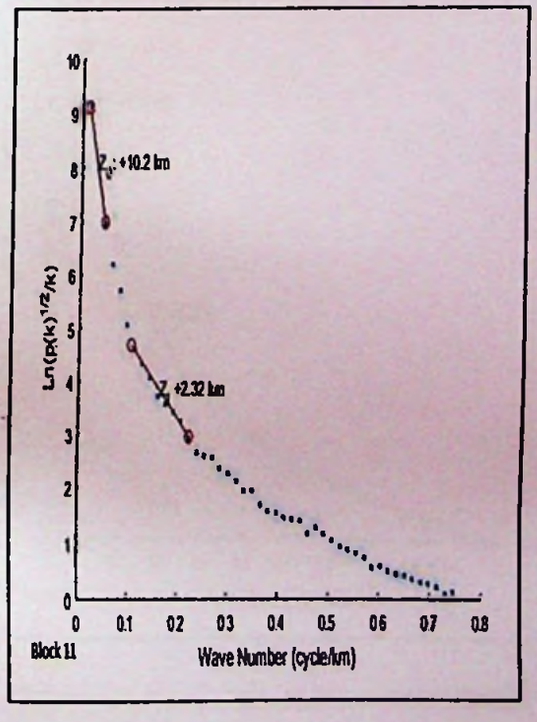

Ln(p(k)^1/2/k)
Z0 : +12.7 km
Z1 +3.03 km
Block 6
Wave Number (cycle/km)

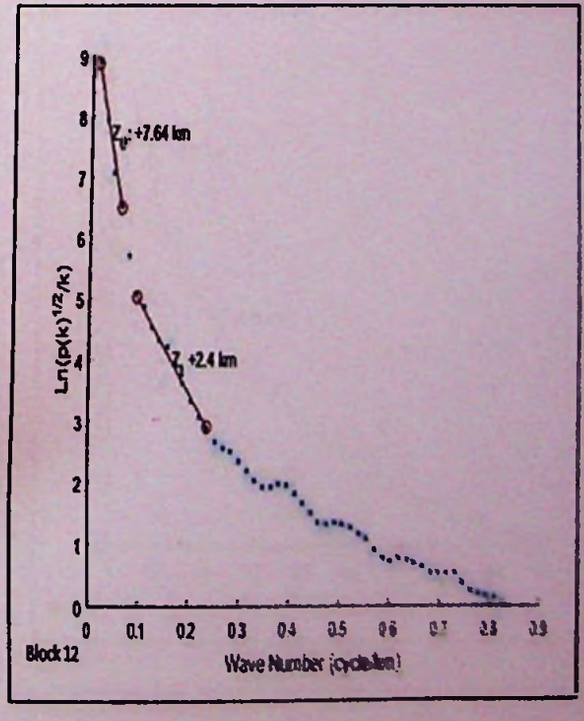

Ln(p(k)^1/2/k)
Z0 : +9.4 km
Z1 +2.52 km
Block 7
Wave Number (cycle/km)

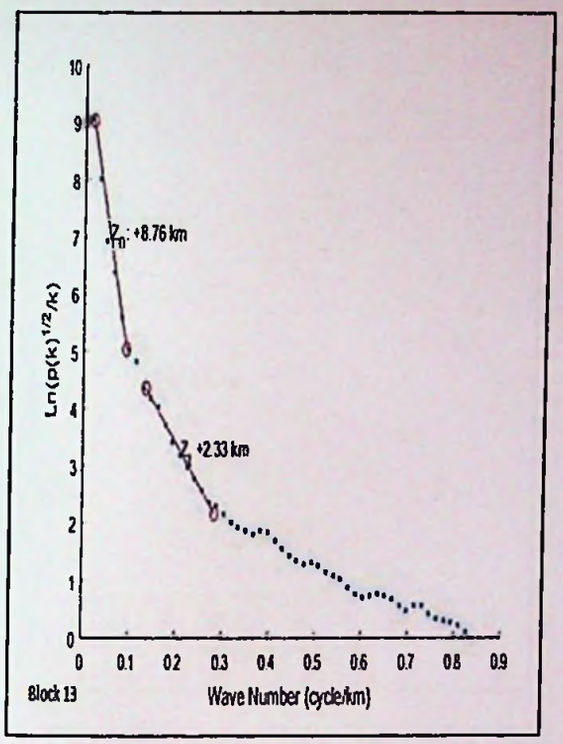

Ln(p(k)^1/2/k)
Z0 : +6.04 km
Z1 +1.78 km
Block 8
Wave Number (cycle/km)

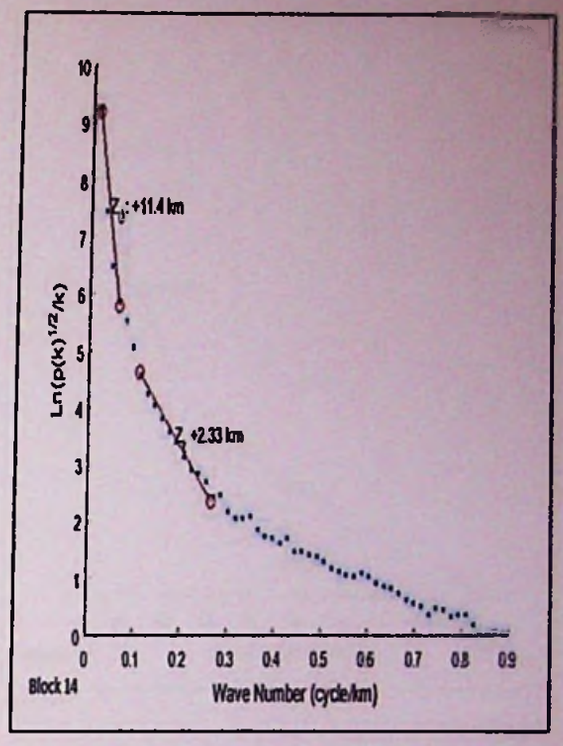

Z0 : +9.69 km
Z : +1.86 km
Ln(p(k)^1/2/k)
Wave Number (cycle/km)
Block 9

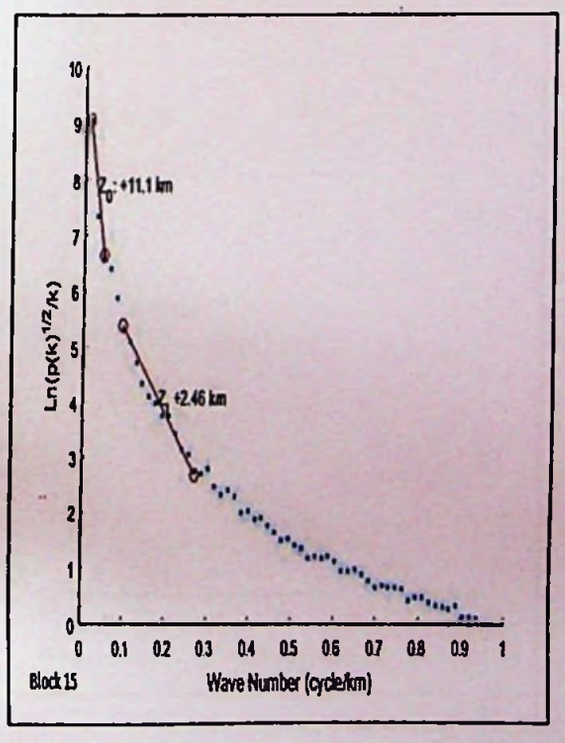

Z0 : +13.4 km
Z : +2.09 km
Ln(p(k)^1/2/k)
Wave Number (cycle/km)
Block 10

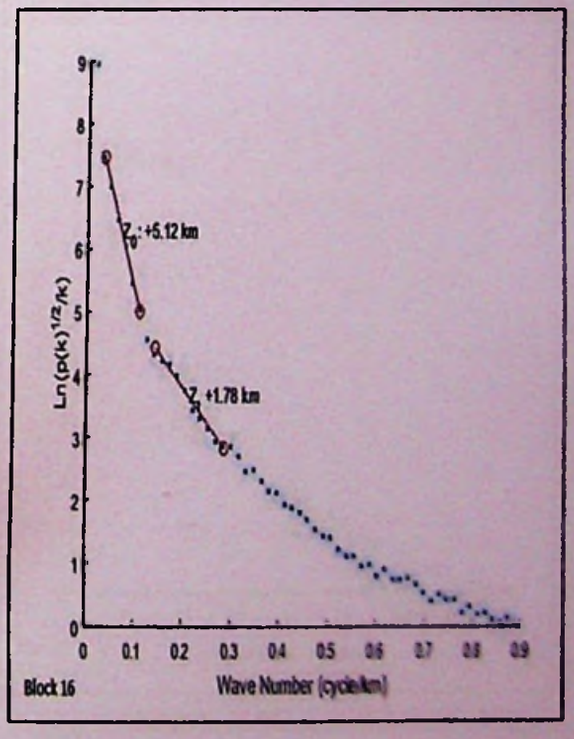

Z0 : +10.2 km
Z : +2.32 km
Ln(p(k)^1/2/k)
Wave Number (cycle/km)
Block 11

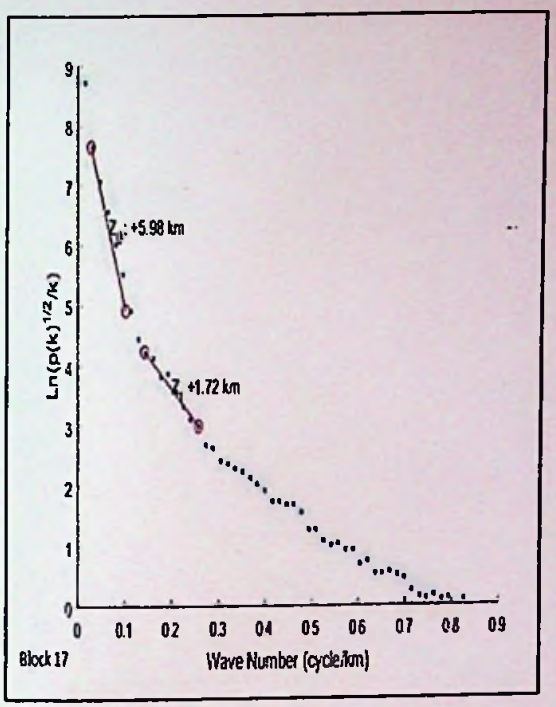

Z0 : +7.64 km
Z : +2.4 km
Ln(p(k)^1/2/k)
Wave Number (cycle/km)
Block 12

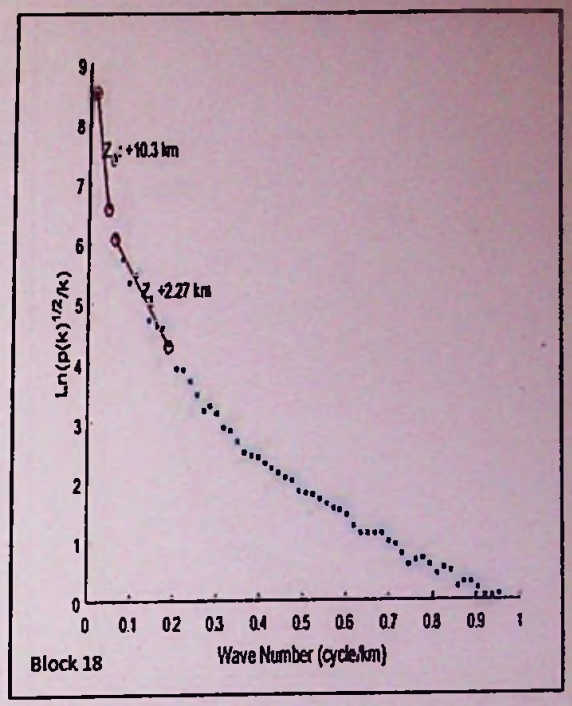

Ln(p(k)^1/2/k)
Z0 : +8.76 km
Z : +2.33 km
Block 13
Wave Number (cycle/km)

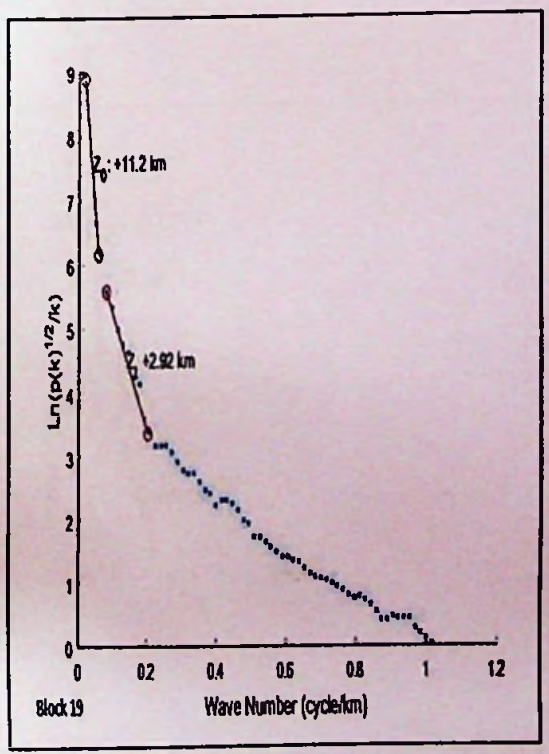

Ln(p(k)^1/2/k)
Z0 : +11.4 km
Z : +2.33 km
Block 14
Wave Number (cycle/km)

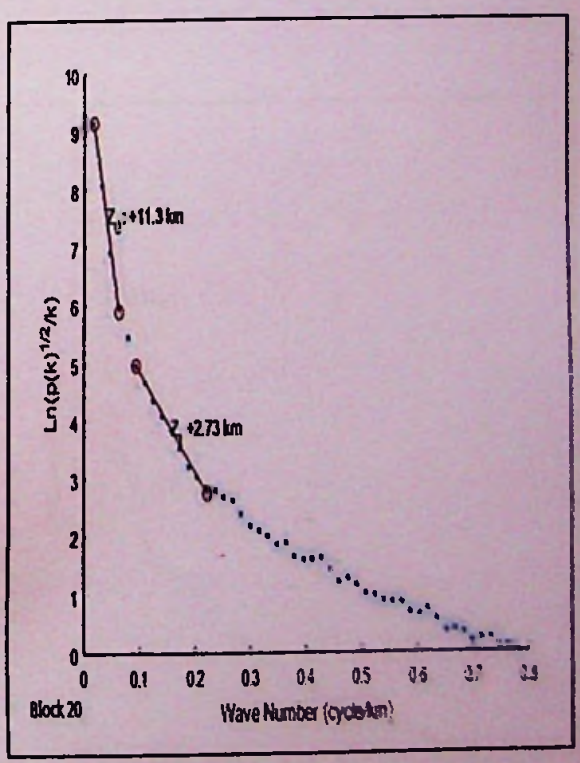

Ln(p(k)^1/2/k)
Z0 : +11.1 km
Z : +2.46 km
Block 15
Wave Number (cycle/km)

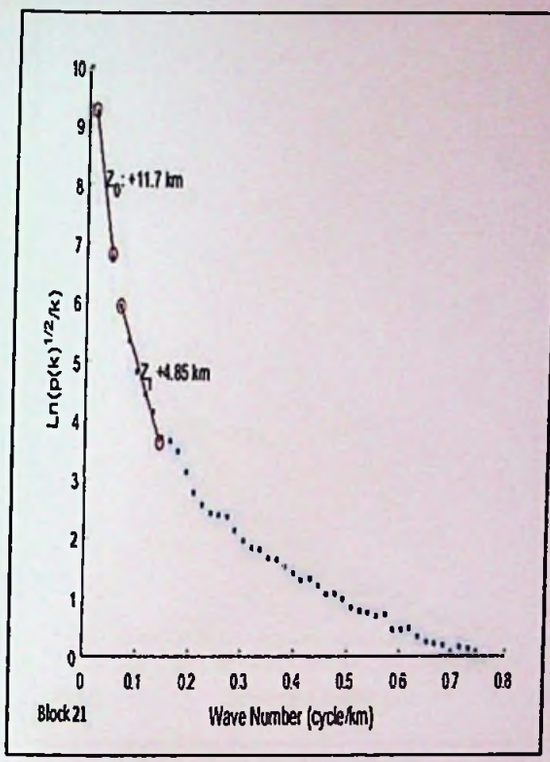

Ln(p(k)^1/2/k)
Z0 : +5.12 km
Z : +1.78 km
Block 16
Wave Number (cycle/km)

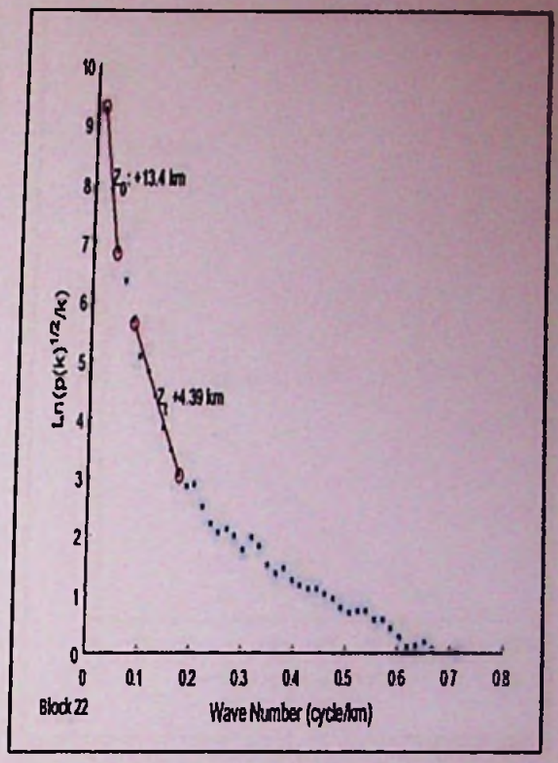

Ln(p(k)^1/2/k)
Z0 : +5.98 km
Z1 : +1.72 km
Block 17
Wave Number (cycle/km)

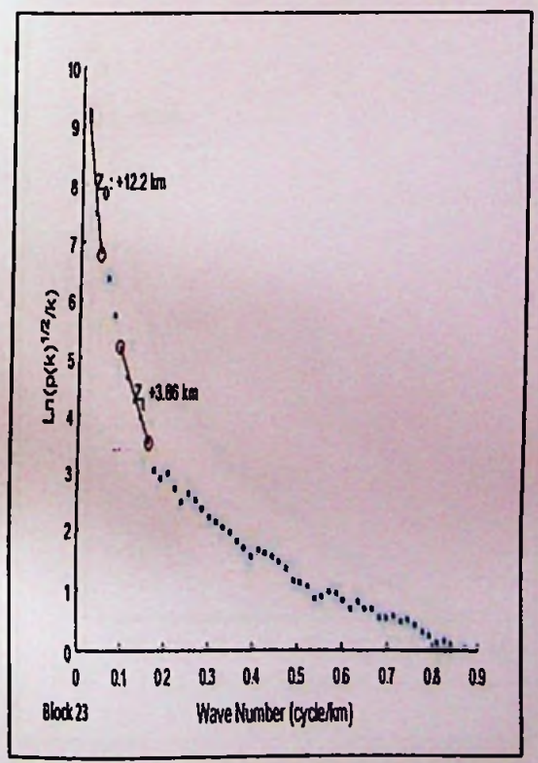

Ln(p(k)^1/2/k)
Z0 : +10.3 km
Z1 : +2.27 km
Block 18
Wave Number (cycle/km)

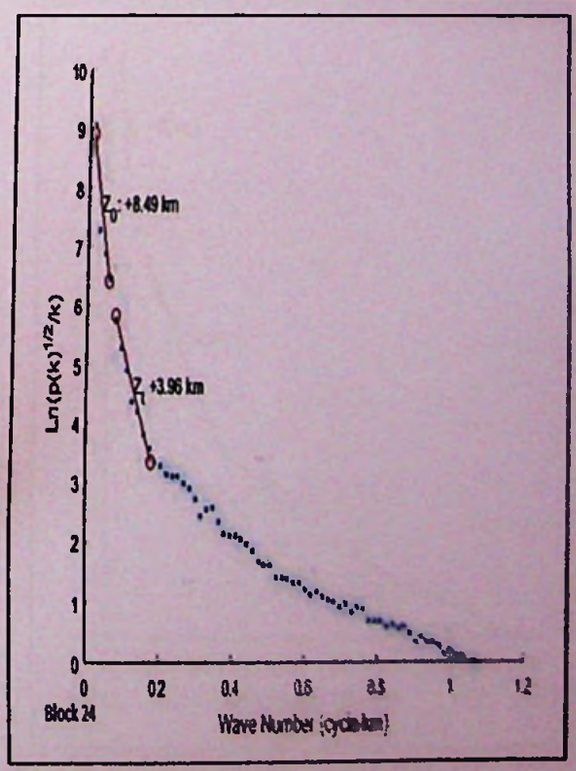

Ln(p(k)^1/2/k)
Z0 : +11.2 km
Z1 : +2.92 km
Block 19
Wave Number (cycle/km)

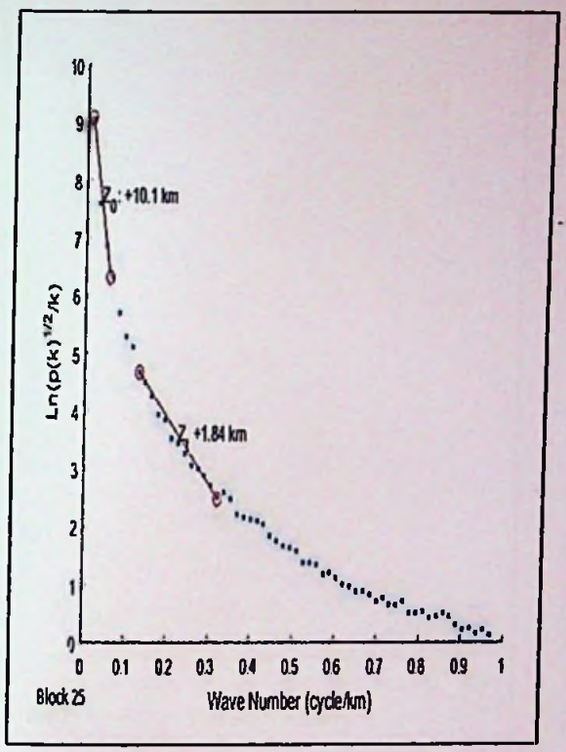

Ln(p(k)^1/2/k)
Z0 : +11.3 km
Z1 : +2.73 km
Block 20
Wave Number (cycle/km)

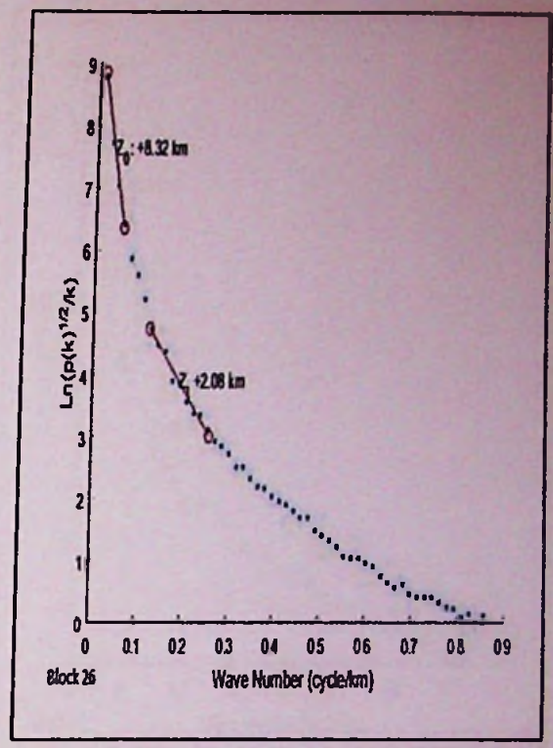

Ln(p(k)^1/2/k)
Z0 : +11.7 km
Z1 +4.85 km
Block 21
Wave Number (cycle/km)

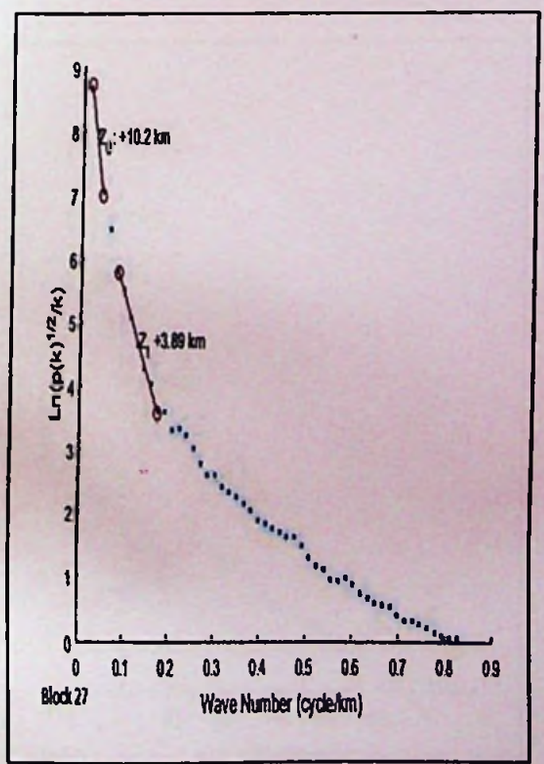

Ln(p(k)^1/2/k)
Z0 : +13.4 km
Z1 +4.39 km
Block 22
Wave Number (cycle/km)

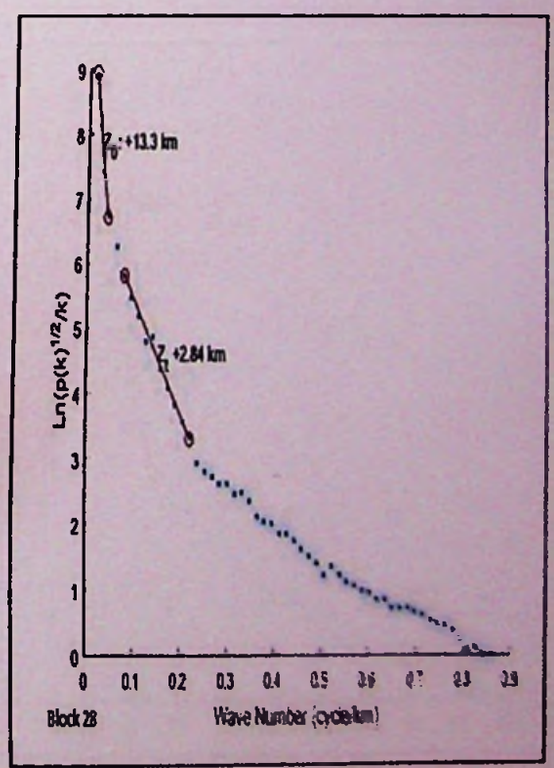

Ln(p(k)^1/2/k)
Z0 : +12.2 km
Z1 +3.86 km
Block 23
Wave Number (cycle/km)

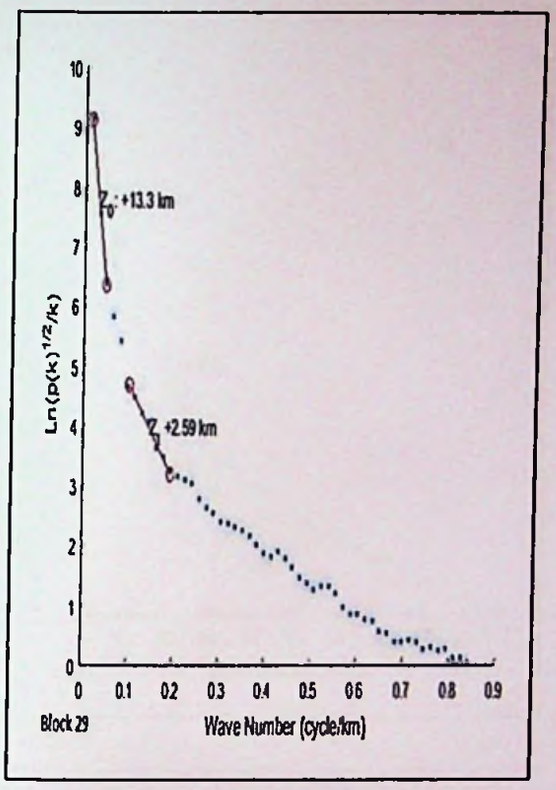

Ln(p(k)^1/2/k)
Z0 : +8.49 km
Z1 +3.96 km
Block 24
Wave Number (cycle/km)

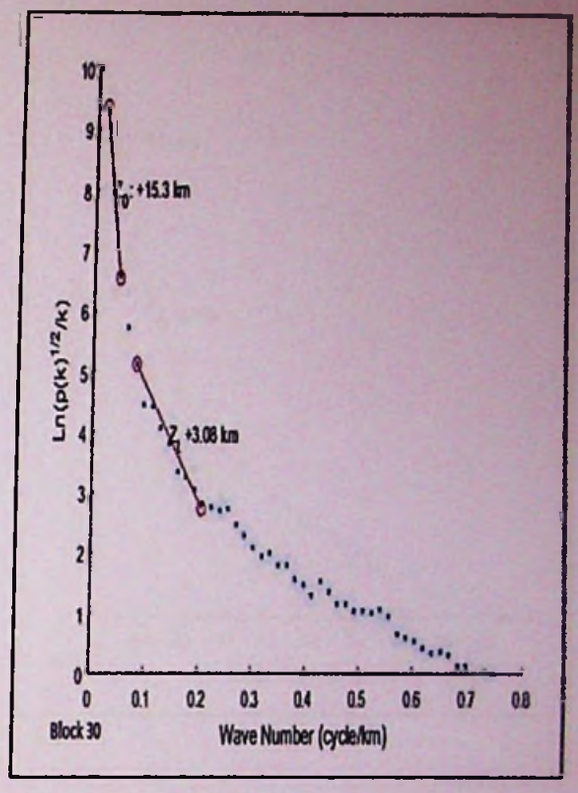

Ln(p(k)^1/2/k)
Z0 : +10.1 km
Z1 : +1.84 km
Block 25
Wave Number (cycle/km)

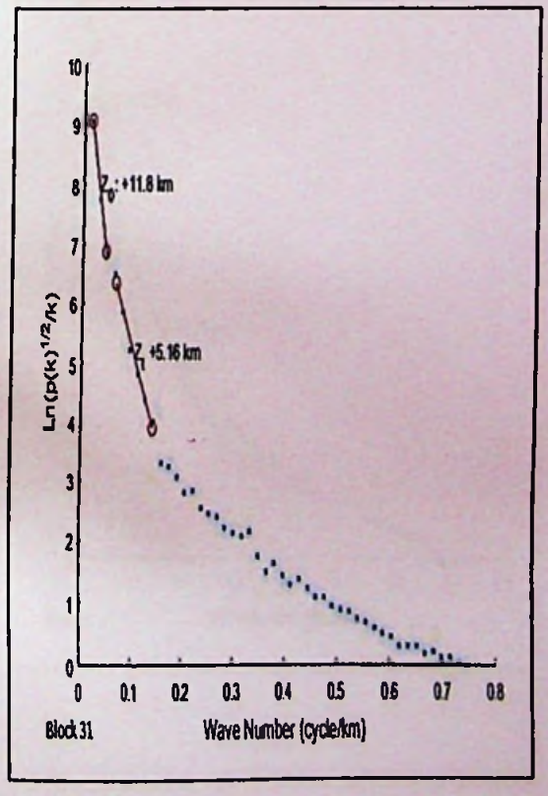

Ln(p(k)^1/2/k)
Z0 : +8.32 km
Z1 : +2.08 km
Block 26
Wave Number (cycle/km)

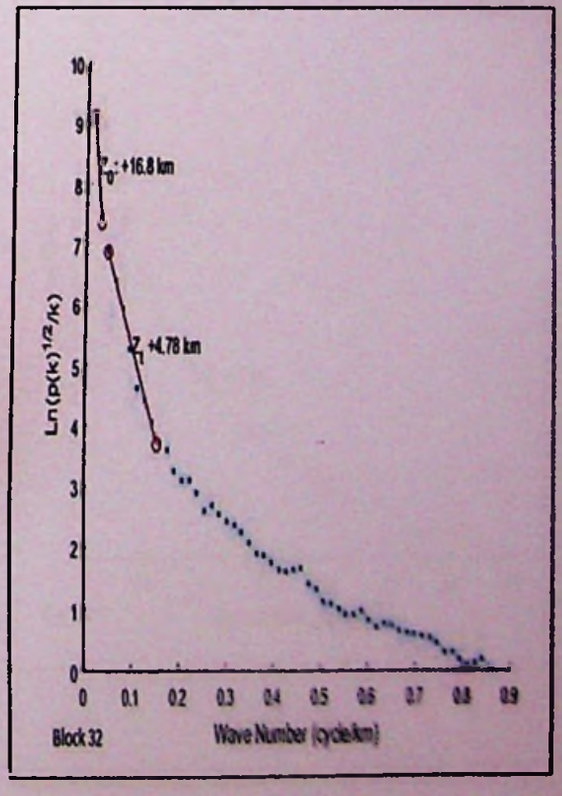

Ln(p(k)^1/2/k)
Z0 : +10.2 km
Z1 : +3.89 km
Block 27
Wave Number (cycle/km)

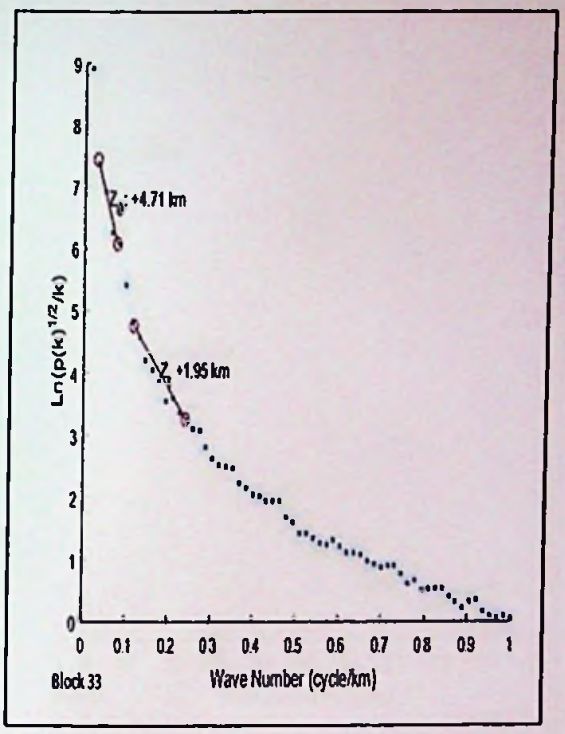

Ln(p(k)^1/2/k)
Z0 : +13.3 km
Z1 : +2.84 km
Block 28
Wave Number (cycle/km)

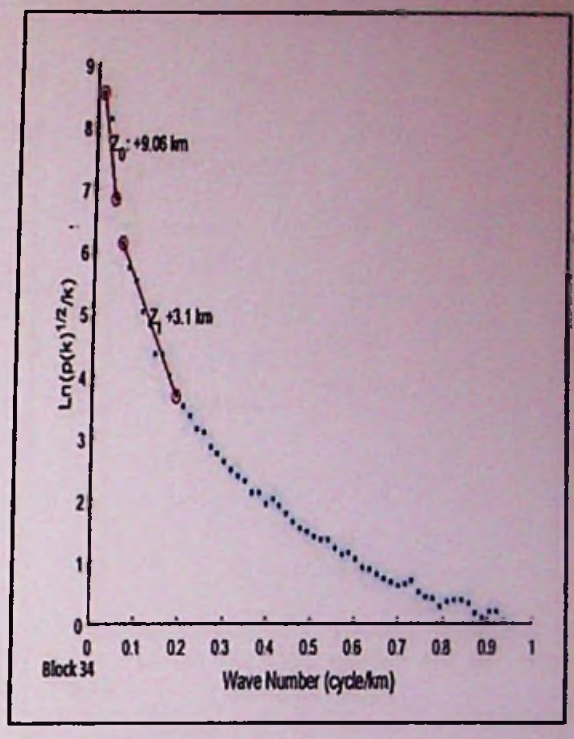

Ln(p(k)^1/2/k)
Z0 : +13.3 km
Z1 +2.59 km
Block 29
Wave Number (cycle/km)

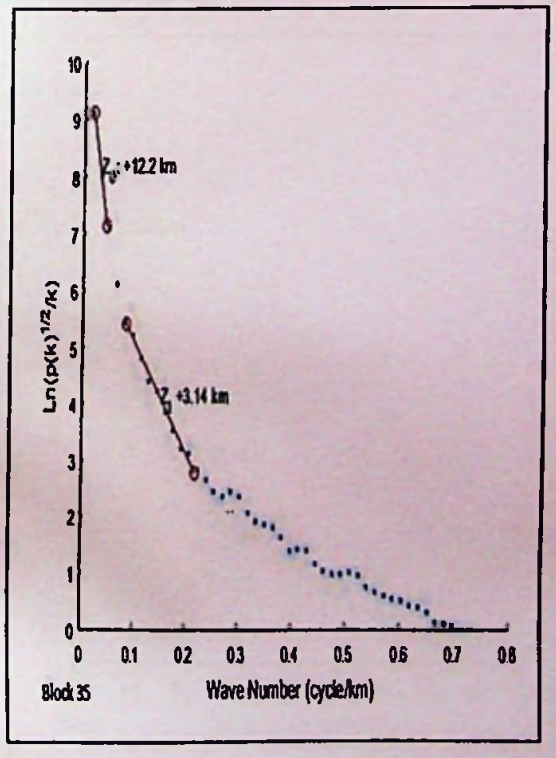

Ln(p(k)^1/2/k)
Z0 : +15.3 km
Z1 +3.08 km
Block 30
Wave Number (cycle/km)

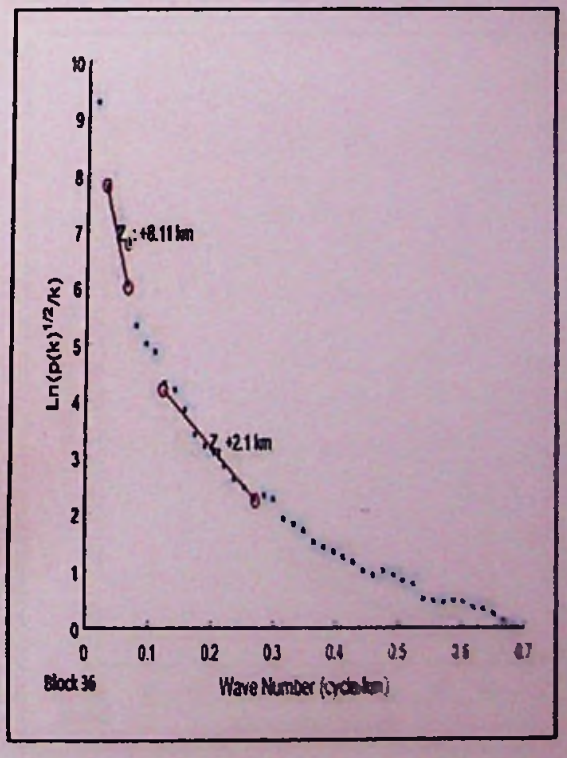

Ln(p(k)^1/2/k)
Z0 : +11.8 km
Z1 +5.16 km
Block 31
Wave Number (cycle/km)

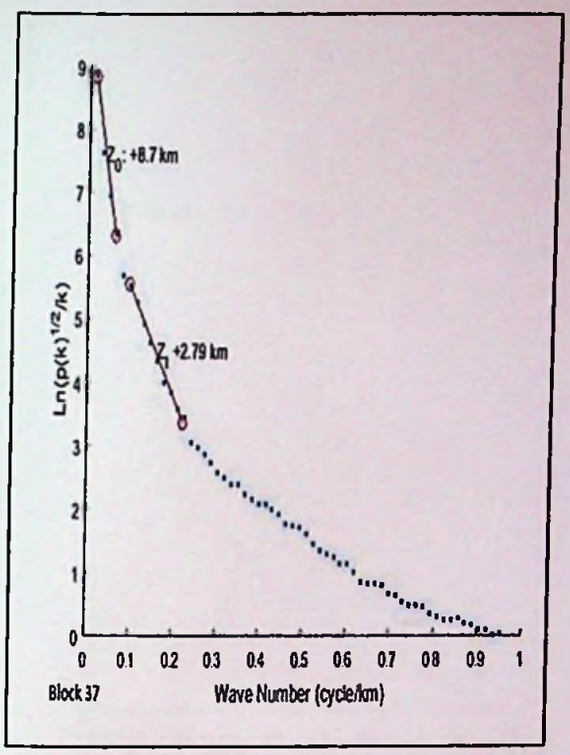

Ln(p(k)^1/2/k)
Z0 : +16.8 km
Z1 +4.78 km
Block 32
Wave Number (cycle/km)

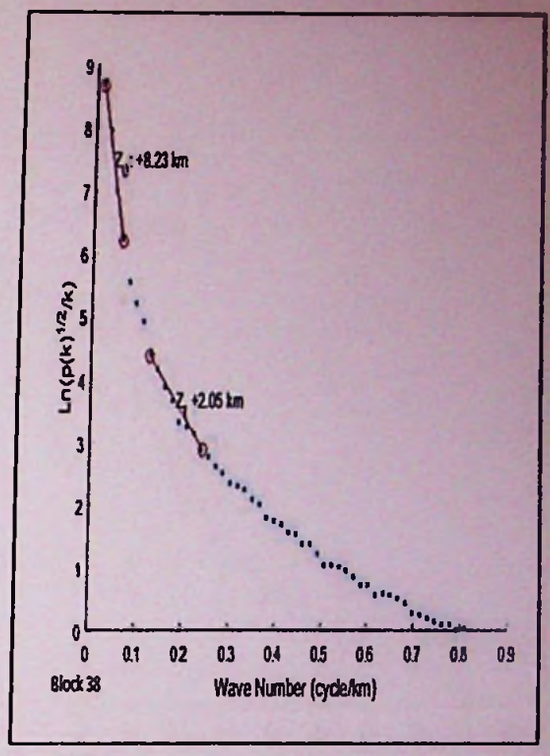

Ln(p(k)^1/2/k)
Z0 : +4.71 km
Z1 +1.95 km
Block 33
Wave Number (cycle/km)

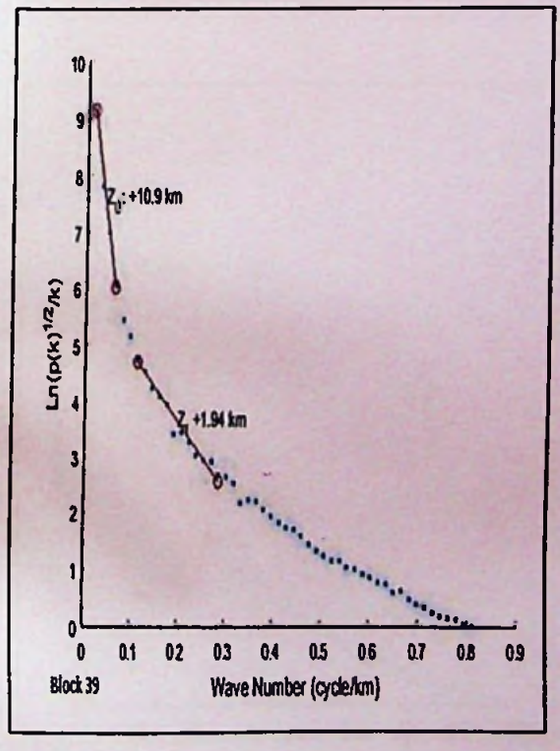

Ln(p(k)^1/2/k)
Z0 : +9.06 km
Z1 +3.1 km
Block 34
Wave Number (cycle/km)

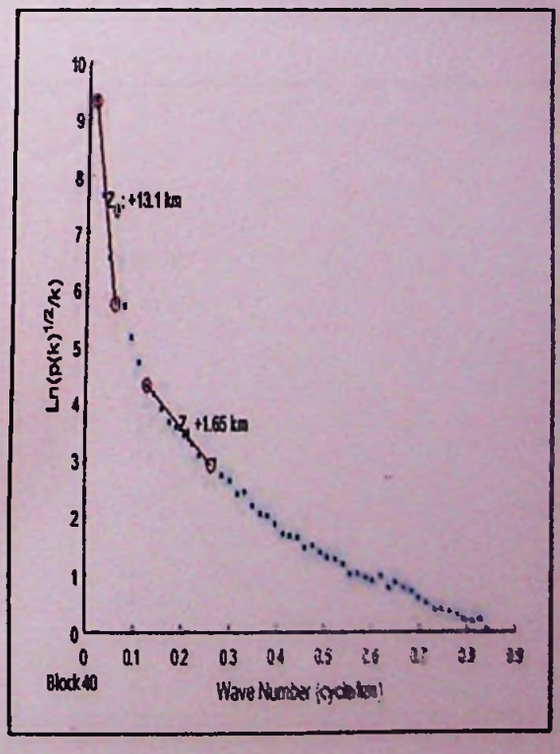

Ln(p(k)^1/2/k)
Z0 : +12.2 km
Z1 +3.14 km
Block 35
Wave Number (cycle/km)

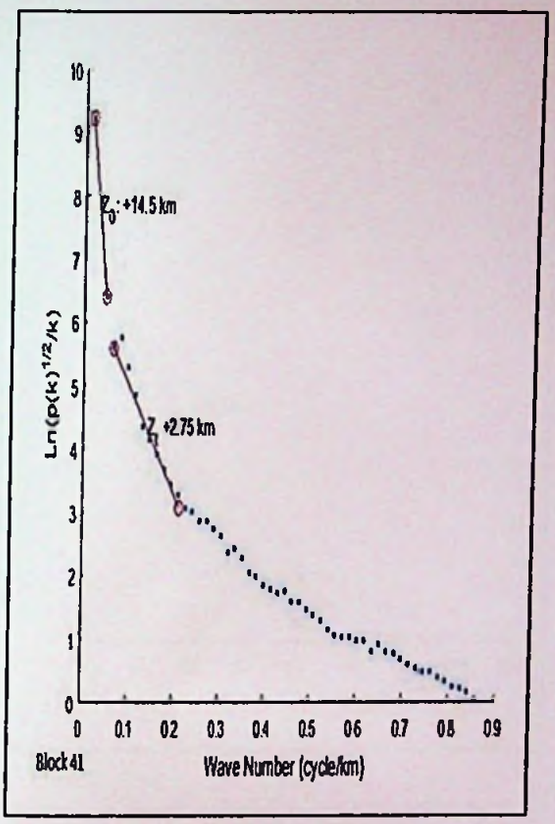

Ln(p(k)^1/2/k)
Z0 : +8.11 km
Z1 +2.1 km
Block 36
Wave Number (cycle/km)

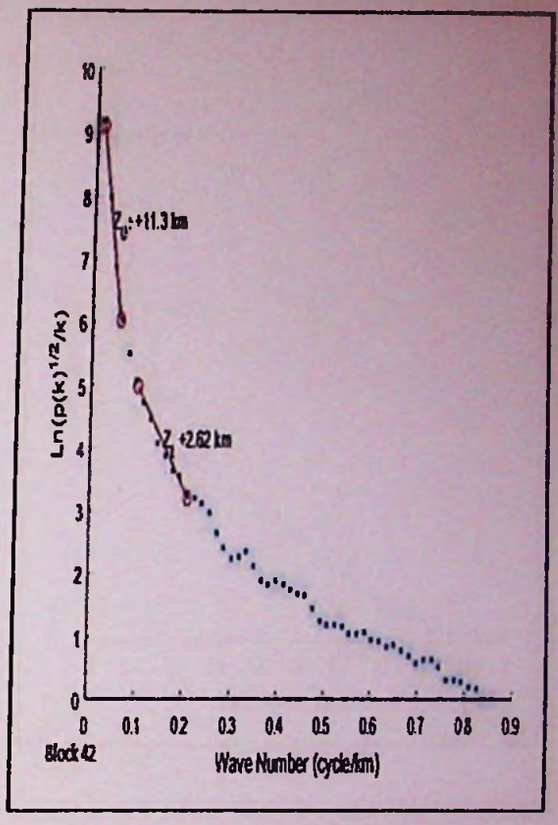

Z0 : +8.7 km
Z1 +2.79 km
Ln(p(k)^1/2/k)
Wave Number (cycle/km)
Block 37

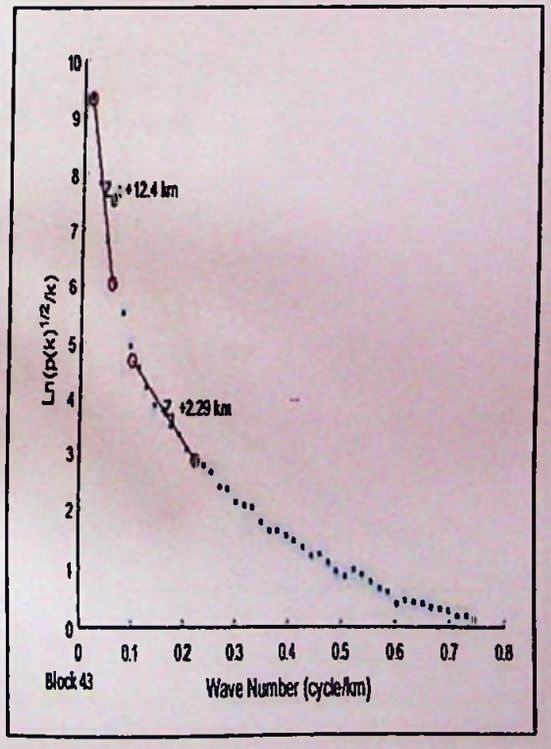

Z0 : +8.23 km
Z1 +2.05 km
Ln(p(k)^1/2/k)
Wave Number (cycle/km)
Block 38

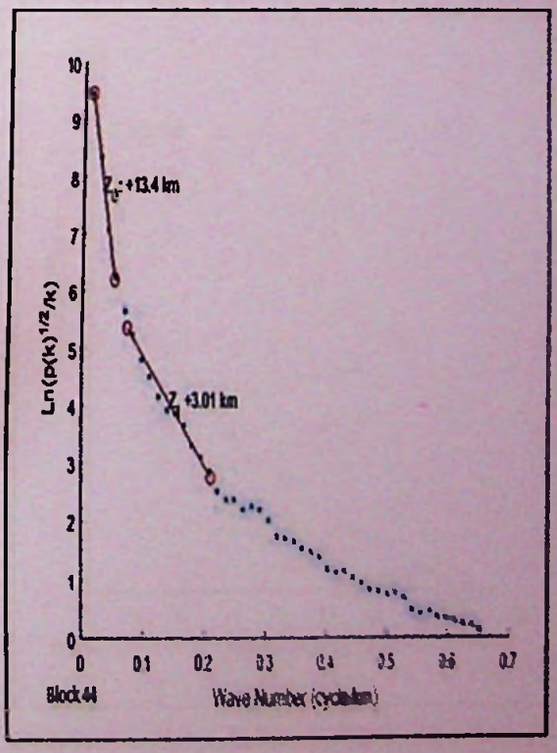

Z0 : +10.9 km
Z1 +1.94 km
Ln(p(k)^1/2/k)
Wave Number (cycle/km)
Block 39

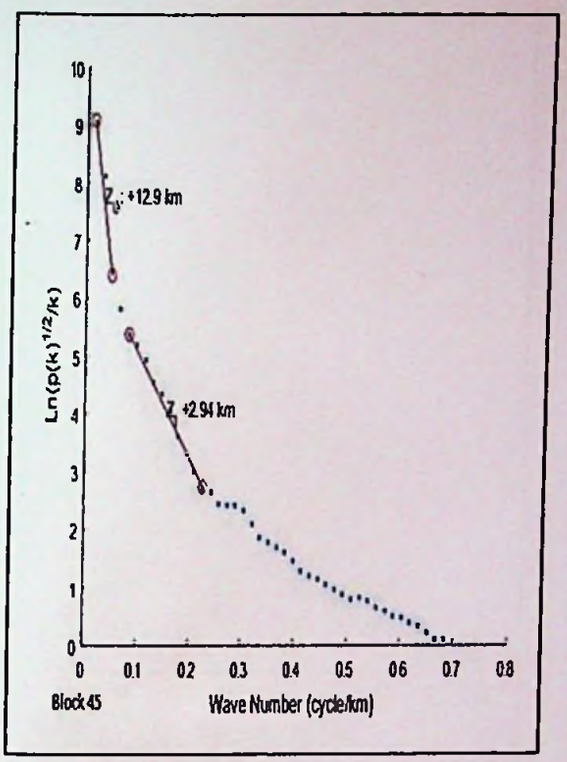

Z0 : +13.1 km
Z1 +1.65 km
Ln(p(k)^1/2/k)
Wave Number (cycle/km)
Block 40

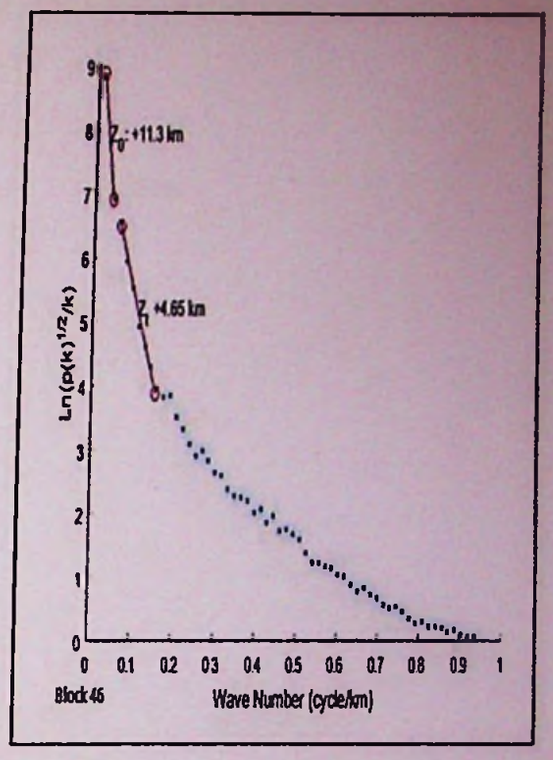

Ln(p(k)^1/2/k)
Z0 : +14.5 km
Z1 +2.75 km
Block 41
Wave Number (cycle/km)

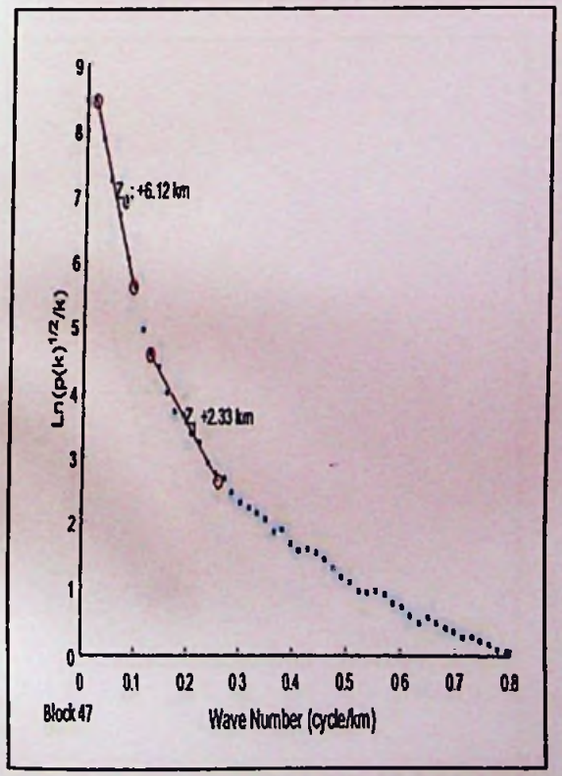

Ln(p(k)^1/2/k)
Z0 : +11.3 km
Z1 +2.62 km
Block 42
Wave Number (cycle/km)

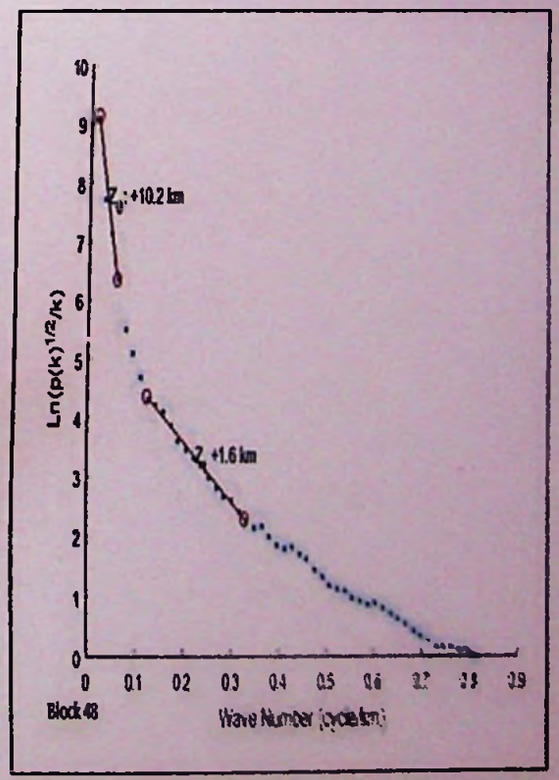

Ln(p(k)^1/2/k)
Z0 : +12.4 km
Z1 +2.29 km
Block 43
Wave Number (cycle/km)

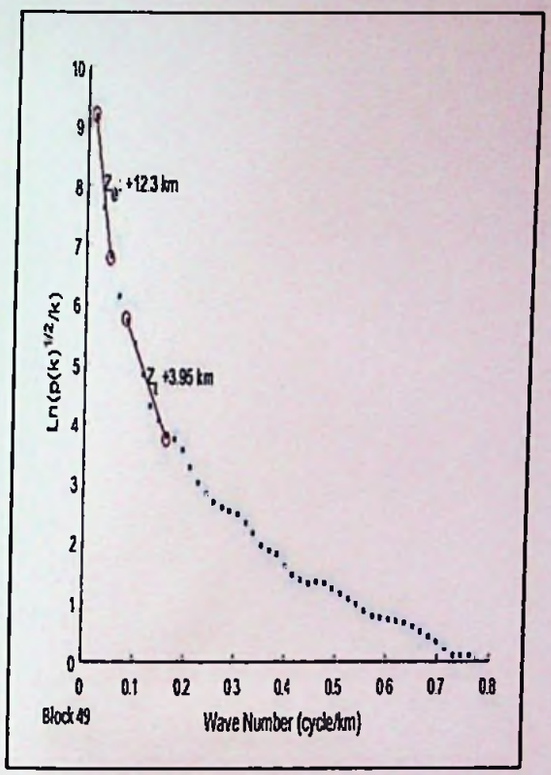

Ln(p(k)^1/2/k)
Z0 : +13.4 km
Z1 +3.01 km
Block 44
Wave Number (cycle/km)

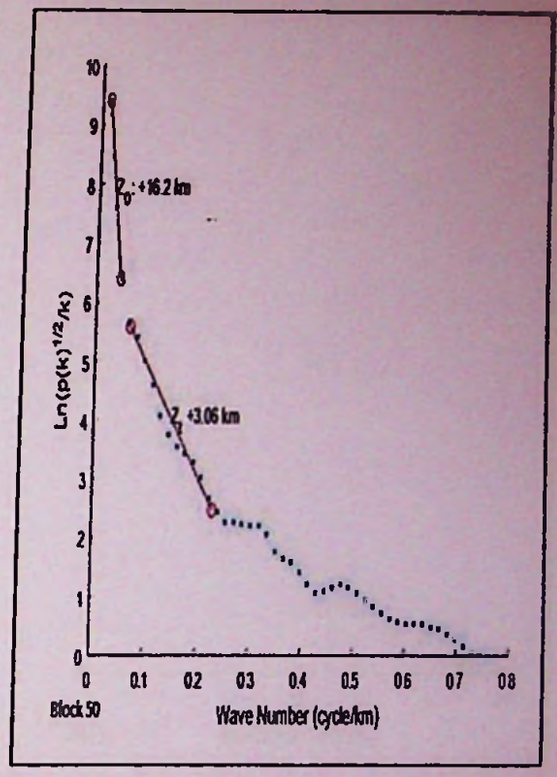

Ln(p(k)^1/2/k)
Z0 : +12.9 km
Z : +2.94 km
Block 45
Wave Number (cycle/km)

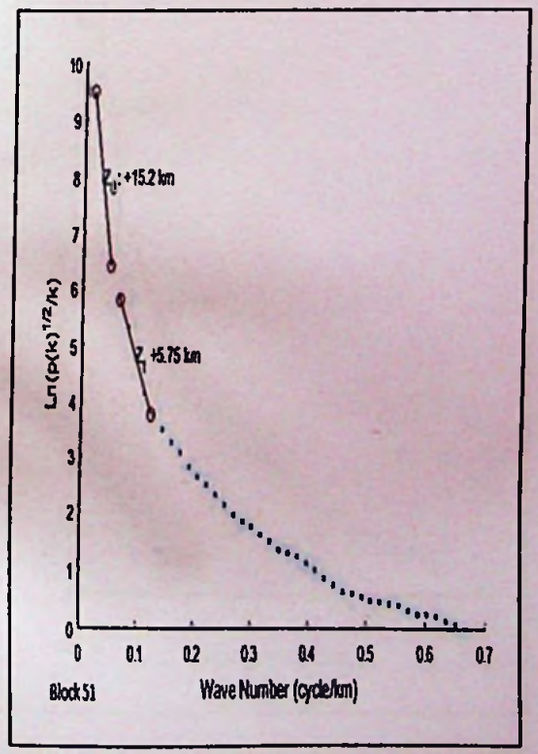

Ln(p(k)^1/2/k)
Z0 : +11.3 km
Z : +4.65 km
Block 46
Wave Number (cycle/km)

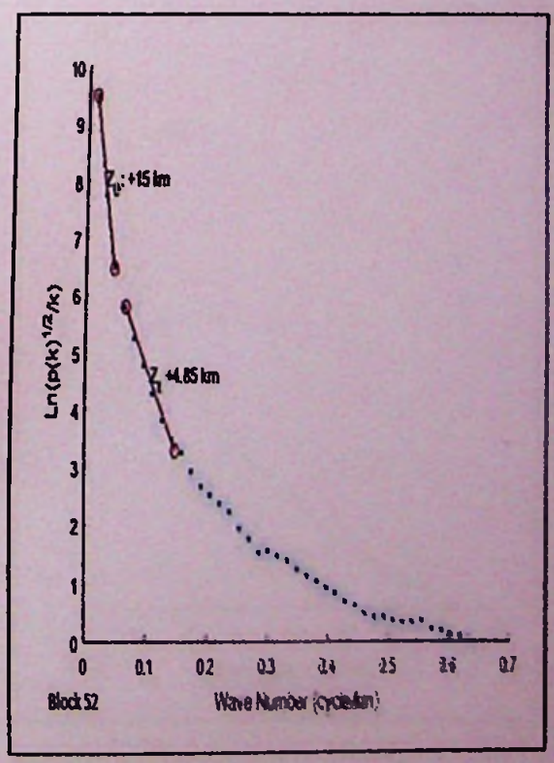

Ln(p(k)^1/2/k)
Z0 : +6.12 km
Z : +2.33 km
Block 47
Wave Number (cycle/km)

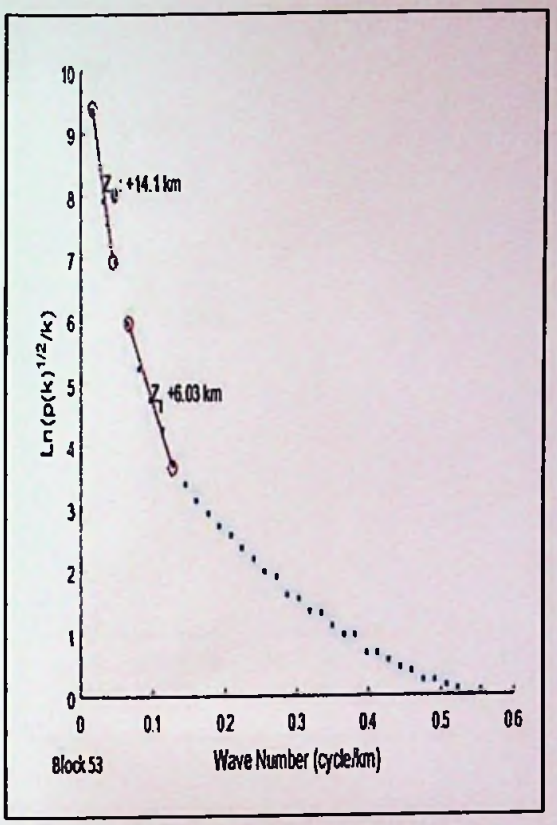

Ln(p(k)^1/2/k)
Z0 : +10.2 km
Z : +1.6 km
Block 48
Wave Number (cycle/km)

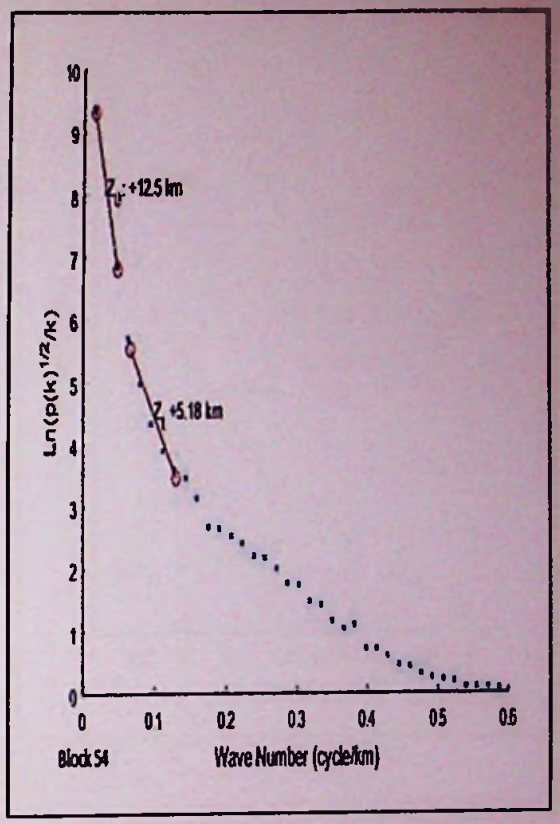

Ln(p(k)^1/2/k)
Z0 : +12.3 km
Z1 +3.95 km
Block 49
Wave Number (cycle/km)

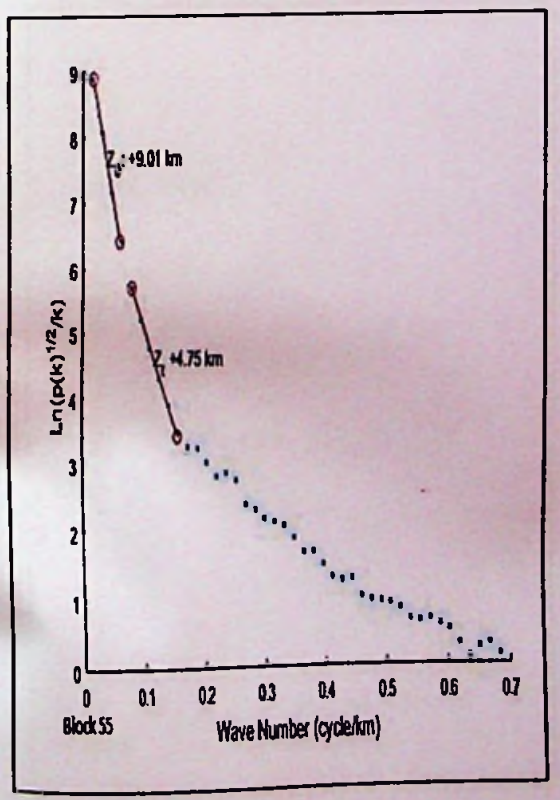

Ln(p(k)^1/2/k)
Z0 : +16.2 km
Z1 +3.06 km
Block 50
Wave Number (cycle/km)

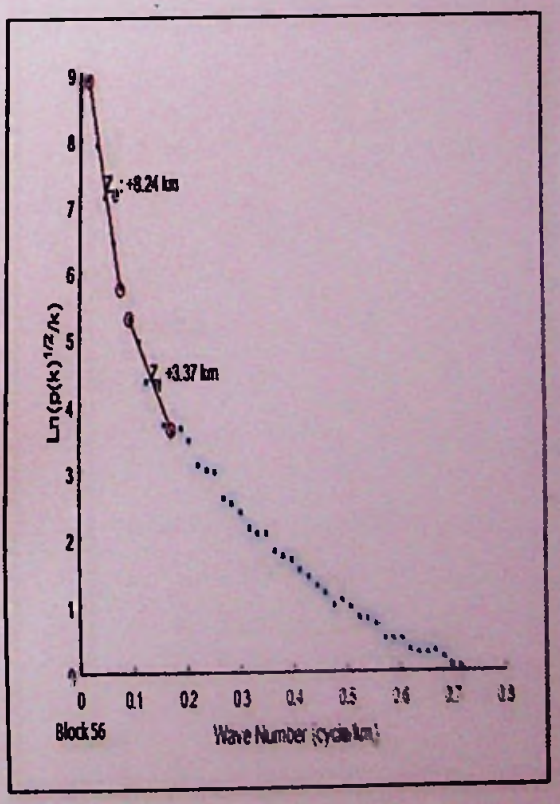

Ln(p(k)^1/2/k)
Z0 : +15.2 km
Z1 +5.75 km
Block 51
Wave Number (cycle/km)

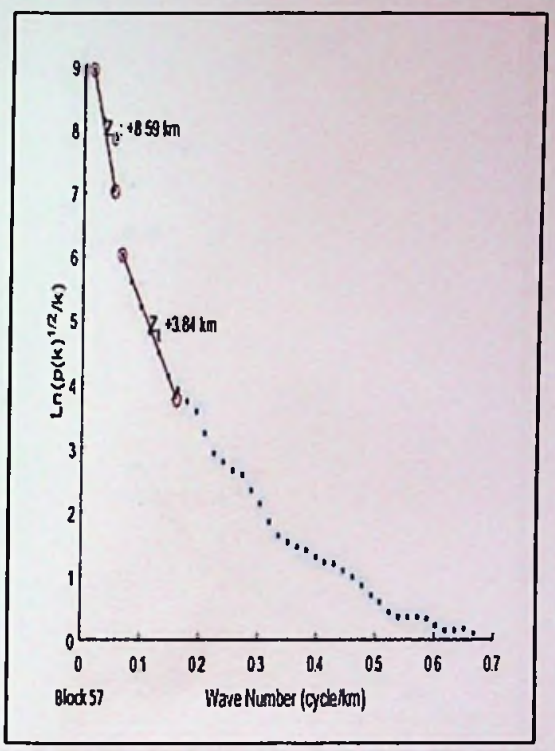

Ln(p(k)^1/2/k)
Z0 : +15 km
Z1 +4.85 km
Block 52
Wave Number (cycle/km)

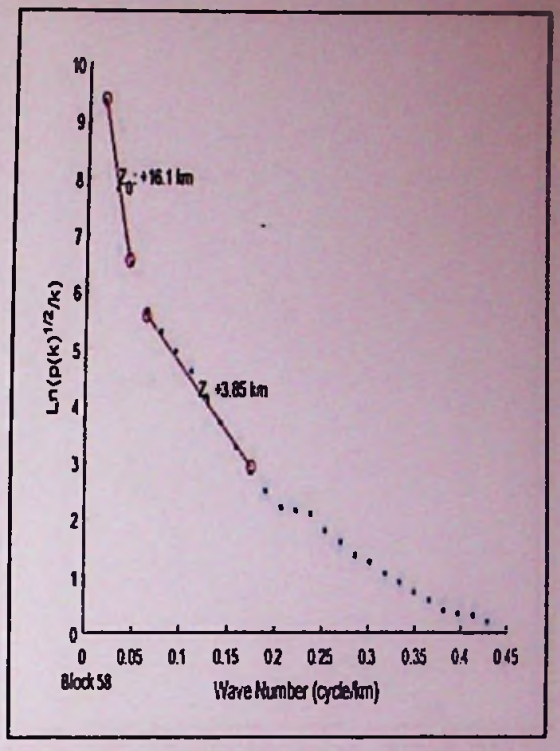

Ln(p(k)^1/2/k)
Z0 : +14.1 km
Z1 +6.03 km
Wave Number (cycle/km)
Block 53

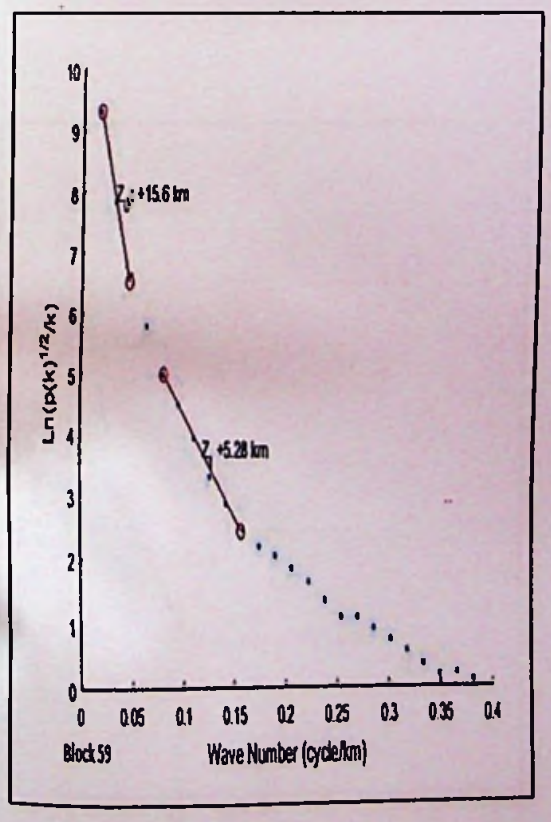

Ln(p(k)^1/2/k)
Z0 : +12.5 km
Z1 +5.18 km
Wave Number (cycle/km)
Block 54

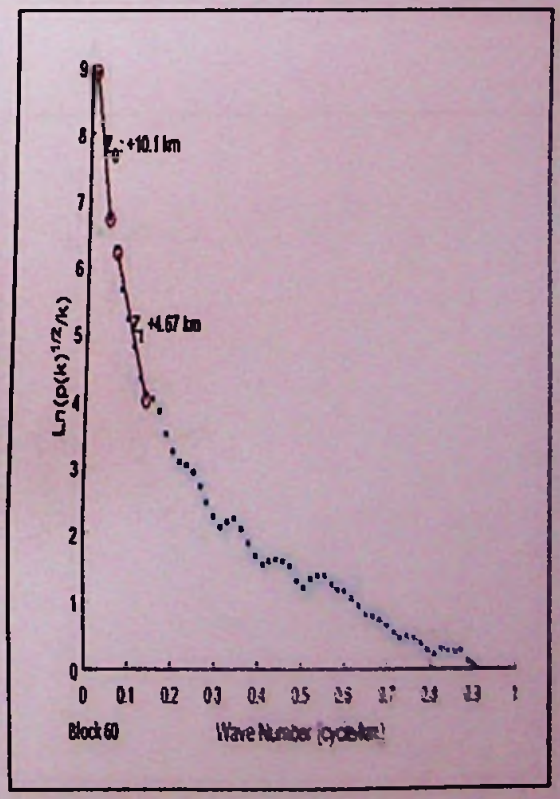

Ln(p(k)^1/2/k)
Z0 : +9.01 km
Z1 +4.75 km
Wave Number (cycle/km)
Block 55

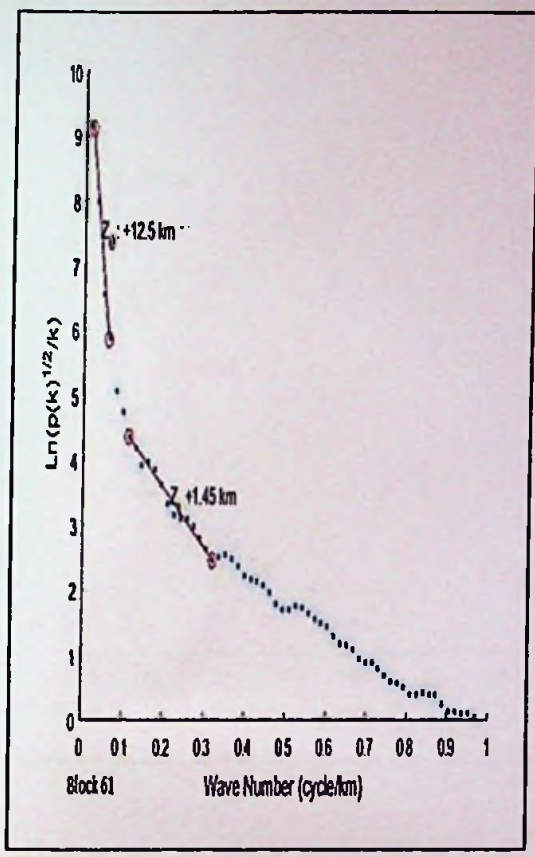

Ln(p(k)^1/2/k)
Z0 : +8.24 km
Z1 +3.37 km
Wave Number (cycle/km)
Block 56

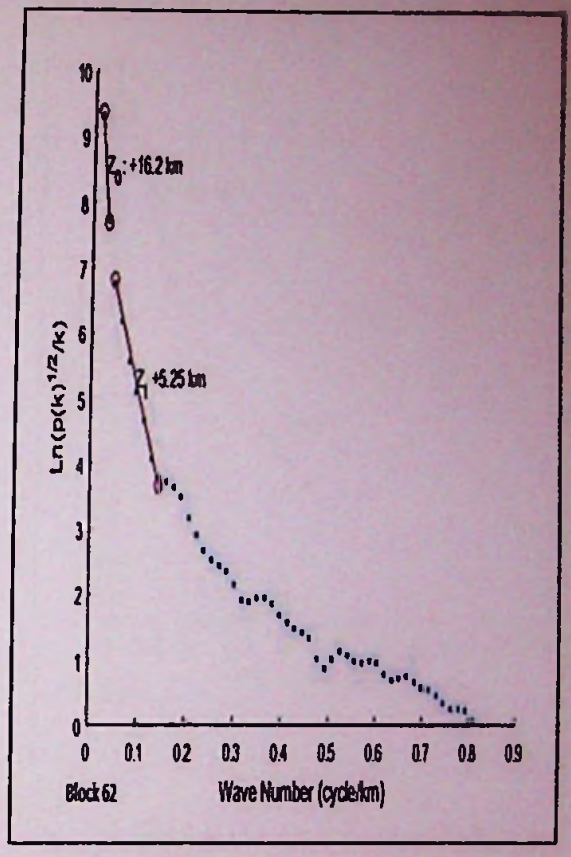

Ln(p(k)^1/2/k)
Z0 : +8.59 km
Z1 : +3.84 km
Block 57
Wave Number (cycle/km)

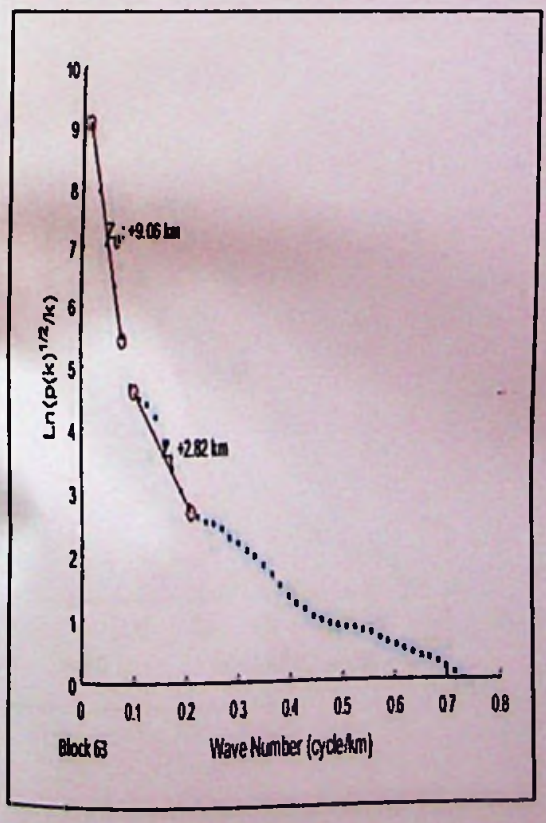

Ln(p(k)^1/2/k)
Z0 : +16.1 km
Z1 : +3.85 km
Block 58
Wave Number (cycle/km)

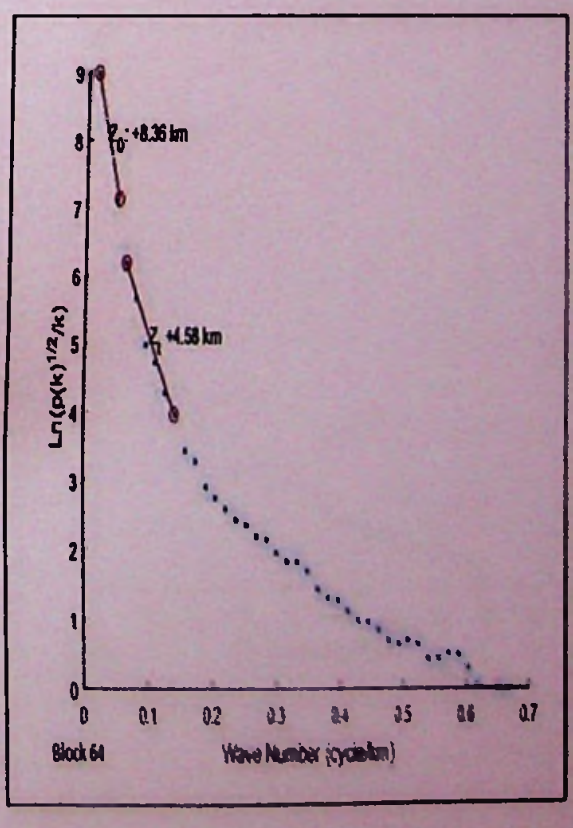

Ln(p(k)^1/2/k)
Z0 : +15.6 km
Z1 : +5.28 km
Block 59
Wave Number (cycle/km)

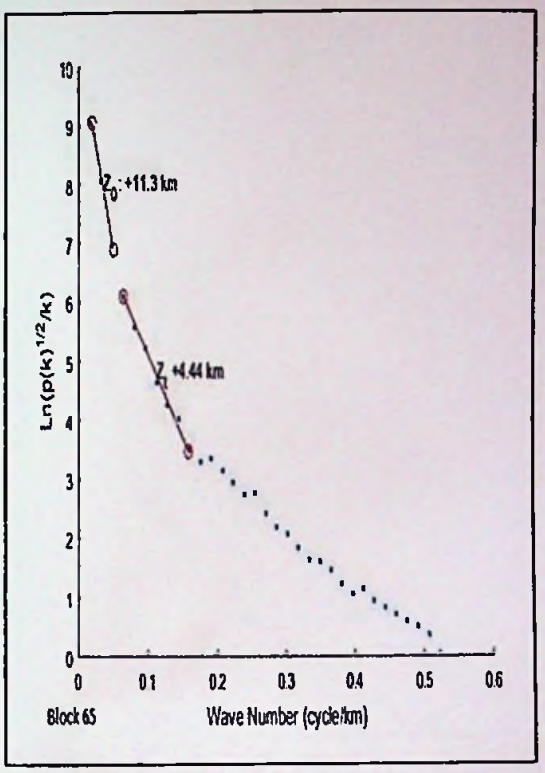

Ln(p(k)^1/2/k)
Z0 : +10.1 km
Z1 : +4.67 km
Block 60
Wave Number (cycle/km)

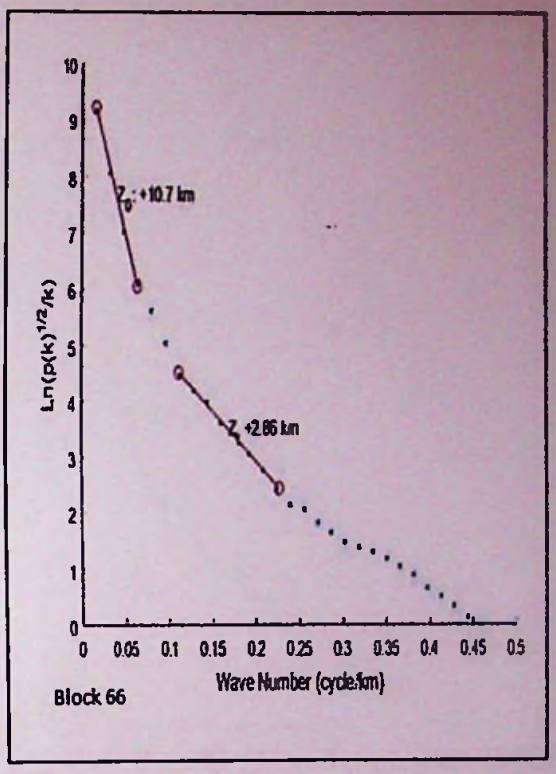

Ln(p(k)^1/2/k)
Z0 : +12.5 km
Z1 : +1.45 km
Block 61
Wave Number (cycle/km)

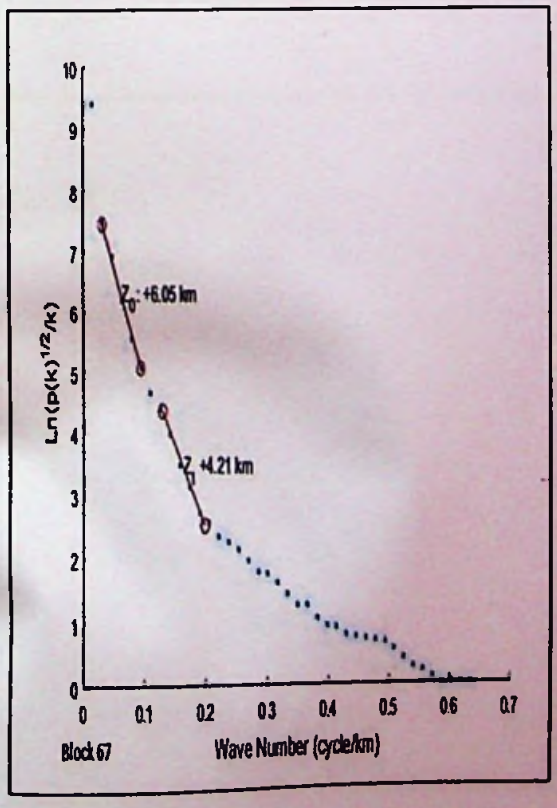

Ln(p(k)^1/2/k)
Z0 : +16.2 km
Z1 : +5.25 km
Block 62
Wave Number (cycle/km)

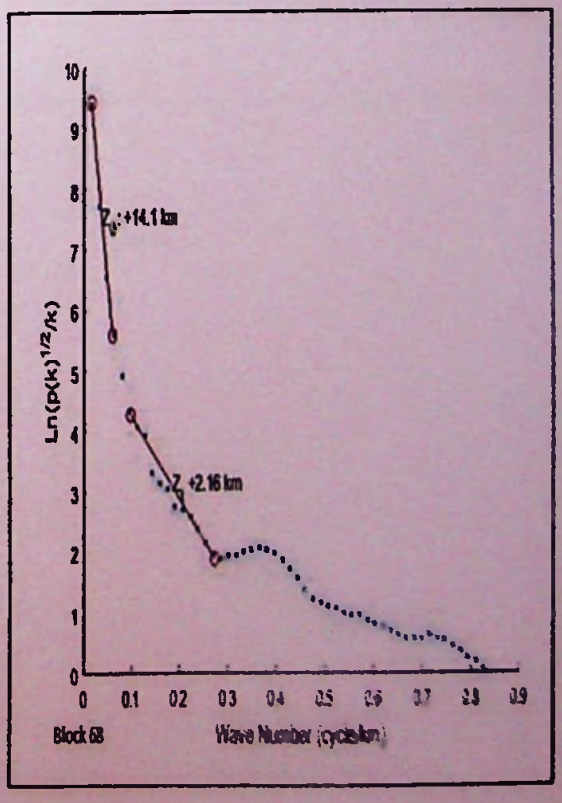

Ln(p(k)^1/2/k)
Z0 : +9.06 km
Z1 : +2.82 km
Block 63
Wave Number (cycle/km)

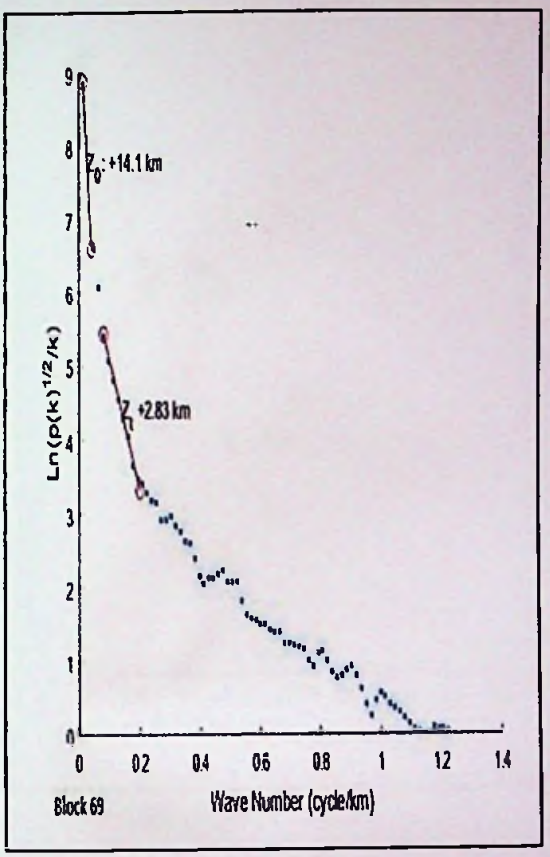

Ln(p(k)^1/2/k)
Z0 : +8.36 km
Z1 : +4.58 km
Block 64
Wave Number (cycle/km)

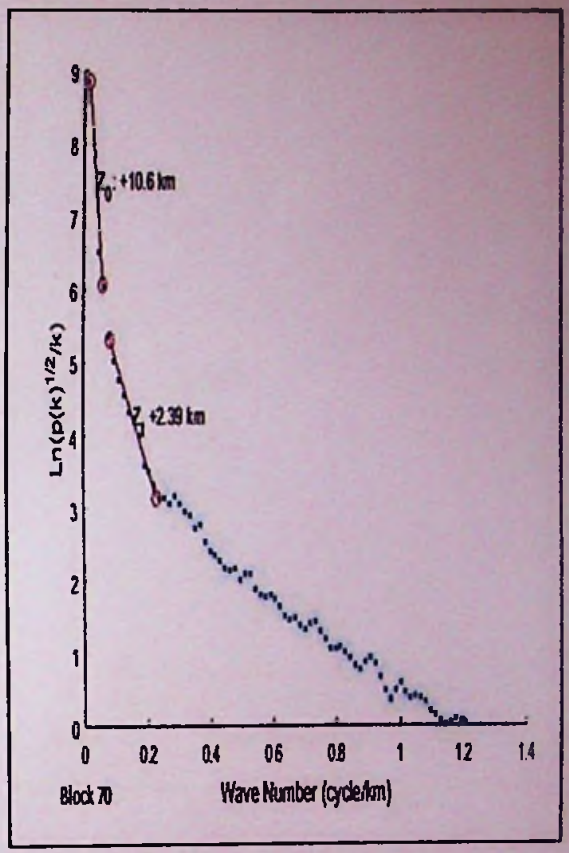

Ln(p(k)^1/2/k)
Z0: +11.3 km
Z1 +4.44 km
Wave Number (cycle/km)
Block 65

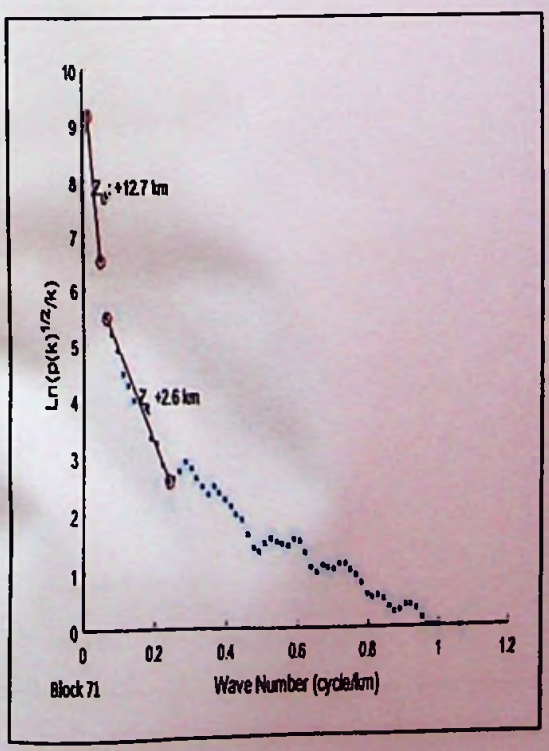

Ln(p(k)^1/2/k)
Z0: +10.7 km
Z1 +2.86 km
Wave Number (cycle/km)
Block 66

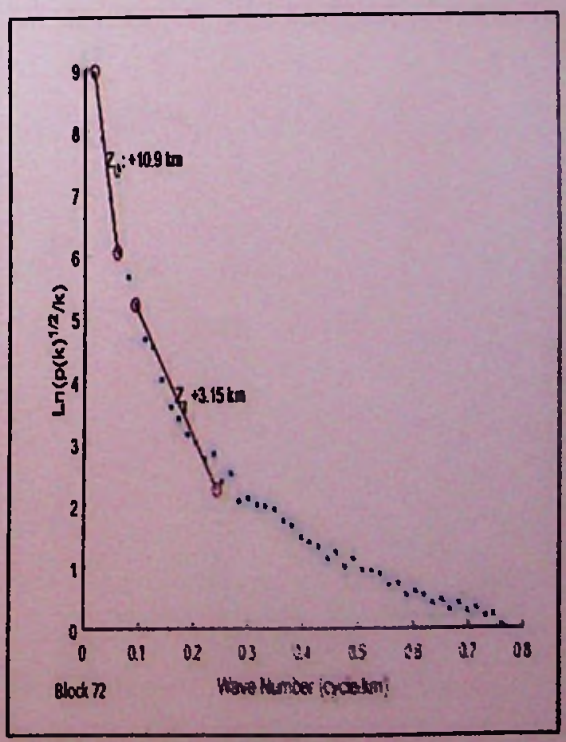

Ln(p(k)^1/2/k)
Z0: +6.05 km
Z1 +4.21 km
Wave Number (cycle/km)
Block 67

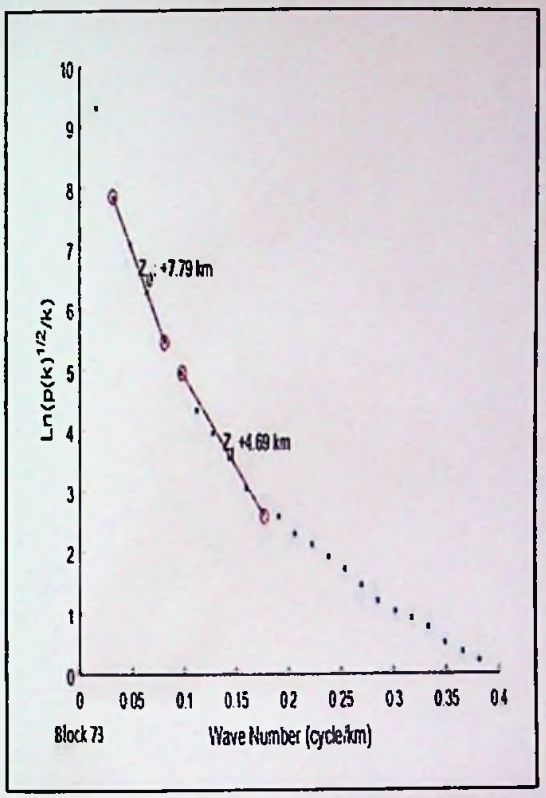

Ln(p(k)^1/2/k)
Z0: +14.1 km
Z1 +2.16 km
Block 68

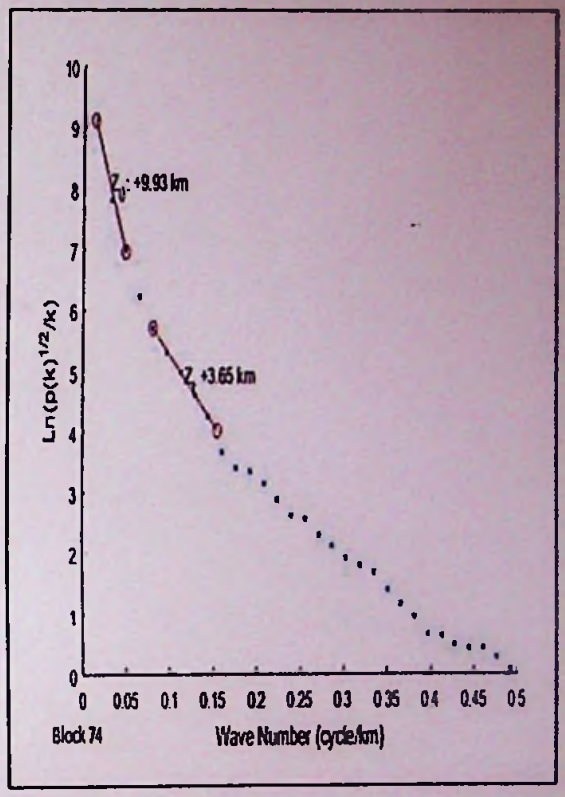

Z0 : +14.1 km
Z1 +2.83 km
Ln(p(k)^1/2/k)
Wave Number (cycle/km)
Block 69

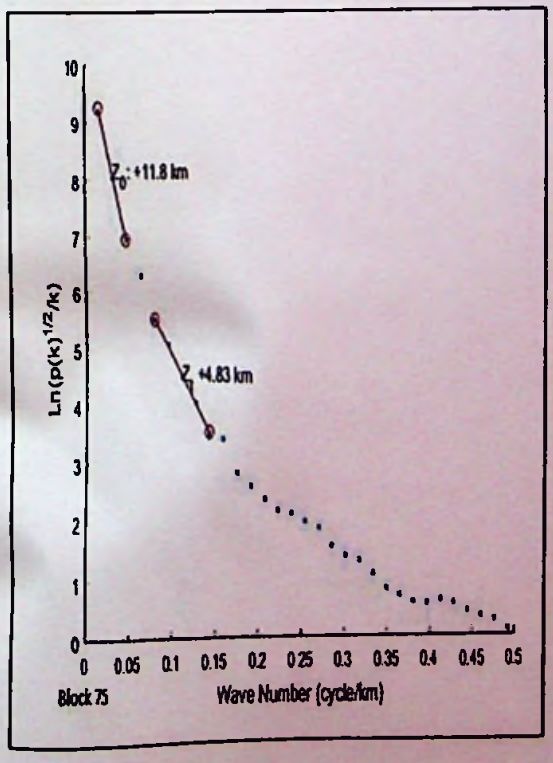

Z0 : +10.6 km
Z1 +2.39 km
Ln(p(k)^1/2/k)
Wave Number (cycle/km)
Block 70

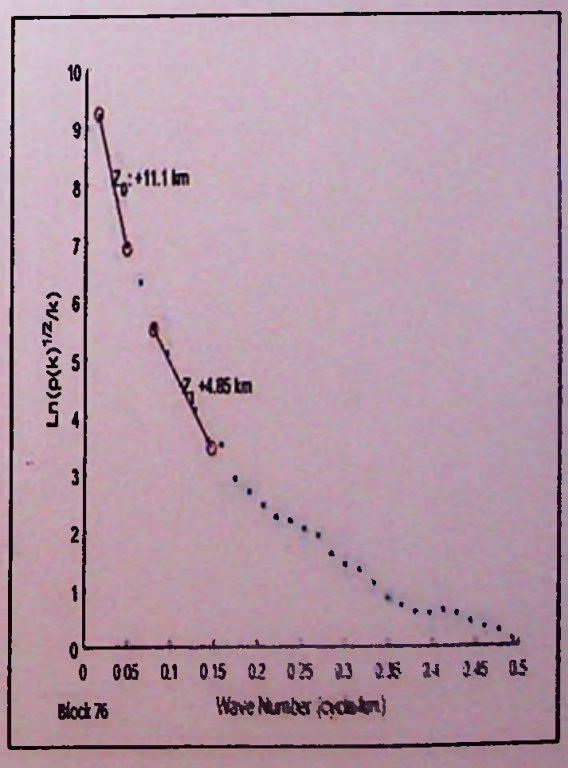

Z0 : +12.7 km
Z1 +2.6 km
Ln(p(k)^1/2/k)
Wave Number (cycle/km)
Block 71

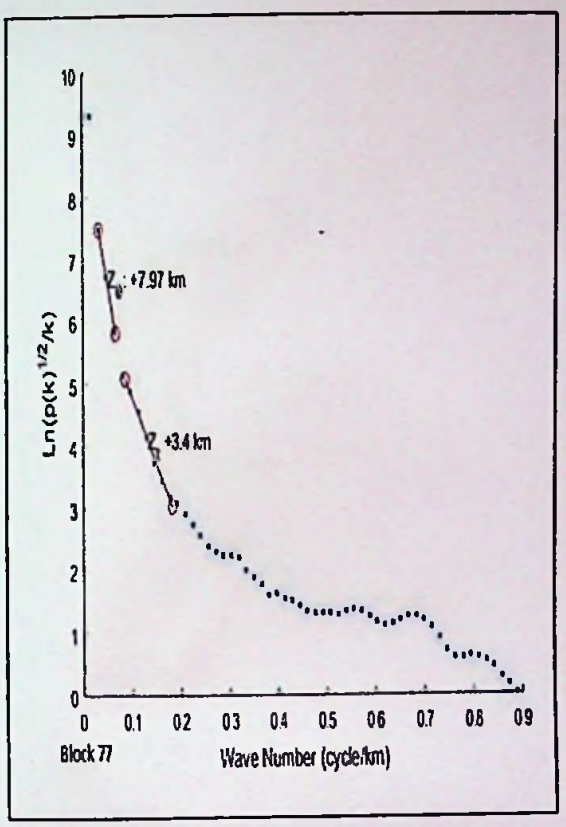

Z0 : +10.9 km
Z1 +3.15 km
Ln(p(k)^1/2/k)
Wave Number (cycle/km)
Block 72

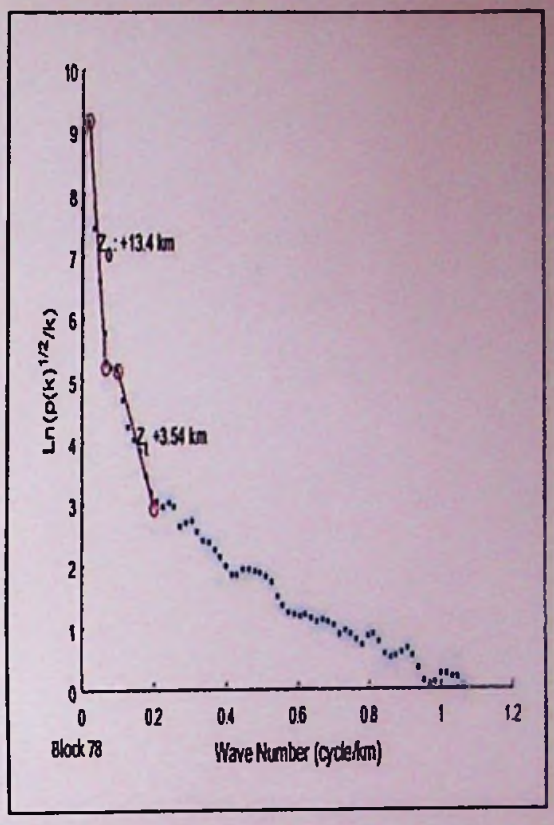

Ln(p(k)^1/2/k)
Z0 : +7.79 km
Z1 +4.69 km
Block 73
Wave Number (cycle/km)

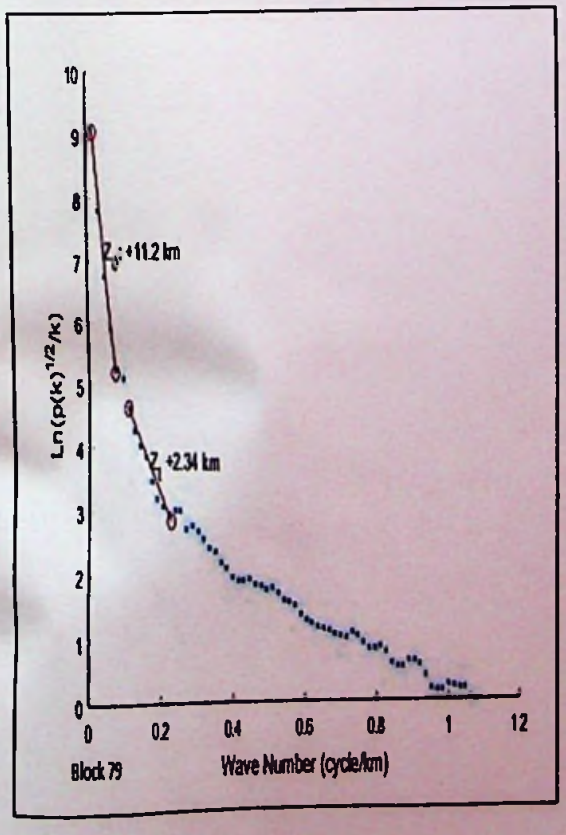

Ln(p(k)^1/2/k)
Z0 : +9.93 km
Z1 +3.65 km
Block 74
Wave Number (cycle/km)

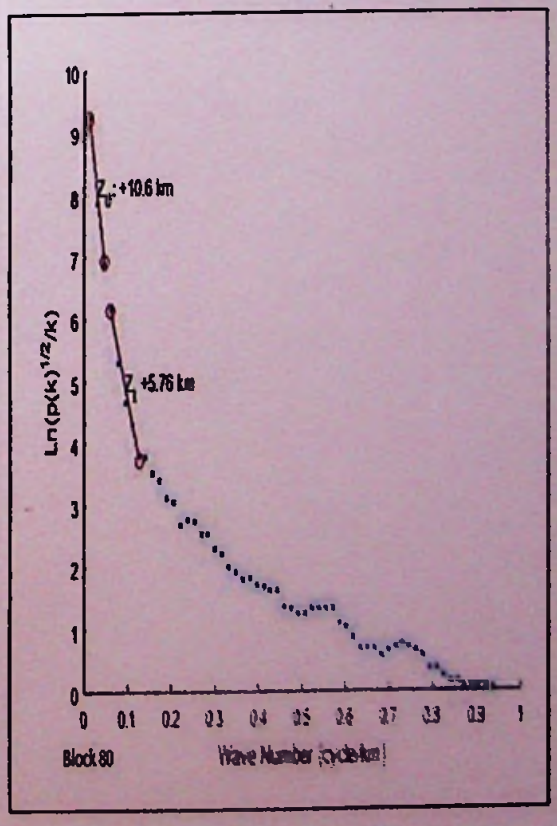

Ln(p(k)^1/2/k)
Z0 : +11.8 km
Z1 +4.83 km
Block 75
Wave Number (cycle/km)

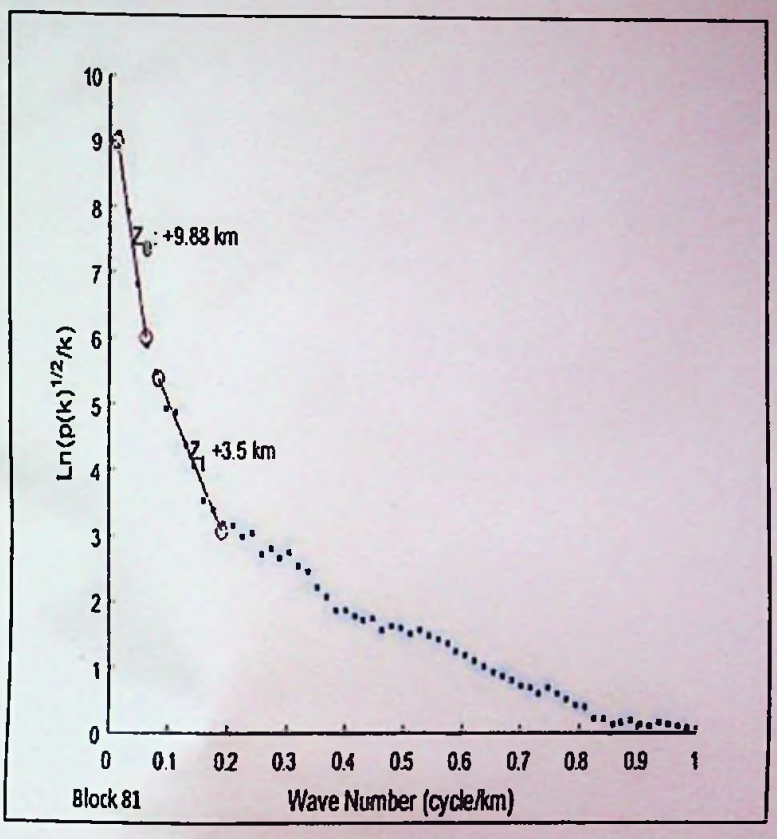

Ln(p(k)^1/2/k)
Z0 : +11.1 km
Z1 +4.85 km
Block 76
Wave Number (cycle/km)


Ln(p(k)^1/2/k)
Z0 : +7.97 km
Z1 +3.4 km
Block 77
Wave Number (cycle/km)


Ln(p(k)^1/2/k)
Z0 : +13.4 km
Z1 +3.54 km
Block 78
Wave Number (cycle/km)


Ln(p(k)^1/2/k)
Z0 : +11.2 km
Z1 +2.34 km
Block 79
Wave Number (cycle/km)


Ln(p(k)^1/2/k)
Z0 : +10.6 km
Z1 +5.76 km
Block 80
Wave Number (cycle/km)


10
9
8
7
6
5
4
3
2
1
0
Ln(p(k)^1/2/k)
Z0: +9.88 km
Z1 +3.5 km
0
0.1
0.2
0.3
0.4
0.5
0.6
0.7
0.8
0.9
1
Block 81
Wave Number (cycle/km)